Dissertation
submitted to the
Combined Faculties for the Natural Sciences and for Mathematics
of the Ruperto Carola University of Heidelberg, Germany
for the degree of
Doctor of Natural Sciences

presented by
Dipl.-Phys.: Frank Weidner
born in: Ansbach

Oral examination: 8.6.2005

Development and Application of a Versatile Balloon-Borne DOAS Spectrometer for Skylight Radiance and Atmospheric Trace Gas Profile Measurements

Referees: Prof. Dr. Ulrich Platt
Prof. Dr. Konrad Mauersberger

Development and Application of a Versatile Balloon-Borne DOAS Instrument for Skylight Radiance and Atmospheric Trace Gas Profile Measurements

In the framework of this thesis, a novel balloon-borne DOAS instrument was developed, characterized in the laboratory and employed during 5 stratospheric balloon flights. Its light weight and small size allows versatile applications on different platforms and under several observation geometries (scanning and fixed limb, nadir, and direct sunlight).

Skylight radiances in the UV/visible range between 330 and 550 nm are measured, and the recorded spectra are analyzed for column densities of O_3, NO_2, BrO, H_2O, and O_4 along the line of sight by applying the Differential Optical Absorption Spectroscopy (DOAS) method.

Radiative Transfer (RT) calculations are used to (a) simulate the measured quantities and (b) infer vertical profiles of O_3, NO_2, and BrO concentrations. Since the measurements were performed under a variety of viewing geometries, they provide a stringent validation of the applied Monte Carlo RT model.

The new method of atmospheric trace gas profiling by balloon-borne UV/vis limb scatter measurements is tested against simultaneous measurements of the same parameters available from in-situ, or UV/vis/near IR solar occultation observations performed on the same payload. Reasonable agreement is found between (a) measured and RT calculated limb radiances and (b) inferred limb O_3, NO_2, and BrO and correlative profile measurements when properly accounting for all relevant atmospheric parameters (temperature, pressure, aerosol extinction, and major absorbing trace gases). Additionally, scanning limb observations provide time-resolved profile information of radicals during sunset.

Entwicklung und Einsatz eines vielseitig anwendbaren ballongestützten DOAS Instruments zur Messung von Streulichtradianzen und atmosphärischen Spurenstoffprofilen

Im Rahmen der vorliegenden Arbeit wurde ein neuartiges, ballongestütztes DOAS Instrument entwickelt, im Labor charakterisiert and auf 5 stratosphärischen Ballonflügen eingesetzt. Sein leichtes Gewicht und seine kleinen Abmessungen erlauben einen vielfältigen Einsatz auf unterschiedlichen Plattformen und unter mehreren Beobachtungsgeometrien (Limbmessungen mit festem bzw. variablem Elevationswinkel, Nadir- und direkte Sonnenlichtbeobachtungen).

Streulicht Radianzen im UV und sichtbaren Wellenlängenbereich zwischen 330 und 550 nm werden gemessen. Die aufgenommen Spektren werden mittels der Differentiellen Optischen AbsorptionsSpektroskopie (DOAS) nach Säulendichten von O_3, NO_2, BrO, H_2O und O_4 entlang des Lichtweges ausgewertet.

Strahlungstransportrechnungen werden benutzt, um (a) die gemessenen Größen zu simulieren und (b) vertikale Profile von O_3, NO_2 und BrO zu erhalten. Da die Messungen unter einer Vielzahl von Beobachtungsgeometrien durchgeführt wurden, bieten sie einen gute Validierung des benutzten Monte Carlo Strahlungstransportmodels.

Die neuartige Methode, atmosphärische Spurenstoffprofile aus ballongestützen Messungen limbgestreuter UV/vis Strahlung zu gewinnen, wird mittels simultaner Messungen derselben Parameter durch in-situ oder UV/vis/nah-IR Sonnenokkultationsmessungen auf derselben Ballonnutzlast überprüft. Es wird eine vernünftige Übereinstimmung zwischen (a) gemessen und mittels Strahlungstransportrechnungen ermittelten Limbradianzen und (b) den errechneten O_3-, NO_2-, und BrO-Profilen und den gleichzeitigen Profilmessungen der anderen Instrumente gefunden, wenn alle relevanten atmosphärischen Parameter (Temperatur, Druck, Aerosolextinktion und die am stärksten absorbierenden Spurengase) richtig berücksichtigt werden. Zusätzlich bieten die Limbmessungen mit variblem Elevationswinkel zeitaufgelöste Profilinformation von Radikalen während des Sonnenuntergangs.

Contents

1 Introduction **11**

2 Atmospheric Chemistry and Dynamics **15**

2.1 Atmospheric Composition and Dynamics 15

2.1.1 Vertical Structure of the Atmosphere 15

2.1.2 Atmospheric Composition 17

2.1.3 The Troposphere and its Dynamics 17

2.1.4 The Stratosphere and its Dynamics 19

2.2 Stratospheric Ozone Chemistry 20

2.3 Stratospheric Nitrogen Chemistry 23

2.3.1 Sources and Sinks of Stratospheric NO_x and NO_y 23

2.3.2 NO_y partitioning 25

2.4 Stratospheric Halogen Chemistry 26

2.4.1 Stratospheric Chlorine Chemistry 26

2.4.2 Stratospheric Bromine Chemistry 28

2.4.3 Stratospheric Iodine Chemistry 30

2.5 Polar Ozone and the Ozone Hole 32

2.6 Stratospheric Water 35

3 Methods **37**

3.1 Differential Optical Absorption Spectroscopy (DOAS) 37

3.1.1 Theory 38

3.1.2 DOAS Evaluation Software 44

3.1.3 Error Sources 44

3.2 Radiative Transfer Calculations 53

3.2.1 Definition of the Radiometric Quantities 53

3.2.2 Scattering and Absorption 54

3.2.3 The Radiative Transfer Equation (RTE) . . . 58
3.2.4 Analytical Approaches to the RTE . . . 58
3.2.5 The Monte Carlo Approach to the RTE . . . 59
3.2.6 The Monte Carlo Radiative Transfer Model (RTM) TRACY . . . 59
3.3 Profile Retrieval . . . 62
3.4 Chemical Modeling . . . 63
3.4.1 The SLIMCAT 3-D Chemical Transport Model (CTM) . . . 63
3.4.2 The 1-D Chemical Box Model LABMOS . . . 64

4 Instrumental and Experimental Details 65

4.1 Setup of the miniDOAS Instrument . . . 65
4.1.1 miniDOAS mk.1 . . . 65
4.1.2 miniDOAS mk.2 . . . 68
4.2 Characterization of the Instrument . . . 69
4.2.1 Instrumental Noise . . . 69
4.2.2 Detector Linearity . . . 72
4.2.3 Spectrograph Stray Light . . . 74
4.3 Observation Geometry . . . 75
4.4 DOAS Evaluation . . . 76
4.4.1 Wavelength Calibration of the Spectrograph . . . 76
4.4.2 General . . . 77
4.4.3 O_3 Evaluation . . . 78
4.4.4 NO_2 Evaluation . . . 81
4.4.5 O_4 Evaluation . . . 81
4.4.6 H_2O Evaluation . . . 81
4.4.7 BrO Evaluation . . . 81
4.4.8 Determination of the Solar Reference Offset . . . 82
4.5 Absolute Radiometric Calibration . . . 83
4.6 The LPMA/DOAS Balloon Payload . . . 83
4.6.1 The Gondola . . . 83
4.6.2 The LPMA Fourier Transform Interferometer . . . 84
4.6.3 The Direct Sunlight DOAS . . . 84

5 Sensitivity Studies and Error Analysis 87

5.1 Sensitivity of the TRACY RT Calculations . . . 87

5.1.1 Aperture Angle of the Telescope . . . 87

5.1.2 Wavelength . . . 90

5.1.3 Elevation Angle of the Detector . . . 91

5.1.4 Azimuth Angle of the Detector . . . 94

5.1.5 Aerosols . . . 97

5.1.6 Scanning Limb Observations . . . 100

5.1.7 Optimization of the Observation Geometry . . . 100

5.2 Sensitivity of the Profile Retrieval . . . 103

5.2.1 Detecting Low Trace Gas Amounts in Front of Large Backgrounds . . . 103

5.2.2 Photochemical Effects . . . 105

5.2.3 Effect of the *a priori* Profile . . . 106

5.2.4 Error Analysis . . . 108

6 Results and Discussion 119

6.1 Flights and Observations . . . 119

6.2 Kiruna 2002 . . . 119

6.2.1 Flight Conditions . . . 119

6.2.2 Instrument Performance . . . 121

6.2.3 O_3 measurements . . . 122

6.3 Kiruna 2003 . . . 125

6.3.1 Flight Conditions . . . 125

6.3.2 Instrument Performance . . . 127

6.3.3 Absolute Limb Radiance Measurements . . . 127

6.3.4 O_3 Results . . . 128

6.3.5 NO_2 Results . . . 132

6.3.6 O_4 Results . . . 134

6.3.7 Scanning Limb Measurements . . . 136

6.3.8 Nadir Measurements . . . 138

6.4 Aire-sur-l'Adour 2003 . . . 140

6.4.1 Flight Conditions . . . 140

6.4.2 Instrument Performance . . . 142

6.4.3 O_3 Results . . . 144

6.4.4 NO_2 Results . . . 144

6.5 Kiruna 2004 . . . 147
6.5.1 Flight Conditions . . . 147
6.5.2 Instrument Performance . . . 148
6.5.3 Absolute Limb Radiance Measurements . . . 148
6.5.4 O_3 Results . . . 154
6.5.5 NO_2 Results . . . 157
6.5.6 BrO Results . . . 157
6.5.7 O_4 Results . . . 159
6.5.8 H_2O Results . . . 161
6.5.9 Upper Limits of Stratospheric IO . . . 164
6.5.10 Scanning Limb Measurements . . . 166
6.6 Teresina 2004 . . . 172
6.6.1 Direct Sunlight Measurements . . . 172
6.6.2 Application of the miniDOAS Instrument on the MIPAS-B2 Gondola . . . 175

7 Conclusions **177**
7.1 Summary . . . 177
7.2 Outlook . . . 178

A Technical Manual **181**
A.1 Profile Retrieval . . . 181
A.1.1 RT Modeling . . . 181
A.1.2 Profile Inversion . . . 182

Publications **185**

Bibliography **187**

Acknowledgements **201**

Chapter 1

Introduction

The discovery of the Antarctic ozone hole (*Farman et al.*, 1985) was an important milestone in atmospheric research. Although it had been already known before that anthropogenic emissions of nitrogen and halogen species reduce the stratospheric ozone burden (*Crutzen*, 1970; *Molina and Rowland*, 1974), the observed almost total destruction of ozone at altitudes where concentrations are usually maximum (i.e. between 12 and 20 km) was quite unexpected. It showed that the fragile equilibrium state of the earth's atmosphere can be significantly disturbed by even relatively small anthropogenic interferences.

Due to the important role the stratospheric ozone layer plays for life on earth by efficiently shielding the surface from biologically dangerous UV radiation, a fact already found in the 19^{th} century by *Cornu* (1879) and *Hartley* (1881), the discovery of its destruction sparked immense research activities. By now, the mechanisms of the ozone hole formation are believed to be qualitatively understood (e.g. *Crutzen and Arnold* (1986); *Solomon et al.* (1986); *Toon et al.* (1986)). Chlorofluorocarbons (CFC) were identified as the precursor substances of the ozone destroying species. Consequently, their production was regulated and, finally, stopped in the Montreal Protocol (1987) and its amendments.

This scientific success was achieved by precise observations and chemical modeling of stratospheric processes. Since then, the ozone layer is constantly monitored by total ozone column measurements from ground stations and satellites in nadir geometry (i.e. looking straight downwards) like TOMS[1] and GOME/ERS-2 (*Burrows et al.*, 1999a) etc. Satellites have the advantage of global coverage and long-term measurements, allowing precise trend observations not only of ozone but also, e.g., halogen species. Satellites in solar occultation geometry (observation of direct sunlight during sunset or sunrise) offer the possibility of vertical profile measurements, however, with limited global coverage. The most recent generation of atmospheric satellites (OSIRIS/Odin (*Murtagh et al.*, 2002; *Llewellyn et al.*, 2004) and SCIAMACHY/Envisat (*Burrows et al.*, 1995)) combine the advantages of both methods, as they allow for the retrieval of the vertical distribution of trace gas concentrations independent of the solar position during daytime by the observation of limb scattered skylight as function of tangent height in the UV and visible spectral range. The profile retrieval requires accurate Radiative Transfer (RT) calculations to model the average path the light traveled through the atmosphere on its way from the sun to the detector. Together with the gigantic data amount involved, this effort has only become possible in the recent years thanks to increased computational power. Consequently, the novel methods require careful validation by correlative ground-based, aircraft, or balloon-borne measurements. For stratospheric trace gas profiling up to altitudes well above the ozone layer (up to ~ 40 km), balloon measurements allow a much higher sensitivity by diving through the profile compared to satellites looking on it from outside and, therefore, play a key role in validation of satellite profile measurements.

[1] http://toms.gsfc.nasa.gov/

Balloon-borne in-situ sensors (e.g. Electro Chemical Cell (ECC) ozone sondes) are regularly launched from many stations worldwide providing precise ozone profiles at all latitudes and seasons. Balloon-borne optical measurements in the UV, visible, and IR spectral range have the advantage of retrieving profiles of several species at the same time but require larger instruments and are, thus, more costly and only performed during larger campaigns. The results obtained from such measurements are not only important for satellite validation but also increase our understanding of chemical and dynamical atmospheric processes. The mentioned modeling of the atmosphere by 3-D Chemical Transport Models (CTM) requires precise observations of all relevant species as initialization and to validate their output parameters.

This work presents one of the most stringent tests ever to validate the individual steps in the still novel method of atmospheric trace gas profiling from limb scatter measurements. The first effort of stratospheric NO_2 profile measurements were already performed by *McElroy* (1988), however, with technological limitations regarding the applied spectrograph and RT calculations compared to today's possibilities. The following steps were realized in the frame of this thesis:

- Development of an new UV/visible DOAS instrument optimized for balloon-borne application with a particular emphasis on compact design to allow versatile applications on several platforms and stable optical imaging to achieve sensitive detection of important stratospheric trace gases
- Application of the Differential Absorption Spectroscopy (DOAS) method (*Platt et al.*, 1979) to the recorded spectra allows the detection of O_3, NO_2, H_2O, O_4, and also weakly absorbing radicals like BrO, and potentially OClO, IO, OIO, or CH_2O.
- Application of a novel backward Monte Carlo RT model developed by *von Friedeburg* (2003) to interpret the measured parameters.
- Absolute calibration of the instrument prior to the balloon flight to measure spectrally resolved limb radiances and validation of the RT model on the absolute radiance level.
- Validation of the RT calculated weighting functions (i.e. relative contribution of individual altitudes to the total observed absorbance) by comparison of measured trace gas Slant Column Densities (SCD) to RT simulations using correlative trace gas measurements performed on the same gondola during balloon ascent and solar occultation by well established in-situ (ECC ozone sonde) and UV/visible/IR direct sunlight sensors (LPMA/DOAS (*Camy-Peyret et al.*, 1993; *Ferlemann et al.*, 2000)) for a variety of observation geometries (fixed limb during balloon ascent, scanning limb during balloon float and nadir observations).
- Retrieval of vertical trace gas profiles using the Maximum A Posteriori (MAP) algorithm developed by *Rodgers* (1976) and comparison to correlative profile measurements from the same balloon gondola to demonstrate the overall feasibility of the novel method of atmospheric trace gas profiling by balloon observation of limb scattered UV/visible radiation.
- Retrieval of time-dependent profile information from scanning limb measurements during balloon float and comparison to photochemically calculated profiles as function of Solar Zenith Angle (SZA) for the radical NO_2.

The present thesis is organized as follows. Chapter 2 gives a brief overview about atmospheric dynamics and chemistry with particular emphasis on the stratosphere and the chemistry of the species under investigation, namely ozone and the NO_y and halogen families. Chapter 3 discusses the methods used for the analysis and interpretation of the measurements. They include the Differential Optical Absorption Spectrometry (DOAS), the employed Monte Carlo Radiative Transfer Model 'TRACY', the Maximum A Posteri (MAP) inversion technique for the vertical profile retrieval, and chemical modeling

of stratospheric trace gas profiles. Chapter 4 describes the setup of the newly developed balloon-borne miniDOAS instrument and the LPMA/DOAS balloon payload, and gives a characterization of the instrument. Experimental details about the DOAS evaluation and the absolute radiometric calibration are also given. Chapter 5 reports on sensitivity exercises studying the sensitivity of the RT calculations on input parameters. The second topic is a detailed error analysis of the retrieved vertical profiles. In chapter 6, the results obtained during 5 measurement campaigns are discussed. A comparison of measured and RT calculated limb radiances is discussed and the retrieved vertical O_3, NO_2, and BrO concentration profiles are compared to correlative profile measurements of the same species obtained by in-situ and direct sunlight DOAS measurements deployed on the same gondola. Chapter 7 concludes the thesis with a summary and an outlook.

Chapter 2

Atmospheric Chemistry and Dynamics

2.1 Atmospheric Composition and Dynamics

2.1.1 Vertical Structure of the Atmosphere

Barometric Formula

The atmosphere is the gaseous layer surrounding our planet attached to it by gravity. The pressure at a given altitude is thus given by the weight of the gas above. At sea level, it is under normal conditions (i.e. at 25^{o}C): $p_0 = 1013\,\text{hPa} := 1\,\text{atm}$. The air density, under these condition, is $\varrho_0 = 2.5 \cdot 10^{19}\,\text{cm}^{-3}$. Assuming constant temperature throughout the atmosphere, the pressure as a function of altitude can be written as (*barometric formula*):

$$p(z) = p_0 \cdot e^{-\frac{z}{z_0}}, \tag{2.1}$$

with the *scale height* $z_0 = \frac{k\ T}{m\ g}$. A good estimate for the whole atmosphere is $z_0 \approx 8\ km$. This implies that the pressure drops to half of its value every $z_{\frac{1}{2}} \approx 5.5\,\text{km}$. This simplified view on the atmosphere suffers from some serious misassumptions, i.e. the temperature is anything but constant throughout the atmosphere (see below) so that the calculated scale height is just a rough estimate. Especially at colder temperatures, e.g. in the stratosphere, the pressure decreases faster leading to scale heights of only $\sim 6\,\text{km}$.

The Atmospheric Temperature Profile and Vertical Structure

The atmosphere can be subdivided into several layers with distinct boundaries, called pauses, according to their temperature (see figure 2.1). In the lowermost layer, the *troposphere*, the temperature profile is governed by adiabatic expansion and compression during elevation and sinking of air masses. The motor for this motion is the solar radiation. During the day, the Earth's surface is heated up, the warm air elevates and is cooled by expansion. An additional cooling occurs in the upper troposphere by radiative cooling in the Infra Red (IR) wavelength range by water. This causes a temperature profile decreasing by $5 - 10\,\text{K}/\text{km}$ and a temperature minimum on the top of the water vapor atmosphere called the *tropopause*. It is generally higher up and, thus, its temperature is lower the higher the tropospheric water content is which again is determined by the surface temperature. So the tropopause altitude ranges between $17 - 18\,\text{km}$ with temperatures of $\sim -80^o$C in the tropics, and between $9 - 13\,\text{km}$ with temperatures of $\sim -50^o$C at higher latitudes, with the lowest tropopause heights occurring in the polar

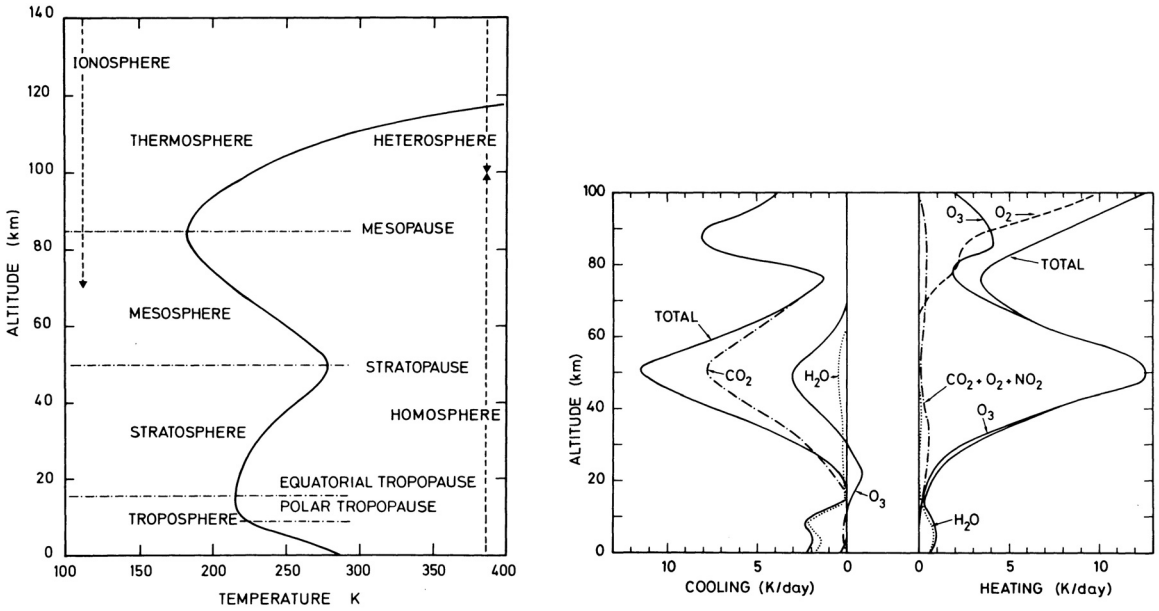

Figure 2.1: Left panel: thermal structure of atmospheric layers. Adopted from (*Brasseur and Solomon*, 1986). Right panel: Vertical distribution of solar short wave heating rates by O_3, O_2, NO_2, H_2O, CO_2, and of terrestrial long wave cooling rates by CO_2, O_3, and H_2O. Adopted from (*London*, 1980).

Table 2.1: Composition of the water vapor free atmosphere (permanent constituents). Adopted from (*Roedel*, 2000)

Gas	Molar Mass	%-vol	%-mass
N_2 (Nitrogen)	28.02	78.09	75.73
O_2 (Oxygen)	32.00	20.95	23.14
Ar (Argon)	39.94	0.93	1.28
Air (average)	28.97	100	100

winter. Due to convection causing this temperature profile, there is a constant, though decreasing with increasing altitude, mixing of the troposphere. In the *stratosphere* the conditions are vice versa. The radiative cooling in and below the tropopause and the heating in the upper stratosphere by the increasing absorption of solar radiation lead to an increasing temperature profile and, thus, little convective and mixed layering. In contrast to the troposphere, the radiative budget is determined by absorption of solar radiation and emission of thermal IR radiation. Only in the polar winter stratosphere, the temperature is slightly decreasing with altitude with a below adiabatic rate of $1 - 2\,^{\mathrm{K}}/_{\mathrm{km}}$. On top of the *stratopause* which is given by a temperature maximum around 50 km, there is the *mesosphere* where temperatures decrease again due to similar reasons as in the troposphere. Above $\sim 75 - 80$ km (*mesopause*), the temperature is again strongly increasing due to the absorption of solar UV radiation (mainly by oxygen) up to values of $1200 - 1500$ K (*thermosphere*). The higher atmospheric layers (above 50 km) is also called *ionosphere* because of the occurrence of ions and free electrons. Finally, the *heterosphere* in an altitude above 100 km denotes the layer where the elements are no longer mixed but layered according to their mass, e.g. above 1000 km there is only hydrogen.

2.1.2 Atmospheric Composition

The major gaseous constituents are given in table 2.1. Additionally, many trace gases important for atmospheric chemistry and climate exist. The most important are CO_2 ($\sim 370 - 380\,\mathrm{ppm}$[1]), CO ($\sim 0.1\,\mathrm{ppm}$), O_3 (between 0.05 ppm in the troposphere and 5 ppm in the stratosphere), halogen species (some hundred ppt in the troposphere), nitrogen oxides (NO_x, between 0.01 ppb in clean air up to 1 ppm in heavily polluted air) and sulphur compounds ($0.1 - 100\,\mathrm{ppb}$), among many others. Due to the fact that 99 % of all atmospheric gases reside below 40 km, this region, i.e. the troposphere and the stratosphere, are the central research topic of atmospheric sciences.

Further important atmospheric constituents are the aerosols. Aerosols, in generally, are all forms of solid or liquid particles floating in the atmosphere. Liquid aerosols are droplets consisting mainly of water (tropospheric clouds or fog) or acid. Solid aerosols are e.g. dust or soot particles. Aerosols can appear in a manifold of shapes, sizes and densities depending on their origin which affects their optical properties. This makes them difficult to handle in radiative transfer which they decisively influence. Their number density N (see figure 2.2) lies in the range between $10^5\,\mathrm{cm}^{-3}$ for heavily polluted air, $10^3\,\mathrm{cm}^{-3}$ for clean continental air, and $10^2\,\mathrm{cm}^{-3}$ for very clean maritime air. Their mass concentration are between $30 - 150\,\mu\mathrm{g/m}^3$ over continents. Aerosol particle sizes typically range between 10 nm and $10\,\mu$m. The size distribution of aged aerosols with radii larger than $\sim 0.1\,\mu$m can be described by a potential distribution (Junge distribution):

$$n^*(r) = \frac{dN(r)}{d\log(r^*)} \sim r^{-s}, \tag{2.2}$$

with $s \approx 3.5 \pm 1$. $r^* = r/r_0$ is the dimensionless radius normalized to a unit radius r_0. The size distribution often has several maxima, called modes, even for a given aerosol type. They can be attributed to the production and age processes of the particles. Two principal classes of aerosol production exist. Firstly, aerosols can be generated by homogeneous condensation of supersaturated vapors from the gas phase (*homogeneous nucleation*). Such vapors can originate from chemical reactions of initially gaseous atmospheric constituents (e.g. sulfuric acid vapors from sulfur dioxide). Secondly, already condensed particles (e.g. mineral dust or sea salt spray) can be raised from the ground by wind. Already floating solid particles can serve as condensation nuclei (*heterogeneous processes*).

Another important issue in tropospheric radiative transfer are clouds. Clouds consist of either condensed water droplets or ice particles and can be classified according to their droplet number density and water content. Clouds influence the radiative transfer and, thus, tropospheric trace gas measurements in many ways. In addition to preventing direct sun measurements, clouds prolong the light path in scattered light measurements. Clouds also have a higher albedo than the earth surface (except for ice, see table 3.2.2). Clouds are difficult to treat in quantitative RT calculations due to their manifold of manifestations which are generally not exactly known.

2.1.3 The Troposphere and its Dynamics

The troposphere contains the air we breath. So changes in its composition by pollution directly affects human health. But its chemical composition also interacts with climate and, thus, weather phenomena which also affects life on earth. CO_2 concentrations, e.g., have dramatically risen since the beginning of industrialization and still do, which might cause a global temperature rise of several degrees. This effect might be amplified by an increase in the H_2O content which also is an important greenhouse gas.

[1] ppm =parts per million, i.e 1 trace gas molecule among 1 million air molecules. Also used are the abbreviations ppb =parts per billion, and ppt =parts per trillion

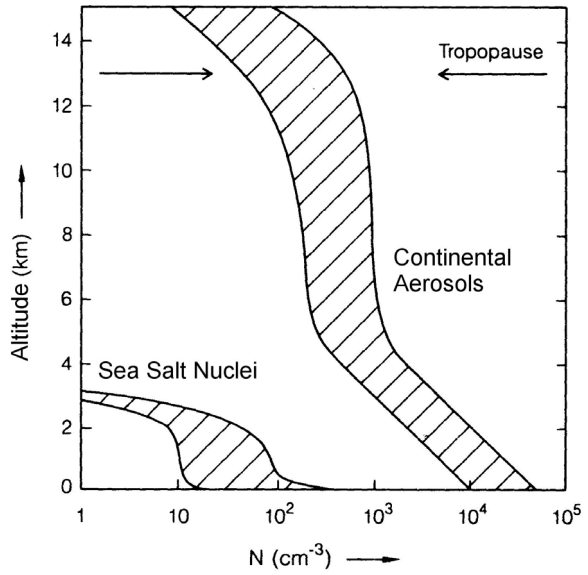

Figure 2.2: Number density vs. altitude for sea salt aerosols (lower left) and continental aerosols (farther right). The arrows denote the approximate tropopause height. Adopted from (*Roedel*, 2000).

The troposphere itself can be subdivided into several layers according to their dynamics. The lowermost millimeters form the *molecular viscous layer* whose name denotes that its dynamics is governed by molecular viscosity while above it is dominated by turbulent diffusion. The next $20 - 200\,\mathrm{m}$ form the *Prandtl layer* where surface friction force dominates over other forces e.g. caused by pressure gradients. The transition to the *free troposphere* above $\sim 1000\,\mathrm{m}$ whose dynamics is dominated by global circulation patterns occurs in the *Ekman layer* where the wind directions changes steadily from the ground wind directions to the direction of the geostrophic winds of the free troposphere. All these layers combined form the *planetary boundary layer* or *mixing layer* which is characterized by steady mixing. This layer is especially interesting when studying the effects of pollution as most of it occurs there.

The free troposphere is dominated by global circulation patterns which are briefly discussed in the following. The global circulation is driven by the strong differences in solar radiation between the tropics and the higher latitudes. The dominating wind system in the tropics up to $\sim 30^o - 35^o$ northern and southern latitude are the *trade winds*, which blow pretty smoothly from northeast on the northern and from southeast on the southern hemisphere, respectively. In the equatorial region they meet forming the Inner Tropical Convergence zone (ITC). The trade winds are driven by the uplift of hot humid air in the zone of the strongest solar radiation. Hence, air has to stream towards the equator and this air is distracted to the west by the Coriolis force. This causes the air pressure to be rather low in the ITC and to increase towards higher latitudes where the air descends again. This circulation pattern is referred to as *Hadley-cell*. Around $\sim 30^o - 35^o$ of latitude, there is the subtropical high pressure belt which is characterized by high pressure, regularly calm winds and a vertical wind component directed downwards. Further poleward, from $35^o - 70^o$, the zone of west wind drift attaches with typically westerly winds which are not as uniform as in the tropics but disturbed by cyclones and anti-cyclones and waves of different wavelengths. The west wind drift are thermal winds caused by the temperature gradient between (sub-)tropical and higher latitudes. At the polar front (subpolar deep pressure rim) the cold air masses from high latitudes and the warmer ones from the moderate latitudes hit. This region is characterized by low pressure which is increasing again towards the poles. At high polar latitudes there are circumpolar east winds at lower altitudes caused by downward winds that are deflected eastwards by the Coriolis force.

2.1.4 The Stratosphere and its Dynamics

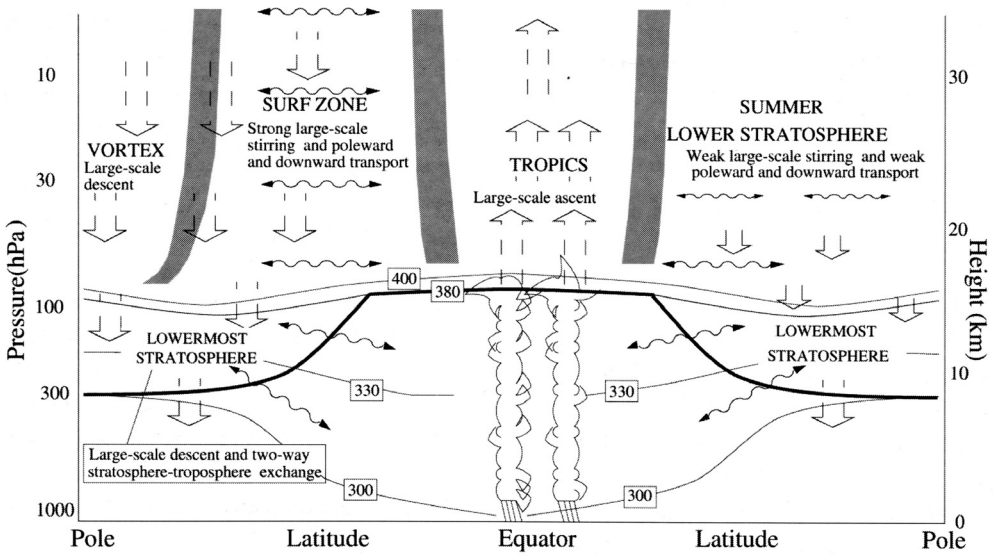

Figure 2.3: Schematic view of the principal regions of the lower stratosphere with distinct transport characteristics. Broad arrows denote the diabatic circulation, wavy arrows denote stirring along isentropic surfaces. The thick black line denotes the tropopause and the thin black lines isentropic surfaces. Isentropic surfaces in the remainder of the stratosphere may be assumed to be roughly horizontal. Adopted from (*WMO*, 1999)

The significance of the stratosphere for life on Earth lies in the fact that it hosts the ozone layer which efficiently shields the surface from life endangering solar UV radiation. Due to anthropogenic pollution the stratospheric ozone concentration has decreased within the last decades which sparked an intense research on the processes leading to this ozone depletion. Stratospheric ozone and trace gas measurements are the main focus of this work, so a brief overview about stratospheric dynamics and chemistry is given in this and the following sections.

The most prominent feature of stratospheric dynamics are the strong zonal winds which can be qualitatively explained as thermal winds. The tropical tropopause and lower stratosphere are very cold compared to the polar stratosphere on the respective summer hemisphere which is heated up by strong solar radiation. This poleward temperature gradient leads to a westward circulation according to the principles of thermal winds. This is why on top of the tropospheric west wind drift there are stratospheric east winds and the poles are circulated by an enormous anticyclonic vortex. On the winter hemisphere, the polar stratosphere is even colder than the tropical stratosphere due to the negligible solar radiation so that the resulting thermal winds are westerlies as in the troposphere. While the summerly east winds are a pretty smooth circulation, the winterly west winds show an uneven structure with wave movements, instabilities and a strong meridional component. That is why there is hardly any meridional mixing in summer while it is rather intense during winter. This can be seen, e.g. in the ozone distribution: ozone produced in the tropical stratosphere can be transported to higher latitudes during winter while this transport breaks down during summer causing lower ozone values in high latitudes during fall compared to spring. An exception marks the polar vortex, which is built during polar night due to the strong temperature gradient between the dark polar stratosphere and the still sunlit stratosphere in the lower latitudes which prevents any meridional mixing. There is also a

strong difference between the northern and southern hemispheres due to the different distribution of the continents on the surface. While the southern hemisphere is dominated by oceans and a circumpolar land mass, the northern hemisphere is more structured with oceans and mountains. This also disturbs the stratospheric circulation which is generally more turbulent with stronger meridional mixing in the northern compared to the southern hemisphere. This is especially true for the Antarctic vortex which is generally more stable and, hence, colder than its Arctic counterpart which is typically more disturbed by intermediate warmings and never inhibits mixing with mid-latitude air totally. This also an impacts the ozone hole which is more severe in the Antarctic (see section 2.5). In spring, the vortex breaks down and the circulation pattern changes from winter to summer type (final warming). This causes fragments of the vortex to be transported to mid-latitudes, e.g. ozone-poor Antarctic air can affect the stratosphere over Australia.

Of particular interest are the exchange processes between troposphere and stratosphere as basically all anthropogenic pollutants, except for e.g. exhaust gases of supersonic jets, are emitted into the troposphere and, hence, enter the stratosphere from there. The low stratospheric water content suggests that the main entry to the stratosphere occurs via the very cold tropical tropopause which acts as a cold-trap. This is explained by the ascent of air in the ITC which continues through the tropopause into the stratosphere. In the extra-tropical stratosphere, the air generally descends and, thus, can enter the troposphere. This effect is strongest in the polar vortex and weakest in the summer hemisphere, and is, e.g., the origin of most of the ozone in the free troposphere. Additionally, there is dynamic mixing of stratospheric and tropospheric air by diabatic and isentropic transport between the $310-380\,\mathrm{K}$ potential temperature (Θ) levels, especially in the region of the subtropical jets at the tropopause breaks. So, following *Hoskins* (1991), the atmosphere can be subdivided into three sections. An *overworld* above the $\Theta = 380\,\mathrm{K}$ isentrope (which is the tropical tropopause height by definition) that is globally above the tropopause, an *underworld* below $\Theta \approx 300 - 310\,\mathrm{K}$ that always belongs to the troposphere, and a *middleworld* in between where the isentropes cut the tropopause and, hence, adiabatic mixing between troposphere and stratosphere is possible. The characteristic exchange times between lower and middle stratosphere range between some months and two years while the timescales for stratosphere troposphere exchange are typically faster so that the mentioned times are also valid for the stratosphere troposphere mixing, an average number for which is $15 - 18$ months.

As a conclusion it should be emphasized that a combination of the mentioned dynamical as well as the radiative and chemical processes described in the following sections are responsible for the observed global distribution of ozone and other species. Experimentally, transport processes can be studied by measuring long-lived species, called tracer species, like CH_4 or N_2O. Theoretically, the combination of these processes can be studied in state-of-the-art 3D Chemical-Transport Models (3D CTM) like, e.g., SLIMCAT (*Chipperfield*, 1999), the KArlsruhe SImulation model of the Middle Atmosphere (KASIMA, *Ruhnke et al.* (1999)), or REPROBUS (*Lefèvre et al.*, 1994, 1998).

2.2 Stratospheric Ozone Chemistry

The first explanation of the formation and destruction of stratospheric ozone was given by *Chapman* (1930). Molecular oxygen (O_2) is photolyzed by ultraviolet radiation ($\lambda \leq 242\,\mathrm{nm}$) which produces oxygen atoms that react with molecular oxygen to ozone via a three-body reaction:

$$O_2 \xrightarrow{h\nu} O + O \qquad (\lambda \leq 242\ nm) \tag{R2.1}$$

$$O + O_2 \xrightarrow{M} O_3 \tag{R2.2}$$

The ozone loss is given by its photolysis with UV radiation ($\lambda \leq 310\,\mathrm{nm}$) followed by the reaction with another oxygen atom or ozone:

$$\mathrm{O_3} \xrightarrow{h\nu} \mathrm{O_2 + O(^1D)} \qquad (\lambda \leq 310\,\mathrm{nm}) \tag{R2.3}$$

$$\mathrm{O(^1D)} \xrightarrow{M} \mathrm{O} \tag{R2.4}$$

$$\mathrm{O_3} \xrightarrow{h\nu} \mathrm{O_2 + O} \qquad (\lambda \leq 1180\ nm) \tag{R2.5}$$

$$\mathrm{O + O} \xrightarrow{M} \mathrm{O_2} \tag{R2.6}$$

$$\mathrm{O + O_3} \longrightarrow \mathrm{2\,O_2} \tag{R2.7}$$

The photolysis of O_2 (reaction R2.1) and thus the O_3 production occurs mainly in the upper stratosphere where radiation at short wavelengths occurs with high intensity. Together with the O_3 photodissociation reactions (R2.3 and R2.5) an equilibrium builds up. Note that by O_3 photolysis atomic oxygen is produced which reacts back to O_3 in the order of seconds (reaction R2.2). An important issue is the timescales on which the reactions occur. This leads to the definition of *families*. The species are grouped in a way that family members can be transformed to other members of the family on short timescales while the lifetime of the whole family is rather long. So the O_x family is defined as the sum of odd-oxygen (e.g. O_3, $O(^1D)$).

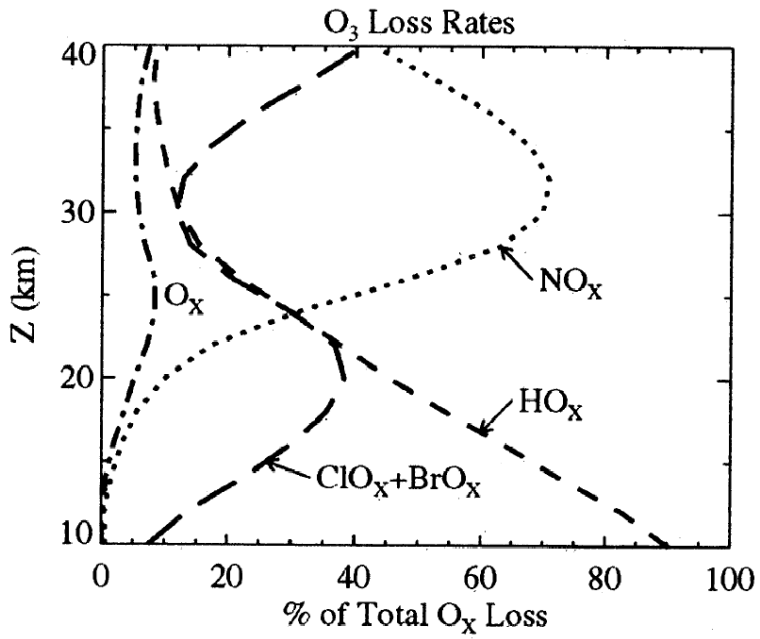

Figure 2.4: O_3 loss rates due to the catalytic cycles involving the HO_x, ClO_x+BrO_x, NO_x, and O_x families, respectively as a percentage of total O_3 loss rates for 60^oN in October as calculated for the 1990s using JPL-97 values (*DeMore et al.*, 1997). Adapted from *Portmann et al.* (1999).

The so obtained O_3 abundances are qualitatively correct, e.g. they predict a concentration maximum in the lower stratosphere but are quantitatively much higher than the measured ones which means that additional O_3 loss processes must exist. Additionally to the O_3 destruction by atomic oxygen several O_3 destroying catalytic reactions exist:

$$\mathrm{X + O_3} \longrightarrow \mathrm{XO + O_2} \tag{R2.8}$$

$$\mathrm{XO + O} \longrightarrow \mathrm{X + O_2} \tag{R2.9}$$

$$\text{net :} \quad \mathrm{O_3 + O} \longrightarrow \mathrm{2\,O_2} \tag{R2.10}$$

where X stands for one of the radicals OH (HO_x-cycle (*Bates and Nicolet*, 1950)), NO (NO_x-cycle (*Crutzen*, 1970; *Johnston*, 1971)), Cl (ClO_x-cycle (*Molina and Rowland*, 1974)), or Br (BrO_x-cycle (*Wofsy et al.*, 1975)). The OH-radical can destroy O_3 also without O atoms:

$$\mathrm{OH} + \mathrm{O_3} \longrightarrow \mathrm{HO_2} + \mathrm{O_2} \quad \text{(R2.11)}$$

$$\mathrm{HO_2} + \mathrm{O_3} \longrightarrow \mathrm{OH} + 2\,\mathrm{O_2} \quad \text{(R2.12)}$$

$$\text{net :} \quad 2\,\mathrm{O_3} \longrightarrow 3\,\mathrm{O_2} \quad \text{(R2.13)}$$

This cycle is especially important at lower altitudes where less atomic oxygen is available. There is another type of catalytic cycle involving species of different families without need for O atoms:

$$\mathrm{X} + \mathrm{O_3} \longrightarrow \mathrm{XO} + \mathrm{O_2} \quad \text{(R2.14)}$$

$$\mathrm{Y} + \mathrm{O_3} \longrightarrow \mathrm{YO} + \mathrm{O_2} \quad \text{(R2.15)}$$

$$\mathrm{XO} + \mathrm{YO} \longrightarrow \mathrm{X} + \mathrm{Y} + \mathrm{O_2} \quad \text{(R2.16)}$$

$$\text{net :} \quad 2\,\mathrm{O_3} \longrightarrow 3\,\mathrm{O_2} \quad \text{(R2.17)}$$

with X=OH and Y=Cl or Y=Br, or X=Cl and Y=Br, respectively. These combined cycles are also more relevant in the lower stratosphere. The halogen cycles are most important at altitudes around $\sim 20\ km$, while the NO_x cycle dominates near ~ 30 km. The relative importance of the different cycles is summarized in figure 2.4. The plotted numbers are calculated for mid-latitudes (60^oN) in October. The relative contributions are different at other latitudes or seasons and, especially, inside the polar vortex where the dramatic ozone losses in spring are dominated by halogen species (see section 2.5).

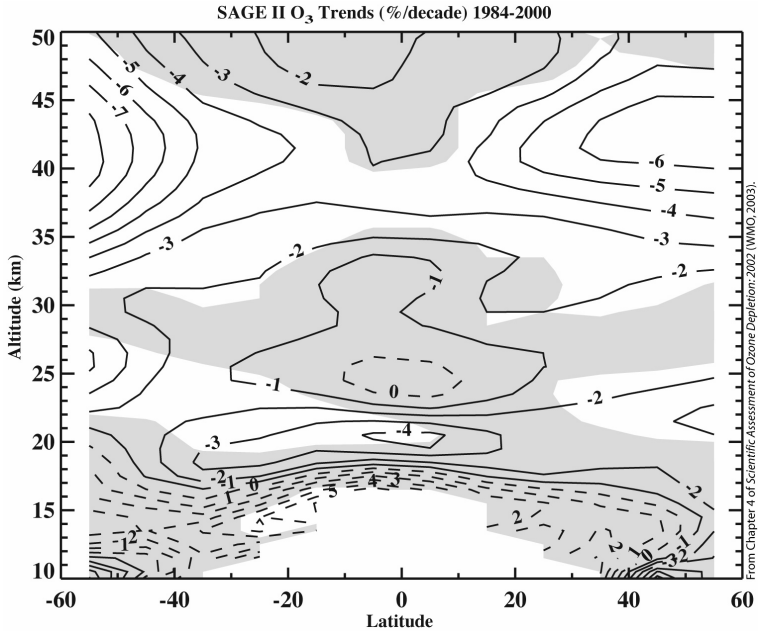

Figure 2.5: Meridional cross section of O_3 profile trends derived from SAGE v6.1 data in the period 1984-2000. Trends were calculated in percent per decade relative to the overall time average. Shaded areas are statistically insignificant at the 2σ (95 %) level. Updated from *Wang et al.* (2002).

Due to anthropogenic emissions, the global total ozone column has decreased within the past years (also see next sections for details). In the period 1997-2001, the global average was $\sim$ 3 % below the pre-1980 values (*WMO*, 2003). The lowest annually averaged total column since the beginning of systematic global observations in the mid-1960s occurred in 1992-1993 with values 5% below the

pre-1980 average. However, the ozone trends differ for different seasons and latitudes. In the tropics (25^oN-25^oS), no significant trend could be observed in the 1980-2000 period, but only a decadal variation of ~ 3 % peak-to-peak approximately in phase with the solar 11-year cycle. Total column ozone loss becomes statistically significant in the 25^o-35^o latitude bands of each hemisphere. In mid-latitudes (35^o-60^o), the total column in the 1997-2001 period is below the pre-1980 average by $\sim 2-4$ % in the northern hemisphere summer-autumn and winter-spring period, and by ~ 6 % year-round in the southern hemisphere. The observed ozone profile trends also show significant deviations for different altitudes (see figure 2.5). The ozone loss is strongest in the $30-50$ km range with a maximum negative decadal trend of $7-8$ % for the 35^o-60^o latitude bands of both hemispheres for the period 1979-2000, as observed by the SAGE-II satellite instrument (*Wang et al.*, 2002).

Due to the decrease in stratospheric chlorine loading over the next 50 years, the total global ozone column is expected to increase in future. For the present time, a leveling of ozone values is expected, but, because of the year-to-year variability, it could take as long as a decade to clearly measure it. For quantitative prediction of O_3 recovery, several effects are relevant next to the halogen abundances. E.g., stratospheric cooling, mainly due to further CO_2 increases, is predicted to enhance future ozone increases in the upper stratosphere. A recovery to pre-ozone-hole-values (i.e. pre-1980) is predicted to be significant by 2050 by model calculations.

2.3 Stratospheric Nitrogen Chemistry

Nitrogen species play an important role in stratospheric chemistry with respect to ozone. On the one hand, they are responsible for ozone depletion (NO_x cycle), but on the other hand, they can transfer ozone destructive halogen species into passive reservoir species.

2.3.1 Sources and Sinks of Stratospheric NO_x and NO_y

Nitrogen species are grouped into two families: odd nitrogen NO_x=NO+NO_2 and all reactive nitrogen NO_y=NO+NO_2+NO_3+$2N_2O_5$+HNO_3+HO_2NO_2+$ClONO_2$+$BrONO_2$. The major source of stratospheric NO_x is the reaction of $O(^1D)$ with N_2O:

$$O(^1D) + N_2O \longrightarrow 2\,NO \qquad (58\ \%) \tag{R2.18}$$

$$\longrightarrow N_2 + O_2 \tag{R2.19}$$

N_2O itself is transported into the stratosphere from the troposphere. Tropospheric N_2O sources are both natural and anthropogenic. The major contributions come from oceans and tropical forests. But as a consequence of biomass burning and the use of artificial fertilizers, the tropospheric N_2O level has risen from $260-285$ ppb (pre-industrial) to $315-317$ ppb (January 2001, (*Prinn et al.*, 2000; *Hall et al.*, 2002)) with an average annual growth rate of ~ 0.75 ppb (*WMO*, 2003). N_2O is an inert gas with a lifetime of 120 ($97-137$) years. There is no destruction process known in the lower stratosphere. Besides the N_2O oxidation (reaction R2.18) there is also N_2O photolysis, which is responsible for ~ 90 % of its removal:

$$N_2O \xrightarrow{h\nu} N_2 + O(^1D) \qquad (\lambda \leq 398\ nm) \tag{R2.20}$$

Another important source of NO_y in the higher atmosphere (mesosphere and lower thermosphere) via N_2 dissociation by Solar Proton Events (SPE), Galactic Cosmic Rays (GCR) and Energetic Electron Precipation (EEP). Quantitative, global estimates of their contribution to the total NO_y production are not available.

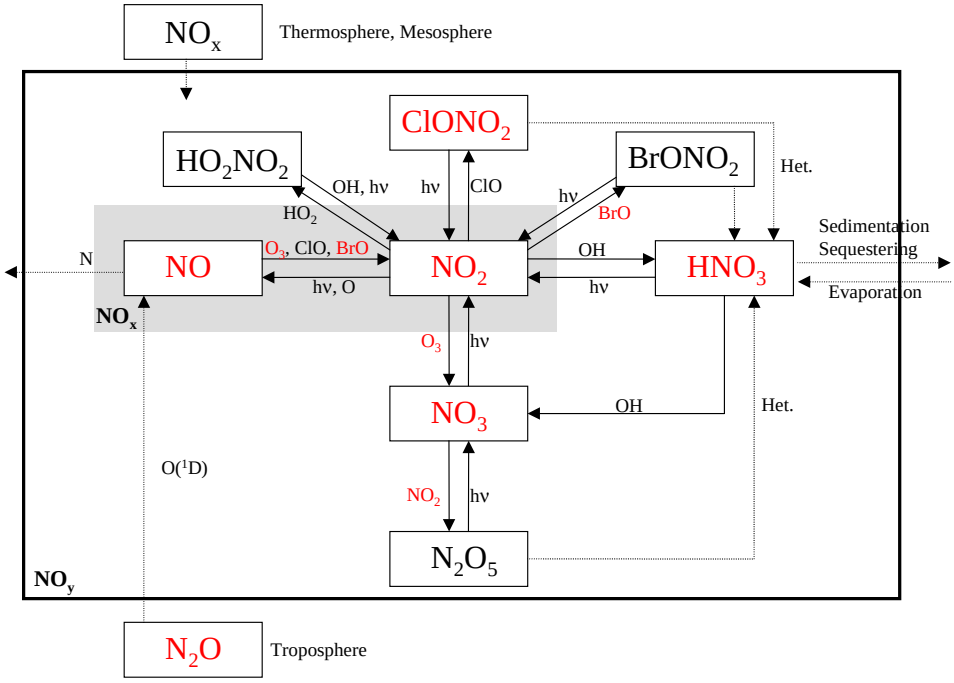

Figure 2.6: Overview on stratospheric NO_y chemistry. Shown are the sources, sinks and pathways (dotted lines: heterogeneous pathways) of the NO_y family. The species marked in red can be measured with the instruments on the LPMA/DOAS balloon payload. (taken from *Bösch* (2002)).

The major sink of stratospheric NO_y is the reaction with atomic nitrogen which is only available above $\sim 30\,\mathrm{km}$ via NO photolysis:

$$\mathrm{NO + N \longrightarrow N_2 + O} \tag{R2.21}$$

During daytime, NO and NO_2 are in a photochemical equilibrium via the reactions:

$$\mathrm{NO + O_3 \longrightarrow NO_2 + O_2} \tag{R2.22}$$
$$\mathrm{NO_2 + O_2 \longrightarrow NO + O_3} \tag{R2.23}$$
$$\mathrm{NO_2 \xrightarrow{h\nu} NO + O} \qquad (\lambda \leq 405\,\mathrm{nm}) \tag{R2.24}$$

Additionally, NO (equation R2.22) oxidation can occur by oxidants other than O_3, like HO_2, CH_3O_2 and ClO. The ratio of NO:NO_2 (*Leighton ratio*) is about 1 : 1 during daytime. With the beginning of the night, NO is rapidly converted to NO_2 due to the missing NO_2 photolysis. NO_2 is oxidized to NO_3 by O_3:

$$\mathrm{NO_2 + O_3 \longrightarrow N_3 + O_2} \tag{R2.25}$$

NO_3 does not exist during daytime because of its fast photolysis:

$$\mathrm{NO_3 \xrightarrow{h\nu} NO_2 + O} \qquad (\lambda \leq 587\,\mathrm{nm}) \tag{R2.26}$$
$$\mathrm{\xrightarrow{h\nu} NO + O_2} \qquad (\lambda \leq 1180\,\mathrm{nm}) \tag{R2.27}$$

NO_3 reacts with NO_2 into the nighttime reservoir species N_2O_5:

$$\mathrm{NO_3 + NO_2 \longrightarrow N_2O_5} \tag{R2.28}$$

which reacts back to NO_2 and NO_3 by collisional decomposition or photolysis during day:

$$N_2O_5 \xrightarrow{M} NO_3 + NO_2 \quad \text{(R2.29)}$$

$$N_2O_5 \xrightarrow{h\nu} NO + O_2 \qquad (\lambda \leq 1252\,\text{nm}) \quad \text{(R2.30)}$$

As all of the NO_3 is destroyed during day, N_2O_5 decreases during the course of the day to restore the old NO_x values. The result of these processes is the typical 'tilt tub-shaped' diurnal variation of NO_2 (*Otten*, 1997). During polar night, N_2O_5 is transformed into HNO_3 by heterogeneous reactions on PSC surfaces (see also section 2.5):

$$N_2O_5 + HCl \longrightarrow HNO_3 + ClONO_2 \quad \text{(R2.31)}$$

$$N_2O_5 + H_2O \longrightarrow 2\,HNO_3 \quad \text{(R2.32)}$$

HNO_3 and, thus, NO_y is also removed out of the gas phase by the formation of PSCs (*denitrification*).

NO_2 plays a crucial role in ozone chemistry as it transforms ozone destroying species into reservoir species:

$$NO_2 + OH \xrightarrow{M} HNO_3 \quad \text{(R2.33)}$$

$$NO_2 + ClO \xrightarrow{M} ClONO_2 \quad \text{(R2.34)}$$

$$NO_2 + BrO \xrightarrow{M} BrONO_2 \quad \text{(R2.35)}$$

The catalysts can be reactivated by photolysis:

$$HNO_3 \xrightarrow{h\nu} NO_2 + OH \qquad (\lambda \leq 604\,\text{nm}) \quad \text{(R2.36)}$$

$$ClONO_2 \xrightarrow{h\nu} Cl + NO_3 \qquad (\lambda \leq 735\,\text{nm}) \quad \text{(R2.37)}$$

$$\xrightarrow{h\nu} ClO + NO_2 \qquad (\lambda \leq 1065\,\text{nm}) \quad \text{(R2.38)}$$

$$BrONO_2 \xrightarrow{h\nu} Br + NO_3 \qquad (\lambda \leq 861\,\text{nm}) \quad \text{(R2.39)}$$

$$\xrightarrow{h\nu} BrO + NO_2 \qquad (\lambda \leq 1129\,\text{nm}), \quad \text{(R2.40)}$$

or by reactions with the OH radical

$$HNO_3 + OH \longrightarrow NO_3 + H_2O. \quad \text{(R2.41)}$$

2.3.2 NO_y partitioning

An important question in stratospheric nitrogen chemistry is the contribution of the individual species to the total NO_y abundance (*NO_y partitioning*). It is determined by the different life times of the individual species and the time constants of the reactions mentioned in the previous section.

Both the production and destruction of HNO_3 are slow processes, so HNO_3 only has a small impact on the diurnal variation of NO_x. During polar winter HNO_3 becomes the by far dominant NO_y species due to the heterogeneous process continuously converting N_2O_5 into HNO_3 (reactions R2.31 and R2.32) and the inefficiency of the HNO_3 destruction processes (reactions R2.36 and R2.41). This effect of denitrification is an important prerequisite for the formation of the polar ozone hole.

As N_2O is the major source of stratospheric NO_y (reactions R2.20 and R2.18), the distribution of NO_y and N_2O are photochemically linked. This correlation defines $NO_y{}^*$ (=standard climatological NO_y) and any deviation of the actual NO_y from it is a sign of denitrification (*Rinsland et al.*, 1996). Below 30 km, NO_y and N_2O are almost linearly anti-correlated (*Loewenstein et al.*, 1993). The slope of this lower stratospheric correlation is controlled by a combination of photochemistry and dynamics. Higher up ($30 - 70$ km), the correlation is dominated by the increasing destruction of NO_y by reaction R2.21

and becomes non-linear as it reaches a maximum. Above $\sim 70\,\mathrm{km}$, NO_y increases rapidly with altitude and is predominately composed of NO (*Michelsen et al.*, 1998).

2.4 Stratospheric Halogen Chemistry

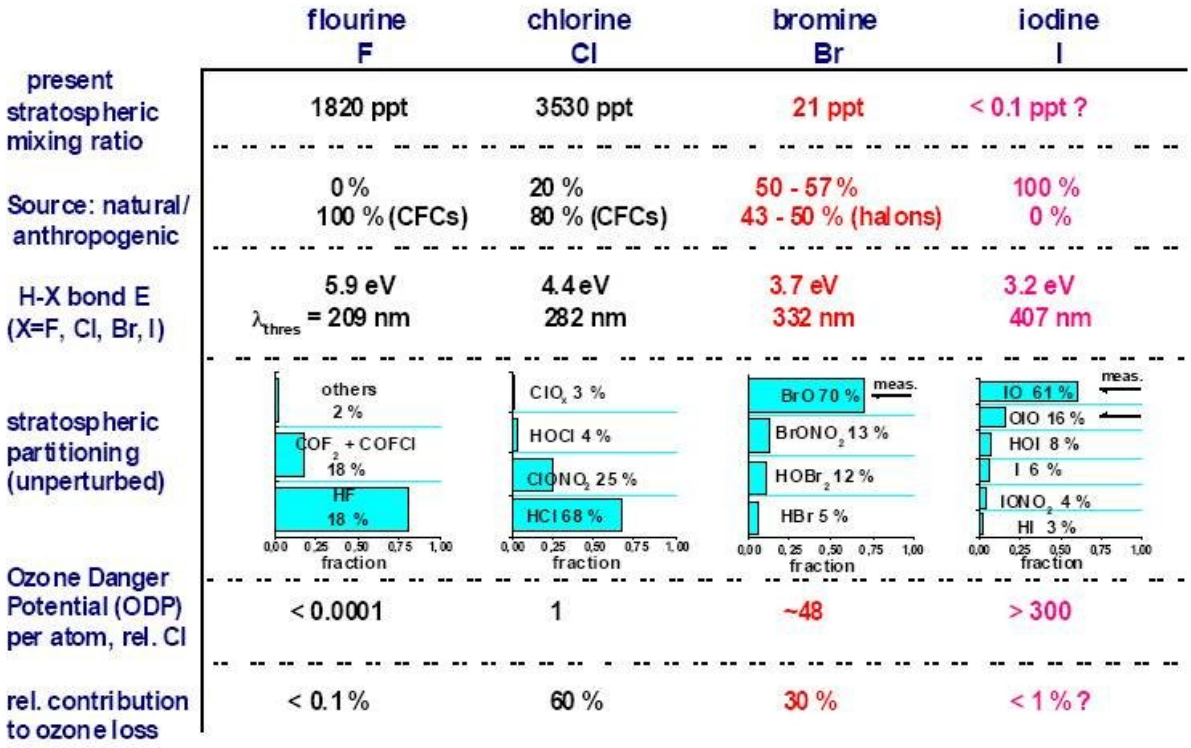

Figure 2.7: Overview about halogen species in the stratosphere and their contribution to ozone depletion.

Halogen species play an important role in stratospheric ozone destruction and are dominantly responsible for the formation of the polar ozone hole. Figure 2.7 gives an overview of the stratospheric abundances and partitioning of halogen species and their significance for ozone loss. Due to their strong bonding, fluor species are very stable and do not play a role in ozone depletion. From chlorine over bromine to iodine, the source gases get less stable and, thus, their Ozone Destruction Potential (ODP) increases. The major contribution to ozone destruction ($\sim$ 60 %) is by chlorine due to its high stratospheric abundances, but bromine also plays an important role as its much lower abundances ($\sim$ 0.6 % of chlorine) is compensated by a $\sim$ 50 times higher ODP. The contribution of iodine species is still not totally clear as there are no exact measurements of its stratospheric load. In the following, the chemistry of the latter three halogen families is briefly discussed.

2.4.1 Stratospheric Chlorine Chemistry

Similarly to the NO_x family, a reactive chlorine family can be defined as ClO_x=Cl+ClO+2Cl_2O_2. Stratospheric ClO_x has several sources all of which originate from chlorinated organic compounds that release Cl atoms either by photolysis or OH or O(^{1}D) initiated oxidation chains. The only relevant natural source is methyl chloride (CH_3Cl) (see figure 2.8, left panel). The most prominent anthropogenic

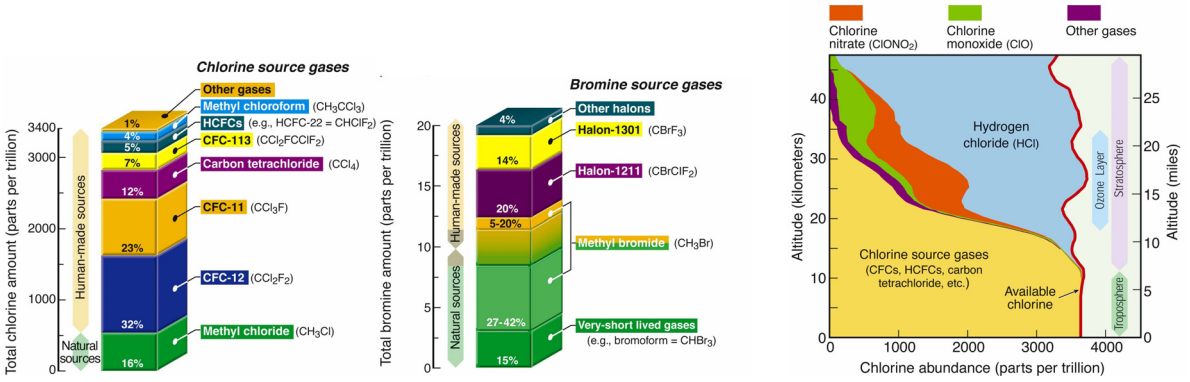

Figure 2.8: Left 2 panels: Overview about the chlorine and bromine source gases, respectively. Right panel: Measurements of chlorine source gases and reactive chlorine species from space for November 1994, 35^o-49^{o}N. The available chlorine ($Cl_y{}^*$) determined by the source gases is nearly constant with altitude up to 47 km.

sources are the ChloroFluoroCarbons (CFC). CFCs are chemically inert gases with a low water solubility, are photostable in the troposphere and, hence, have long tropospheric lifetimes ranging from years to centuries resulting in a uniform distribution. After the Montreal protocol (1997) and the amendment of Copenhagen (1989) and London (1992), the industrial production of CFCs was limited and, finally, stopped. They were replaced by partly halogenated substitutes (HCFCs) that are less stable and, thus, have a shorter atmospheric lifetime. Their portion is small but still growing. Summarizing, organic chlorine in the stratosphere continues to decline slowly, and inorganic chlorine in the stratosphere has stabilized (*WMO*, 2003).

Once released from the organic source, chlorine participates in a number of reactions. As in the case of NO_x, ClO_x is dominated by a fast cyclic transformation between Cl and ClO:

$$\mathrm{Cl + O_3 \longrightarrow ClO + O_2} \tag{R2.42}$$
$$\mathrm{ClO + NO \longrightarrow Cl + NO_2} \tag{R2.43}$$
$$\mathrm{ClO + OH \longrightarrow Cl + HO_2} \tag{R2.44}$$
$$\mathrm{ClO + O \longrightarrow Cl + O_2} \tag{R2.45}$$

and the photolysis of ClO

$$\mathrm{ClO} \xrightarrow{h\nu} \mathrm{Cl + O} \tag{R2.46}$$

The main temporary reservoir species are formed by reactions with NO_2, HO_2 and CH_4:

$$\mathrm{ClO + NO_2} \xrightarrow{M} \mathrm{ClONO_2} \tag{R2.47}$$
$$\mathrm{ClO + HO_2 \longrightarrow HOCl + O_2} \tag{R2.48}$$
$$\mathrm{Cl + HO_2 \longrightarrow HCl + O_2} \tag{R2.49}$$
$$\mathrm{Cl + CH_4 \longrightarrow HCl + CH_3} \tag{R2.50}$$

The active species can be regenerated from $ClONO_2$ and HOCl by photolysis:

$$\mathrm{ClONO_2} \xrightarrow{h\nu} \mathrm{Cl + NO_3} \quad (\lambda \leq 735\,\mathrm{nm}) \tag{R2.51}$$
$$\xrightarrow{h\nu} \mathrm{ClO + NO_2} \quad (\lambda \leq 1065\,\mathrm{nm}) \tag{R2.52}$$
$$\mathrm{HOCl} \xrightarrow{h\nu} \mathrm{Cl + OH} \quad (\lambda \leq 500\,\mathrm{nm}) \tag{R2.53}$$

HCl photolysis only occurs for $\lambda \leq 205\,\text{nm}$ and is, hence, very inefficient but HCl can be split by reaction with OH:

$$\text{HCl} + \text{OH} \quad \longrightarrow \quad \text{Cl} + \text{H}_2\text{O} \tag{R2.54}$$

From the above reactions, only the HOCl photolysis is efficient so that most of the chlorine resides in the inactive species HCl and ClONO_2. A significant activation to ClO_x only occurs between $30 - 45\,\text{km}$ while for altitudes $\sim 50\,\text{km}$ nearly all chlorine resides as HCl (*Solomon* (1999), see also figure 2.8, right panel). As a result, chlorine mainly contributes to ozone destruction in the upper stratosphere, except under ozone-hole conditions where heterogeneous processes lead to a significant chlorine activation (see section 2.5). At low temperatures, chlorine activation can also occur on liquid sulfate aerosols in mid- and polar latitudes (*Solomon et al.*, 1998).

2.4.2 Stratospheric Bromine Chemistry

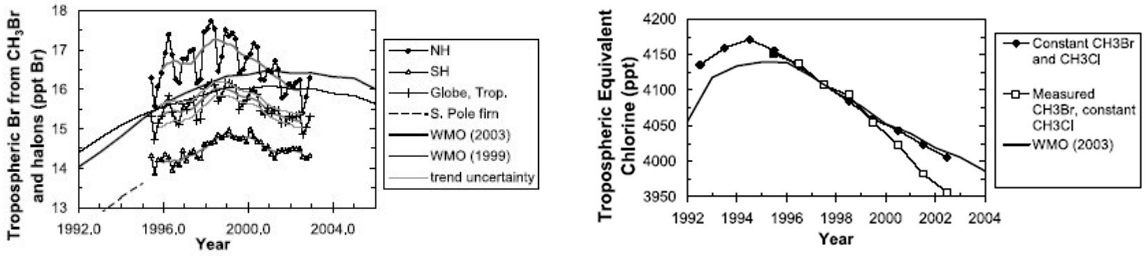

Figure 2.9: Left panel: Mean tropospheric Br from NOAA-CDML flask measurements of CH_3Br and the most abundant halons (symbols), and in recent WMO scenario calculations. Right panel: Changes in the global tropospheric burden of both brominated and chlorinated ozone depleting gases in recent years expressed as Equivalent Cl ($\text{ECl} = \text{Cl} + 45 \cdot \text{Br}$) compared to WMO scenario Ab (*WMO*, 2003). Adopted from *Motzka et al.* (2003).

Bromine species have an important impact on global ozone destruction. About half of the polar ozone depletion occurs due to bromine catalysts. The sources of stratospheric reactive bromine (BrO_x=Br+BrO) are about half natural and half anthropogenic (see figure 2.8, middle panel). The most important source is methyl bromide (CH_3Br) contributing by almost 50 %. CH_3Br is released both naturally (biomass burning, oceans) and anthropogenically (agriculture, leaded gasoline, etc.) with a natural contribution between $60 - 90$ %. It has a lifetime of ~ 0.7 years (*WMO*, 2003). Measurements of Antarctic firn air indicate a positive trend of Br_y from CH_3Br $2 - 2.5$ ppt in the 1950-1995 period (*Sturges et al.*, 2001). CH_3Br has peaked 1998 and has since declined by nearly 5 % (*Motzka et al.*, 2003). Another important source are halogenated hydrocarbon gases (halons) mostly used in fire extinguishers. Although controlled by the Montreal protocol, their global mean is still slightly increasing, due to the use of large halon stocks and the continued production in developing countries, by a mean annual rate of 0.1 ppt which is much slower than was observed in the mid-1990s (*Motzka et al.*, 2003). Consequently, the sum of Br_y from the most abundant halons and CH_3Br peaked in 1998 and declined thereafter in the troposphere at a mean annual rate of -0.25 ± 0.09ppt (mean over 1999-2002, *Motzka et al.* (2003)). This also caused the tropospheric Equivalent Chlorine ($\text{ECl} = \text{Cl} + 45 \cdot \text{Br}$) to decrease faster than expected in *WMO* (2003) (see figure 2.9).

The stratospheric total inorganic bromine (Br_y) for early 1999 in air of 5.6-year mean age is estimated to 21.5 ± 3ppt from BrO measurements and $18.4(+1.8, -1.5)$ppt from organic precursor measurements. The

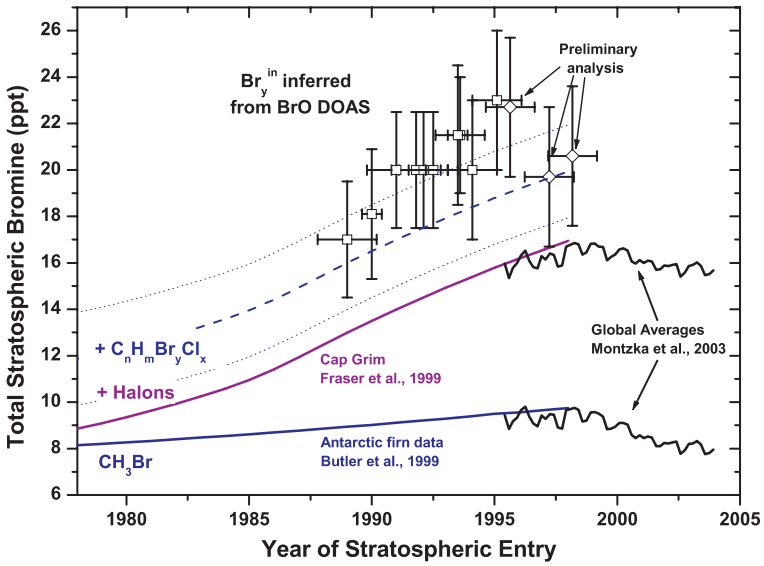

Figure 2.10: Recent history of the total organic (Br_y^{org}) and inorganic (Br_y^{in}) stratospheric bromine budget (taken from *Dorf et al.* (2005), see also *Fraser et al.* (1999); *Butler et al.* (2000); *Montzka et al.* (2003)).

slight offset allows for the possibility of a bromine influx of $3.1(-2.9, +3.5)$ppt from the troposphere to the stratosphere (*Pfeilsticker et al.*, 2000). This question might be answered by a future balloon flight in the tropics where most of the tropospheric influx to the stratosphere occurs. An average annual increase of Br_y of 0.7ppt is found by balloon-borne DOAS measurements in the years 1996-2000 (*Harder et al.* (1998, 2000); *Fitzenberger et al.* (2000); *Pfeilsticker et al.* (2000), see figure 2.10) which is broadly consistent with the increase of tropospheric organic bromine over this time period. *Salawitch et al.* (2005) suggests that inorganic Br_y at and above the tropopause is $4 - 8$ ppt greater than assumed in models used in past trend assessment studies. This study concludes that enhanced Br_y causes photochemical loss of ozone below 14 km to change from being controlled by HO_x catalytic cycles (primarily HO_2+O_3) to a situation where loss by the BrO+HO_2 cycle is also important.

As in case of ClO_x, several reactions transform Br to BrO and vice versa:

$$\mathrm{Br} + \mathrm{O_3} \longrightarrow \mathrm{BrO} + \mathrm{O_2} \quad \text{(R2.55)}$$
$$\mathrm{BrO} + \mathrm{NO} \longrightarrow \mathrm{Br} + \mathrm{NO_2} \quad \text{(R2.56)}$$
$$\mathrm{BrO} + \mathrm{ClO} \longrightarrow \mathrm{BrCl} + \mathrm{O_2} \quad \text{(R2.57)}$$
$$\longrightarrow \mathrm{Br} + \mathrm{OClO} \quad \text{(R2.58)}$$
$$\longrightarrow \mathrm{Br} + \mathrm{ClOO} \quad \text{(R2.59)}$$
$$\mathrm{BrO} + \mathrm{O} \longrightarrow \mathrm{Br} + \mathrm{O_2} \quad \text{(R2.60)}$$
$$\mathrm{BrO} \xrightarrow{h\nu} \mathrm{Br} + \mathrm{O} \qquad (\lambda \leq 515\,\mathrm{nm}) \quad \text{(R2.61)}$$

The major reservoir species are formed by reactions with NO_2, HO_2, ClO, and CH_2O

$$\mathrm{BrO} + \mathrm{NO_2} \xrightarrow{M} \mathrm{BrONO_2} \quad \text{(R2.62)}$$
$$\mathrm{BrO} + \mathrm{HO_2} \longrightarrow \mathrm{HOBr} + \mathrm{O_2} \quad \text{(R2.63)}$$
$$\mathrm{BrO} + \mathrm{ClO} \longrightarrow \mathrm{BrCl} + \mathrm{O_2} \quad \text{(R2.64)}$$
$$\mathrm{Br} + \mathrm{HO_2} \longrightarrow \mathrm{HBr} + \mathrm{O_2} \quad \text{(R2.65)}$$
$$\mathrm{Br} + \mathrm{CH_2O} \longrightarrow \mathrm{HBr} + \mathrm{CHO} \quad \text{(R2.66)}$$

The active BrO_x species are again released by photolysis:

$$BrONO_2 \xrightarrow{h\nu} Br + NO_3 \qquad (\lambda \leq 861\,nm) \tag{R2.67}$$

$$\xrightarrow{h\nu} BrO + NO_2 \qquad (\lambda \leq 1129\,nm) \tag{R2.68}$$

$$HOBr \xrightarrow{h\nu} Br + OH \qquad (\lambda \leq 578\,nm) \tag{R2.69}$$

$$BrCl \xrightarrow{h\nu} Br + Cl \qquad (\lambda \leq 546\,nm) \tag{R2.70}$$

Additionally, Br is rapidly regenerated from HBr by a reaction with OH:

$$HBr + OH \longrightarrow Br + H_2O \tag{R2.71}$$

Because of the rather long wavelength absorption of the reservoir species, their photolysis is very efficient throughout the whole stratosphere. Consequently, the bromine partitioning is shifted more towards the active species compared to chlorine.

Reaction R2.58 is the only relevant source of OClO in the lower stratosphere. Its fast photolysis

$$OClO \xrightarrow{h\nu} ClO + O \qquad (\lambda \leq 470\,nm) \tag{R2.72}$$

prevents the production of large abundances during daytime. However, OClO is widely used as an indicator for chlorine activation and ozone depletion (*Solomon et al.*, 1987; *Erle*, 1999; *Fitzenberger*, 2000; *Wagner et al.*, 2001). Recent simultaneous observations of significant OClO and NO_2 amounts (*Riviere et al.*, 2003) suggest that some uncertainties in the interaction between nitrogen and halogen species. *Canty et al.* (2005) finds that production of OClO occurs more slowly than implied by standard photochemistry. If the yield of BrCl from the reaction of BrO + ClO is increased from 7 % (JPL 2002 value) to 11 % (near the upper limit of the uncertainty), good agreement is found between measured and modeled nighttime OClO. This study highlights the importance of accurate knowledge of BrO + ClO reaction kinetics as well as air parcel trajectories for proper interpretation of nighttime OClO.

An important sink of $BrONO_2$ is the hydrolysis on the surface of PSCs or liquid sulphate aerosols. The hydrolysis together with further heterogeneous reactions can lead to substantial bromine activation also outside the polar vortex (*Erle et al.*, 1998).

2.4.3 Stratospheric Iodine Chemistry

The role of reactive iodine species (IO_x=I+IO) in stratospheric ozone depletion is not yet clear as there are no direct measurements of their abundances which indicates only small amounts. However, due to its high ODP which is more than 300 times higher than that of chlorine, iodine may contribute up to 10 % to total ozone destruction. From balloon-borne DOAS measurements, an upper limit for total I_y in the lower stratosphere ($\leq$ 0.1 ppt) is inferred. This would imply a rather small impact of iodine on ozone ($\leq$ 1 %) (*Bösch et al.*, 2003). In the troposphere, iodine oxides (IO and OIO) could be measured in the midlatitude marine boundary layer (*Alicke et al.*, 1998, 1999; *Hebestreit*, 2001) and in polar latitudes (*Wittrock et al.*, 2000; *Frieẞet al.*, 2001; *Allan et al.*, 2001). The source of tropospheric I_y is believed to be the rapid photolysis of alkyl iodides (e.g. CH_3I, CH_2I_2, C_2H_5I, CH_2ClI). These species are released into the atmosphere from supersaturated oceanic surface waters where they are formed as metabolic byproducts of many maritime algae species (*Davis et al.*, 1996). Additionally, biomass burning may emit some methyl iodide (CH_3I) (*Andreae et al.*, 1996). There are no significant, known anthropogenic sources. CH_3I abundances in the range of $0.1 - 1$ ppt have been reported from the middle and upper troposphere of the tropics and subtropics (*Andreae et al.*, 1996). Unfortunately, no observations of inorganic gaseous iodine are yet available from the upper troposphere and the stratosphere. However, some iodine tied to upper tropospheric aerosols with mixing ratios (possibly) up to 1 ppt were detected (*Murphy et al.*, 1997; *Murphy and Thompson*, 2000).

The discrepancy between the measured tropospheric and the inferred upper limits of stratospheric I_y amounts gives rise to the question if much less iodine enters the stratosphere than frequently assumed or if the stratospheric iodine chemistry, briefly discussed in the following, is still too poorly understood. The first question can best be tackled by precise measurements at the stratospheric entry, i.e. the tropical tropopause, while the second question would require further laboratory studies of the iodine chemistry under stratospheric conditions.

The impact of iodine species on the stratospheric ozone chemistry was first investigated by *Solomon et al.* (1994). They concluded that already 1 ppt of total gaseous iodine would possibly dominate the ozone destruction in the lowermost stratosphere at mid- and high latitudes in winter and suggested that interhalogen reactions can lead to rapid ozone loss:

$$\begin{aligned} X + O_3 &\longrightarrow XO + O_2 && \text{(R2.73)}\\ I + O_3 &\longrightarrow IO + O_2 && \text{(R2.74)}\\ XO + IO &\longrightarrow X + I + O_2 && \text{(R2.75)}\\ &\longrightarrow XOO + I && \text{(R2.76)}\\ &\longrightarrow IX + O_2 && \text{(R2.77)} \end{aligned}$$

where X is either Cl or Br. The I:IO ratio is determined by the above reactions and further influenced by the IO photolysis:

$$IO \xrightarrow{h\nu} I + O \qquad (\lambda \leq 500\,\text{nm}) \qquad \text{(R2.78)}$$

and the reaction of IO with NO and, possibly, OH:

$$\begin{aligned} IO + NO &\longrightarrow I + NO_2 && \text{(R2.79)}\\ IO + OH &\longrightarrow I + HO_2 && \text{(R2.80)}\\ & && \text{(R2.81)} \end{aligned}$$

IO_x is transformed to reservoir species (HI, HOI, and $IONO_2$) by reactions with HO_2 and NO_2:

$$\begin{aligned} IO + HO_2 &\longrightarrow HOI + O_2 && \text{(R2.82)}\\ I + HO_2 &\longrightarrow HI + O_2 && \text{(R2.83)}\\ IO + NO_2 &\xrightarrow{M} IONO_2 && \text{(R2.84)} \end{aligned}$$

The active species are again released by photolysis:

$$\begin{aligned} HI &\xrightarrow{h\nu} I + H \qquad (\lambda \leq 401\,\text{nm}) && \text{(R2.85)}\\ HOI &\xrightarrow{h\nu} I + OH \qquad (\lambda \leq 554\,\text{nm}) && \text{(R2.86)}\\ IONO_2 &\xrightarrow{h\nu} IO + NO_2 && \text{(R2.87)}\\ &\xrightarrow{h\nu} I + NO_3 && \text{(R2.88)} \end{aligned}$$

The photolysis of HOI and $IONO_2$ is very fast and, hence, their daytime abundances are small. The photolysis of HI is inefficient as its absorption occurs mainly in the short UV. Hence, HI is mainly destroyed by reaction with OH:

$$\begin{aligned} HI + OH &\longrightarrow I + H_2O && \text{(R2.89)}\\ & && \text{(R2.90)} \end{aligned}$$

This chemical scheme suggests that IO is by far the dominant I_y species in the lower stratosphere during daytime (*Wennberg et al.*, 1997; *Pundt et al.*, 1998; *Bösch et al.*, 2003). Therefore, the ozone depletion potential per molecule is much higher than that of Cl or Br (e.g. $\text{ODP(I)} > 300 \cdot \text{ODP(Cl)}$).

A still open question is whether or not the OIO molecule is photolytically stable. The ab initio calculations of *Misra and Marshall* (1998) suggest a threshold for the OIO photolysis of 418 nm while its visible absorption spectrum covers the wavelength range 480 – 660 nm (*Himmelmann et al.*, 1996; *Cox et al.*, 1999; *Ingham et al.*, 2000). The absorption of OIO below 480 nm is, if occuring at all, weak and, hence, rapid photolysis does not occur as it does for OClO or OBrO. However, *Allan et al.* (2001) found that OIO must largely predissociate to $I + O_2$ following the absorption and computed extremely fast tropospheric photolysis rates. It is known from laboratory studies that OIO is formed by reactions of IO with either ClO or BrO or by selfreaction with IO:

$$IO + ClO \longrightarrow OIO + Cl \quad \text{or products} \tag{R2.91}$$
$$IO + BrO \longrightarrow OIO + Br \quad \text{or products} \tag{R2.92}$$
$$IO + IO \longrightarrow OIO + I \quad \text{or products} \tag{R2.93}$$

Its sinks are reactions with NO and OH:

$$OIO + NO \longrightarrow IO + NO_2 \tag{R2.94}$$
$$OIO + OH \longrightarrow HOI + O_2 \tag{R2.95}$$

OIO is observed in the marine boundary layer with mixing ratios up to 8 ppt (*Hebestreit*, 2001; *Allan et al.*, 2001). It may form a major gaseous reservoir in the polar stratosphere in winter as its photolysis is weak and the NO concentrations are low while ClO and BrO concentrations are high.

Another question still subject of laboratory and field investigations is whether iodine oxides, i.e. IO and OIO, selfreact and subsequently polymerize into larger, stable chains as indicated by studies of *Vogt et al.* (1999); *Hoffmann et al.* (2001).

2.5 Polar Ozone and the Ozone Hole

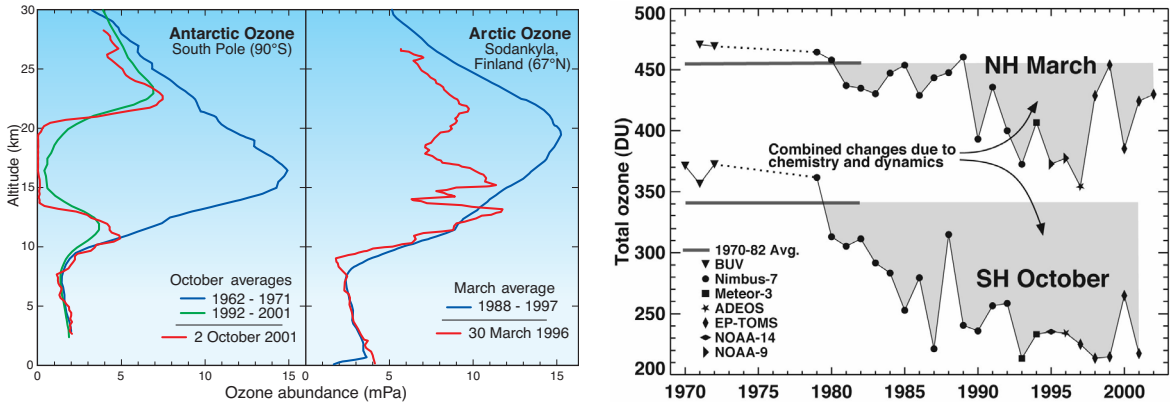

Figure 2.11: Left panel: Typical Antarctic and Arctic ozone profiles under ozone hole conditions (red and green lines, respectively) compared to unaffected conditions (blue lines). Right panel: Time series of the average Antarctic and Arctic total ozone columns in October and March, respectively. The symbols denote satellite measurements and the horizontal gray lines the average total ozone for the years 1970 to 1982. The gray shading shows the combined differences resulting from chemical losses and dynamical processes. Updated by *Newman et al.* (1997). Adopted from (*WMO*, 2003).

Anthropogenic effects on stratospheric chemistry became most obvious to a wider public through the discovery of the so-called *ozone hole* over Antarctica in early 1985 by *Farman et al.* (1985). The polar

Table 2.2: PSC classification according to their optical properties following e.g. *David et al.* (1998).

Type	Signal	Depolarization	Shape	Composition	Temperature
PSC 1a	weak	significant	non-sperical	NAT (solid)	$< -77^oC$
PSC 1b	very weak	negligible	spherical	STS (liquid)	$< -77^oC$
PSC 2	large	strong	non-spherical	ice (solid)	$< -85^oC$

ozone hole is caused by catalytic O_3 destruction involving halogenes under certain conditions that occur in the Antarctic every winter/spring season and, to a lesser degree, also in the Arctic winter. In the Antarctic, it leads to an almost total O_3 destruction in the altitude region where usually the O_3 maximum lies and it typically covers the entire area south of the polar circle. This can be seen in figure 2.11 (left panel) where the typical present situation during ozone hole conditions is compared to measurements before its appearance. Average October values in the ozone layer between 14 and 20 km are reduced by 90 % from pre-1980 values. The Arctic ozone layer is still present in spring as shown by the average March profile obtained over northern Finland between 1988 and 1997. However, March Arctic ozone values are often below pre-1980 average. This can also be seen when looking at the total polar ozone (see figure 2.11, right panel). After 1982, significant polar ozone loss is found which is generally stronger in the Antarctic. In the following, the mechanisms leading to this ozone depletion are briefly discussed.

The formation of the ozone hole includes several stages. The first stage is the formation of the polar vortex due to strong meridional temperature gradients between the sunlit mid-latitudes and the dark polar regions during polar night. This leads to strong circumpolar thermal winds that inhibit meridional mixing of in- and extra-vortex air.

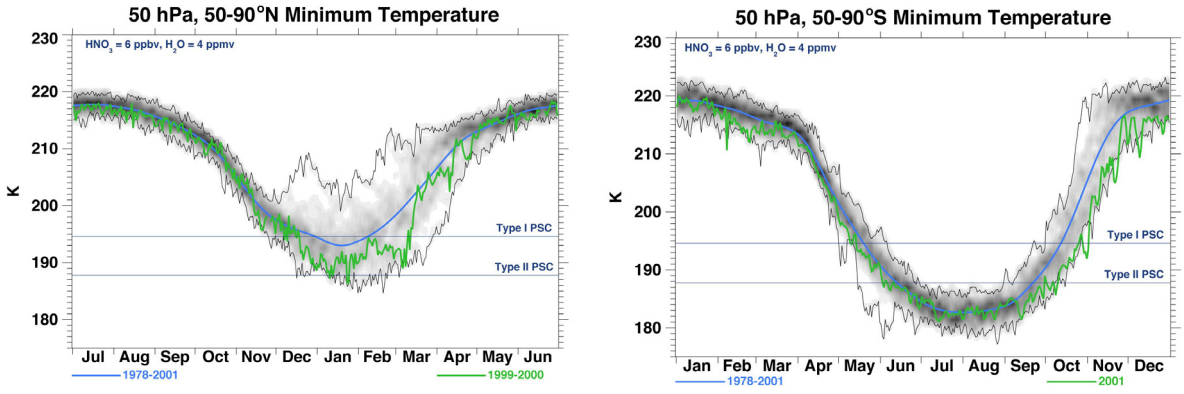

Figure 2.12: Time series of the minimum temperature in the Arctic ($50-90^o$N, left panel) and Antarctic ($50-90^o$S, right panel) on the 50 hPa level. The blue line shows the 1978-2001 mean, and the thin black lines show the maximum-minimum values. Shading shows the density of observation, with heavy shading indicating high and light shading a low probability. The green line shows the values for 1999-2000 (right panel) and 2001 (left panel). Data were processed as in *Scaife et al.* (2000). The horizontal lines indicate the threshold temperature for PSC formation. Adopted from (*WMO*, 2003).

The temperatures in the lower stratosphere drop well below the Polar Stratospheric Cloud (PSC) threshold temperature for several months within the Antarctic vortex (see figure 2.12), another key prerequisite for the ozone hole formation. Although already known for more than a century, the name PSC was first invented by *McCormick et al.* (1982) who presented satellite measurements of high-altitude clouds in the Arctic and Antarctic stratosphere. They can be liquid or solid and mainly consist of water, nitric acid, and sulfuric acid. PSCs can be classified according to their LIDAR (=LIght Detection

And Ranging) backscatter signals (see table 2.2). The mechanisms for the formation and the exact constitution of PSCs is still subject of research. It was first believed that PSCs consist mostly of water ice. These stratospheric ice clouds (now referred to as PSC type 2) are usually optically thick and brilliant in color. They can occur when the temperature falls below the freezing point ($T_{ice} \approx -85^o$C). But *McCormick et al.* (1982) also observed optically thinner PSCs at warmer temperatures (type 1 PSCs). *Crutzen and Arnold* (1986) and *Toon et al.* (1986) suggested that these consist of solid Nitric Acid Trihydrate (NAT=$HNO_3 \cdot 3H_2O$) which is supported by laboratory measurements of *Hansen and Mauersberger* (1988) who showed that the NAT crystal is stable a few degrees above the ice frost point ($T_{NAT} \approx -77^o$C) under stratospheric conditions. Nitric Acid Dihydrate (NAD=$HNO_3 \cdot 2H_2O$) could also form stable particles up to temperatures of 2.5^{o}C below T_{NAT}. Type 1a particles typically have diameters in the range of $1 - 10\,\mu$m (*WMO*, 2003), but also HNO_3 containing particles believed to be NAT (or NAD) rocks have been observed by *Fahey et al.* (2001). The observed number concentrations cover a wide range between $10^{-5} - 1\,\mathrm{cm}^{-3}$, with the lower concentrations for the bigger diameters. *Voigt et al.* (2000) brought the first direct evidence for the existence of NAT particles in the stratosphere by balloon-borne in-situ measurements finding an H_2O/HNO_3 mole rate in a PSC layer with a stoichiometric ratio of 3 : 1. Nitric acid containing PSCs can also occur in the form of liquid Supercooled Ternary $H_2SO_4/HNO_3/H_2O$ Solutions (STS) which are formed by the ubiquitous Stratospheric Sulfate Aerosol (SSA) particles, i.e. H_2SO_4/H_2O solutions, taking up large amounts of HNO_3 at temperatures below -80^oC (*Carslaw et al.*, 1994), which are then called PSC type 1b.

PSCs affect the stratospheric chemistry in two ways. Firstly, they cause a decrease in NO_y by uptake of HNO_3 (*denitrification*), and secondly, on the surfaces of the PSC particles, heterogeneous reactions build up large abundances of ClO_x out of otherwise unreactive reservoir species (*chlorine activation*):

$$\mathrm{ClONO_2(g) + HCl(s) \longrightarrow Cl_2(g) + HNO_3(s)} \quad \text{(R2.96)}$$
$$\mathrm{ClONO_2(g) + H_2O(s) \longrightarrow HOCl(g) + HNO_3(s)} \quad \text{(R2.97)}$$
$$\mathrm{HOCl(g) + HCl(s) \longrightarrow Cl_2(g) + H_2O(s)} \quad \text{(R2.98)}$$

Also bromine reservoir species are activated:

$$\mathrm{BrONO_2(g) + HCl(s) \longrightarrow BrCl(g) + HNO_3(s)} \quad \text{(R2.99)}$$
$$\mathrm{ClONO_2(g) + H_2O(s) \longrightarrow HOBr(g) + HNO_3(s)} \quad \text{(R2.100)}$$
$$\mathrm{HOBr(g) + HCl(s) \longrightarrow BrCl(g) + H_2O(s)} \quad \text{(R2.101)}$$

These reactions cannot occur in gasphase as the activation energy is not available. With the return of sunlight in polar spring, the photolytically unstable compounds Cl_2 and HOCl are rapidly photolyzed to ClO_x:

$$\mathrm{Cl_2} \xrightarrow{h\nu} \mathrm{2\,Cl} \qquad (\lambda \leq 495\,\mathrm{nm}) \quad \text{(R2.102)}$$
$$\mathrm{HOCl} \xrightarrow{h\nu} \mathrm{Cl + OH} \qquad (\lambda \leq 500\,\mathrm{nm}) \quad \text{(R2.103)}$$

These processes in the absence of NO_x which prevents $ClONO_2$ formation lead to ClO_x concentrations up to 100 times above what is usually observed.

The chemical O_3 destruction occurs primarily by two gas-phase catalytic cycles, the ClO-dimer cycle (*Molina and Molina*, 1987) and the ClO/BrO cycle (*McElroy et al.*, 1986):

$$\text{Cycle 1:} \quad \mathrm{ClO} + \mathrm{ClO} \xrightarrow{M} \mathrm{ClOOCl} \tag{R2.104}$$
$$\mathrm{ClOOCl} \xrightarrow{h\nu} 2\,\mathrm{Cl} + \mathrm{O_2} \tag{R2.105}$$
$$2\,(\mathrm{Cl} + \mathrm{O_3} \longrightarrow \mathrm{ClO} + \mathrm{O_2}) \tag{R2.106}$$
$$\text{net:} \quad 2\,\mathrm{O_3} \longrightarrow 3\,\mathrm{O_2} \tag{R2.107}$$

$$\text{Cycle 2:} \quad \mathrm{BrO} + \mathrm{ClO} \longrightarrow \mathrm{Br} + \mathrm{Cl} + \mathrm{O_2} \tag{R2.108}$$
$$\longrightarrow \mathrm{BrCl} + \mathrm{O_2} \tag{R2.109}$$
$$\mathrm{BrCl} \xrightarrow{h\nu} \mathrm{Br} + \mathrm{Cl} \tag{R2.110}$$
$$\mathrm{Br} + \mathrm{O_3} \longrightarrow \mathrm{BrO} + \mathrm{O_2} \tag{R2.111}$$
$$\mathrm{Cl} + \mathrm{O_3} \longrightarrow \mathrm{ClO} + \mathrm{O_2} \tag{R2.112}$$
$$\text{net:} \quad 2\,\mathrm{O_3} \longrightarrow 3\,\mathrm{O_2} \tag{R2.113}$$

Of lesser importance is a third cycle requiring atomic oxygen:

$$\text{Cycle 3:} \quad \mathrm{ClO} + \mathrm{O} \longrightarrow \mathrm{Cl} + \mathrm{O_2} \tag{R2.114}$$
$$\mathrm{Cl} + \mathrm{O_3} \longrightarrow \mathrm{Cl} + \mathrm{O} \tag{R2.115}$$
$$\text{net:} \quad \mathrm{O_3} + \mathrm{O} \longrightarrow 2\,\mathrm{O_2} \tag{R2.116}$$

The abundances of BrO determine the removal rate by cycle 2. It is less important in the Antarctic with higher chlorine activation but may account for up to 60 % of the Arctic ozone loss in cold winters (*Chipperfield and Pyle*, 1998). In contrast to ClO, the abundance of BrO is not strongly affected by reactions involving PSCs because less than half of the available inorganic bromine budget is sequestered in reservoirs such as $BrNO_3$ and HBr.

With increasing solar radiance, renoxification, i.e. the release of NO_x out of reservoir species, begins and the ozone depletion is thus slowed down and finally ends. In case of denitrification, this cannot happen until the final break-down of the vortex and, thus, mixing with mid-latitudinal air resupplies polar NO_x.

2.6 Stratospheric Water

An important issue in atmospheric radiative transfer and climate research is the amount of stratospheric water. Due to the fact H_2O mixing ratios are smaller by several orders of magnitude in the stratosphere compared to the troposphere, (*Brewer*, 1949) postulated that the air enters the stratosphere via the very cold tropical tropopause which act as a cold trap dehydrating the air. However, thes dehydration effects are still subject of research. Central question is the discrepancy between the observed average H_2O mixing ratio of the air entering the stratosphere ($[H_2O]_e = (3.7 \pm 0.25)$ ppm (*SPARC*, 2000)) and the average tropical tropopause temperature which lies significantly above the dewpoint corresponding to the stated H_2O mixing ratio. However, only few measurements of the water concentration of the $TropicalTransitionLayer$ (TTL) exist (*Holton and Gettelmann*, 2001). Next to dynamical reasons (e.g. *Sherwood and Dessler* (2001)), the existence of $Sub-VisibleCirrus$ (SVC) might be an explanation of the mentioned discrepancy. Several potential methods for SVC formation exist. One of them is by strong convection causing clouds to penetrate into the stratosphere. Temperature gradient and water vapor cause ice formation. Finally, large crystals fall, while small crystals remain as SVC. Another potential

mechanism of SVC formation includes freezing on also lifted aerosols. *Hartmann et al.* (2001) showed that tropopause cirrus crucially affects the heat balance of the stratosphere and may be important in dehydrating the air. Thus the study of thin cirrus may contribute to the understanding of the dehydration, dynamics, and radiative balance of the tropical tropopause layer (*Clark et al.*, 2003).

The major chemical source of H_2O in the stratosphere is by oxidation of methane which can be approximately described by the following pseudo-reaction equation considering only the stable end products:

$$CH_4 \quad \longrightarrow \quad 2H_2O + CO_2 \tag{R2.117}$$

The experimentally determined H_2O-yield per CH_4 molecule is 1.94 ± 0.27 (*Dessler et al.*, 1994) or 1.975 ± 0.03 (*Zöger et al.*, 1999b,a), i.e. close to 2. This leads to constant value of the *potential water* (*Brasseur and Solomon*, 1986):

$$2\,[CH_4] + [H_2O] \quad = \quad cons \approx 8\,\text{ppm}. \tag{R2.118}$$

Oltsman and Hofmann (1995) first observed a statistically significant increase of stratospheric H_2O with balloon-borne frostpoint-hygrometer measurements over Boulder, Colorado. This positive trend is confirmed by several studies over the last decades (*SPARC*, 2000) and lies in the order of $1\,\%/_{\text{a}}$ or $40\,\text{ppb}/_{\text{a}}$.

Chapter 3

Methods

3.1 Differential Optical Absorption Spectroscopy (DOAS)

The Differential Optical Absorption Spectroscopy was decisively developed at the IUP Heidelberg (e.g. *Platt et al.* (1979, 1980); *Platt and Perner* (1980)). Since then, it has evolved into a versatile method for atmospheric remote sensing.

DOAS applications can be subdivided into 2 principal categories: passive and active ones. Active DOAS systems use an artificial lamp as light source. At the end of the light path, a mirror (retro-reflector) reflects the light back to a spectrograph analyzing its spectral composition and, thus, providing information on the trace gas abundance along the light path. As the measured absorbance is proportional to the length of the observed light path, the detection limit of the DOAS system gets lower with increasing length of the light path as long as enough light is reflected to the detector. Long light paths can be achieved by either setting up the mirror as far away as possible (Long Path (LP) DOAS, e.g. *Platt et al.* (1979)), or, in order to obtain local trace gas information, by using a multi-reflection cell (e.g. White Cell or Herriot Cell). Setups with several mirrors and, thus, several light paths are also in use, e.g. with mirrors in different altitudes to provide profile information or in more sophisticated setups to provide, e.g., 2D pollution information (DOAS tomography). However, due the need of lamps and mirrors, active DOAS is limited to ground-based measurements of the lower-most part of the boundary layer. In contrast, passive DOAS uses an extraterrestrial light source, mostly the sun, but also lunar or stellar light can be used. This allows, additionally to ground-based applications, measurements from any imaginable platform like ships, aircrafts, balloons or satellites (*Platt and Stuz*, 2005, in press). Passive DOAS measurements can be subdivided into two major categories, the first one using direct solar, lunar or stellar light, and the second one scattered sun light. The direct sun light measurements have the advantage of a high amount of analyzed photons and an easy geometry, but are limited to trace gas measurements along the line-of-sight from the detector to the sun. Ground-based applications are additionally limited to cloud-free conditions. For balloon measurements e.g., stratospheric profiles can be retrieved during the ascent of the balloon or during sunset and sunrise (solar occultation). The solar occultation technique is also used by several satellites (POAM, HALOE which, in fact, do not use the DOAS technique, or SCIAMACHY/Envisat (*Burrows et al.*, 1995)). As solar measurements are obviously limited to daytime, nighttime measurements can be performed by lunar observations from the ground, balloon (SALOMON (*Renard et al.*, 2000; *Berthet et al.*, 2003)) or from satellites (SCIAMACHY), or stellar observations from balloon (AMON (*Renard et al.*, 1996, 1998)) or satellite platforms (GOMOS/Envisat). Within the last few years, many DOAS applications have been developed using scattered or reflected solar light. By the analysis of several light paths through

the atmosphere, Multi AXis (MAX)-DOAS applications (see *Hönninger et al.* (2000); *Hönninger et al.* (2004)) can, e.g., provide vertical profile information on trace gases in the boundary layer, or when performed from an aircraft (AMAX-DOAS (*Wang et al.*, 2003; *Heue et al.*, 2005)), of the Upper Troposphere/Lower Stratosphere (UT/LS) region. Another very recent ground-based application is the use of a 2D scanning detector to obtain 2D trace gas information, e.g. the emission of a smokestack (Imaging DOAS, *Lohberger* (2003)). Several recent satellites use scattered skylight as source either by looking down in nadir geometry analyzing the sunlight reflected from the Earth's surface or atmosphere to obtain total column information of atmospheric trace gases (GOME/ERS-2, ILAS, SCIAMACHY, OMI/EOS-AURA, or GOME-2/METOP), or in limb geometry which allows to retrieve vertical profiles by analyzing light scattered at different tangent heights (OSIRIS/ODIN, e.g. *Sioris et al.* (2003); *von Savigny et al.* (2003); *Haley et al.* (2004) or SCIAMACHY, e.g. *von Savigny et al.* (2004)). Also the miniDOAS balloon measurements in limb and nadir geometry presented in this work are an example of atmospheric skylight DOAS measurements. Scattered sunlight measurements allow the largest possible freedom of viewing geometries, but also require precise radiative transfer calculations, which are computationally expensive and require the knowledge of atmospherical parameters like temperature, pressure and aerosol extinction profiles, or cloud conditions.

3.1.1 Theory

Beer-Lambert Law

The extinction of light with a given spectral intensity $I(\lambda)$ passing through an air layer element dl, neglecting emission and scattering of light into the direction of the considered light beam, can be written as:

$$dI(\lambda) = -I(\lambda)\ (\alpha_s(\lambda) + \alpha_a(\lambda))\ dl, \tag{3.1}$$

where $\alpha_s(\lambda)$ and $\alpha_a(\lambda)$ are the scattering and absorption coefficients, respectively. The sum of $\alpha_s(\lambda)$ and $\alpha_a(\lambda)$ is called extinction coefficient. Neglecting inelastic Raman scattering, the coefficient $\alpha_s(\lambda)$ includes Mie scattering on aerosols and droplets and molecular Rayleigh scattering:

$$\alpha_s(\lambda) = \sigma_{Rayl}(\lambda) \cdot n_{Rayl} + \sigma_{Mie}(\lambda) \cdot n_{Mie}, \tag{3.2}$$

where σ is the scattering cross section and n is the density of the respective scatterers. Taking into account all absorbers i with a non-zero absorption cross section σ_i at wavelength λ and their density n_i, the absorption coefficient $\alpha_a(\lambda)$ can be written as

$$\alpha_a(\lambda) = \sum_i \sigma_i(\lambda) \cdot n_i. \tag{3.3}$$

Integration of equation 3.1 along the light path L yields the *Beer-Lambert law*:

$$I(\lambda) = I_0(\lambda)\ \exp\left\{ -\int_L (\alpha_s(\lambda) + \alpha_a(\lambda))\, dl \right\}. \tag{3.4}$$

An important quantity is the optical density (or depth) τ, defined as:

$$\tau(\lambda) = -\ln\left\{ I(\lambda)/I_0(\lambda) \right\}. \tag{3.5}$$

Using this definition, the *Beer-Lambert law* (equation 3.4) can be written as

$$I(\lambda) = I_0(\lambda)\ \exp\left\{ -\tau(\lambda) \right\}. \tag{3.6}$$

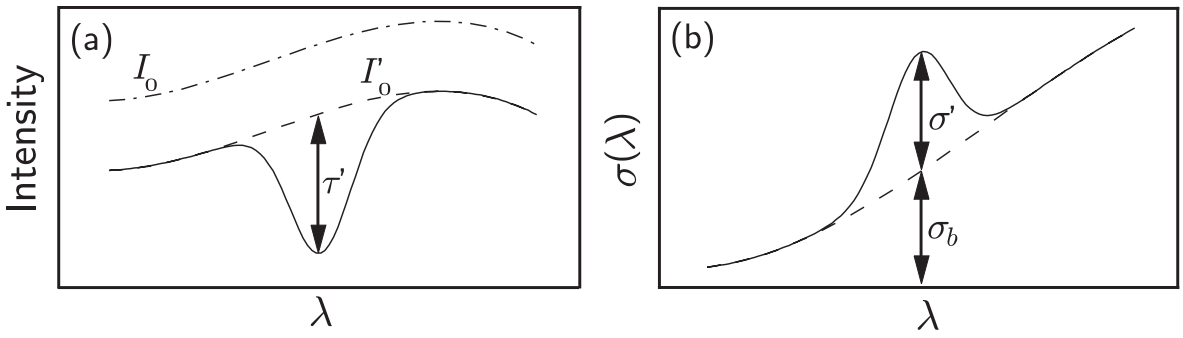

Figure 3.1: Schematic illustration of the DOAS principle. In the left panel the differential optical density τ' is illustrated. In the right panel the split of the absorption cross section σ into a broad band σ_b and a narrow band component σ' is shown.

The DOAS Principle

In atmospheric measurements, the quantities of interest are the densities of the absorbing trace gases n_i along the light path. These could only be obtained from the measured intensity $I(\lambda)$ if one knew exactly the light intensity without atmospheric extinction $I_0(\lambda)$ (i.e. the extraterrestrial solar intensity) and the extinction due to Rayleigh and Mie scattering σ_s, which is generally not the case. Also only one absorber could be obtained at a given wavelength.

The Differential Optical Absorption Spectroscopy overcomes these limitations by analyzing whole spectra (i.e. intensities measured at several wavelengths). It is based on the fact that the Rayleigh and Mie scattering cross sections σ_{Rayl} and σ_{Mie} change only weakly with wavelength, while the molecular absorption cross section σ_i usually consist of narrow absorption bands (i.e. are strongly wavelength-dependant), often overlaid by a broad continuum. Hence, the absorption cross section σ of a certain species is split into a broad band (σ_b) and a narrow band component (σ', called differential absorption cross section):

$$\sigma = \sigma_b + \sigma'. \tag{3.7}$$

The absorption coefficient can be rewritten in the same way:

$$\alpha_a = \alpha_{a,b} + \alpha'_a. \tag{3.8}$$

So equation 3.4 can be rewritten

$$I(\lambda) = I_0(\lambda)\, \exp\left\{ -\int_L (\alpha_s(\lambda) + \alpha_{a,b} + \alpha'_a(\lambda))\, dl \right\} = I'_0(\lambda)\, \exp\left\{ -\int_L \alpha'_a(\lambda)\, dl \right\}, \tag{3.9}$$

where

$$I'_0(\lambda) = I_0(\lambda)\, \exp\left\{ -\int_L (\alpha_s(\lambda) + \alpha_{a,b})\, dl \right\} \tag{3.10}$$

includes all the broad band absorption structures.

Similar to equation 3.5 the differential optical density τ' can be defined as:

$$\tau(\lambda)' = -\ln\left\{I(\lambda)/I'_0(\lambda)\right\} = \int_L \sum_i \sigma_i(\lambda)' \cdot n_i\, dl = \sum_i \tau'_i(\lambda). \tag{3.11}$$

This is illustrated in figure 3.1.

In a rather simple approach, the broad band structures could be removed by high pass filtering. In practice, usually a Fraunhofer reference spectrum $I_0(\lambda)$ with no (or only little) atmospheric absorption

is used, and the broad band absorption is approximated by a polynomial.

Assuming constant pressure and temperature along the light path (or absorption cross sections that are independent of pressure and temperature), the differential absorption cross section σ_i' for species i is independent of the light path and the differential optical density τ_i' can be written as:

$$\tau_i'(\lambda) = \int_L \alpha_a'(\lambda)\, dl = \sigma_i'(\lambda) \cdot \int_L n_i\, dl = \sigma_i'(\lambda) \cdot SCD_i, \tag{3.12}$$

with the Slant Column Density SCD. Hence, the SCD is the quantity obtained by the DOAS method. In praxis, the assumption of σ_i being constant with p is mostly fulfilled for atmospheric pressures, but the absorption cross section is generally not independent of temperature, which is a serious shortcoming of the DOAS approach. However, it can be overcome by the use of several (mostly two) cross section sections of the same species obtained at different temperatures in the spectral analysis (see also the corresponding section).

Spectral Retrieval

In this section it is described how the DOAS principle is applied to an actual measured spectrum. The incoming solar light is spectrally analyzed by a spectrograph and recorded by a detector (e.g., as in the case of the miniDOAS instrument, a linear CCD array detector). So the instrumental properties of the spectrograph have to be accounted for. The finite resolution of the spectrograph can be described by a convolution of $I(\lambda)$ with the (wavelength dependent) instrument function H

$$I^*(\lambda) = I(\lambda) \circ H = \int I(\lambda - \lambda') \cdot H(\lambda')\, d\lambda' \tag{3.13}$$

The instrument function describes the effects of the width of the entrance slit and the properties of the grating. Usually the instrument function is measured with narrow emission lines from low pressure lamps (e.g. from an HgCd lamp). During the recording process, the incident intensity in a certain wavelength range $\Delta\lambda(i)$ is mapped to a discrete pixel i with center wavelength $\lambda(i)$

$$I(i) = \int_{\lambda(i)-\Delta\lambda(i)/2}^{\lambda(i)+\Delta\lambda(i)/2} I^*(\lambda')\, d\lambda'. \tag{3.14}$$

Note that $I(i)$ stands for the intensity recorded by pixel i for a given incident intensity $I(\lambda)$. Using the equations discussed in the last section its logarithm can be written as:

$$\ln I(i) = \ln I_0(i) - \left(\sum_{j=1}^{m} SCD_j \cdot \sigma_j(i) + R(i) + A(i) + N(i) \right), \tag{3.15}$$

where $\sigma_j(i)$ stands for the differential cross section either brought to the instrumental resolution by convolving a high resolution cross section from the literature with the instrument function similar to equation 3.13 or a cross section recorded with the same instrument. The broad band components like Mie or Rayleigh extinction are expressed by $R(i)$. Any structures in the spectrum caused by the spectrograph itself are summarized by $A(i)$. $N(i)$, finally, describes the inevitable detector and photon noise.

The goal of the DOAS retrieval is to obtain the SCD_j of the m absorbers. Therefore, an appropriate model function $F(i)$ is used for the approximation of $\ln I(i)$.

$$F(i) = \ln I_0(i, d_{0,0}, d_{1,0}...) - \left(\sum_{j=1}^{m} a_j \cdot \sigma_j(i, d_{0,j}, d_{1,j}...) + P_p(i) \right) \tag{3.16}$$

The cross sections $\sigma_j(i)$ and $I_0(\lambda)$ are input data to the retrieval procedure while the m scaling factors a_j, the p polynomial coefficients c_h and the additional parameters $d_{x,j}$, $(j = 0...m)$ are the output. The resulting a_j then correspond to the SCD_j of the respective absorber. The broad band structures are approximated by a polynomial $P_p(\lambda)$ of degree p (usually p is between 2 and 5):

$$P_p(i) = \sum_{h=0}^{p} c_h (i - i_c)^h \tag{3.17}$$

with the center pixel i_c of the considered spectral range. To account for possible differences in the wavelength-pixel mapping of $I_0(i)$ and $\sigma_j(i)$ compared to $I(i)$, the reference spectra $I_0(i)$ and $\sigma_j(i)$ can be shifted and squeezed/stretched, expressed by the spectral alignment parameters $d_{j,k}$. The parameter $d_{j,0}$ describes a shift of the wavelength-pixel mapping by $d_{j,0}$ pixels. If $d_{j,1} \neq 0$, the spectrum is additionally linearly squeezed, i.e., pixel i is shifted by $d_{j,1}(i - i_c)$ pixels. For $k > 1$ the parameter $d_{j,k}$ describes a squeeze of higher order, usually not used. The misalignment of the different spectra is a result of different measurement conditions (e.g., ambient temperature, pressure) which can never be completely avoided. Especially when using a highly structured light source like the sun, the shift and stretch parameters of $I_0(i)$ with respect to $I(i)$ have to be determined very precisely.

The spectral analysis consists of a *linear least square fit* to derive the parameters a_j and c_h and a *non-linear Levenberg-Marquardt fit* to determine the parameters $d_{j,k}$ so that

$$\chi^2 = \sum_{i=0}^{n} \left(\frac{\ln I(i) - F(i)}{\varepsilon_i} \right)^2 \tag{3.18}$$

is minimized. Here, n is the number of pixels of the spectral range used for the retrieval and ε_i is the measurement error of the i^{th} diode resulting from measurement noise. Usually, a constant measurement error is assumed for all diodes, i.e. $\varepsilon_i = \varepsilon = const.$

The fitting procedure starts with a linear least-square fit with initial values for $d_{j,k}$. The retrieved values for a_j and c_h are then input parameters for a Levenberg-Marquardt fit. Only one iterative step is performed and new values for $d_{j,k}$ are obtained, which in turn are used for a new call of the linear fit. The result of the linear fit is again used for a new call of the non-linear fit etc. If one of several stopping conditions for the Levenberg-Marquardt fit is fulfilled (e.g. convergence of the fit represented by very small changes of χ^2 from one step to the next(usually 10^{-6}), or after a certain number of iterations, or if the nonlinear method becomes unstable) the whole procedure is aborted.

To account for instrumental stray light caused by reflections inside the spectrograph (e.g. by light of the 0^{th} or 2^{nd} and higher orders of the grating), an *intensity offset* $O(i)$ can be introduced which is a polynomial of up to 2^{nd} order. The product of $O(i)$ and the mean intensity $\overline{I}$) of the spectrum is directly subtracted from the measured intensity, i.e. the left side of equation 3.15 is replaced by $\ln(I(i) - O(i) \cdot \overline{I})$. Its coefficients are additional parameters of the non-linear fit.

Error Analysis

Linear Least Squares Fit

The linear least-squares fit will yield the best possible result and the correct errors if several assumptions are valid: (1) The errors of the pixel intensities $I(i)$ must have a finite variance. If the error of $I(i)$ is dominated by photo-electron noise and, thus, the errors are Poisson distributed this assumption is valid. (2) The normal least-square fit used in most of the analysis procedures assumes that the errors of $I(i)$ are independent, which is not always the case (see below). (3) The systematic error of $I(i)$ is zero. If this is not fulfilled, a bias is introduced in the results. (4) The trace gas cross sections σ_i must

be linearly independent. Correlations between the σ_i's can lead to unrealistic fit results. The validity of these assumption must be checked for every DOAS instrument, measurement and evaluation.

The solution $\overrightarrow{\beta} = (c_0, \ldots, c_p, a_1, a_1, \ldots, a_m)$ (vector combining the $(p+1)$ coefficients of the polynomial and the m trace gas abundances) of the linear least-squares fit is given by:

$$\begin{aligned}
\overrightarrow{\beta} &= \left[\overleftrightarrow{X}^T \overleftrightarrow{X}\right]^{-1} \overleftrightarrow{X}^T \overrightarrow{J}, \\
\widehat{\sigma}^2 &= [n-(m+p+1)]^{-1} \left[\overrightarrow{J} - \overleftrightarrow{X}\overrightarrow{\beta}\right]^T \left[\overrightarrow{J} - \overleftrightarrow{X}\overrightarrow{\beta}\right], \\
\overleftrightarrow{\Theta} &= \widehat{\sigma}^2 \left[\overleftrightarrow{X}^T \overleftrightarrow{X}\right]^{-1}.
\end{aligned} \tag{3.19}$$

where $\overrightarrow{J} = (\ln(I(i))$ is the logarithm of the spectrum to be analyzed and $\overleftrightarrow{X}$ is the coefficient matrix given by the $(p+1)$ arguments of the polynomial $P_p(i)$ and the m reference spectra σ_j:

$$\overleftrightarrow{X} = \begin{pmatrix}
1 & (0-i_c)^1 & (0-i_c)^2 & \cdots & (0-i_c)^p & \sigma_1(0) & \sigma_2(0) & \cdots & \sigma_m(0) \\
1 & (1-i_c)^1 & (1-i_c)^2 & \cdots & (1-i_c)^p & \sigma_1(1) & \sigma_2(1) & \cdots & \sigma_m(1) \\
1 & (2-i_c)^1 & (2-i_c)^2 & \ldots & (2-i_c)^p & \sigma_1(2) & \sigma_2(2) & \cdots & \sigma_m(2) \\
\vdots & \vdots & \vdots & \ddots & \vdots & \vdots & \vdots & \ddots & \vdots \\
1 & (n-i_c)^1 & (n-i_c)^2 & \cdots & (n-i_c)^p & \sigma_1(n) & \sigma_2(n) & \cdots & \sigma_m(n)
\end{pmatrix} \tag{3.20}$$

Its number of columns is given by the number of the number of parameters $(p+1)+m$ to be fitted, and its number of lines by the number of pixels $(n+1)$ of the analyzed wavelength interval. $\overleftrightarrow{\Theta}$ is the *covariance matrix* of the analysis. Its diagonal elements are used to calculate the error of the fit parameters β_j:

$$\Delta\beta_j = \sqrt{\Theta_{jj}}. \tag{3.21}$$

Its off-diagonal elements allow to compute the *correlation coefficients* C_{vw}:

$$C_{vw} = \frac{\Theta_{vw}}{\sqrt{\Theta_{vv}\Theta_{ww}}}. \tag{3.22}$$

The *correlation matrix* $\overleftrightarrow{C}$ is normalized in a way that all diagonal values have a value of 1, with all other elements between ± 1. The correlation coefficients C_{vw} are a measure of the correlation of the v^{th} parameter with the w^{th} parameter. An absolute value of C_{vw} near 1 indicates a large correlation of the two parameters.

$\widehat{\sigma}$ is the error of the intensity of one pixel estimated by the fit. If ε_i is not explicitly given, $\widehat{\sigma}$ is used as measurement error instead, e.g. to calculate χ^2. A significant overestimation of the real measurement errors ε_i (estimated by considering the different noise contributions) is an indication of an inadequate model function or of systematical errors. Further, it can be shown that $\widehat{\sigma}$ is equal to the root-mean-square (rms) of the remaining residual $Res(i) = \ln I(i) - F(i)$, if the number of pixels n contained in the spectral fitting range is clearly larger than the number of linear parameters of the fitting procedure (sum of the number of cross sections and the degree of the polynomial $m + (p+1)$).

Nonlinear Levenberg-Marquardt Fit

In contrast to the linear least-square fit, the Levenberg-Marquardt method is an iterative numerical procedure. The reference spectra $\sigma_j(i)$ and $\ln I_0(i)$ are aligned to $\ln I(i)$ by varying $d_{j,k}$ in order to minimize χ^2. Therefore, $\sigma_j(i)$ and $\ln I_0(i)$ have to be recalculated for the new wavelength-pixel mapping, usually by cubic spline interpolation. The Levenberg-Marquardt method also gives an estimate of the errors $\Delta d_{j,k}$ of the alignment parameters. As the alignment parameters are input data for the linear fit, the errors $\Delta d_{j,k}$ influence the results of the linear fit. To investigate this dependence, a numerical

method is used (*Stutz and Platt*, 1996). A spectrum is calculated consisting of the various reference spectra scaled, shifted and squeezed according to the results of the linear fit. In addition, the spectrum is shifted and squeezed as given by the errors $\Delta d_{j,k}$. The results of the linear fit performed with the original spectrum and the spectra additionally shifted and squeezed allows to infer the errors of the linear parameters caused by the errors of the alignment. Assuming this error and the statistical error of the linear fit to be independent, the total error is obtained by Gaussian error propagation.

Effect of the Residual Structure

Generally, the remaining residual structure $Res(i) = \ln I(i) - F(i)$ of the procedure does not consist of pure noise. A pure noise spectrum is characterized by completely independent pixel intensities, i.e. structures having a width of one pixel, which is a necessary prerequisite for the validity of the error calculation for the linear fit. Real residuals, however, often show structures with widths of more than one pixel, i.e. the pixels are not independent. Theoretically, the dependencies of the measurement errors can be described by the variance-covariance matrix. If this matrix is known, the linear fit procedure can be extended in a way that the calculation of the fit results also considers the error interdependencies (*Albritton et al.*, 1976). If the variance-covariance matrix is not known, a numerical method can be used to examine the influence of these residual structures on the fit results and its errors (*Stutz and Platt*, 1996). Smoothing of a pure noise spectrum with a running mean results in a spectrum similar to the residuum that is normally found. The variance-covariance matrix can then easily be calculated by varying the width of the smoothing filter until the the width of the generated structures are of the same order as the width of the residual structures. However, this variance-covariance matrix has to be recalculated for every measured spectrum, a very time-consuming and uncomfortable procedure. Therefore, empirical correction factors for errors given by the fitting procedure are inferred based on Monte Carlo simulations. It can be shown that only the fit errors need to be corrected, the changes of the fit results are small. Smoothed noise spectra with a running mean of different width are added to absorption lines with different half-widths. For all combinations of filter widths and half widths of the absorption lines a linear fit is performed. The resulting variations of the fit parameters allow to derive correction factors, which can be found in *Stutz and Platt* (1996). Instead of using smoothed noise spectra, this analysis can be performed with residual spectra calculated by cyclic displacement of the channels of the residuum of the fitting procedure (*Hausmann et al.*, 1997).

The occurrence of stable residual structures is not captured by this method. Systematical errors can bias the fitting procedure in two ways. First, these residual structures can be misinterpreted as molecular absorptions and second, the fitting errors are wrongly estimated. A method to investigate the impact of spectral artifacts on the DOAS evaluation can be found in *Hausmann et al.* (1999). However, this method is restricted to irregular, non-reproducible structures generated within the optical setup, while it is not valid in the presence of reproducible systematic structures like improperly removed Fraunhofer structures.

The Detection Limit

An important quantity to judge the quality of trace gas measurements is the theoretical *detection limit*. The detection limit can be defined as the lowest measurable value for a fit parameter a_j or as the smallest detectable average optical density $\overline{D}_{limit}$. For the latter, an average optical density $\overline{D_j}$ of a reference spectrum σ_j is defined. $\overline{D_j}$ is given by three times the standard deviation of the reference spectrum:

$$\overline{D_j} = 3 \cdot \left[\frac{1}{n-1} \sum_{i=1}^{m} \left(\sigma_j(i) - \overline{\sigma}_j \right)^2 \right]^{1/2} \tag{3.23}$$

As the estimation of the detection limit requires time-consuming Monte-Carlo calculations, only the linear problem is considered (neglecting the uncertainties of the wavelength-pixel mapping). Defining

the detection limit $\overline{a}_j$ as the value of a_j with a relative error of 0.5 yields

$$\overline{a}_j = 2 \cdot \sqrt{\Theta_{jj}} = 2 \cdot \Delta\beta_j. \tag{3.24}$$

This still requires the calculation of the covariance matrix $\overleftrightarrow{\Theta}$ (i.e. the DOAS fit has to be performed). Simplification of the expression for $\overleftrightarrow{\Theta}$ allows to derive an expression for the smallest detectable average optical density $\overline{D}_{limit}$ (*Stutz*, 1996):

$$\overline{D}_{limit} \approx \widehat{\sigma} \frac{6}{\sqrt{n-1}} \tag{3.25}$$

with the mean noise of the measurement $\widehat{\sigma}$ and the number of pixels n. Hence, for a given noise level (which has to be estimated) and number of pixels used for the evaluation, the theoretical detection limit can be obtained. However, if an evaluation is performed, equation 3.24 can be used instead for the calculation of the detection limit.

3.1.2 DOAS Evaluation Software

Several software packages are available that can be used for DOAS evaluation. The first one, historically, is 'MFC' (*Gomer et al.*, 1995), which performs the complete error propagation as described above, and the calculation of the covariance and correlation matrices, but it does not allow the fitting of an intensity offset polynomial. Additionally, it has a script language for automation. As an MS-DOS program it has certain restrictions regarding the spectra that can be treated, e.g. it is limited to 1024 pixels per spectrum in its release version, which makes it hard to use with the Ocean Optics USB2000 that has 2048 pixels per spectrum. A Linux version of MFC with Graphical User Interface (GUI), called 'XDoas', has been developed by *Grassi* (2002) which overcomes the DOS restrictions regarding the loadable spectra. Unfortunately, it is not completely bugfree. The software used in this work is 'WinDOAS' developed at BIRA/IASB (*Fayt and van Roozendael*, 2001). It allows the fitting of an additive polynomial and also to fix certain parameters a_j of the fit. Disadvantage of this software are a different error calculation neglecting the influence of the uncertainty of the non-linear parameters on the linear ones, and the absence of a script language and spectrum manipulation functionality which basically limits its application to the sole fitting process. Nevertheless, it is widely used and tested so that it became a standard in DOAS evaluation. Just recently, the latest 32bit version of the Windows DOAS tool 'DOASIS', developed at the IUP Heidelberg by *Kraus* (2004), became available. It combines all the above listed features such as GUI, script language (based on JScript and the Microsoft .Net framework) for spectrum manipulation and fitting, and also has the possibility of fitting an intensity offset but still requires validation.

3.1.3 Error Sources

The precision of the fit results is determined by the statistical fluctuations, i.e. noise, of the measured intensities. Additionally, there are several effects, that are inaccurately treated by the model function described above. These effects result in systematical errors which affect the accuracy of the measurement. Also, the estimation of the fitting error will be distorted. For some effects, it is possible to find a correction term which can be included in the model function. In this subsection, a brief overview about the various effects, arising from instrumental shortcomings as well as from deficits of the model function, is given.

Noise Contributions

Several effects contribute to the noise of the measurement. The statistical errors of the fitted parameters and the theoretical detection limit are determined by the noise of the measurement.

The physical limit of every measurement is given by the *photoelectron noise* σ_{ph}. It is due to the statistical distribution of the number of electrons generated by the photons illuminating the detector pixel. They are distributed according to Poisson statistics, so σ_{ph} is given by

$$\sigma_{ph} = \sqrt{\alpha \cdot N_{e,total}} \sim \sqrt{N_{photons}}, \tag{3.26}$$

with the maximum number of photo electrons $N_{e,total}$, which can be calculated from the semiconductor capacity and the charge voltage, and the degree of saturation α.

The *dark-current noise* σ_d of a single detector photodiode is due to the statistical variance of the dark current across the junction. The dark current electrons are Poisson distributed and, thus, for an integration time t and a mean number of dark current electrons per time n the noise is obtained by

$$\sigma_d = \sqrt{n \cdot t} \tag{3.27}$$

The mean number of dark current electrons depends strongly on the temperature of the photodiode. Before every DOAS evaluation the measured spectra are corrected for dark current, i.e. a recorded dark spectrum brought to the same integration time as the measured spectrum is subtracted. So, strictly, σ_{dc} has to be multiplied by a factor of $\sqrt{2}$. Also, this correction assumes that the dark current is linear in the integration time which is true for short integration times but becomes increasingly incorrect for long integration times as the dark current per time decreases with increasing saturation of the detector pixel.

Another important noise contribution is the *electronic offset noise*. The electronic offset is added to the photoelectron current before its A/D conversion to ensure positive values. Furthermore, there are several *electronic noise* contributions σ_{el}, e.g. caused by the readout process, by the preamplifier, or by the analog-to-digital converter. All these noise contributions are random noise and, thus, decrease when several spectra are added:

$$\sigma_{offset} \sim N^{-\frac{1}{2}}, \tag{3.28}$$

where N is the number of scans.

All noise contributions can be added up quadratically to get the total noise σ_{tot}:

$$\sigma_{tot} = \sqrt{\sigma_{ph}^2 + \sigma_{dc}^2 + \sigma_{el}^2} \tag{3.29}$$

For short integration times, the dark current noise can usually be neglected. Consequently, the total noise consists of the signal dependant photoelectron noise (the most dominant contribution for high saturation α) and the offset noise. The two latter are both proportional to $N^{-\frac{1}{2}}$ so that the signal-to-noise ratio can be increased by co-adding subsequently recorded spectra.

Correlations

An important issue potentially leading to large systematical errors are correlations between the cross sections included in the fit. These effects are hard to describe quantitatively. In fact, the residual structure as a measure of the quality of the DOAS evaluation can even become smaller when structures are improperly fitted by correlating cross sections. Several typical examples exist. Firstly, correlations may occur between weakly structured absorbers like O_3 or, especially, O_4 and the polynomial. This problem can be avoided (or, at least minimized) a by choosing the polynomial degree as low as possible.

It is also important to check whether the fit parameters are in a reasonable order of magnitude, e.g. not negative. Secondly, correlations exist when including a pseudo-absorber correcting for the Ring effect and an additive intensity offset correcting for instrumental stray lights. This can be avoided by only using either of them. However, both effects exist, so excluding either Ring or intensity offset can yield larger residua. Obviously, two (or more) cross sections of the same absorber at different temperatures are quite similar in structure and, thus, strongly correlate. This can be avoided by a mathematical orthogonalization procedure which makes the cross sections linearly independent. But also cross sections of different absorbers can show cross correlations or can correlate with the spectrum itself or structures improperly removed out of the spectrum. An example is the recently discovered center-to-limb-darkening effect that might create large fake IO absorptions in solar occultation measurements (*Bösch et al.*, 2003). Correlations between the cross sections can be investigated by analyzing the covariance matrix that is computed for every DOAS evaluation (equation 3.19). Generally, correlations increase with the degrees of freedom of the fit and decrease with increasing fit range, i.e. numbers of pixels.

Temperature and Pressure Dependence of the Absorption Cross Section

Most of the UV/vis absorption cross sections show a strong dependence on temperature and, to a lesser degree, on pressure, i.e. the absolute value and the shape of the cross section change with temperature. This affects the spectral evaluation in two ways. Firstly, the temperature dependence can directly lead to different fit parameters a_j for different temperatures due to a change of the absolute value. Secondly, an altering shape can result in large residual structures. Hence, if the temperature dependence of the cross section of a strong absorber is not taken into account, the detection of underlying weak absorbers may be impossible. First some general remarks about treating the temperature dependence are given, then some characteristics of the temperature and pressure dependence of the cross sections used in this work (O_3, NO_2, BrO, O_4, and H_2O, see figure 3.2) are briefly discussed.

In order to minimize the effects of the temperature dependence of the cross sections on the residual, cross sections measured at several different temperatures are included. If the temperature dependence is approximately linear, two cross sections are sufficient to cover a large temperature region, i.e. the region where the temperature dependence is linear. As the two cross sections generally strongly correlate, they have to be orthogonalized. Therefore, they are fitted by a polynomial to get their differential structure, and one of them is orthogonalized with respect to the other one which serves as base. So the orthogonalized cross sections just consists of the structures not included in the base cross sections. If the temperature dependence is weak and/or the temperature range of the probed air masses is small, the optical density of the orthogonalized cross section is small while the optical density of the fit parameter of the base cross section is similar as if only one temperature were fitted. Note that the fit parameter of the orthogonalized cross section cannot be interpreted as a slant column density. The difference of the absolute size of the cross sections at different temperatures can be corrected by a procedure described in *Butz et al.* (2005). Two DOAS evaluations at two different temperatures are performed. Then, an average temperature along the line of sight weighted with the actual profile is calculated and the obtained SCD values for the two evaluations are averaged according to the average temperature.

A detailed study of the temperature dependence of the ozone absorption in the Chappuis band ($410-760\,\mathrm{nm}$) can be found in *Burkholder and Talukdar* (1994) or more recently for the wavelength range $230-850\,\mathrm{nm}$ by *Voigt et al.* (2001). Near the peak of the Chappuis band ($550-650\,\mathrm{nm}$) the cross section varies slightly ($< 1\%$), while at wavelengths outside the peak it decreases with decreasing temperature. For example, at 420 nm the absorption cross section decreases by 40% when the temperature decrease from 298 K to 220 K. A pressure dependence is not observed.

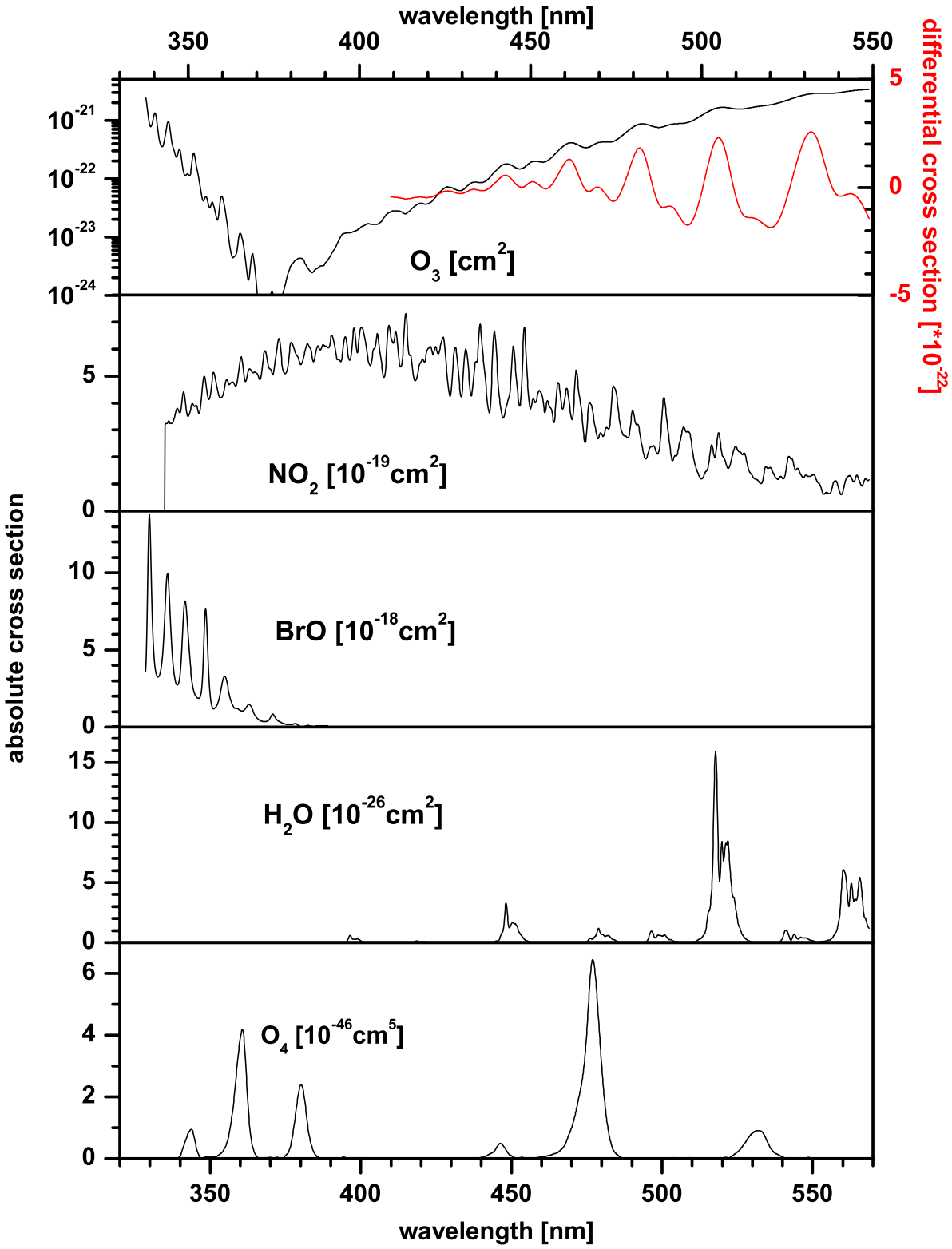

Figure 3.2: Cross sections of the trace gases used convolved to the instrumental resolution

The temperature dependence of the NO_2 cross section in the visible wavelength range has been quite profoundly studied (*Davidson et al.*, 1988; *Amoruso et al.*, 1993; *Harwood and Jones*, 1994; *Kirmse et al.*, 1997; *Harder et al.*, 1997; *Pfeilsticker et al.*, 1999). The NO_2 cross section can be described as a bell-shaped envelope with a superimposed differential structure. The temperature effect on the cross section is a slight broadening of the envelope with increasing temperature while the amplitude of the superimposed fluctuations decrease. The effect of the broadening of the envelope is largest for the red tail of the cross section, while for the UV the envelope does not change significantly with temperature. Thus, no (or only a very small) dependence of the integrated cross section on the temperature is found. The differential cross section shows an asymmetric increase with decreasing temperatures. The differential cross section has a smaller negative temperature coefficient in the neighborhood of the peaks and a larger positive coefficient in the region in between. The magnitude of this temperature variation depends on the wavelength and the spectral resolution of the instrument used. For a resolution of 0.54 nm (FWHM) the differential cross section at 448 nm increases almost linearly with decreasing temperature by about 38% from 298 K to 200 K (*Pfeilsticker et al.*, 1999). Additionally, at very high spectral resolution, the differential cross section shows a large dependence on pressure. However, for the low spectral resolution of typical DOAS spectrographs, this effect is not important.

The temperature and pressure dependence of the O_4 absorption is investigated by *Osterkamp* (1997) and *Pfeilsticker et al.* (2001). They find that the shape of the O_4 collisional pair absorption cross section does not depend on pressure or temperature, while the magnitude of the cross section decreases by about 11% when increasing the temperature by 50 K.

The H_2O absorption shows large variations for changing temperatures and pressures. For H_2O, most of the individual rotational-vibrational lines of the electronic transitions are identified and the absorption line properties are known (*Rothman et al.*, 2003) so that the cross section can be calculated for different pressures and temperatures. Since stratospheric water vapor concentrations are small and, hence, most of the absorption occurs in the troposphere, it is sufficient to use an H_2O cross section for an average tropospheric temperature and pressure.

The Ring Effect

The Ring effect is caused by the filling-in of Fraunhofer lines by inelastic Raman scattering (*Grainger and Ring* (1962), see also section 3.2.2). It can be corrected for by including a so called Ring cross section σ_{Ring} as pseudo-absorber in the fit. According to a first order expansion series, the Ring cross section is given as (*Chance and Spurr*, 1997):

$$\sigma_{Ring} = \frac{I_{Raman}}{I_{Rayleigh}} \approx \frac{I_{Raman}}{I}, \tag{3.30}$$

where I_{Raman} is the Raman scattered, $I_{Rayleigh}$ the Rayleigh scattered, and $I = I_{Rayleigh} + I_{Raman}$ the total intensity.

The Ring cross section can be calculated by the DOAS tools MFC, DOASIS and WinDOAS. The used algorithms and, thus, also the results are quite different, so a brief comparison of the three Ring tools is given here. The clearest calculations can be performed with MFC as every individual step is traceable. The Raman spectrum I_{Raman} can be calculated directly from the measured spectrum using the 'Y' command (*Gomer et al.*, 1995). For the calculations of I_{Raman}, the spectrum is assumed to consist of pure Rayleigh scattered radiation. As the measured spectrum consists of both Rayleigh and Raman scattered radiation the Rayleigh spectrum $I_{Rayleigh}$ is given by the difference of the measured spectrum I_{meas} and the calculated I_{Raman}. With these results a Ring spectrum σ_{Ring} can be calculated according

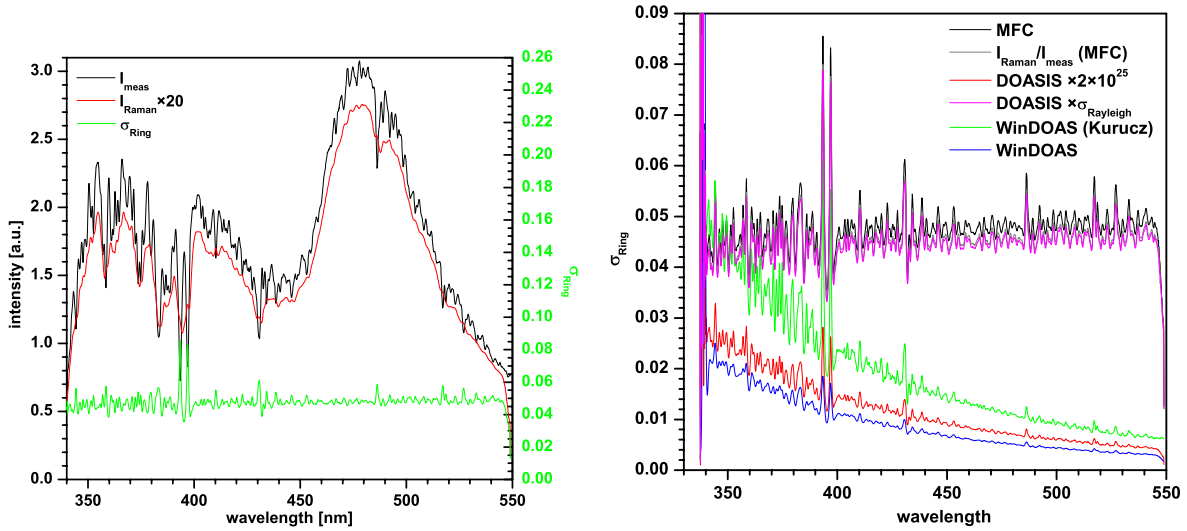

Figure 3.3: Left panel: Measured solar spectrum I_{meas}, Raman spectrum I_{Raman} calculated with MFC, and therewith calculated Ring cross section σ_{Ring}. Right panel: Comparison of σ_{Ring} calculated with MFC by $I_{Raman}/(I_{meas} - I_{Raman})$ (black line) and I_{Raman}/I_{meas} (gray line), σ_{Ring} calculated with DOASIS multiplied by a constant (red line) and multiplied by $\sigma_{Rayleigh}$ (magenta line), and σ_{Ring} calculated with WinDOAS using a high resolved Kurucz spectrum (green line) and the measured I_{meas} (the same as used for the MFC and DOASIS calculations) as reference (blue line).

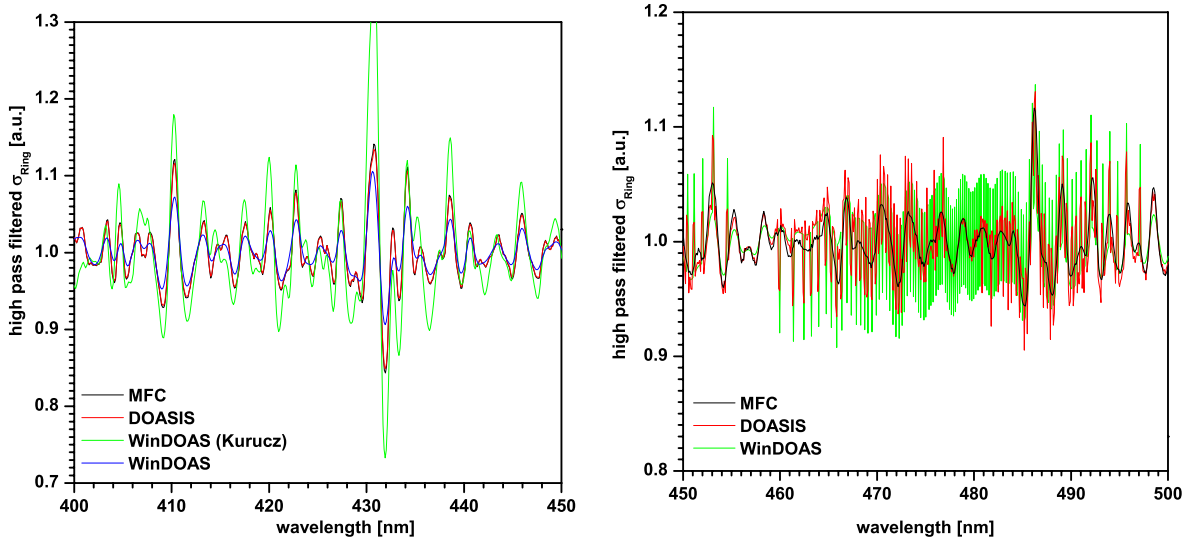

Figure 3.4: Left panel: high pass filtered σ_{Ring} obtained with MFC (black line), DOASIS (red line, and WinDOAS with Kurucz (green line) and self-recorded reference (blue line). Right panel: same as left panel but for another self recorded solar spectrum. σ_{Ring} from MFC is shown in black, DOASIS in red, and WinDOAS (self recorded reference, only) in green.

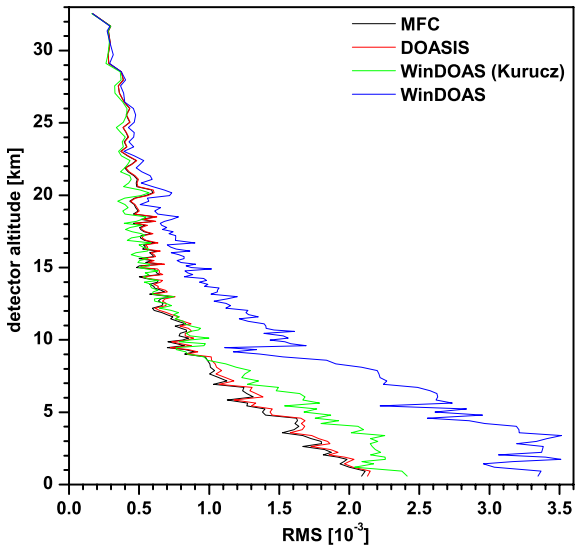

Figure 3.5: RMS residual of a BrO DOAS evaluation vs. detector altitude using σ_{Ring} calculated with MFC (black line), DOASIS (red line), and WinDOAS using a high resolved Kurucz solar spectrum (green line) and the self-recorded solar spectrum (blue line).

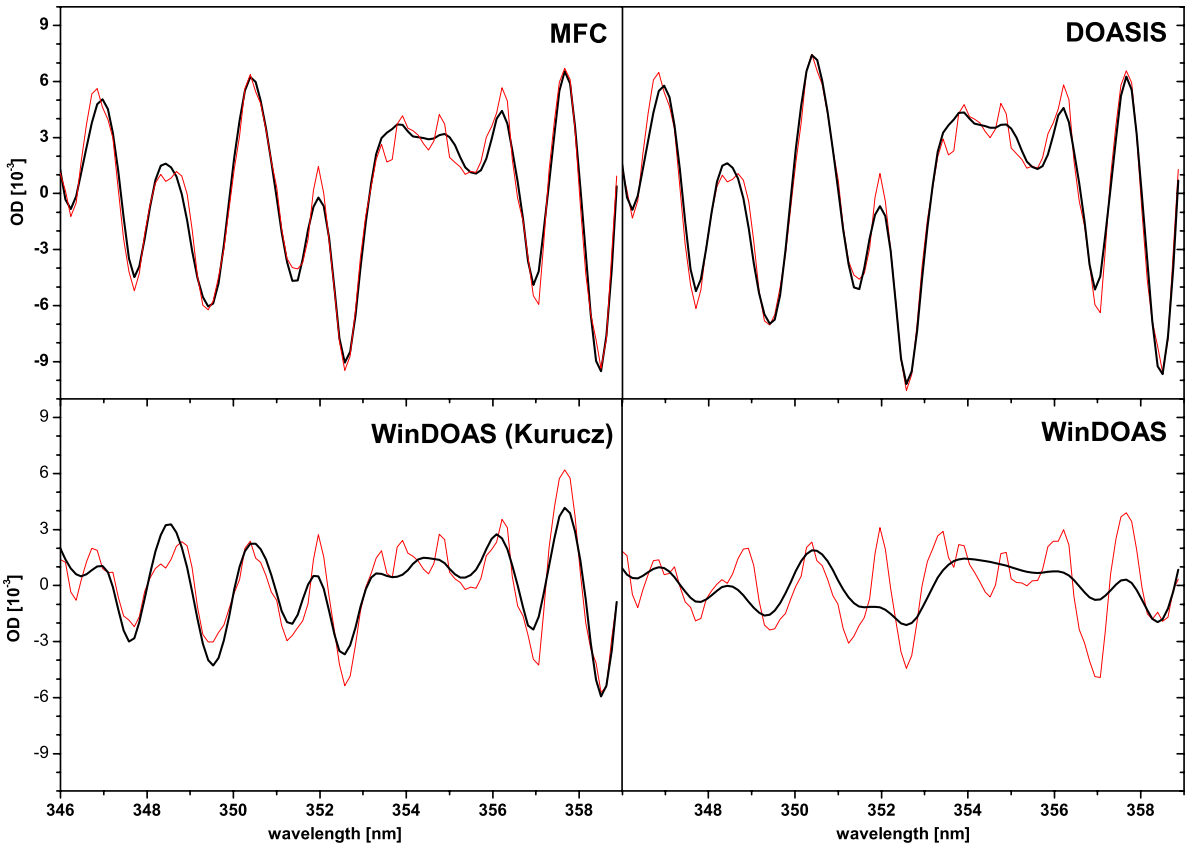

Figure 3.6: DOAS fit using the Ring cross section calculated by MFC (upper left), DOASIS (upper right), and WinDOAS (lower panels), respectively. Shown is the optical density (OD) of the fitted σ_{Ring} (red line) and the latter plus the residual (black line). The evaluated spectrum was recorded at $6.8\,\mathrm{km}$.

to equation 3.30:

$$\sigma_{Ring} = \frac{I_{Raman}}{I_{meas} - I_{Raman}}. \tag{3.31}$$

An example of the Ring cross section calculation is shown in figure 3.3 (left panel). It can be seen that the Raman spectrum is smaller by a factor of ~ 20 in the entire wavelength range. Consequently, σ_{Ring} is in the order of 0.05 with strong structures at the Fraunhofer lines.

In DOASIS, the Raman spectrum cannot be calculated separately, the Ring tool calculates σ_{Ring} directly from the input solar spectrum. The resulting spectrum (see figure 3.3, right panel, red line) looks kind of strange on the first view as it has units of 10^{-28}. It shows approximately a λ^{-4} dependance. Multiplying the DOASIS σ_{Ring} by $\sigma_{Rayleigh}$ (see equations 3.43ff.) results in a cross section very close to I_{Raman}/I_{meas} with I_{Raman} calculated by MFC (see figure 3.3, right panel, magenta line).

The WinDOAS Ring tool is thought for usage of a high resolution solar spectrum like Kurucz as reference. Therefore, the solar spectrum is convolved with the instrumental slit function. Using a solar reference recorded with the actual instrument does not yield useful results as the spectrum is interpolated to a higher resolution during the calculation to be convolved again with the instrument slit function which is mathematically absurd. Additionally, the resulting σ_{Ring} has a λ^{-4} dependance as in the case of the DOASIS ring tool. This might be useful for direct sunlight measurements where the fraction of Rayleigh and Raman scattered light decreases with wavelength but in case of stray light measurements when I_{meas} already consists predominately of Rayleigh scattered radiation the so obtained σ_{Ring} is not useful. A comparison of the differential structures of the Ring cross sections which can be obtained by high-pass filtering is shown in figure 3.4 (left panel) for an arbitrarily chosen wavelength interval. σ_{Ring} from MFC and DOASIS are almost identical while that calculated by WinDOAS shows broader lines as a result of the convolution during the calculation. This can lead to significantly higher residuals of the DOAS evaluation as shown in figure 3.5 for the example of a BrO evaluation no independent whether a high resolved Kurucz or the actual reference spectrum is used for the calculation of σ_{Ring}. By looking at the evaluation (see figure 3.6), it can be clearly seen that at lower altitudes where the Ring effect is strongest, the spectral features caused by the Ring effect are well removed if the MFC or DOASIS calculated σ_{Ring} are used, while the fit of the WinDOAS σ_{Ring}'s yield much worse results. At higher altitudes, σ_{Ring} calculated with WinDOAS (Kurucz reference) yields lower residuals than the MFC or DOASIS calculated σ_{Ring}. At these altitudes, the Ring features are not as clear, so it might be that the, obviously worse σ_{Ring} (WinDOAS, Kurucz) compensates for structures caused by other effects than the Ring effect.

Another strange observation is shown in figure 3.4 (right panel). σ_{Ring} calculated with MFC looks as expected but the results from MFC and WinDOAS have intriguing pixel structures which look similar but are not identical. Obviously, some variable got to the limit of its computing precision during the calculation. It is also interesting that the problem does not occur at all wavelengths e.g. around 455 nm or 498 nm, σ_{Ring} from both DOASIS and WinDOAS look normal.

Summarizing all the above observations, it can be concluded that the Ring calculations by MFC are the most trustable and also traceable. Despite its λ^{-4} dependence, σ_{Ring} calculated by DOASIS shows the same differential structures yielding the same residuals in the DOAS evaluation. However, the algorithm has, obviously numerical, problems under certain conditions. The Ring tool from WinDOAS cannot be recommended for stray light measurements as both methods (i.e. using a Kurucz or self recorded reference) yield different differential structures eventually leading to higher residuals compared to the other candidates.

The Solar I_0 Effect

The DOAS method assumes the measured spectrum to be well approximated by a model function $F(\lambda)$ (equation 3.16):

$$F(\lambda) = \ln\left\{\int I_0(\lambda)\, H(\lambda-\lambda')\, d\lambda'\right\} - \left(\sum_{j=1}^{m} a_j \int \sigma_j(\lambda)\, H(\lambda-\lambda')\, d\lambda' + P_p(\lambda)\right), \tag{3.32}$$

with the symbols used in section 3.1.1. However, the logarithm of the measured spectrum $I^*(\lambda) = I(\lambda) \circ H$ is given by:

$$\ln I^*(\lambda) = \ln\left\{\int I_0(\lambda) \exp\left(\sum_{j=1}^{m} SCD_j\, \sigma_j(\lambda) + R(\lambda)\right)\, H(\lambda-\lambda')\, d\lambda'\right\}, \tag{3.33}$$

Equation 3.32 can only properly describe equation 3.33 if $I_0(\lambda) = const$ and $SCD_j \cdot \sigma_j(\lambda) \ll 1$. Even though the Fraunhafer reference spectrum $I_0(\lambda)$ is highly structured, its impact is small as shown by *Huppert* (2000) by numerical tests for the example of a DOAS BrO evaluation but can, nevertheless, lead to disturbing residual structures. For atmospheric applications, the second assumption is usually fulfilled except for some absorbers or very long light paths. This especially affects the evaluation of small absorbers underlying strong absorbers as in the case of BrO (*Aliwell et al.*, 2002). This can be avoided by using I_0*-corrected cross sections* $\sigma_{I_0}(\lambda)$ instead of simply convoluted ones (*Johnston*, 1996):

$$\sigma_{I_0}(\lambda) = \frac{1}{SCD} \frac{\int I_0(\lambda)\, e^{SCD\cdot\sigma(\lambda)}\, H(\lambda-\lambda')\, d\lambda}{\int I_0(\lambda)\, H(\lambda-\lambda')\, d\lambda}. \tag{3.34}$$

An initial SCD has to be chosen, usually the maximum measured. σ_{I_0} can be computed, e.g., using WinDOAS if a highly resolved cross section and solar spectrum are available. Another possibility to correct for this effect would be to record the cross section directly with the instrument and the sun as light source which is, however, experimentally very complicated.

Discretization Effects

Changes of the pixel-wavelength mapping of the measured spectra and the molecular cross sections with respect to the solar reference spectrum are corrected by shifts and squeezes. For that purpose, the cross sections and the measured spectra have to be interpolated by splines. This approximation is the better the higher the sampling ratio, i.e. the number of pixels per FWHM of the instrument function, is. *Roscoe et al.* (1996) found that the sampling errors become small for a sampling ratio > 4.5. This criterium is fulfilled for the used spectrographs with a sampling ratio between $8-10$ pixels per FWHM (see section 4.1).

For the fitting procedure, molecular cross sections at the instrumental resolution are required. For that, usually, highly resolved cross sections from the literature are convolved with the instrument function obtained from measurements of low pressure lamps with emission lines reasonably smaller than the instrumental resolution. However, the instrument function is not constant over the entire spectral range of the spectrometer. This means that the convolved cross sections are not exactly what the instrument would measure. This leads to systematical errors, i.e. higher residual structures, for large optical densities. For molecular absorptions this effect is usually small, except for the case of the evaluation of small absorbers underlying stronger absorbers, e.g., as in the case of BrO. This problem can be avoided by using molecular cross sections measured with the instrument itself rather than convolved ones. However, due to the constant changes of the setup of the instrument this experimentally very costly procedure has not been done for the miniDOAS spectrometer. Especially high residual structures occur,

if a convolved (*Kurucz et al.*, 1984) reference spectrum is used for the evaluation which is necessary to retrieve the absolute absorption in the measured solar reference spectrum so that this approach becomes almost impossible (see chapter 6).

Instrumental Shortcomings

For an ideal DOAS evaluation a stable optical imaging is crucial. A change in ambient pressure and temperature can lead to a change of the resolution and/or the pixel-wavelength mapping due to mechanical relaxation and change of the refractive index of the air inside the spectrometer. Consequently, this leads to additional residual structures. One reason for the structures are the different sensitivity of the individual pixels of the CCD array. The sensitivity of the pixels can be obtained experimentally by measuring an unstructured spectrum, e.g., of a halogen lamp. By dividing the measured spectra by the low pass filtered lamp spectrum, the effect of the non-constant diode sensitivity in case of a shift can be reduced (see, e.g., section 4.2.1).

Spectrometer stray light is caused by reflections of light from higher orders of the grating or light with wavelengths outside the detection range. The stray light causes an additive offset to the measured intensity and, thus, changes the optical density of the Fraunhofer lines or the molecular absorption. It can be reduced by using filters cutting off the undetected wavelengths. It can also be removed during the fitting process by including an intensity offset polynomial.

Further effects potentially causing additional residual structures are the Etalon effect caused by multiple reflections on thin parallel surfaces or the memory effect which causes strong structures of one spectrum to also appear in the next one. Residual structures can also be caused by the grating itself or the glass fibers when different modes are excited. All these effects are considered to be small and not further investigated.

3.2 Radiative Transfer Calculations

3.2.1 Definition of the Radiometric Quantities

The *radiation flux* ϕ is defined as the incident radiation energy per time:

$$\phi = \frac{dE}{dt} \; [W] \tag{3.35}$$

Differentiating ϕ with respect to wavelength gives the *spectral flux* ϕ_λ:

$$\phi_\lambda = \frac{d\phi}{d\lambda} = \frac{d^2E}{dt \; d\lambda} \; \left[\frac{W}{nm}\right]. \tag{3.36}$$

The flux per solid angle can be defined as *intensity* I:

$$I = \frac{d\phi}{d\Omega} \; \left[\frac{W}{sr}\right]. \tag{3.37}$$

The spectral flux on an arbitrarily orientated area element is defined as *(spectral, planar) irradiance* E_λ:

$$E_\lambda = \frac{d\phi_\lambda}{dA} \; \left[\frac{W}{nm \; m^2}\right]. \tag{3.38}$$

Taking into account only the perpendicular part of the incident light $dA_\perp$ and the solid angle $d\Omega$ gives the *(spectral) radiance* L_λ, sometimes simply called intensity I_λ:

$$L_\lambda = \frac{d^2\phi_\lambda}{dA_\perp\, d\Omega} \left[\frac{W}{nm\ m^2\ sr}\right]. \tag{3.39}$$

Integrating the radiance over the half sphere considering the factor $\cos\theta$ yields the irradiance:

$$E_\lambda = \int_{2\pi} L_\lambda \cos\theta\, d\Omega, \tag{3.40}$$

where θ is the angle between the incident radiation and the normal of dA. The irradiance is of importance when the direction of the incoming radiation plays a role e.g. when calculating heating rates. Integrating the radiance over the whole sphere without considering its direction, i.e. neglecting $\cos\theta$, defines the *actinic flux* F_λ, sometimes also called *scalar irradiance*:

$$F_\lambda = \int_{4\pi} L_\lambda\, d\Omega \left[\frac{W}{nm\ m^2}\right]. \tag{3.41}$$

This quantity is of interest in photochemistry where the direction of the incoming light is not important.

3.2.2 Scattering and Absorption

Rayleigh Scattering

Rayleigh scattering occurs if the wavelength of the radiation is considerably larger than the dimensions of the scatterers, e.g. molecules.

The cross section σ_R was first derived by Lord Rayleigh (1842-1919) and, thus, carries his name:

$$\sigma_R = \frac{8\,\pi^3\,\alpha^2}{3\,\varepsilon_0^2\,\lambda^4}, \tag{3.42}$$

where α is the *polarizability* of the respective molecule. More accurate calculations by *Brasseur and Solomon* (1986) yield the empirical formula:

$$\sigma_R = \frac{4.0\cdot 10^{-28}}{\lambda^{3.916+0.074\,\lambda+0.05\,\lambda^{-1}}}\ [\mathrm{cm}^2],\ \text{with } \lambda \text{ given in } [\mu\mathrm{m}]. \tag{3.43}$$

Another accurate empircial formula is given by *Nicolet* (1984):

$$\sigma_R = \frac{4.02\cdot 10^{-28}}{\lambda^{4+x}}\ [cm^2\,],\ \text{with } \lambda \text{ given in } [\mu\mathrm{m}], \tag{3.44}$$

$$x = 0.04 \text{ for } \lambda\ >\ 0.55\,\mu\mathrm{m}$$

$$x = 0.389\ \lambda + 0.09426/\lambda - 0.3228 \text{ for } 0.2\,\mu\mathrm{m} < \lambda < 0.55\,\mu\mathrm{m}.$$

More recent calculations by *Chance and Spurr* (1997) taking into account, e.g. the anisotropy of the polarizability of nitrogen and oxygen molecules, give an average polarizability:

$$\alpha = \sqrt{\frac{(n-1)^2}{4\,\pi^2\,N_0^2}}, \tag{3.45}$$

where n is the refractive index and $N_0 = 6.02205\cdot 10^{23}\,mol^{-1}$ is Avogadro's number. They also give an empirical formula for the Rayleigh cross section:

$$\sigma_R = \frac{3.9993\cdot 10^{28}\,\lambda^{-4}}{1 - 1.069\cdot 10^{-2}\lambda^{-2} - 6.681\cdot 10^{-5}\,\lambda^{-4}}\ [cm^2],\ \text{with } \lambda \text{ given in } [\mu\mathrm{m}], \tag{3.46}$$

which is the formula used for the treatment of Rayleigh scattering in the RTM TRACY. Due to the factor of λ^{-4}, Rayleigh scattering is strongly wavelength dependent. This can be illustrated by looking at the free path length $l_R = 1/(\varrho\,\sigma_R)$, with the air density ϱ which is typically $2.7 \cdot 10^{19}\,\mathrm{cm}^{-3}$ at ground level. It is $\sim 160\,\mathrm{km}$ for red light ($\lambda = 650\,\mathrm{nm}$), $\sim 50\,\mathrm{km}$ for blue light ($\lambda = 490\,\mathrm{nm}$) and only $\sim 14\,\mathrm{km}$ for UV light ($\lambda = 360\,\mathrm{nm}$). This explains why the sky is blue as most of the red light reaches the ground directly while the blue part of the spectrum gets scattered more and reaches the ground not only directly from the sun but from the entire hemisphere. When the sun is low above the horizon during sunrise and sunset it appears red because all the blue parts of the spectrum are scattered out of the direct beam.

The *differential cross section* for unpolarized light is given by:

$$\frac{d\sigma_R}{d\Omega} = \sigma_R \cdot p_R(\theta), \tag{3.47}$$

with the *phase function* $p_R(\theta)$ describing the angular dependence of Rayleigh scattered radiation and the angle θ between incident and scattered radiation. The phase function for unpolarized light can be written as:

$$p_R(\theta) = \frac{3}{4}\,(1 - \cos^2\theta), \tag{3.48}$$

or, more accurately taking into account the molecules' polarization anisotropy (*Penndorf*, 1957), as:

$$p_R(\theta) = 0.7629\,(1 - 0.932\,\cos^2\theta). \tag{3.49}$$

Raman Scattering

In contrast to Rayleigh scattering, where the wavelength of the incident and the scattered photon is the same (i.e. elastic process), Raman scattering is an inelastic process occuring if the scattering molecule changes its state of excitation. If only the the rotational state is altered ($\Delta\nu = 0$) it is called Rotational Raman Scattering (RRS). If also the vibrational state changes ($\Delta\nu \pm 0$) the term Rotational-Vibrational Raman Scattering (RVRS) is used. Only discrete amounts of energy given by the energy difference of the molecule's excitation state before and after the scattering process can be absorbed or emitted, respectively. As a consequence, the spectrum of light scattered off molecules consists of a strong Rayleigh line surrounded by several closely spaced vibrational Raman bands each consisting of several rotational Raman lines, i.e. Stokes lines ($\Delta J = +2$, S-branch) and Anti-Stokes ($\Delta J = -2$, O-branch). For air, i.e. O_2 and N_2, RRS frequency shifts of up to $\pm 200\,\mathrm{cm}^{-1}$ occur. For RVRS a vibrational shift of $\pm 2331\,\mathrm{cm}^{-1}$ for nitrogen and $\pm 1555\,\mathrm{cm}^{-1}$ for oxygen has to be added. As the RVRS is by an order of magnitude weaker than the RRS, only RRS is usually regarded in atmospheric RT.

The RRS cross section is given by:

$$\sigma_{RRS} = \frac{256\;\pi\gamma^2 f_N\;b_{N,J,N',J'}}{27\;\lambda'^4}, \tag{3.50}$$

with the polarization anisotropy γ (given in [cm^3]), the Placzek-Teller coefficients b, the fractional populations in the initial state f_N and the wavelength of the shifted line λ' (in [cm]). For details about the calculation of the σ_{RRS} for O_2 and N_2 see *Bussemer* (1993); *Burrows et al.* (1996); *Haug* (1996); *Sioris and Evans* (1999); *Funk* (2000). σ_{RRS} has the same wavelength dependence as $\sigma_{Rayleigh}$ (i.e. $\sim \lambda^{-4}$) and also the phase function is the same as in the elastic case. The ratio of Raman and Rayleigh scattering lies in the order of some percents.

Measurements of scattered sunlight are affected by Raman scattering which causes a 'filling in' of the Fraunhofer lines. This is referred to as *Ring effect* (*Grainger and Ring*, 1962). The Ring effect must

be corrected for in the DOAS evaluation (see section 3.1.3). In the RTM TRACY inelastic scattering is not yet included as only one wavelength is considered during the calculations.

Mie Scattering

Apart from molecular scattering also scattering off particles with dimensions in the order of the wavelength, e.g. aerosols or cloud droplets, occurs. In contrast to Rayleigh scattering, where cross section and phase functions can be found rather easily, these scattering processes are much harder to describe mathematically as they depend on many parameters of the scatterers such as size, shape, reflectivity, etc. Under the assumption of spherical particles the *Mie theory* can be applied.

The Mie scattering off spherical liquid droplets can be compared to the diffraction from a pinhole. Interference results in angular dependent minima and maxima. It usually requires rather complex calculations to derive exact cross sections and phase functions which are usually done numerically. As Mie scattering not only depends on the wavelength but also on the size, i.e. the radius r, of the particle, the size parameter $\alpha = 2\,\pi\,r/\lambda$ is used. For a given α, the Mie extinction function $E(\alpha)$, i.e the extinction cross section normalized to the particle cross section, can be calculated. In reality, aerosols are not all of the same size but they are a mixture of aerosols with different sizes described by the size distribution function $n(r)$. If the size distribution is known a macroscopical extinction coefficient $k_e(\lambda)$ can be obtained:

$$k_e(\lambda) = \int_0^\infty \pi\,r^2\,E(\alpha)\,n(r)\,dr. \tag{3.51}$$

For aerosols larger than 0.1 μm, $n(r)$ usually obeys an r^{-s} dependence, with $s \approx 4$. Substituting this into equation 3.51 yields a simple λ dependence for k_e:

$$k_e(\lambda) \sim \lambda^{3-s}, \tag{3.52}$$

so that the wavelength dependence is by far smaller than in the Rayleigh case.

The phase function of an aerosol mixture is obtained as an average over the aerosol sizes weighted with their size distribution. This phase function can be approximatively described by the Henvey-Greenstein functions (*Henvey and Greenstein*, 1941):

$$p_{Mie,HG}(\theta) = \frac{1-g^2}{(1+g^2-2\,g\,\cos\theta)^{\frac{3}{2}}}, \tag{3.53}$$

where g is the asymmetry coefficient which describes the degree of 'forward-peakedness' of the scattering process. If $g = 0$ the phase function becomes 1 for all angles (isotropic case). If $g = 1$ the entire intensity is scattered in forward direction. For atmospheric aerosols g lies between 0.6 and 0.7 (*Perliski and Solomon*, 1993). In this case the phase functions show a monotonous decrease with increasing θ.

Light cannot only be scattered off aerosols but also be absorbed. The ratio between scattering and total extinction is called *single scattering albedo* ϖ:

$$\varpi = \frac{k_s}{k_s + k_a}, \tag{3.54}$$

where k_s and k_a are the extinction parameters for scattering and absorption, respectively.

In continental air, the free path length for aerosol extinction is 45 km in the red ($\lambda = 600$ nm) and 25 km in the blue ($\lambda = 400$ nm).

Table 3.1: Typical albedo values for different surface types.

surface type	albedo ω
Earth average with clouds	30 %
Ocean	5 %
Urban areas	10 %
Ice, clouds	$70 - 80$ %

Surface Scattering

Another important aspect in atmospheric radiative transfer is the scattering off the ground. The key quantity in this context is the *albedo* ω, defined as the ratio of the reflected (I_r) and the incident intensity I_i:

$$\omega = \frac{I_r}{I_i}. \tag{3.55}$$

The values of ω are quite variable depending on the surface type. Some typical values are given in table 3.2.2.

Note that the albedo is also wavelength dependent and typically decreases in the UV. The surface scattering can be mathematically described as Lambertian reflection. The Lambertian phase function is given by:

$$p_{Lambertian}(\theta) = \frac{\cos\theta}{\pi}, \tag{3.56}$$

with π^{-1} as normalization constant. As a consequence, an illuminated Lambertian surface of constant albedo has the same brightness to a detector at every viewing angle. This is because the area of the surface seen by the detector increases with $1/\cos\theta$ and, thus, cancels out the $\cos\theta$ decrease of the scattering probability. But, on the other hand, the observed brightness depends on $\cos\theta_i$ of the incident radiation, i.e. the Earth's brightness decreases with setting sun.

Cloud Scattering

The radiative transfer within clouds is rather difficult to handle and still subject of intense research. Water clouds can be seen as a dense accumulation of water droplets. So every photon undergoes several Mie scatterings inside the cloud. After $\sim 7 - 8$ scattering processes the photon has lost any memory of its initial direction. So when only interested in detectors outside, optically thick clouds, i.e. clouds that are significantly thicker than their free path length, can be parameterized phenomenologically. Every photon incident on a cloud can either be reflected, absorbed, or transmitted. Reflections off a cloud can be treated in the same way as reflection off the ground as the top of most cloud covers can be approximated by a Lambertian reflector with an albedo ranging between $70 - 80$ %. As the transmitted photons have been multiply scattered inside the cloud, they are emitted on the bottom of the cloud with a constant phase function, i.e. the same probability for every angle. So, theoretically, clouds can be described by the three parameters cloud coverage (i.e. fraction of the sky that is covered by clouds), cloud albedo and transmittance. In quantitative radiative transfer calculations for real scenarios clouds, nevertheless, are quite problematic, especially for space-borne measurements in nadir geometry, as the cloud coverage is quite variable and, thus, strongly alters the total albedo. Clouds can also partly shield the troposphere and, hence, influence the measured total columns of trace gases that have significant abundances in the troposphere (e.g. NO_2 or BrO). So cloud detection is an important issue for these kinds of measurements.

3.2.3 The Radiative Transfer Equation (RTE)

The Radiative Transfer Equation (RTE) is a continuity equation describing the change in radiance of radiation passing through the atmosphere.

The loss of radiation (extinction e_λ) in the incoming direction is given by:

$$dI^e_\lambda = -e_\lambda\, I_\lambda\, ds = -(k_a(\lambda) + k_s(\lambda))\, I_\lambda\, ds, \tag{3.57}$$

where k_a and k_s are the absorption and scattering coefficients, respectively, defined by $k = n\,\sigma$, with the number density n and the cross section σ summed over all scatterers and absorbers. Sources of radiation are thermal emission and scattering into the outgoing direction:

$$dI^{th}_\lambda = B(\lambda, T)\, k_a(\lambda)\, ds, \tag{3.58}$$

with the Planck function $B(\lambda, T) = \dfrac{2\,\hbar\, c^2}{\lambda^5}\ \dfrac{1}{\exp\left(\frac{h\,c}{\lambda\, k\, T}\right) - 1}$.

$$dI^s_\lambda = k_s(\lambda) \int_0^\pi \int^{2\pi} I^s_\lambda \frac{S(\varphi, \theta)}{4\pi}\, d\varphi\, \sin\theta\, d\theta, \tag{3.59}$$

with the scattering phase function $S(\varphi, \theta) = \dfrac{4\pi}{\sigma_s}\ \dfrac{d\sigma_s}{d\Omega}$.

Adding all these terms yields the RTE:

$$\frac{dI_\lambda}{ds} = -I_\lambda\, (k_a(\lambda) + k_s(\lambda)) + B(\lambda, T)\, k_a(\lambda) + k_s(\lambda) \int_0^\pi \int^{2\pi} I^s_\lambda \frac{S(\varphi, \theta)}{4\pi}\, d\varphi\, \sin\theta\, d\theta, \tag{3.60}$$

Complications in solving the RTE arise from the improper knowledge of the spatial distributions of the scatterers (aerosols, cloud particles, ...) and their physical properties, the value of the scattering phase function S for solid particles, and the values of the absorption and scattering coefficients for all solid particles, liquids and relevant atmospheric gases. Additionally, the earth's sphericity make things more complicated.

3.2.4 Analytical Approaches to the RTE

As it is not possible to analytically solve the RTE in general, simplifications have to be made. E.g., neglecting multiple scattering and thermal emission yields the *Lambert-Beer-Law* (see corresponding section 3.1.1). Neglecting any scattering, i.e. $k_s \ll k_a$ which is valid e.g. in the IR, yields the *Schwarzschild equation*:

$$\frac{dI_\lambda}{ds} = -k_a(\lambda)\, (I_\lambda - B(\lambda, t)). \tag{3.61}$$

Other solution approaches simplify the geometry, like the *two stream approximation*. It considers a plane parallel atmosphere with horizontally homogeneous layers.

In the two stream model the radiation is divided into an up- and a downwelling part. This approach can be extended by considering more than two directions. The radiance is then calculated along these directions or 'ordinates' leading to the *discrete ordinate method* (*Dahlbeck and Stammes*, 1991). This method is implemented in the Radiative Transfer Model (RTM) 'UVspec/DISORT' developed by the Norwegian Institute for Air Research (NILU) (*Kylling*, 1995). It treats multiple scattering by aerosols and clouds in higher orders in plane parallel geometry with spherical geometry and the direct beam including refraction in pseudo-spherical geometry. Refraction was modified to full spherical by the Belgian Institute for Space Aeronomy (BIRA-IASB) (see *von Friedeburg* (2003), chapter 7).

The *finite difference method* separates the direct from the diffuse, i.e. at least once scattered, radiation. A widely used example for this method is 'SCIATRAN' developed by the IUP Bremen (*Buchwitz et al.*, 1998). It treats the direct beam including refraction in full spherical geometry and full multiple scattering in pseudo-spherical geometry. It iteratively solves the RTE to achieve convergence to full sphericity.

Another method is *raytracing*. This technique computes the attenuation of the radiation from the sun through a layered (either plane parallel or spherical) atmosphere to the detector. Usually, only single scattering is allowed. Examples are 'AMFHD' (*Frank*, 1991) for zenith scattered light and 'DAMF' (*Schulte*, 1996) for direct sunlight. DAMF is used for the calculation of the air mass factors for the balloon-borne direct sunlight measurements (see chapter 4.6.3). As the direct intensity is so much higher than the diffuse one, treating the scattering out of the detector's line of sight is sufficient while scattering into the detector's line of sight can be neglected.

3.2.5 The Monte Carlo Approach to the RTE

The Monte Carlo method, generally, can be used to model physical processes with multiple outcomes occurring with certain probabilities. The advantage of this approach is that, even if analytical solutions to a problem are difficult or even impossible to find, it will still yield a reasonable result if enough model calculations are performed to get a reasonable statistics. This means that, in contrast to analytical models, no simplifications, e.g. regarding earth's sphericity etc., have to be made.

In radiative transfer, the propagation of a single photon can be seen as a random walk from the sun through the atmosphere to the detector. On its way, several processes can change the photon's direction by scattering or, when considering an ensemble of identical photons, its intensity by absorption. As the probabilities of all these processes are known (if all relevant atmospheric parameters are known), the path of the photon can be modeled. This is done by drawing a random number in $[0, 1]$. If the number lies in a certain interval depending on a certain process' probability, this process occurs and the photon is e.g. scattered to a different direction of propagation. This is repeated until the photon finally reaches the detector. However, this method is not practicable as it would require an average of $\sim 10^{22}$ modeled photon paths to get one that actually hits a detector of typical size. One idea to overcome this problem is the backward Monte Carlo approach. As all interactions of the photon with matter are invertible it is also possible to model a photon traveling backwards from the detector to the sun. But still, this would require a lot of modeled photons as the sun only covers a fraction of $\sim 5.4 \cdot 10^{-6}$ (derived from the sun's half aperture angle of 0.267^o (*Meeus*, 1992)) of the total sky. So the strict Monte Carlo principle that everything occurs randomly has to be abandoned at the point of the last scattering before the photon leaves the atmosphere. At this point it is 'forced' to the sun so that, as a consequence, all modeled photons that are at least scattered once finally hit the sun.

3.2.6 The Monte Carlo Radiative Transfer Model (RTM) TRACY

The Monte Carlo implementation in the RTM TRACY (Trace gas RAdiative monte Carlo Ymplementation) developed by *von Friedeburg* (2003) based on routines from *Morgner* (2003) is briefly described in the following. Its predecessor, the RTM 'AMFTRAN' developed by *Marquard* (1998); *Marquard et al.* (2000), also used the backward Monte Carlo technique to account for multiple scattering. AMFTRAN also included off-axis and satellite nadir geometry to be used for GOME measurements. Many effects of radiative transfer, e.g. related to O_4 measurements, can be reproduced. But AMFTRAN does not support all geometries including airborne off-axis or balloon-borne limb or very slant lines of sight in ground-based off-axis geometry and it suffers from problems with high SZA and is limited to a fixed

altitude grid. It also does not allow for the calculation of BoxAMFs (i.e. discretized weighting functions) which are required for the profile retrieval of the balloon-borne limb measurements (see section 3.3).

Motivation and Requirements to the RTM

The balloon-borne limb geometry at high SZA which is used in the frame of this work demands for highly accurate radiative transfer calculations. For SZA$>70^o$ Earth's sphericity complicates geometrical calculations. Especially when more than one scattering event occurs, which is the case especially at low altitudes, any geometrical approximations get invalid. The presence of aerosols of different types and, hence, different phase functions further complicates the problem of deriving exact light paths and, hence, air mass factors. Several different light paths contribute to a scattered light measurement and must be computed properly to simulate the measured SCDs.

The following requirements for the simulations of the balloon-borne limb measurements are implemented in the RTM TRACY

- all scattering and attenuation processes relevant to the radiative transfer including albedo
- multiple trace gas concentration and aerosol load profiles
- aerosol scattering parameterizations
- atmospheric refraction
- variable detector locations: latitude, longitude, and altitude
- variable viewing directions: rotation of the line of sight with respect to two perpendicular axes (elevation and azimuth angle)
- variable field of view of the detector, e.g. spherical or elliptical
- variable discretisation of the atmosphere in all 3 dimensions
- supports 3D variations in atmospheric parameters[1]

The Backward Monte Carlo Implementation

The backward Monte Carlo implementation of the RTM TRACY is discussed in detail in (*von Friedeburg* (2003), chapter 6 and A.1), so here only a brief overview is given. For a reference of all in- and output parameters see also (*von Friedeburg*, 2004).

In order to make the rather costly Monte Carlo calculations more efficient several deviations from the strict modeling of real photons are made. The first one is the concept of Photon Units (PU). Instead of a single photon, an ensemble of identical photons with a given intensity or weight is modeled. This concept facilitates the treatment of albedo reflection and absorption. In the case of modeling a single photon, an absorption process or reflection at a surface with an albedo < 1 would lead to the annihilation of the photon with a certain probability. Thus, the calculated photon path until that event would be useless. In the case of a PU simply its intensity is weighted with the absorption or reflection probability. For simplicity, the denotation photon is used to refer to the PUs in the following.

The photon's path is modeled in a three dimensionally discretized atmosphere. In z-direction (altitude) several layers can be defined which can again be subdivided into two dimensional atmosphere segments, referred to as 'voxels'. Despite the possibility of 3D calculations, only 1D calculations, i.e. discretization

[1] in the frame of this work only 1D calculations are performed for the sake of computing time

only along the z-axis, are performed in this work as the spacial inhomogeneities within a given altitude layer are rather small and the measurements are not sensitive to them anyway. Additionally, 3D discretization would lead to more voxels and, thus, much longer computation times. Each of these voxels, i.e. altitude layers in our case, are given certain parameters such as air density, trace gas or aerosol content as input. Additionally, the lowermost voxel's bottom, i.e. the surface, can reflect photons according to the given albedo. In a similar manner, clouds are treated as an infinitesimally thin layer at a certain voxel limit given by the cloud altitude which can reflect, absorb or transmit the photon.

As denoted by the term 'backward Monte Carlo', the photons are launched from the detector and their path towards the sun is modeled. Therefore, the photon starts at the user-defined detector position and its initial direction of propagation is diced out according to the detectors pointing direction and field of view. Next, the 'raytracer' calculates the path to the next voxel intersection and the distance to it along the photon's direction. Then it is diced out if any scattering or absorption occurs along that path. In case of a scattering event its type (i.e. Rayleigh or Mie) and location is diced out. At the voxel intersection, the photon's deviation from its incident direction due to refraction given by the different refractive indices of the two neighboring voxels is calculated. However, the refraction feature is turned off for the RT calculations presented in this thesis as its implementation is not yet fully validated. Then, according to the scattering phase function, its new direction is diced out and the routine starts anew until the photon finally reaches the defined top of the atmosphere. As it is extremely unlikely that a modeled photon hits the sun by chance ($p \approx 5.4 \cdot 10^{-6}$) due to the small fraction of the sky that is covered by the sun another deviation from the strict Monte Carlo concept is done by 'forcing' the photon into the Sun's direction after the last scattering process. This means that at the last scattering event, the photon's new direction is not randomly chosen, but its intensity is weighted with the probability of being scattered into the sun's direction and the photon's direction is set towards the sun. This method implies that every photon has to be scattered at least once and, thus, every photon that leaves the atmosphere without being scattered is not counted. This is rather unlikely for detector's placed at low altitudes but becomes more probable with increasing altitude or detector elevation angle. It is also not checked whether the unscattered photon reaches the sun, so that direct sun light conditions cannot be modeled in the current version of TRACY, a feature that might be implemented in future and is implemented in some older versions.

Output Parameters of TRACY

After a reasonable number of simulated photons (typically some thousands), all successful, i.e. at least once scattered, photon paths are summed up weighted with their respective intensities and the results are derived. Among many other parameters (for a complete list see (*von Friedeburg*, 2004)), the program computes the so-called Box Air Mass Factors (BoxAMF), i.e. discretized weighting functions, which are defined as the ratio of the averagely traveled light path inside a given voxel and its height. These are also used to calculate the slant column absorption of the trace gases by multiplying their concentration with the BoxAMF and the voxel height and summing up over all voxels. These simulated SCDs can be directly compared to the measurements. Another output is the radiance in the direction of detection which can also be directly compared to the measured absolute radiance assuming a homogeneous radiance over the detector's field of view (or at least a linear inhomogeneity in vertical direction so that it is averaged out).

Validation of TRACY

'Tracy' has been validated against the, already mentioned, analytical RTMs SCIATRAN and DISTORT (see *von Friedeburg* (2003), chapter 7 for results of the comparison exercises), as well as several measurements (see e.g. *Hönninger et al.* (2004); *Wagner et al.* (2004)).

Another stringent test to the model's absolute radiance and photon path calculations are the balloon-borne limb measurements presented in this work (see chapter 6) as they are conducted under rather difficult conditions, e.g. high SZA up to 95^o and very slant light paths through the atmosphere with BoxAMFs reaching 200 and more.

3.3 Profile Retrieval

The output of the DOAS evaluation of the measurement spectra, e.g. during balloon ascent or limb scanning, are Slant Column Densities (SCD) as a function of detector/tangent heights. The BoxAMF, output by the radiative transfer calculations, are used to derive vertical concentration profiles. Therefore, the BoxAMF-matrix $\overleftrightarrow{\mathrm{AMF}}$ has to be inverted, which is an inversion problem as described by *Rodgers* (2000).

Mathematically, the inversion problem can be formulated as follows:

$$\overrightarrow{SCD} = \overleftrightarrow{\mathrm{AMF}} \cdot \overrightarrow{VCD}, \tag{3.62}$$

$$\overrightarrow{VCD} = \overleftrightarrow{\mathrm{AMF}}^{-1} \cdot \overrightarrow{SCD}, \tag{3.63}$$

where $\overrightarrow{SCD}$ is a vector containing all the measured SCD values and $\overrightarrow{VCD}$ is a vector containing the desired Vertical Column Densities (VCD) on the grid used in the RT calculation. From these, the concentration at every altitude layer can be inferred by dividing by the layers' height d_i: $c_i = VCD_i/d_i$.

The inversion problem cannot be solved by simple matrix inversion of $\overleftrightarrow{\mathrm{AMF}}$ for several reasons. Firstly, the problem is overdetermined because there are generally more measurements contained in $\overrightarrow{SCD}$ than there are altitude layers in $\overrightarrow{VCD}$ so that $\overleftrightarrow{\mathrm{AMF}}$ is not a square matrix and, thus, cannot be unequivocally inverted. Secondly, the measurements generally do not contain information about all the altitudes of $\overrightarrow{VCD}$, so an initial guess (*a priori* information) is necessary for these altitudes in order to get reasonable results for the VCD-values of the altitudes the measurements contain information about.

Following chapter 4 of (*Rodgers*, 2000), a best estimate $\overrightarrow{\widehat{VCD}}$ considering the measurements and their errors and the *a priori* information and its error can be found by a method called the *Maximum A Posteriori* (MAP) solution or the *Maximum Likelihood* (ML) solution (this term is, strictly speaking incorrect but, however, widely used). It can be written as follows:

$$\overrightarrow{\widehat{VCD}} = (\overleftrightarrow{\mathrm{AMF}}^T \overleftrightarrow{\mathrm{S}}_{SCD} \overleftrightarrow{\mathrm{AMF}} + \overleftrightarrow{\mathrm{S}}_{ap}^{-1})^{-1} (\overleftrightarrow{\mathrm{AMF}}^T \overleftrightarrow{\mathrm{S}}_{SCD} \overrightarrow{SCD} + \overleftrightarrow{\mathrm{S}}_{ap}^{-1} \overrightarrow{VCD}_{ap}), \tag{3.64}$$

where $\overleftrightarrow{\mathrm{S}}$ is a covariance matrix defined as a diagonal matrix containing the squared errors, e.g. $\overleftrightarrow{\mathrm{S}}_{SCD} = \mathrm{diag}(\overrightarrow{\Delta SCD})^2$. $\overrightarrow{VCD}_{ap}$ is the *a priori* profile that has to be estimated, e.g. from chemical model output or other measurements, and $\overleftrightarrow{\mathrm{S}}_{ap}$ is its covariance. The covariance for $\overrightarrow{\widehat{VCD}}$ can be obtained by:

$$\overleftrightarrow{\widehat{\mathrm{S}}} = (\overleftrightarrow{\mathrm{AMF}}^T \overleftrightarrow{\mathrm{S}}_{SCD} \overleftrightarrow{\mathrm{AMF}} + \overleftrightarrow{\mathrm{S}}_{ap}^{-1})^{-1}, \tag{3.65}$$

and its *averaging kernel* matrix $\overleftrightarrow{\mathrm{A}}$ by

$$\overleftrightarrow{\mathrm{A}} = (\overleftrightarrow{\mathrm{AMF}}^T \overleftrightarrow{\mathrm{S}}_{SCD} \overleftrightarrow{\mathrm{AMF}} + \overleftrightarrow{\mathrm{S}}_{ap}^{-1})^{-1} \overleftrightarrow{\mathrm{AMF}}^T \overleftrightarrow{\mathrm{S}}_{SCD} \overleftrightarrow{\mathrm{AMF}}. \tag{3.66}$$

The averaging kernels give information about the quality and information content of the retrieved profile. Each row of the averaging kernel matrix tells where the information of the corresponding VCD_i is taken from. Ideal would be a delta function for each row, i.e. a value of 1 at column i and 0 everywhere else, so that the averaging kernel matrix would be the unit matrix. The area of the averaging kernel, i.e. the sum of its elements, should also be close to 1 for altitude levels where the retrieval is accurate. Generally, the area can be seen as a rough measure of the fraction of the corresponding profile point that comes from the measurements, rather than from the *a priori*. The half-width of the averaging kernel gives information about the altitude resolution of the retrieved profile. A value bigger than 1 suggests to repeat the retrieval on a wider grid. A value close to 1 indicates that the altitude grid was appropriately chosen but, as the FWHM cannot become smaller than 1 due to the discretisation, an even better resolution might be possible. The trace of the averaging kernel matrix gives the number of independent points in the retrieved profile. If this number is lower than the number of altitude layers used the inversion should be repeated on a wider grid. The reason for this is that too many output layers might cause artefacts in the retrieved profile, i.e. a too low value for one altitude is compensated by a too high value in the next one causing oscillations as a result. The retrieval method works in a way that it 'decides' whether to take the information from the measurements or the *a priori* profile based on the errors given in the respective covariance matrices. The covariance of the measurement is determined by the measurement errors but the error of the *a priori* can be taken e.g. from climatology. If it is unknown, its number has to be chosen carefully. If it is too small the retrieval could disregard information from the measurements. If it is too big or the *a priori* profile is wrongly chosen, the algorithm can produce fake features in the retrieved profile that might be mistaken as profile information. So it is important to always check the averaging kernels.

3.4 Chemical Modeling

In order to interpret the time-dependent profile observations during scanning limb measurement mode at balloon float, profiles as function of SZA are calculated by chemistry models. The output profiles of the photochemically active radical NO_2 can be validated by the measurements. Calculations from two models are used in the frame of this thesis being briefly described in the following.

3.4.1 The SLIMCAT 3-D Chemical Transport Model (CTM)

SLIMCAT is an off-line CTM being forced by the UK Meteorological Office (UKMO) analyzes for the horizontal winds and temperatures (*Chipperfield and Pyle*, 1998; *Chipperfield*, 1999). The vertical (diabatic) motion is calculated from the MIDRAD radiation scheme (*Shine*, 1987). Included in the model is a detailed stratospheric chemistry scheme involving the O_x, NO_y, Cl_y, Br_y, and HO_x families and long-lived tracer like N_2O, CH_4, or CO among others. The rate coefficients are based on the JPL-2002 kinetic data (*Sander et al.*, 2003). The photolysis rates are calculated using 4-dimensional lookup-tables (with pressure altitude, temperature, O_3 column, and SZA as coordinates) based on a scheme by *Lary and Pyle* (1991). Also included is heterogeneous chemistry on liquid and solid PSCs and mid-latitude sulphate aerosols. The standard simulations are performed on 24 isentropic levels ranging from ground to ~ 60 km with a horizontal resolution of $7.5^o \times 7.5^o$.

3.4.2 The 1-D Chemical Box Model LABMOS

The 1-D Chemical Box Model LABMOS[2] developed at the IUP Heidelberg (e.g. (*Erle*, 1999; *Fitzenberger*, 2000; *Bösch*, 2002)) allows for photochemical scaling of measured profiles of radicals like NO_2 or BrO. Stratospheric chemistry is modeled on 19 potential temperature (Θ) levels between 336 K (≈ 10.5 km) and 1520 K (≈ 42 km). Aerosol loads are taken from *Deshler et al.* (2003) as recommended by *Dufour et al.* (2005). NO_x is initialized with the measured NO_2 profile while all other relevant species are taken from the SLIMCAT output corresponding to the time and place of the measurement. Its chemistry scheme is based on JPL-2002 kinetic data (*Sander et al.*, 2003) and includes the most important gas phase, photolytical, and heterogeneous reactions of the O_x, NO_y, HO_x, ClO_x and BrO_x families. Photolysis rates are interpolated with respect to pressure, temperature, overhead ozone and solar zenith angle (SZA) from a lookup table where the actinic fluxes are calculated as recommended by *Lary and Pyle* (1991) and validated for j_{NO_2} by *Bösch et al.* (2001).

[2]=LAgrangian MOdel of the Stratosphere

Chapter 4

Instrumental and Experimental Details

The novel mini-DOAS spectrometer has been designed for low weight ($\approx$ 5 kg) and low power consumption (7.5 W), with particular emphasis being put on stable optical imaging and a reasonably large signal to noise ratio. While the former characteristic offers the chance for versatile applications, the latter feature is found to be necessary for the detection of O_3, NO_2 and in particular of the weakly absorbing gases (e.g. OClO, BrO, OIO, or IO), based on the experience with the direct sunlight DOAS (*Ferlemann et al.*, 1998, 2000; *Harder et al.*, 1998, 2000; *Bösch et al.*, 2003).

In the first section of this chapter, the setup of the mini-DOAS instrument is described. In the second sectioned, a detailed characterization of the performance and noise contribution of the spectrometer is given. and its performance both in the lab and during the balloon flights is discussed. A

4.1 Setup of the miniDOAS Instrument

This section describes the setup of the miniDOAS. The instrument has constantly been updated and new features have been added. Two stages of the development, in the following referred to as "mk.1" and "mk.2", are distinguished. The first subsection describes the early setup of the instrument (mk.1) used during the first four balloon flights (see table 6.1). The second section discusses the current setup of the instrument used from 2004 on (mk.2) and its advantages compared to the mk.1.

4.1.1 miniDOAS mk.1

The mini-DOAS instrument consists of 5 major parts (see figure 4.1): (a) 2 light intake telescopes for simultaneous nadir and limb observations (the latter being mounted on an automated elevation scanner), (b) glass fibre bundles which conduct the sky light from the telescopes into the spectrometers, (c) two commercial Ocean Optics USB-2000 spectrometers (d) which are put into a water-ice-bath for temperature stabilization, and finally (e) a single board computer for data handling and storage.

(a) The nadir and limb telescopes each consist of a spherical quartz lense (12.7 mm in diameter, 30 mm focal length) which focuses the incoming scattered skylight onto the round or the rectangular entrance of the glass fiber bundles. During the balloon flight, the nadir telescope is mounted to the bottom of the outer frame of the LPMA/DOAS payload structure, which provides an unobscured view into nadir direction. The limb telescope is mounted on an elevation angle scanner (built by Hofmann Meßtechnik, Rauenberg, Germany) which supports limb observations in a range of $+10^o$ to -20^o elevation angle,

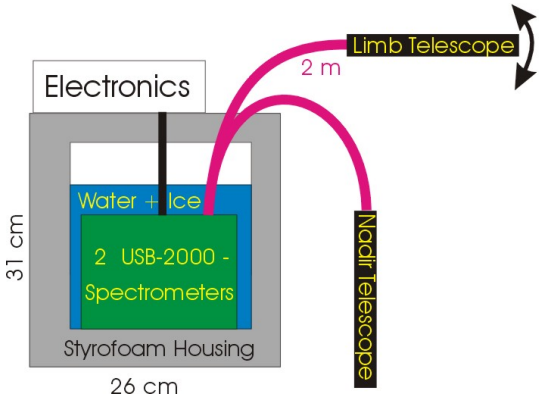

Figure 4.1: Sketch of the mini-DOAS instrument

with step sizes as small as 0.04^o. During the balloon flight, the scanner is mounted on the right hand side (i.e. in a $+90^o$ azimuth angle relative to the sun's azimuth direction) of the azimuth controlled LPMA/DOAS gondola.

(b) Each glass fibre bundle consists of 7 individual quartz glass fibers (100 μm in diameter, 2 m in length, numerical aperture $NA = 0.22$). Glass fibre bundles are used, since they not only allow for a more flexible arrangement of the instrument, but are also known for largely reducing the polarization sensitivity of grating spectrometers (*Stutz and Platt*, 1996, 1997). In fact, laboratory measurements show that by using glass fibre bundles the polarization sensitivity of an Ocean Optics USB 2000 spectrometer is small ($\leq 1\%$). For the nadir observations, the individual glass fibres are arranged in round geometry at the light intake, a mounting which in combination with the telescope supports a field of view (FOV) of 0.6^o. For the limb observations the glass fibres are arranged in a 'rectangular geometry' light intake setup i.e., the individual glass fibre entrances are aligned linearly. This arrangement supports a FOV of 0.19^o in the vertical and 1.34^o in the horizontal direction. Likewise, the glass fibres are linearly aligned at both exits, and the outgoing light is skimmed by a 50 μm wide and 1000 μm high spectrometer entrance slit.

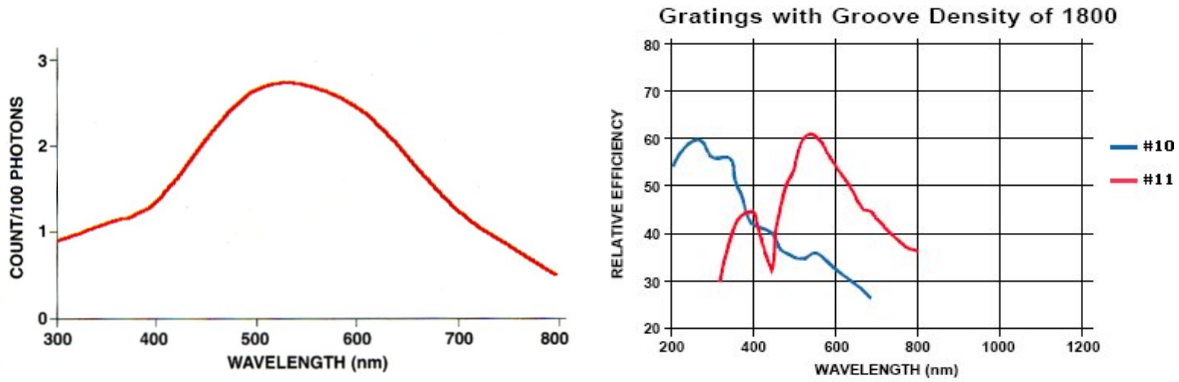

Figure 4.2: Relative efficiency vs. wavelength of the SONY ILX511 CCD detector (left panel) and of the two gratings used (right panel) as given by the manufacturer (*Ocean Optics*, 2004)

(c) The heart of the mini-DOAS balloon instrument consists of two commercial Ocean Optics USB 2000 spectrometers for simultaneous nadir and limb observations. The USB 2000 is a miniature grating spectrometer working in cross Czerny-Turner geometry. Its advantage is the small size ($86 \times 63 \times 30\,\mathrm{mm}^3$), the low weight (270 g) and the high photon detection sensitivity owing to an integrated

Table 4.1: Overview of the different spectrographs used.

Serial#	wavelength region	grating#	
USB2E3197	$327-527\,\mathrm{nm}$	10	mk.1
USB2E3198	$327-527\,\mathrm{nm}$	10	mk.1
USB2G919	$336-550\,\mathrm{nm}$	11	mk.1
USB2G2556	$336-550\,\mathrm{nm}$	10	mk.2
USB2G2557	$336-552\,\mathrm{nm}$	10	mk.2
USB2G365	$178-873\,\mathrm{nm}$	3	mk.2

linear CCD array detector (Sony ILX511). The light enters the spectrometer through an entrance slit ($50\,\mu\mathrm{m} \times 1000\,\mu\mathrm{m}$) from which it is focused by a collimator mirror onto a holographic grating with $1800\,{}^{\mathrm{grooves}}/_{\mathrm{mm}}$. A second mirror focuses the light onto the linear CCD array with 2048 pixels (each pixel is $14\,\mu\mathrm{m}$ wide and $200\,\mu\mathrm{m}$ high). Attached onto the CCD array detector is a cylinder lense which focuses the $1000\,\mu\mathrm{m}$ high entrance slit onto the $200\,\mu\mathrm{m}$ high detector. Also attached to the CCD array detector is the preamplifier and a control logic unit which handle the pre-amplification of the signals, A/D conversion to 12 bit data and communication.

Several USB 2000 spectrometers have been used during the five balloon flights (see Table 4.1). Figure 4.2 shows the relative sensitivity of the CCD array detector and the relative efficiency of the 2 gratings available with a groove density of $1800\,\mathrm{mm}^{-1}$. Grating # 10 is favored because of its higher efficiency in the UV where the CCD detector has a lower sensitivity. Therefore, the whole spectrometer has an almost constant sensitivity over its entire spectral range. Spectrometer # USB2G919 has been delivered with the wrong grating (# 11) built-in and replaced by another spectrometer with the desired grating (# 10) after one flight. An exception is the spectrometer # USB2G365. Its grating has a only $600\,{}^{\mathrm{grooves}}/_{\mathrm{mm}}$, so it covers a much wider spectral region ($178-873\,\mathrm{nm}$) at a lower resolution (3 nm). Hence, its performance cannot be compared to that of the other spectrographs discussed in the following. Some results obtained with this spectrometer are discussed in section 6.6.1.

The spectrographs cover a spectral range of approx. $330-550\,\mathrm{nm}$ at a full width at half maximum (FWHM) resolution of $0.8-1.0\,\mathrm{nm}$, or $8-10\,{}^{\mathrm{pixel}}/_{\mathrm{FWHM}}$ depending on wavelength. This wavelength coverage and resolution should allow for the detection of the atmospheric trace gases O_3, NO_2, O_4, H_2O, BrO, and OClO (and potentially IO, OIO, CH_2O).

(d) Both spectrometers are kept in a waterproof freezer bag, which itself is immersed in a water-ice reservoir ($\sim 2\,\mathrm{liters}$). This ensures a stable spectrometer and CCD array temperature of 0^oC during the entire balloon flight.

(e) Data handling and storage is maintained by a single board PC (type National Geode 200 MHz) equipped with a flash memory. The allocated data are transferred from the spectrometers to the PC via a USB data transfer connection. It supports a data transmission rate fast enough to record a single spectrum every 25 ms. Possible integration times per spectrum as provided by the manufacturer of the spectrometers are in the range of $3-65535\,\mathrm{ms}$. The PC can either be operated under Windows or Linux with our lab-owned DOASIS or XDOAS softwares packages, respectively. Both software tools support the automatic adjustment of the integration time, and recording and storage of the measured spectra. However, the control of the limb scanning stepper motor is only possible with DOASIS so this software is used from the second flight on when the stepper motor has been implemented.

The total size of the instrument is $260 \times 260 \times 310\,\mathrm{mm}^3$ (w/o fibers), its weight is $\sim 2\,\mathrm{kg}$ plus 2 kg of water and ice, and its power consumption is $\sim 7.5\,\mathrm{W}$.

4.1.2 miniDOAS mk.2

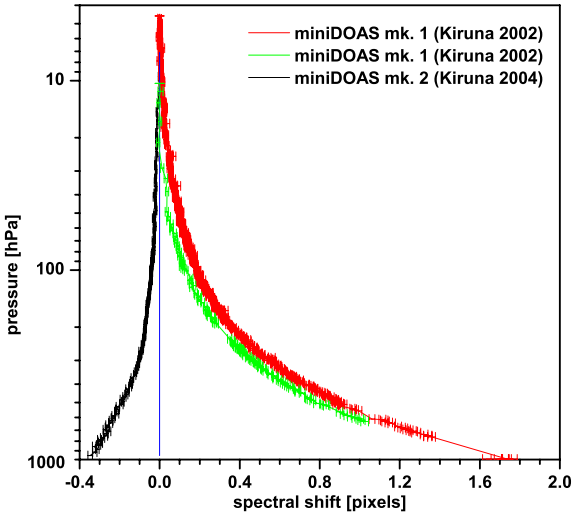

Figure 4.3: Spectral shift of the measured spectra relative to the solar reference recorded at balloon float vs. pressure for the miniDOAS mk.1 compared to mk.2. The solar reference spectra were recorded at 4.6 hPa, 10.3 hPa, and 7.1 hPa for the Kiruna 2002, 2003, and 2004 flights, respectively.

In this section, the instrumental improvements and the performance of the current version of the miniDOAS instrument are discussed.

The biggest problem of the initial setup was the missing pressure stabilization. Hence, the spectrometer optics was always at ambient pressure. When the pressure decreases from ~ 1000 hPa at ground level to ~ 5 hPa at balloon float, the refractive index of the air inside the spectrograph also decreases influencing the optical imaging and resulting in a spectral shift of the recorded spectra of more than one pixel. A pressure sealed housing has been developed to enclose the two spectrometers. The effect on the imaging can be seen in figure 4.3. For the unstabilized mk.1 flights, the spectral shift decreased from ~ 1.7 pixels at ground pressure to zero at float, while the spectral shift is much smaller for the mk.2 flight. The reason for the remaining shift of the pressure stabilized mk.2 instrument is somewhat unclear. As the sign of the shift is the opposite, it cannot be explained by a bad sealing of the instrument, unless the internal design of the different spectrometers used has changed. A possible explanation could be that the instrument was not perfectly sealed and air entered the spectrograph during the ascent thus increasing the pressure inside. This is, however, unlikely as tests on the ground showed that the instrument is stable for many hours. The spectral shift could also be attributed to an imperfect temperature stabilization as a change in temperature also effects the optical imaging of the spectrograph. Unfortunately, there has been no further flight in the mk.2 configuration so far to further investigate this effect.

In order to achieve a stable pressure during flight, a vacuum sealed housing to for the two spectrometers was built. Its design is similar to the housing of the direct sunlight balloon spectrometer. In order to save weight, it is completely made of aluminum. It consists of a pot where the two spectrometers are placed in and a flange which is screwed onto it with a rubber ring in between. On the flange, there are vacuumproof plugs for the two USB cables and feedthroughs for the glass fibers. Therefore, new custom built glass fiber bundles are used. They consist of 11 single fibers each 100 μm in diameter aligned linearly at the exit connected to the spectrometers forming a 1100 μm high slit. This means that the 1000 μm high entrance slit of each spectrometer is completely lit resulting in a higher light throughput compared to the old setup. The glass fiber at the telescope side have the same geometry

as in the mk.1 configuration, i.e. round geometry for the nadir channel and linear geometry for the limb channel. Since 11 fibers are used now the horizontal FOV of the limb telescope increased to 2.1^o. The vertical FOV is still 0.19^o. The FOV of the nadir telescope is now approx. 0.8^o. The sealing was checked in the laboratory. The instrument can keep a pressure below 10^{-1} hPa for over a week. The imaging has also been checked in the laboratory and is stable for over 12 h as long as the temperature is constant. For temperature stabilization, the whole aluminum pot with the spectrographs inside is put into an epoxy glass housing with a water ice mixture inside. The rest of the setup like telescopes and board computer remains unchanged. Due to the additional aluminum housing, the total weight of the instrument (including fibers, stepper motor and electronics) increased to 4.3 kg plus 2.8 kg of water-ice-mixture.

Thanks to the higher light throughput and the strongly decreased spectral shift, much lower residuals can be achieved which allows the evaluation of small absorbers like BrO (for a detailed discussion of the results see section 6.5).

4.2 Characterization of the Instrument

4.2.1 Instrumental Noise

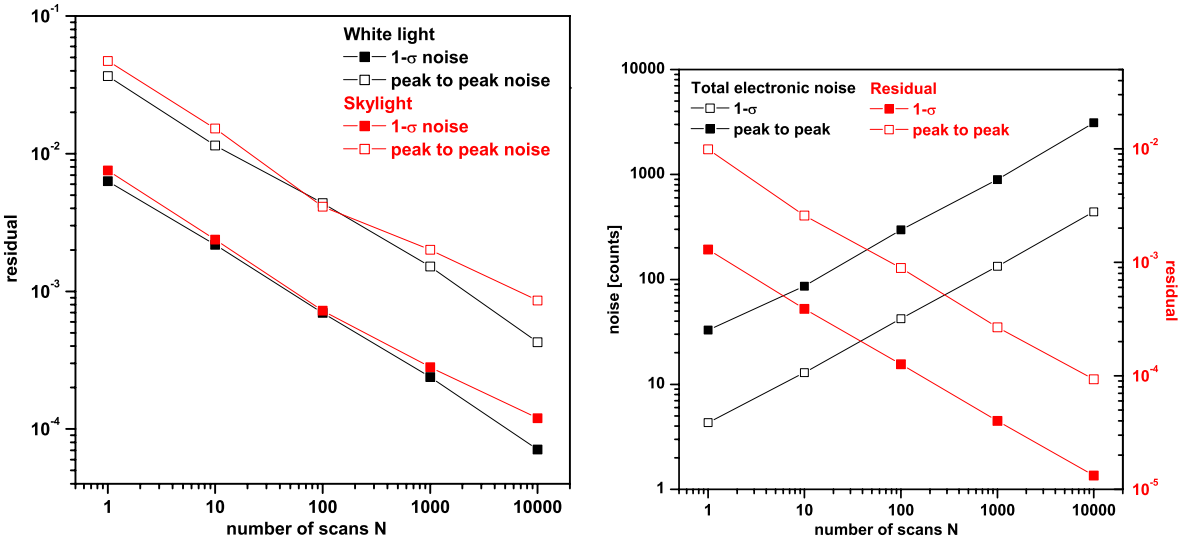

Figure 4.4: Left panel: Root mean square, or 1-σ (filled squares) and peak to peak residual (open squares) as a function of the number of co-added spectra N at 80% illumination level of the CCD array detector for white light of an Ulbricht sphere (black symbols and lines) and skylight (red symbols and lines). Right panel: electronic noise (red symbols and lines) and resulting residuals assuming 80 % saturation level (red symbols and lines) as a function of the number of co-added scans N.

Several effects contribute to the total instrumental noise. There are random noise contribution caused by the detector electronics and the statical noise of the photo-electrons themselves. Additionally, systematic effects, e.g., caused by pixel structures of the detector or a non-linearity of the detector sensitivity contribute to the instrumental noise. In this section, first, the random noise contributions are given quantitatively, and then the systematic noise sources and ways to reduce them are discussed qualitatively.

The most dominant source of noise is caused by the photon-electron statistics. Assuming them to be normally distributed, their 1-σ noise is given by The square root of their number. The well-depth of the CCD-detector is 62500 as given by the manufacturer (*Ocean Optics*, 2004). Assuming a saturation level of 80 % yields an photo-electron shot noise of 224 electrons corresponding to a 1-σ noise of $\sigma_{photo-electron} = 0.474$ % for a single scan. As full saturation corresponds to 4096 counts, 1 count corresponds to ~ 15 photo $-$ electrons. Thus, the photo-electron noise is ~ 15 counts. If a white light source (e.g. a halogen lamp) is used, the noise level of a single spectrum can be experimentally obtained. For structured light sources (e.g. the sun), the noise can only be experimentally measured by dividing two spectra. Also for a DOAS evaluation, the spectrum is divided by a reference spectrum of the same light source. Therefore, always two spectra contribute and, consequently, the noise increases by factor of $\sqrt{2}$. Thus, the physical limit of the residual given by the photo-electron shot noise is $\sigma_{photo-electron} = 0.67$ %.

The second most important noise contribution is caused by the detector and its attached electronics. Noise is caused during the read-out, the pre-amplifying and A/D-conversion processes. As no details about the implemented electronic devices are available, quantitative numbers of the electronic noise can only be obtained experimentally by recording dark spectra, i.e. spectra with no photo-electron noise. Again the statistics is tricky. In figure 4.4, the electronic noise (black lines) is determined experimentally by subtraction of two consecutively measured dark spectra. A noise of 66 electrons (corresponding to 4.4 counts) for 1 scan, which is increasing proportionally to the square root of the number of scans, is found. This yields for a single offset 45.2 electrons or 3.1 counts (i.e. the afore mentioned numbers divided by $\sqrt{2}$)). As 2 spectra with their electronic noise contribute to a DOAS evaluation, the plotted numbers give the real noise contribution caused by the electronics. Assuming 80 % saturation level, the electron contributes to the residual with $\sigma_{electronic} = 0.095$ % for 1 scan. As it is pure random noise, it decreases proportionally with the number of scans which is shown in figure 4.4 by red lines. Note that, strictly speaking, 4 electronic offsets contribute to the DOAS evaluation of 1 spectrum as both the spectrum to be evaluated and the reference spectrum are offset corrected by a dark spectrum (called offset spectrum). However, the offset spectrum is usually recorded with 10000 scans corresponding to a noise of 10^{-5} which can be neglected even for 1000 co-added scans.

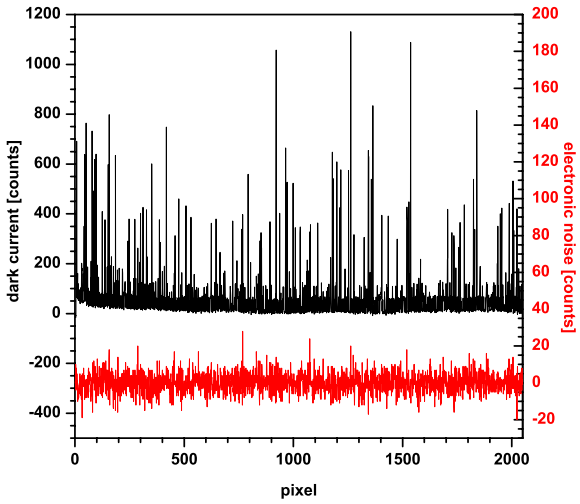

Figure 4.5: Typical dark current spectrum after removal of the electronic offset for 60 s integration time (black line) and resulting noise spectrum (red line), i.e. two subtracted dark current spectra of the same integration time.

The dark current is caused by a discharge of the detector pixels without light impact. The dark current

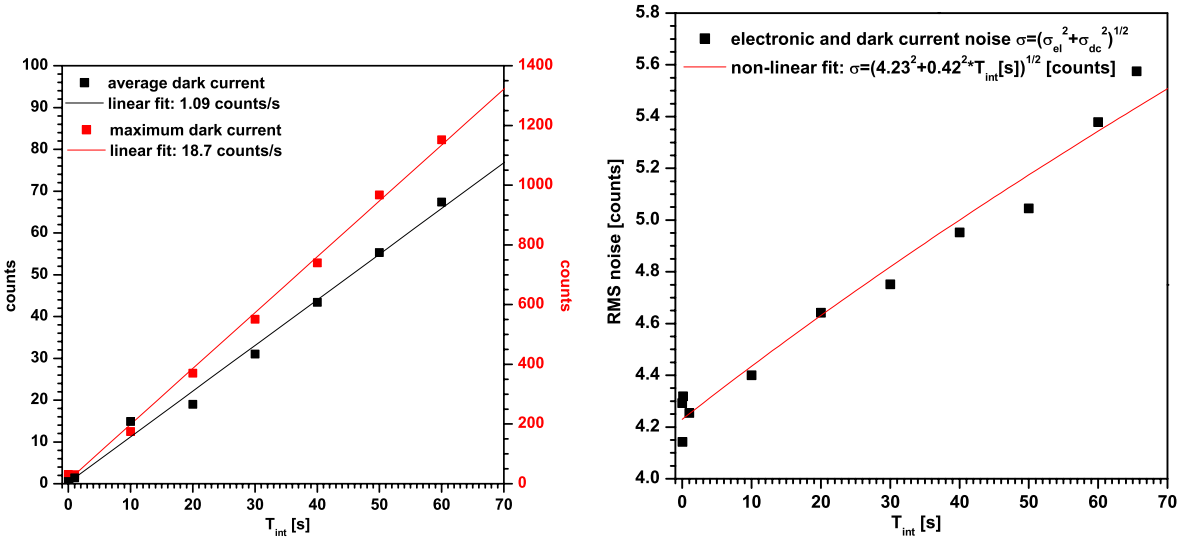

Figure 4.6: Left panel: Average (black squares) and maximum (red squares) dark current vs. integration time (T_{int}) and linear fits of the measured data (solid lines). Right panel: rms noise ($\sigma = \sqrt{\sigma_{el}^2 + \sigma_{dc}^2}$) vs. T_{int} (black squares) and non-linear fit thereof (red line).

spectrum of the SONY ILX511 (see figure 4.5, black line) shows a large pixel to pixel variation e.g., next to pixels with very small dark current there are pixels for which the current is up to 18 $^{\text{counts}}/_{\text{s}}$ (corresponding to 270 $^{\text{electrons}}/_{\text{s}}$) (see figure 4.6, left panel). The average dark current is measured at 1.09 $^{\text{counts}}/_{\text{s}}$ (corresponding to 16.6 $^{\text{electrons}}/_{\text{s}}$). The dark current noise spectrum (see figure 4.5, red line) does not show any structures. The dark current noise cannot be independently measured as the electronic noise σ_{el} is also contributing to the total noise σ of a dark spectrum. However, the electronic noise is constant while the dark current noise is increasing with the square root of the integration time T_{int}: $\sigma_{dc} = x \cdot \sqrt{T_{int}}$. $\sigma = \sqrt{\sigma_{el}^2 + x^2 \cdot T_{int}}$ is non-linearly fitted to the measured rms noise data. A value of $x = 0.42\,^{\text{counts}}/\sqrt{\text{s}}$ is found. For typical integration times of $\sim$ 100 ms during balloon flight, the dark current noise only contributes with $4 \cdot 10^{-5}$ to the total noise (assuming an 80 % saturated spectrum), which is negligible.

The root-mean-square sum of the above contributions[1] gives a total noise of $\sigma_{tot} = 0.68$ %. As all these sources of noise are purely random and proportional to the number of scans, the total noise of the measurement can be reduced by summing up multiple spectra. Figure 4.4 (left panel) shows the total noise at 80% saturation as a function of the number of co-added spectra for both white light and skylight as source. It can be seen that the noise is proportional to the square of the reciprocal number of scans N up to $N = 10000$ for white light as source. For solar light as source, the residual noise is slightly higher at high scan numbers ($N > 1000$), resulting from incompletely removed Fraunhofer residuals. For the white light source, the total noise for a single scan is measured at 0.63% which is close to the above mentioned number of 0.68 % obtained by summing up the theoretical photo-electron shot noise and the measured electronic noise. For a fairly large number of scans the instrument, in fact, operates at the physical limits given by the photo-electron and electronic noise. During balloon flight up to 1000 spectra (corresponding to $\sim$ 20 s integration time) are co-added resulting in a total 1-σ noise of $2.4 \cdot 10^{-4}$.

The most important systematic source of noise are the diode structure. It is caused by the different sensitivity of the individual detector pixels. If the instrument were totally stable this would cause no

[1] $\sigma_{tot} = \sqrt{\sigma_{photo-electron}^2 + \sigma_{electronic}^2}$

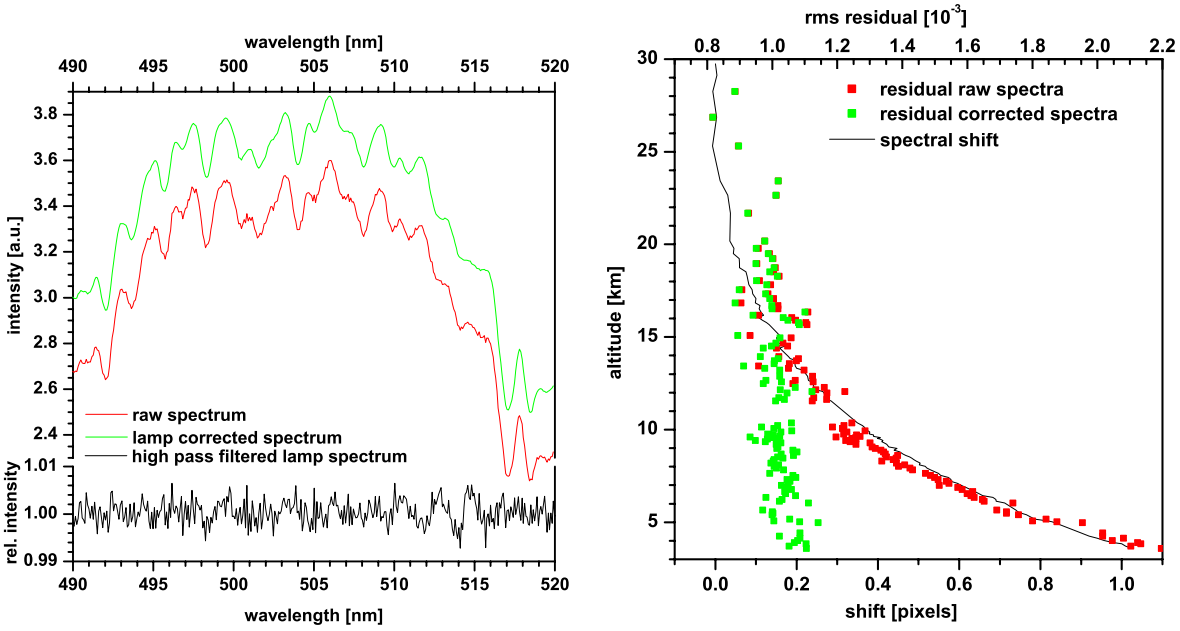

Figure 4.7: Left panel: comparison of a raw (red line) and a corrected spectrum (green line). Also shown is the high pass filtered lamp spectrum (black line) used for the correction. Right panel: spectral shift (black line) and residual of the DOAS evaluations in the visible spectral range ($490 - 520\,\mathrm{nm}$) with (green squares) and without (red squares) lamp correction.

problems as every spectrum is divided by the reference spectrum during the DOAS evaluation process. But if shifts occur due to instable pressure and temperature inside the instrument, every single pixel is not divided by the same pixel of the reference spectrum which causes large residuals by far exceeding the residuals caused by photo-electron and electronic noise. As these structures are very systematic, a remedy for this problem is to divide every spectrum by a high pass filtered white lamp spectrum prior to the DOAS evaluation. This "lamp correction" is illustrated in figure 4.7. In the left panel, the diode structures, i.e. a high pass filtered white lamp spectrum, are shown as well as the noisy raw spectrum and the much smoother corrected spectrum. In the left panel, the impact of the lamp correction is shown by the example of the balloon ascent at Kiruna 2003. Using the uncorrected spectra for the DOAS evaluation results in RMS residuals increasing from $\sim 1 \cdot 10^{-3}$ for shifts < 0.2 pixels to values above $2 \cdot 10^{-3}$ for shifts > 1 pixel. Using the corrected spectra, the residuals have values close to $1 \cdot 10^{-3}$ independent of the spectral shift.

4.2.2 Detector Linearity

An important factor for the quality of a spectrometer is the linearity of the detector. Especially in the case of absolute radiance measurements, any nonlinearity directly affects the accuracy of the result. For DOAS evaluations, a nonlinearity is a minor problem as long as the intensity within the wavelength interval of interest is rather constant. Nevertheless, nonlinearities can introduce additional structures and lead to higher retrieval uncertainties.

The Windows drivers for the spectrometer provided by *Ocean Optics* (2004) have a linearity correction feature. This feature uses a polynomial of 7^{th} degree to calculate a corrected count rate from every

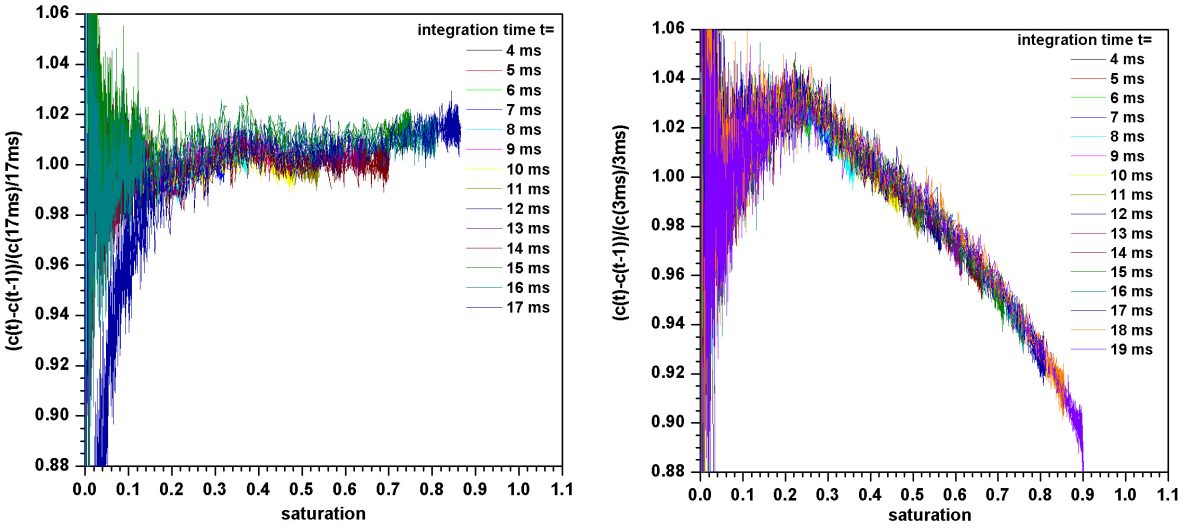

Figure 4.8: Relative sensitivity of the detector with the linearity correction turned on (left panel) and off (right panel). Plotted is the difference of two spectra with 1 ms difference in integration time divided by a spectrum divided by its integration time (17 ms in the left, and 3 ms in the right panel, respectively) vs. the saturation of every single pixel.

measured count rate for every pixel:

$$c' = c : \sum_{j=0}^{7} a_j c^j, \tag{4.1}$$

where c' denotes the corrected and c the uncorrected count rate. However, this feature cannot be switched on by our measurement software DOASIS. So during all balloon flight it was switched off. As I found out only afterwards, it is possible to switch the linearity correction on in the original software OOIBase32 (*Ocean Optics*, 2004). Then the driver performs the linearity correction also when called from the DOASIS software. This will be done for future balloon flights. As all the measured spectra consist of many co-added scans, the linearity correction cannot be performed afterwards for already conducted flights.

The detector linearity is checked in a laboratory measurements. The white light of an Ulbrich sphere, which is also used for the absolute calibration, is used. The current through the lamp is kept constant which ensures a constant light output during the entire measurement series given the voltage stays constant, too, which is the case after the lamp has reached a constant temperature, approx. $30-60$ min after it is switched on. The intensity is measured for integration times ranging between the minimum integration time of the spectrograph (3 ms) up to the time when full saturation is reached (~ 20 ms) in steps of 1 ms. 1000 scans have been added for a better S/N ratio. Then the difference of 2 consecutive spectra, i.e. spectra with 1 ms difference in integration time, is calculated. This difference gives the number of counts which are measured within 1 ms after a certain saturation is reached. These differences obtained for all integration times are normalized by dividing them by a spectrum with the intensity of the lamp measured in 1 ms, obtained by taking one spectrum and dividing it by its integration time. This can be written as:

$$\frac{c(t) - c(t-1)}{\frac{c(T)}{T}}, \tag{4.2}$$

where $c(t)$ is the number of counts measured within the time t, and $c(T)/T$ is a spectrum with integration time T divided by its integration time T. This function is a measure of the sensitivity of every detector

pixel at a certain saturation. This function is plotted vs. the degree of saturation of each pixel of the spectrum $c(t)$ in figure 4.8. The left panel shows the sensitivity with the linearity correction turned on in the driver while the right panel shows a similar measurement with the linearity correction turned off. In an ideal case, i.e. if the detector were perfectly linear and had no noise, all values would be equal to one. Any deviation from one is due to measurement noise or detector nonlinearities. In the uncorrected case, the sensitivity decreases from values near 1.03 for low saturation levels $(0.2 - 0.3)$ to values below 0.9 for a saturation level of 0.9. This value of 0.9 means that the detector sensitivity to photons is 10 % lower for a pixel with 90 % saturation compared to a pixel with 40 % saturation. Note that this does not mean that spectra with a saturation of 90 % have a 10 % lower count rate per time compared to one with a saturation of 40 % as the actual measured count rate is the integral over the shown sensitivity function. However, this nonlinearity effect can result in deviations of higher saturated spectra compared to lower saturated ones in the order of several %. In the linearity corrected case, the sensitivity is almost constant for saturation levels between 0.2 and 0.9 within the uncertainties given by the measurement noise. For saturation levels below 0.1, the measurements are too noisy to allow clear conclusions. The deviations of the curves for different integration times might be due to fluctuations in the lamp's output or the linearity correction itself might lead to these small intensity fluctuations. An explanation is the temperature dependant offset which is always added to every spectrum, i.e. every measured count rate c_i for pixel i is the sum of the actual signal caused by the photoelectrons s_i and an offset value $o_i(T)$ which strongly depends on temperature T, i.e. $c_i = s_i + o_i(T)$. As the offset is not known at the moment a spectrum is recorded, the automatic linearity correction can only take the measured value c_i as input although it should be applied to the signal s_i. However, this error should be small in the case of a temperature stabilized measurement and high saturation levels when s_i gets significantly larger than the offset (the offset is in the order of $1 - 10$ % of the full saturation depending on the temperature and the individual spectrometer). As already mentioned above, the intensity correction cannot be performed afterwards on offset-corrected spectra as it obviously has to be done for every single scan individually and, thus, cannot be applied to spectra consisting of several co-added scans.

4.2.3 Spectrograph Stray Light

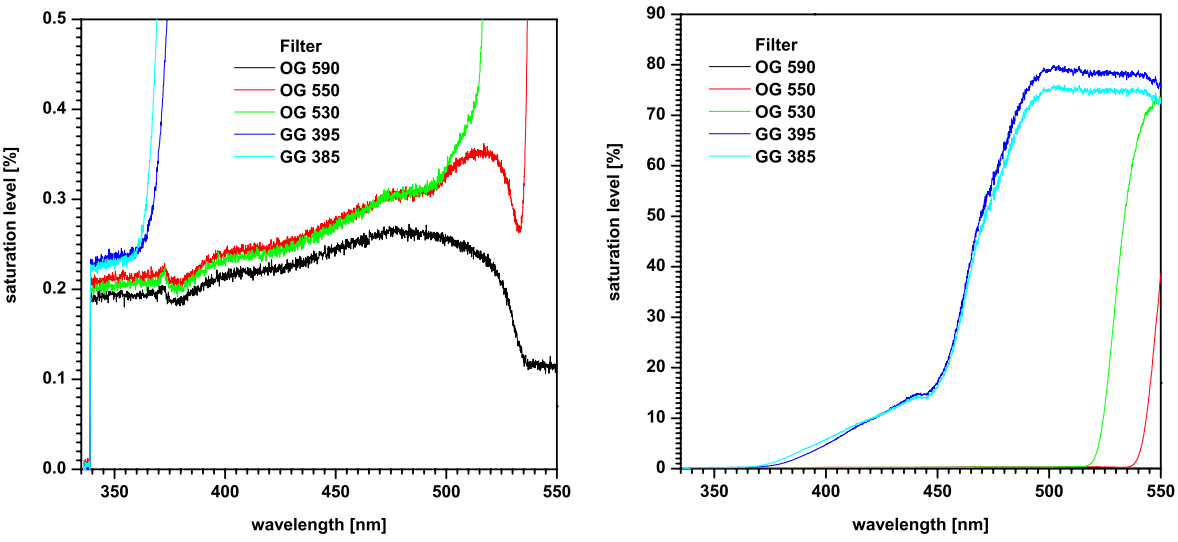

Figure 4.9: Straylight socket determined by filter measurements of light from a halogen lamp.

To estimate the amount of straylight contribution, a series of measurements of the light of a halogen lamp using several filters is performed in the laboratory. The used filters have a throughput near 1 for wavelengths above the cut-off wavelength and a throughput of $< 10^{-5}$ at wavelengths below this wavelength with a transition range of ± 20 nm around the cut-off wavelength. E.g., the used filter type OG530 has a transmission of 0.86 at 550 nm, 0.48 at 530 nm, and $5 \cdot 10^{-5}$ 510 nm. So all light detected at wavelengths below the cut-off wavelength is assumed to be straylight. As the straylight reaches the detector indirectly, it is assumed to be wavelength Figure 4.9 reveals that the straylight socket contributes with to the measured signal by 0.2 % at the low and 0.3 % at the high wavelength end of the detector for full saturation. This means that also for poorly saturated spectra, e.g. in the UV at tropospheric altitudes where the saturation level is only around 20 %, the straylight ratio is around 1 %. It should be noted that for solar radiation as light source the situation might be slightly different but the numbers should be of the same order. This can be seen by comparing the measured curves for the filters with highest (OG 590) and lowest cut-off wavelength (GG 385). Although the OG 590 filter cuts off a big portion of the lamp's output, the straylight is not much lower than for the GG 385 filter. Additionally, the straylight contamination of the measured spectra is corrected for by the additive polynomial in the DOAS fit. Hence, it is believed that straylight does not seriously affect the accuracy of the results of the DOAS fit. For the absolute radiance measurements straylight can lead to errors of up to 1 % in the worst condition, i.e. in the UV at low altitudes where the saturation level of the measured spectra is only around 20 %.

4.3 Observation Geometry

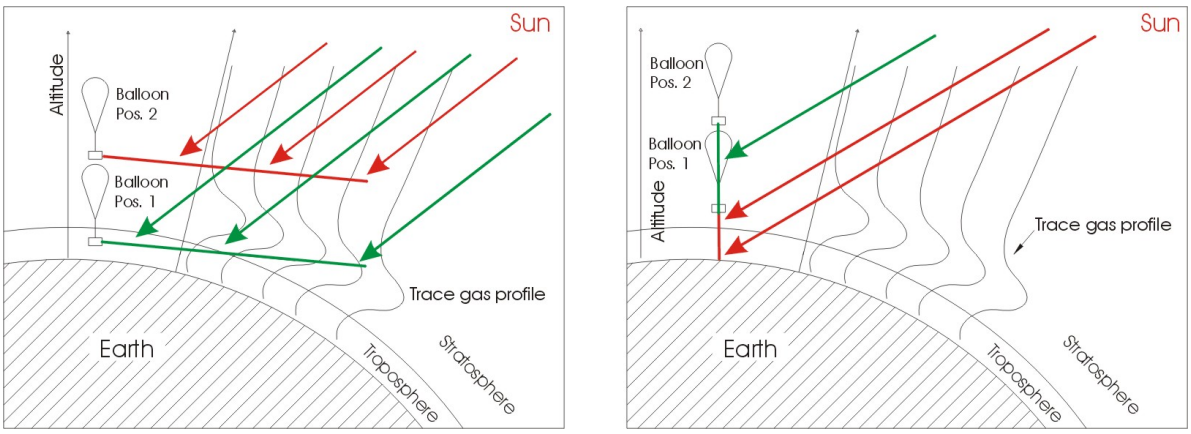

Figure 4.10: Sketch of the viewing geometry for limb (left panel) and nadir observations (right panel).

The miniDOAS instrument can be operated in three observation modes. They are illustrated in figure 4.10. One spectrometer channel is looking in limb direction. Its azimuth angle is kept fixed during the entire flight at an angle of 90^o relative to the sun given the gondola is perfectly azimuth-stabilized. This ensures that the local SZA is constant along most of the light path which is important when measuring photochemically active species like BrO or NO_2. This viewing direction has the disadvantage of being at the minimum of the radiance as the Rayleigh scattering cross section gets minimal for an angle of 90^o to the sun. On the other hand, looking into a relative radiance minimum ensures that the radiance is not strongly changing when the gondola oscillates in azimuthal direction. Looking at an angle of 180^o to the sun would be another option resulting in a higher radiance as long as the SZA is below 90^o. For higher SZA, the telescope would look into the dark hemisphere. Looking into the direction of the sun is

not practicable because of the danger of looking directly into the sun resulting in oversaturated spectra that cannot be evaluated. The elevation angle of the limb telescope is fixed during balloon ascent and vertical profiles can be inferred from the measurements as the balloon ascents through the atmosphere. At balloon float, i.e. when the balloon altitude is more or less constant, the limb telescope's elevation angle is changed and, thus, scanning through the atmosphere. The second spectrometer channel is looking into nadir direction, i.e. straight downwards. It was also tested for direct sun observations (see section 6.6.1).

4.4 DOAS Evaluation

For the DOAS evaluation, the WinDOAS software (*Fayt and van Roozendael*, 2001) is used whose features are briefly described in section 3.1.2.

4.4.1 Wavelength Calibration of the Spectrograph

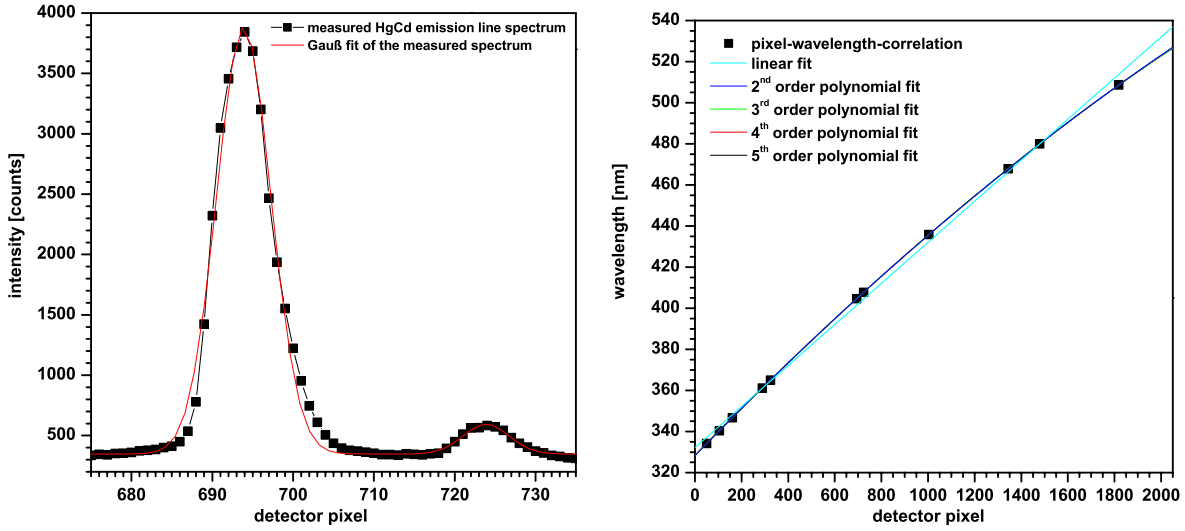

Figure 4.11: Left panel: Example of an HgCd spectrum (black squares) and 2-peak-Gauß fit of the measured spectrum (red line). Right panel: example wavelength-pixel correlation plot (black squares) and $1^{st} - 5^{th}$ order polynomial fit (colored lines) of the experimental data.

An important issue for DOAS evaluation is the exact wavelength calibration of both the measured spectra and the fitted trace gas cross sections. Literature cross sections measured with Fourier Transform (FT) spectrometers are believed to have a very precise wavelength calibration. The wavelength calibration of grating spectrometers is not exactly known and depends on the measurement conditions (e.g. temperature and pressure inside the spectrograph). Hence, it has to be anew determined for every balloon flight by measuring spectral features of known wavelength, e.g. gas emission lines. But also the Fraunhofer lines of the spectra to be evaluated can be used for wavelength calibration.

One way to determine the wavelength calibration is to record the line spectrum of low pressure gas lamps (e.g. mercury-cadmium (HgCd), Neon, Krypton,...) in the laboratory before the balloon flight. However, this method is inaccurate in several aspects. The instrumental conditions (spectrograph temperature and, especially, pressure) and, thus, the wavelength-pixel mapping are different under lab and

flight conditions. The line width of the emission lines is generally much narrower than the spectrograph's resolution. Hence, the lines can be approximated as delta-peaks and the recorded spectrum is given by the instrument function. If the instrument function is can be formulated mathematically (e.g. by a Gaussian), the exact position of the line can be obtained by fitting the respective instrument line shape to the spectrum. If the instrument function is not known, the line position can be approximated (i.e. with 1 pixel uncertainty) by the pixel with maximum intensity. Additional uncertainties are introduced if multiple lines are considered. The positions of the individual lines cannot be determined as exactly as for single lines. In figure 4.11 (left panel), an example of a measured HgCd line spectrum together with a 2-peak-Gauß fit is shown. The instrument function can be very well approximated by a Gaussian although a slight asymmetry is observed. However, the line position can be determined quite precisely. In figure 4.11 (right panel), the obtained pixel-wavelength correlation for all lines are shown. Polynomials with degrees between 1 and 5 are fitted to the experimental data. Except for the linear fit, which significantly deviates from the polynomial fits with higher degrees (up to 10 nm) the obtained fit results are very similar which shows that the non-linearity of the wavelength-pixel-correlation is not very strong.

For sunlight measurements, a more precise wavelength calibration is possible using the Fraunhofer structures. One possible method is to use the calibration feature of WinDOAS. The application of this tool is briefly described here, for more details see (*Fayt and van Roozendael*, 2001). The wavelength range of the spectrograph is split into several regions. In every region, a model-function (e.g. Gaussian) is optimized in a way that its convolution with a high-resolved Kurucz spectrum best matches the measured spectrum. For every region, the instrumental resolution and the wavelength calibration is obtained. This method only yields reasonable results if the instrumental line function is well approximated by the applied function. As shown above, the line function of the used Ocean Optics spectrometers is very close to a Gaussian. The obtained calibration can be checked by the following method. The high-resolution Kurucz spectrum is convolved with the measured instrumental function. The obtained spectrum is used as reference spectrum for a DOAS evaluation. The shift and stretch parameters show deviations of the applied wavelength calibration from that of the analyzed spectrum. The advantage of this method is that it can be used for the same wavelength range the fit is actually performed in. Note that only the solar reference spectrum has to be wavelength calibrated. The analyzed spectra are shifted relative the reference by the DOAS fit algorithm. All the described methods are used for the wavelength calibration of the spectra measured during the balloon flights and its results cross-checked. Hence, the wavelength calibration is believed to be precisely known.

4.4.2 General

All spectra measured during a balloon flight are corrected for offset and dark current prior to the DOAS evaluation. Therefore, offset and dark current spectra recorded either on the ground short before the balloon launch or, if available, at balloon float after sunset are used. Afterwards, the spectra are divided by a high pass filtered white lamp spectrum to eliminate the pixel-to-pixel structures (for details see section 4.2.1).

All high resolution cross sections are convolved to the instrumental resolution with the actual instrumental slit function determined from a recorded line spectra of an HgCd lamp ($\lambda = 468\,\text{nm}$ for the evaluations in the visible range and $\lambda = 360\,\text{nm}$ for the BrO evaluation in the UV).

Also included in the fitting routine is a correction spectrum for the Ring effect (*Grainger and Ring*, 1962) calculated with WinDOAS for the actual Fraunhofer reference. As Fraunhofer reference the first spectrum after reaching float altitude (i.e. with the lowest SZA) is used for which the trace gas absorptions should be minimal. This is definitely the case for absorbers like O_4 and H_2O who have their

highest concentrations in the troposphere and, with restrictions, for O_3 which peaks typically 15 km below float altitude, but not for NO_2 with its maximum near float altitude. This results in negative NO_2-dSCD values throughout most of the flight.

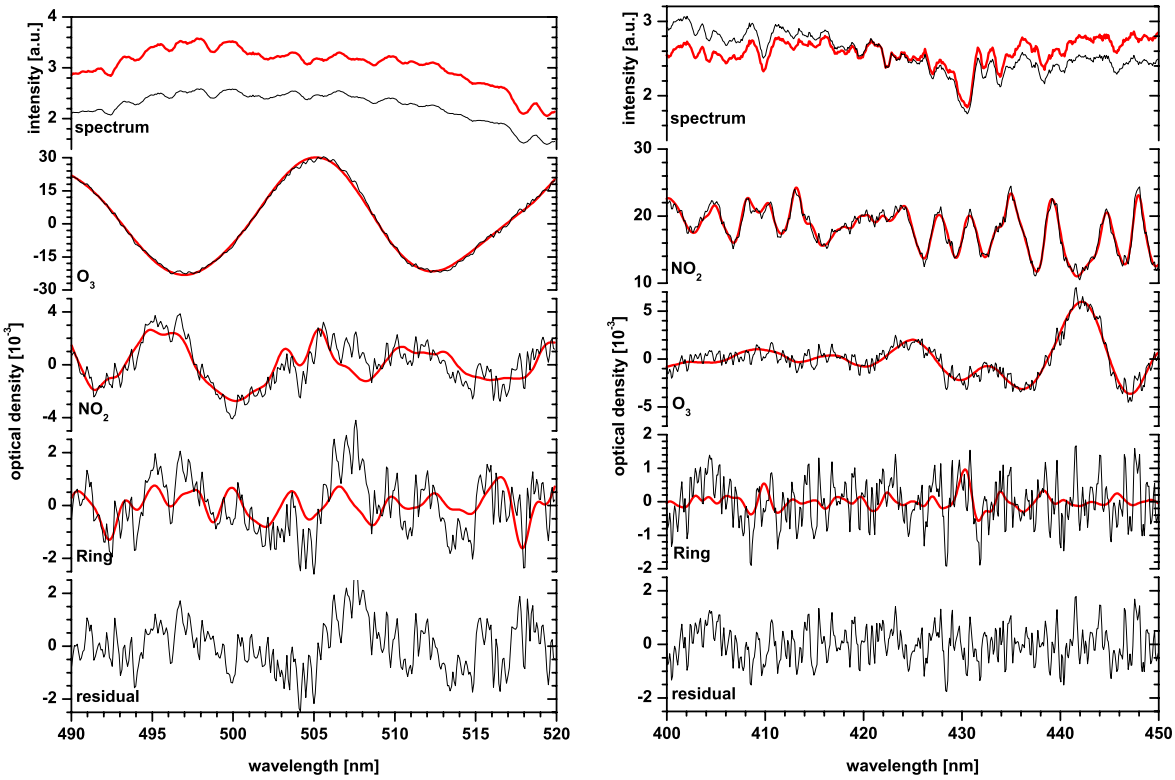

Figure 4.12: Sample DOAS evaluations of the miniDOAS mk.1 instrument for the flight at Kiruna March 23, 2003. Shown is the evaluation of ozone (left panel) and NO_2 (right panel) in the wavelength intervals $490-520\,\mathrm{nm}$ and $400-450\,\mathrm{nm}$, respectively, for a limb observation at float altitude in limbscanning mode ($31.62\,\mathrm{km}$ altitude, -5.5^o elevation angle, 90^o azimuth angle, and 89.9^o SZA for the O_3 evaluation, and $30.94\ km$ altitude, -3.5^o elevation angle, 90^o azimuth angle, and 89.4^o SZA for the NO_2 evaluation, respectively). Shown is the optical density of the absorbance of O_3, NO_2, Ring (red lines) and the latter plus the residual structure (black lines). The upper two traces show the measured (red line) and the Fraunhofer (black line) spectra. The latter is recorded at $29.75\,\mathrm{km}$ altitude, $+0.5^o$ elevation angle, 90^o azimuth angle, and 88.5^o SZA.

4.4.3 O_3 Evaluation

The spectral retrieval of O_3 is performed in the $490-520\,\mathrm{nm}$ range (see table 4.2 and fig. 4.12). The following cross sections are used: O_3 from *Voigt et al.* (2001) at $T = 203\,\mathrm{K}$ or $T = 223\,\mathrm{K}$, NO_2 from *Harder et al.* (1997) at $T = 217\,\mathrm{K}$ and $T = 230\,\mathrm{K}$, while the latter is orthogonalized with respect to the former, H_2O vapor from *Rothman et al.* (2003) at $T = 230\,\mathrm{K}$ and $p = 400\,\mathrm{hPa}$, and O_4 from *Hermans* (2002). All high resolution cross sections are convolved to the instrumental resolution with the actual instrumental slit function determined from a recorded line spectrum of an HgCd lamp ($\lambda = 468\,\mathrm{nm}$). A polynomial of 3^{rd} degree is used to account for the broad band structures. A higher degree is not recommendable as the O_3 cross section is relatively broad so that correlations are likely if the polynomial's degree is too high. Additionally, an additive polinomial of 2^{nd} degree (intensity offset) is

Table 4.2: Trace gas cross sections used for the DOAS evaluation of O_3 in the $490 - 520\ nm$ wavelength region. Note that the cross section at T_2 was orthogonalized with respect to the one at T_1.

Trace Gas	Reference	T_1	T_2
O_3	*Voigt et al.* (2001)	203 K	–
NO_2	*Harder et al.* (1997)	217 K	230 K
H_2O	*Rothman et al.* (2003)	230 K	–
O_4	*Hermans* (2002)	room temp.	–

Table 4.3: Trace gas cross sections used for the DOAS evaluation of NO_2 between $400\ nm$ and $460\ nm$. Note that the cross section at T_2 was orthogonalized with respect to the one at T_1.

Trace Gas	Reference	T_1	T_2
O_3	*Burrows et al.* (1999b)	202 K	221 K
NO_2	*Harder et al.* (1997)	217 K	–
H_2O	*Rothman et al.* (2003)	230 K	–
O_4	*Hermans* (2002)	room temp.	–

Table 4.4: Trace gas cross sections used for the DOAS evaluation of O_4 in the $465 - 490\ nm$ wavelength region. Note that the cross section at T_2 was orthogonalized with respect to the one at T_1.

Trace Gas	Reference	T_1	T_2
O_3	*Voigt et al.* (2001)	203 K	223 K
NO_2	*Harder et al.* (1997)	217 K	230 K
H_2O	*Rothman et al.* (2003)	230 K	–
O_4	*Hermans* (2002)	room temp.	–

Table 4.5: Trace gas cross sections used for the DOAS evaluation of H_2O in the $490 - 520\ nm$ wavelength region. Note that the cross section at T_2 was orthogonalized with respect to the one at T_1.

Trace Gas	Reference	T_1	T_2
O_3	*Voigt et al.* (2001)	203 K	223 K
NO_2	*Harder et al.* (1997)	217 K	230 K
H_2O	*Rothman et al.* (2003)	230 K	–
O_4	*Hermans* (2002)	room temp.	–

Table 4.6: Trace gas cross sections used for the DOAS evaluation of BrO in the $347 - 359\ nm$ wavelength region according to (*Aliwell et al.*, 2002). Note that the cross section at T_2 was orthogonalized with respect to the one at T_1.

Trace Gas	Reference	T_1	T_2
BrO	*Wahner et al.* (1988)	228 K	–
O_3	*Voigt et al.* (2001)	203 K	223 K
NO_2	*Harder et al.* (1997)	230 K	–
O_4	*Hermans* (2002)	room temp.	–

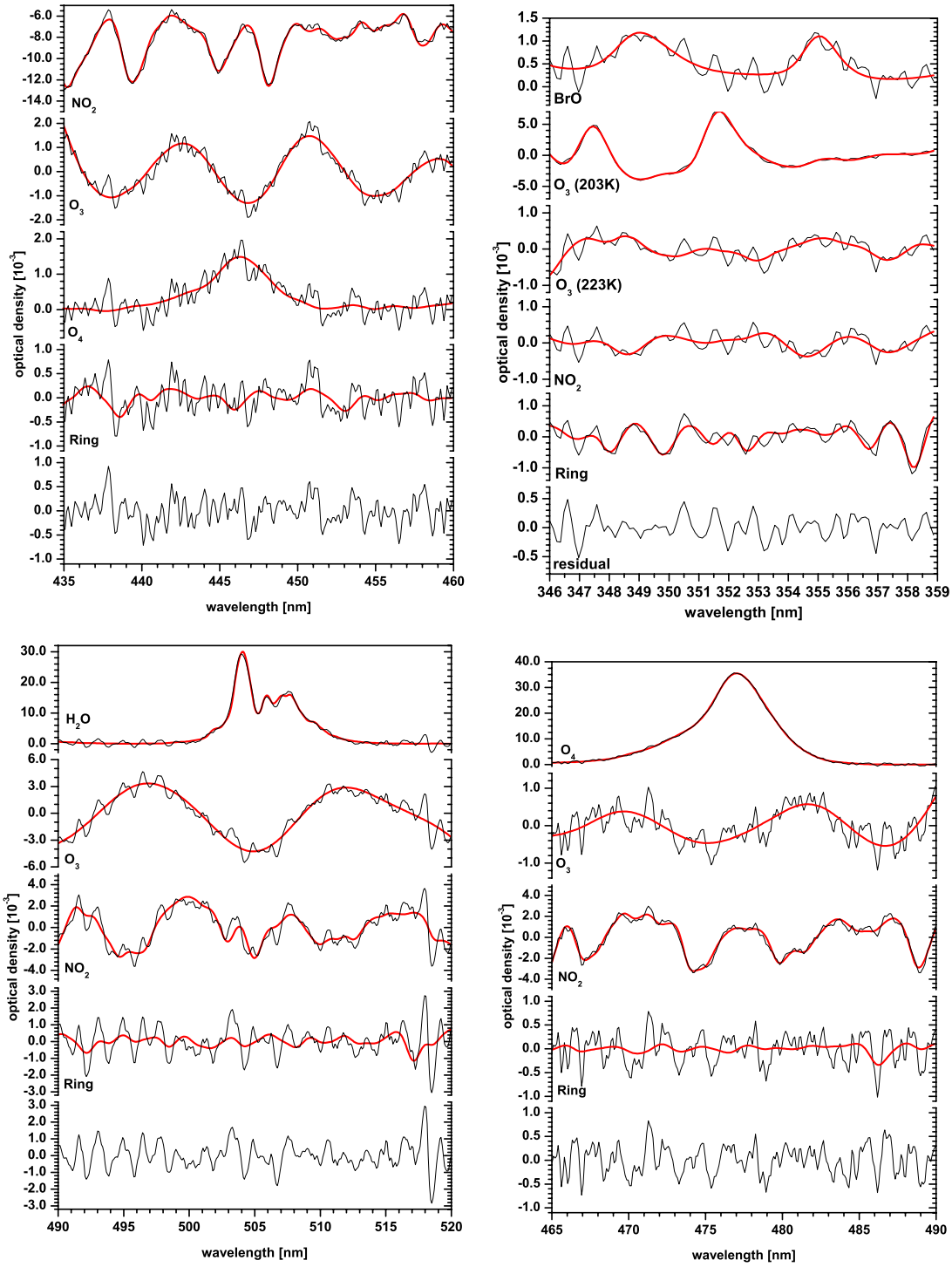

Figure 4.13: Sample DOAS evaluations of the miniDOAS mk.2 instrument for the flight at Kiruna March 24, 2004. Shown is the evaluation of NO_2 (upper left panel), BrO (upper right panel), H_2O (lower left panel) and O_4 (lower right panel) in the wavelength intervals $435-460\,\mathrm{nm}$, $346-359\,\mathrm{nm}$, $490-520\,\mathrm{nm}$ and $465-490\,\mathrm{nm}$, respectively, for limb observations during balloon ascent ($17.33\,\mathrm{km}$ altitude, -1.5^o elevation angle, 90^o azimuth angle, and 79.9^o SZA for the NO_2 evaluation, $24.68\,\mathrm{km}$ altitude and 82.4^o SZA for the BrO evaluation, $2.64\,\mathrm{km}$ altitude and 74.7^o SZA for the H_2O evaluation, and $11.45\,\mathrm{km}$ altitude and 77.5^o SZA for the O_4 evaluation, respectively). Shown is the optical density of the absorbance of the trace gases and Ring cross section (red lines) and the latter plus the residual structure (black lines). The Fraunhofer reference spectrum is recorded at $32.77\,\mathrm{km}$ altitude, -1.5^o elevation angle, 90^o azimuth angle, and 85.4^o SZA.

included to account for spectropgraph's stray light.

4.4.4 NO_2 Evaluation

The spectral retrieval of NO_2 is performed between 400 nm and 460 nm (e.g. in the $435 - 460$ nm wavelength range). The following cross sections are used: O_3 from *Burrows et al.* (1999b) at $T = 202$ K and $T = 221$ K while the latter is orthogonalized with respect to the former, NO_2 from *Harder et al.* (1997) at $T = 217$ K, H_2O vapor from *Rothman et al.* (2003) at $T = 230$ K and $p = 400$ hPa, and O_4 from *Hermans* (2002). In this wavelength interval the O_3 cross section from *Voigt et al.* (2001) recorded with a Fourier Transform spectrometer is rather noisy because the O_3 absorption gets minimal. That is why the cross section from *Burrows et al.* (1999b) recorded with the GOME spectrometer at medium resolution but higher signal to noise ratio is favored. A polynomial of 5^{th} degree is used to account for the broad band structures. Because the NO_2 cross section is highly structured, correlations with the polynomial are unlikely. Additionally, an additive polynomial of 2^{nd} degree (intensity offset) is included to account for spectropgraph's stray light.

4.4.5 O_4 Evaluation

The spectral retrieval of O_4 is performed in the $465 - 490$ nm wavelength interval. The following cross sections are used: O_3 from *Voigt et al.* (2001) at $T = 203$ K and $T = 223$ K while the latter is orthogonalized with respect to the former, NO_2 from *Harder et al.* (1997) at $T = 217$ K and $T = 230$ K, while the latter is orthogonalized with respect to the former, H_2O vapor from *Rothman et al.* (2003) at $T = 230$ K and $p = 400$ hPa, and O_4 from *Hermans* (2002). The particular problem of the DOAS O_4 evaluation is that the O_4 cross section has a rather broad band structure correlating with the polynomial, so the degree of the polynomial is set to 3. No additive polynomial is fitted to minimize correlations as its effect is rather small.

4.4.6 H_2O Evaluation

The spectral retrieval of H_2O is done in the same wavelength interval and with the same cross sections as O_3. Alternatively, a cross section from *Coheur et al.* (2002) is used. For some tests two O_3 cross sections from *Voigt et al.* (2001) at $T = 203$ K and $T = 223$ K, with the latter orthogonalized with respect to the former, have been used. However, due to the small temperature dependence of O_3 in this wavelength region the effect on the H_2O-dSCD is small.

4.4.7 BrO Evaluation

Thanks to the lower residuals that can be achieved with the mk.2 version of the instrument, the weak absorber BrO can also be observed. The spectral retrieval is done according to the advices from *Aliwell et al.* (2002). It is performed in the $346 - 359$ nm wavelength interval with the following cross sections: BrO from *Wahner et al.* (1988) at $T = 228$ K and shifted by $+0.25$ nm to match the wavelength calibration from the IUP Bremen (*Fleischmann et al.*, 2000), O_3 from *Voigt et al.* (2001) at $T = 203$ K and $T = 223$ K while the latter is orthogonalized with respect to the former, NO_2 from *Harder et al.* (1997) at $T = 230$ K and O_4 from *Hermans* (2002). The particular challenge of the BrO evaluation is to detect the rather small BrO absorption, which is only a factor of $\sim 2-5$ above the detection limit, before the background of the much higher O_3 absorption. The O_3 absorption has to be completely removed the spectrum as remaining O_3 structures might be mistaken as BrO. Unfortunately, no self-recorded

O_3 cross sections are available, so that cross sections from the literature convolved with the instrument's slitfunction have to be used. This is a potential source of errors as the line shape is not exactly known so that some structures remain in the residual which can be attributed to O_3. In future, it is planned to record O_3 cross sections with the instrument in the laboratory to further improve the BrO fit. Another crucial point is the choice of an appropriate Ring spectrum. It is found that the Ring cross sections calculated with the WinDOAS program cannot be used for BrO evaluation as their structures are too broad (see section 3.1.3). Using Ring cross sections either calculated with MFC or DOASIS together with an additive polynomial (intensity offset) of 2^{nd} degree significantly reduces the residuals and, thus, improves the fit. The BrO evaluation is also sensitive to the degree of the polynomial used to remove the broad band structures. It is found that the polynomial correlates with the O_4 cross section, as only a small part of the O_4 absorption band lies in the fitting range. If the polynomial's degree is > 2, the O_4-SCDs become unrealistically negative. However, the O_4-SCDs have realistic values for a polynomial of 2^{nd} degree. Consequently, the polynomial's degree is set to 2. The retrieved BrO-SCDs are also sensitive to the chosen fitting range, most likely due to correlations with other cross sections, so the $346 - 359$ nm wavelength interval is chosen as recommended by *Aliwell et al.* (2002).

4.4.8 Determination of the Solar Reference Offset

One particular problem of the DOAS evaluation is that it only yields differential Slant Column Densities (dSCD) as result, i.e. the trace gas abundance of the measurement spectrum minus that of the solar reference spectrum. But the quantity of interest is the absolute SCD which can be inferred from the dSCD only if the trace gas amount contained in the solar reference spectrum is known. This value can usually not be easily determined. Several possibilities are discussed in the following.

The most direct way is to use a solar reference spectrum with no (or known) trace gas absorbtion. Usually, the high resolution Kurucz spectrum convolved to the instrumental resolution is used. However, the use of a Kurucz reference involves large residuals so that this method is only possible for strong absorbers (e.g. O_3 or H_2O). But even if the DOAS evaluation is possible, the strong residual structures caused by the incompletely removed Fraunhofer lines can lead to huge systematical errors, i.e. a constant offset additional to the actual SCD value. In that case, this method cannot be used as it is the offset which is to be determined (for details see the corresponding results sections, e.g. 6.5.5). It would be best to have a reference spectrum recorded with the same instrument with known or little trace gas absorption. This could be obtained by recording spectra at balloon float with a high positive elevation angle of the limb telescope. This, however, implies looking into relative darkness and such a measurement has not been done so far. Another possibility is to use the correlative profile measurements to determine the offset. Therefore, a profile, e.g., inferred from the solar occultation or ozone sonde measurements together with the RT calculated BoxAMF is used to simulate an SCD value for each measured dSCD. The difference is the desired offset value. If the instrument is not altered, this spectrum can be used as a reference for all further balloon flights. Unfortunately, no 2 flights in exactly the same configuration have been conducted so far. Another possibility is to use a profile from a chemical transport model to simulate the SCDs, which works well in the case of BrO where the concentrations above float altitude, i.e. $\sim 32\ km$ are small and well known. For NO_2, however, the concentrations are too high and the uncertainties too big to give reasonable results (for a detailed discussion see the respective result sections).

4.5 Absolute Radiometric Calibration

In this section experimental details about the absolute radiometric calibration performed in cooperation with the IUP Bremen are discussed.

The radiometric calibration of both the nadir and the limb spectrometer is performed in two steps: In a first step, a small, but not absolutely calibrated, Ulbricht sphere is absolutely calibrated against an absolute radiance standard using the miniDOAS spectrometer as transfer device. In a second step, this now absolutely calibrated integrating sphere is used for radiometric calibration of each of the spectrometers, shortly before the actual balloon flight is conducted.

For absolute radiance calibration, a NIST (National Institute of Standards and Technology) calibrated FEL 1000 W irradiance Quartz Tungsten Halogen (QTH) standard (serial number F-455 from OSRAM Sylvania (*Walker et al.*, 1987)) in combination with a calibrated space grade Spectralon diffuser plate manufactured by Labsphere is employed. The same setup has been used for absolute radiometric calibration of SCIAMACHY during the SCIAMACHY calibration campaign (*Dobber*, 1999). The bi-directional reflectance distribution function (BRDF) of the diffuser plate is calibrated in $0-23^o$ geometry by the Dutch company TNO TPD (for more details see TNO TPD report of calibration (*van Leeuwen*, 2003)). NIST provides the calibration at a distance of 50 cm. This means that the radiance reflected from the diffuser plate under an angle of 23^o is known if the NIST lamp is set up at a distance of 50 cm from the diffuser plate. The wavelength dependent radiometric irradiance accuracy of the NIST-FEL lamp ranges between $0.91\% - 1.09\%$, and the long term reproducibility is $0.87\% - 0.96\%$ in the $350 - 654.6$ nm wavelength range (for more details see the NIST report of calibration (844/25 70 96-96-1, 1997). For the radiance transfer measurements, the NIST-FEL lamp and the Spectralon diffuser plate are positioned into the optical axis given by the light intake of the transfer spectrometer as recommended by *Dobber* (1999). The field of view of the spectrometer light intake telescope is small and completely located inside the characterized lamp irradiance plane on the Spectralon diffuser plate. After the measurement is taken, a not yet absolutely calibrated integrating sphere (type BN-102-3) is cross calibrated with the calibrated transfer spectrometer. The uncertainty of the radiance of the NIST-FEL lamp and Spectralon setup in the $300 - 700$ nm region is $2 - 3\%$ as indicated by test measurements performed during the SCIAMACHY calibration campaign (*Gerilowski*, 2004). For the somewhat less ideal conditions in the field, the estimated accuracy of the absolute radiometric calibration for both spectrometers is assessed to 35% at 380 nm, 10% at 440 nm and 4% at 510 nm, including all known sources of uncertainties and errors. The reproducibility of the integrating sphere measurements is better than 1%.

The absolute calibration in the UV, where the accuracy is much worse than in the visible range is cross-checked by comparing the measured limb radiance at two wavelengths (e.g. 360 nm vs. 490 nm), for conditions under which the radiative transfer is simple. Usually, spectra recorded at balloon float altitude, where the radiative transfer is dominated by Rayleigh scattering, are chosen for this test. For further details see section 6.5.3.

4.6 The LPMA/DOAS Balloon Payload

4.6.1 The Gondola

The LPMA/DOAS balloon gondola is based on a gondola developed for astronomical observations by the Observatoire de Genève and was further optimized for atmospheric measurements by *Camy-Peyret et al.* (1995). The gondola can be stabilized in azimuthal direction with an accuracy of about $3 - 6^o$ and 1^o or better in the lower stratosphere and at balloon float altitude, respectively. Therefore the

gondola is aligned to the magnetic field of the earth with a gyroscope. The gondola can be rotated with respect to the much larger balloon. The rotational energy is converted to frictional heat through the torque of a special joint of the gondola and the balloon. The fine-pointing is performed by a suntracker (*Hawat et al.*, 1995), which provides the infrared Fourier Transform Interferometer and the DOAS UV/vis spectrograph with a parallel solar beam. Further the gondola equipment includes pressure and temperature sensors and GPS antennas.

4.6.2 The LPMA Fourier Transform Interferometer

The infrared Fourier Transform Interferometer (FTIR) operated by the french LPMA[2] team is a Michelson interferometer with plane mirrors of the BOMEM DA2.01 type. It has an effective aperture of 45 mm and produces a maximum path difference of $\Delta_{max} = 50\,\mathrm{cm}$ leading to an apodised resolution of $1/\Delta_{max} = 0.020\,\mathrm{cm}^{-1}$. The interferometer is equipped with a two channel output optics with two liquid nitrogen cooled detectors (HgCdTe and InSb, respectively). The spectral signatures of $ClONO_2$, HNO_3, O_3, CH_4, N_2O, NO, and H_2O are covered by the HgCdTe detector (mid-IR) and those of HCl, NO_2, CH_4, and HF by the InSb detector (near-IR) (*Camy-Peyret et al.*, 1995; *Payan et al.*, 1998, 1999). The instrument has also been used to measure H_2O and O_2 in the 920 nm and 760 nm region, respectively, to retrieve CCl_2F_2 in the lower stratosphere, and to obtain CO_2 in the 13 μm region (*Camy-Peyret et al.*, 1999). A multifit algorithm (*Carlotti*, 1988) associated with an efficient minimization of the Levenberg-Marquardt type is used for the simultaneous retrieval of vertical mixing ratio profiles of several trace gases from ascent and occultation data. The algorithm allows to combine the information contained in several micro-windows. The molecular parameters used in the forward model are extracted from the HITRAN2000 database (*Rothman et al.*, 2003). For further details on the LPMA instrument and retrieval see also *Dufour et al.* (2005).

4.6.3 The Direct Sunlight DOAS

The parallel light beam of the suntracker is also used by a direct sunlight DOAS[3] instrument. This spectrometer is optimized for airborne applications and was designed and developed by *Ferlemann et al.* (1998, 2000) and *Harder et al.* (1998). The basic features of the instrument are relatively low weight and power consumption, stability of the spectral imaging and insignificant thermal drift of the spectroscopic system. The instrument consists of two spectrographs in one housing, which analyze the UV and the visible part of the sunlight separately (see figure 4.14). The light enters the spectrograph via two quartz fibres bundles, forming a rectangular entrance slit for each spectrograph on one fibre end. On the other end of the fibres a telescope optic is mounted, intended to average the light received from the sun, to limit the spectral transmission range of the incoming light and to match the f-number of each spectrometer. Coming from the entrance slit, the light reaches a holographic grating, which disperses the light of the respective wavelength range (UV: $316 - 418\,\mathrm{nm}$ with 0.5 nm resolution; visible: $399.9 - 653.0\,\mathrm{nm}$ with 1.5 nm resolution) onto Peltier cooled photodiode arrays. The width of the entrance slit was chosen to fulfill the sampling criteria given by *Roscoe et al.* (1996), i.e. the FWHM of the instrument function should be sampled with more than 4.5 detector pixels. The instrumental resolution is found to be 0.45 nm (= 4.5 detector pixels) and 1.48 nm (= 5.7 detector pixels) for the UV and the vis spectrometer, respectively. The whole spectrometer housing is evacuated and thermally stabilized by a surrounding vessel filled with a water-ice mixture. In addition, a refrigerant circulates in a cooling circuit to regulate the temperature of the optical components and to cool the warm side of the photodiode Peltier elements. Low spectrometer stray light is achieved by suppressing the higher-order

[2] Laboratoire de Physique Molèculaire et Applications

[3] also referred to as solar occultation measurements

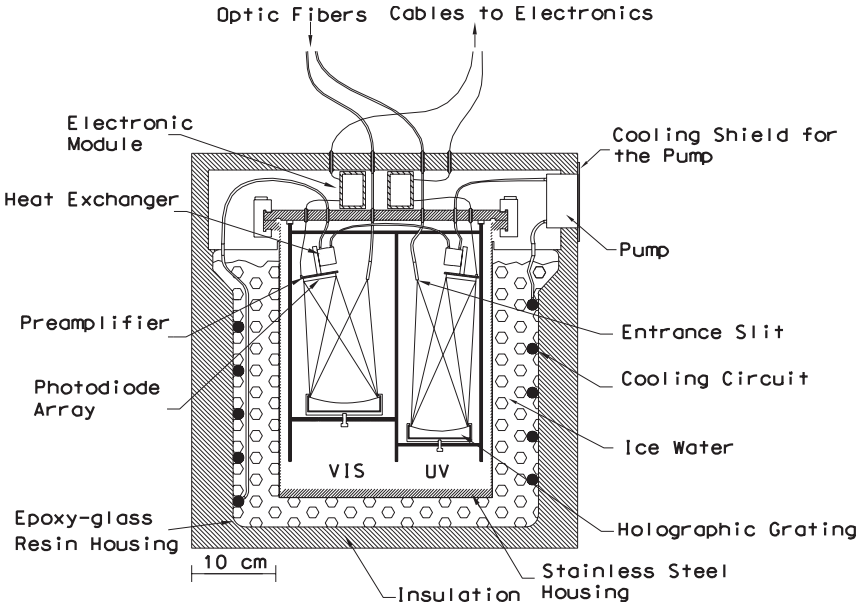

Figure 4.14: Schematic drawing of the direct sunlight DOAS spectrograph. Two holographic grating spectrographs (UV and visible) are integrated into a vacuum-sealed aluminum container. The light enters the spectrographs through two quartz fibre bundles which form an apparent rectangular slit at their end. Light detection is performed with two photodiode array detectors. The whole container is thermostated by a liquid-water-ice-filled vessel surrounding it. In addition, a refrigerant is circulated in a cooling circuit to regulate the temperature of the optical components and to cool the warm side of the Peltier elements.

and zero-order grating reflections by using light traps and, for some flights, by including a dispersive prism preananalyzer for the UV spectrograph (*Vradelis*, 1998). A detailed characterization of the DOAS spectrograph can be found in *Bauer* (1997). In the wavelength range covered by the combination of the UV and vis spectrograph, absorption features of several species can be found, e.g. O_3, BrO, NO_2, OClO, SO_2, HNO_2, HCHO, O_4 etc. in the UV range, and O_3, NO_2, H_2O, O_4, NO_3, OClO, IO, OIO etc. in the vis range. The performance and quality of the direct sunlight DOAS spectrometer has been demonstrated during 13 flights (*Ferlemann et al.*, 1998, 2000; *Harder et al.*, 1998, 2000; *Pfeilsticker et al.*, 2000, 2001; *Fitzenberger et al.*, 2003; *Bösch et al.*, 2001, 2003; *Dorf et al.*, 2005; *Butz et al.*, 2005). The instrument is also cross validated with other balloon-borne and satellite instruments (*Randall et al.*, 2002; *Sugita et al.*, 2002; *Fitzenberger et al.*, 2003; *Pfeilsticker et al.*, 2003; *Sioris et al.*, 2003). Its measurements are therefore used as a reference for the validation of the novel miniDOAS instrument. For the most recent flights, the instrument is absolutely calibrated in the field before flight. For details about the calibration technique and results of the solar irradiance measurements see *Gurlit et al.* (2003, 2004). An Electro-Chemical Cell (ECC) Ozone-Sonde is connected to the control electronics of the DOAS spectrograph providing in-situ information of the O_3-concentration along the balloon trajectory. The O_3-profile measured by the ECC O_3 Sonde is also used for the validation of the miniDOAS O_3-profile measurements.

Chapter 5

Sensitivity Studies and Error Analysis

In this chapter, the influence of uncertainties of the input parameters on the output of the RT calculations is examined. The effects of the errors on the profile retrieval is also discussed. Finally, the findings are used to develop strategies for optimal measurements.

5.1 Sensitivity of the TRACY RT Calculations

In this section, it is reported on sensitivity studies of the RT modeling to the various input parameters needed by TRACY. The parameters under examination are the viewing geometry (detector aperture and its elevation and azimuth angle), wavelength and atmospheric parameters like aerosol load and cloud conditions. If not otherwise stated, the following parameters are used for the simulations: half aperture angle of 0.67^o in vertical, and 0.1^o in horizontal direction. The elevation is 1.5^o below the horizon, the azimuth angle is 90^o to the sun and the wavelength 490 nm

5.1.1 Aperture Angle of the Telescope

First, the effect on the radiative modeling arising from the uncertainty of the field of view of the detector is studied. The telescope's opening aperture is determined geometrically from the focal length of the lens and the size of the entrance slit of the glass fiber bundle (see section 4.1). The horizontal half aperture angle is 0.67^o for the mk.1 and 1.05^o for the mk.2 of the instrument. The vertical half aperture angle is 0.095^o. No measurements of the field of view exist as the angles are very small and, thus, difficult to determine experimentally.

Figures 5.1 - 5.3 show simulated radiance, O_3-SCD, and NO_2-SCD vs. altitude as a function of horizontal (left panels) and vertical aperture angle (right panels). It can be seen that all three quantities do not depend on the vertical aperture angle between 0.1^o and 5^o. In vertical direction, increasing discrepancies are observed for half aperture angles $> 1^o$. However, for horizontal aperture angles $< 0.5^o$ the simulated radiances and SCDs agree within their respective error bars. To summarize, it can be stated that small derivations of the real field from the calculated angles both in vertical and horizontal direction are not expected to affect the radiative transfer calculations.

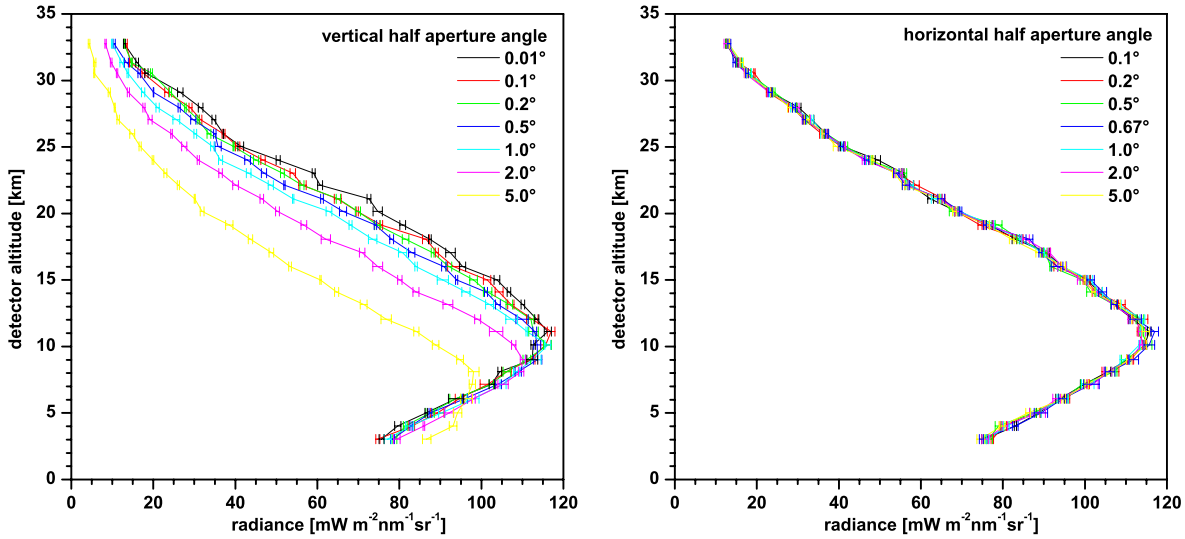

Figure 5.1: RT calculated radiance vs. detector altitude as a function of the aperture angle of the detector in vertical (left panel) and horizontal direction (right panel).

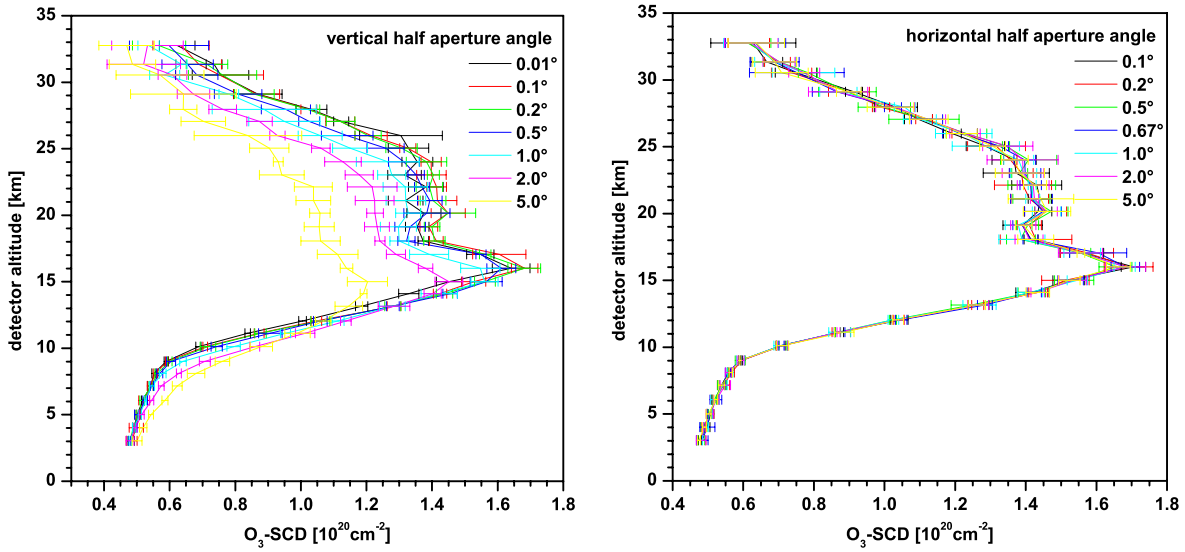

Figure 5.2: Simulated O_3-SCD vs. detector altitude as a function of the aperture angle of the detector in vertical (left panel) and horizontal direction (right panel).

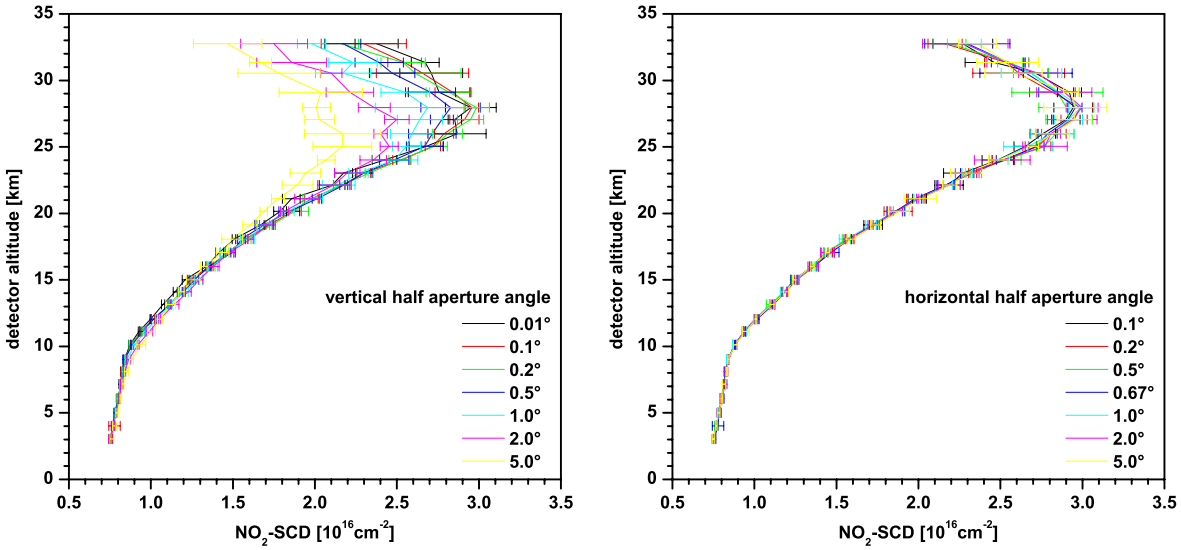

Figure 5.3: Simulated NO_2-SCD vs. detector altitude as a function of the aperture angle of the detector in vertical (left panel) and horizontal direction (right panel).

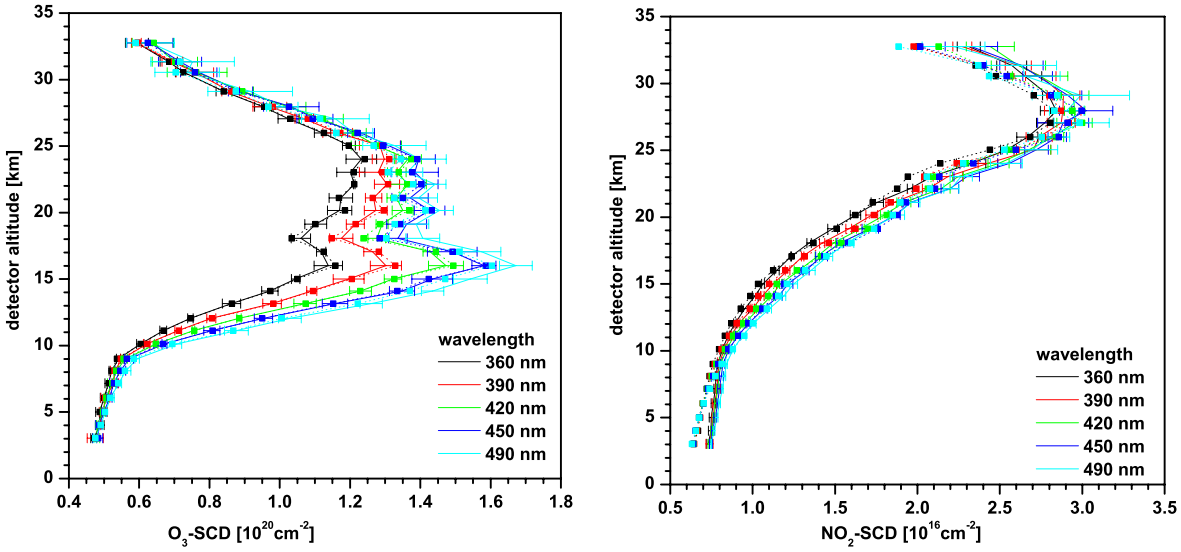

Figure 5.4: Simulated O_3-SCDs (left panel) and NO_2-SCDs (right panel) vs. detector altitude as a function of wavelength. The lines with error bars show the SCD as output by TRACY. The dotted lines with squares show the SCDs calculated from the product of BoxAMF and VCD.

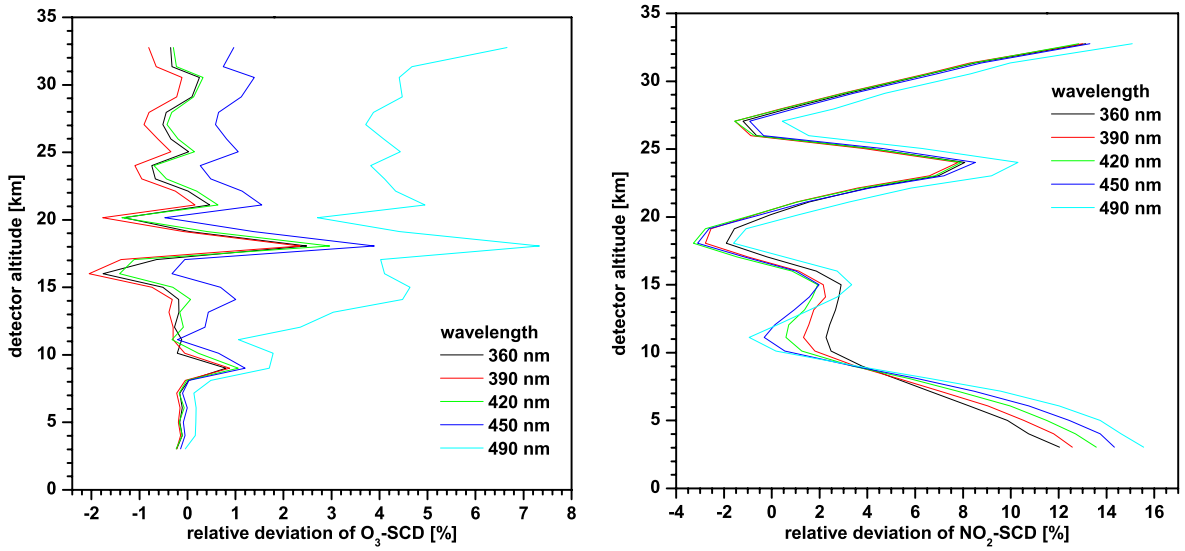

Figure 5.5: Relative deviation of the O_3-SCDs (left panel) and NO_2-SCDs (right panel) obtained by the two methods (see figure 5.4) vs. detector altitude as a function of wavelength.

5.1.2 Wavelength

The wavelength of the analyzed radiation is not really subject to uncertainty. But as DOAS evaluations are typically performed in wavelength intervals of $10 - 50$ nm while the RT is calculated at the center wavelength of the respective inverval, it is important to examine the wavelength dependence of the RT. Absolute radiance measurements are available for every single detector pixel so it can be directly compared to a simulation for the same wavelength, so the wavelength dependence of the radiance is not examined here. In figure 5.4, O_3 and NO_2-SCDs are plotted vs. detector altitude as a function of wavelength between 360 and 490 nm. Two sets of SCDs are plotted for each wavelength. The lines together with error bars are the direct TRACY output. Additionally, the SCD is calculated by multiplying the BoxAMF calculated by TRACY by a vertical profile. Theoretically both methods should yield the same result. However, discrepancies of > 10 % are observed under certain conditions. This can be seen in figure 5.5 where the relative deviation of the results of the two methods is plotted vs. altitude. For O_3-SCDs and wavelengths between 360 and 420 nm the discrepancies are rather small, i.e. < 1 % for most altitudes. For 450 nm the deviations are already higher and for the simulation at 490 nm the SCDs calculated using the BoxAMF are generally smaller than the direct TRACY values by $3 - 7$ %. In the case of NO_2-SCDs, the deviations are generally higher, i.e. > 10 % for the lowest and highest altitudes of the simulation and almost independent on wavelength. The reason for this behavior is unclear.

The O_3-SCDs (see figure 5.4, left panel) show a rather strong wavelength dependence, especially at altitudes in the $10 - 25$ km range. However, the deviations between the simulations decrease with wavelength and are rather small between 450 nm and 490 nm and, thus, should not significantly affect the RT in the $490 - 520$ nm interval where the O_3 DOAS evaluation is performed. NO_2, which has its concentration maximum at higher altitudes, is less affected by the wavelength dependence of the RT. This can be seen in 5.4 (right panel). Again, the wavelength dependence of the RT should be less a problem in the NO_2 evaluation interval ($400 - 450$ nm or $435 - 460$ nm).

5.1.3 Elevation Angle of the Detector

From all parameters the elevation angle of the detector has the strongest impact on the limb measurements. This is examined in the following by simulating limb radiances (figure 5.6), O_3- (fig. 5.7), and NO_2-SCDs (fig. 5.7) as a function of elevation angle. Additionally, the effect of elevational oscillations is studied by calculating radiance weighted averages of the mentioned quantities:

$$\overline{x(\phi_0, \phi_A)} = \frac{I(\phi_0 - \phi_A/2) * x(\phi_0 - \phi_A/2) + I(\phi_0) * x(\phi_0) + I(\phi_0 + \phi_A/2) * x(\phi_0 + \phi_A/2)}{I(\phi_0 - \phi_A/2) + I(\phi_0) + I(\phi_0 + \phi_A/2)}, \quad (5.1)$$

where $x(\phi)$ stands for the quantity of interest (radiance I, O_3-, or NO_2-SCD, respectively), $I(\phi)$ the simulated radiance for elevation angle ϕ, and ϕ_A for the amplitude of the elevational oscillation around elevation angle ϕ_0. As only the value of x at the upper and lower turning point of the oscillation together with $x(\phi_0)$ is taken for the calculation of the average, $\overline{x(\phi_0, \phi_A)}$ for a real oscillation with amplitude ϕ_A around ϕ_0 might be closer to $x(\phi_0)$, i.e the effect is overestimated, or in other words: the shown values of $\overline{x(\phi_0, \phi_A)}$ might describe an oscillation with even larger amplitude than ϕ_A.

Absolute Elevation Angle

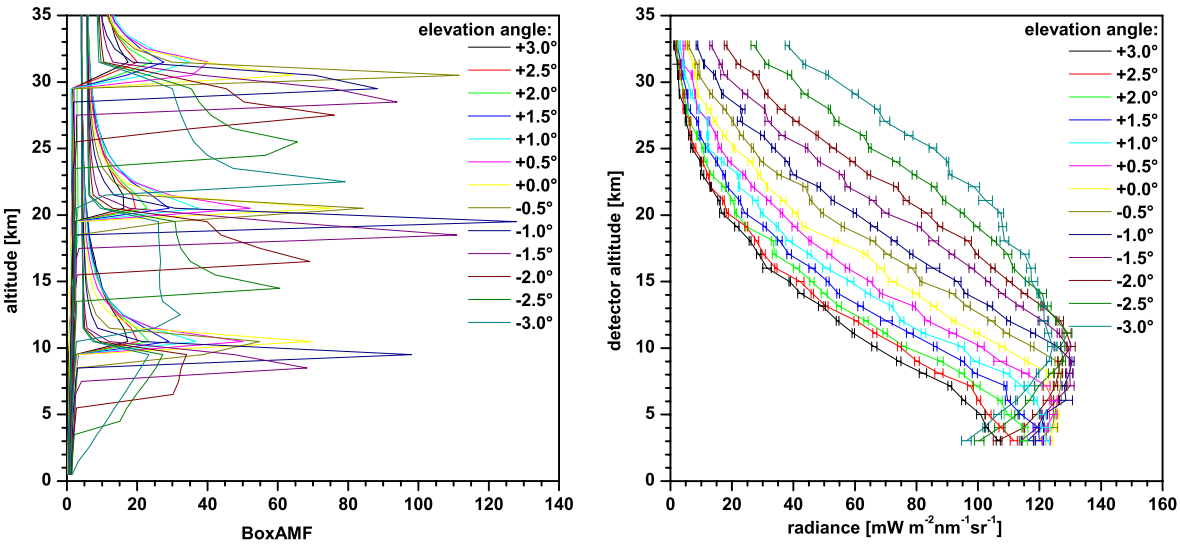

Figure 5.6: Left panel: RT calculated BoxAMF vs. altitude as a function of elevation angle. Right panel: RT calculated limb radiance vs. detector altitude as a function of elevation angle.

It can be clearly seen in that all three considered quantities (limb radiance, O_3- and NO_2-SCD, see figures 5.6 and 5.7 strongly depend on the elevation angle. By looking at the BoxAMF (figure 5.6, left panel), it can be seen that the tangent height (i.e. altitude layer where the BoxAMF gets maximal) is strongly decreasing with deceasing elevation for negative elevation angles. E.g. for -3^o elevation angle, the tangent height is about 7 km below the actual detector altitude and for -1^o about 1 km below. For elevation angles $\geq -0.5^o$, the tangent height coincides with the detector altitude but the BoxAMF, especially at the detector altitude, is strongly decreasing with increasing elevation angle which, consequently, causes a decrease of the trace gas SCDs. Qualitatively, it can be seen that the length of the light path and, thus, the SCDs increase with decreasing elevation angle. As the relative error of the DOAS evaluation decreases with increasing SCD, the sensitivity of the measurements can be increased by looking at a lower elevation angle. Additionally, the radiance is higher for lower elevation

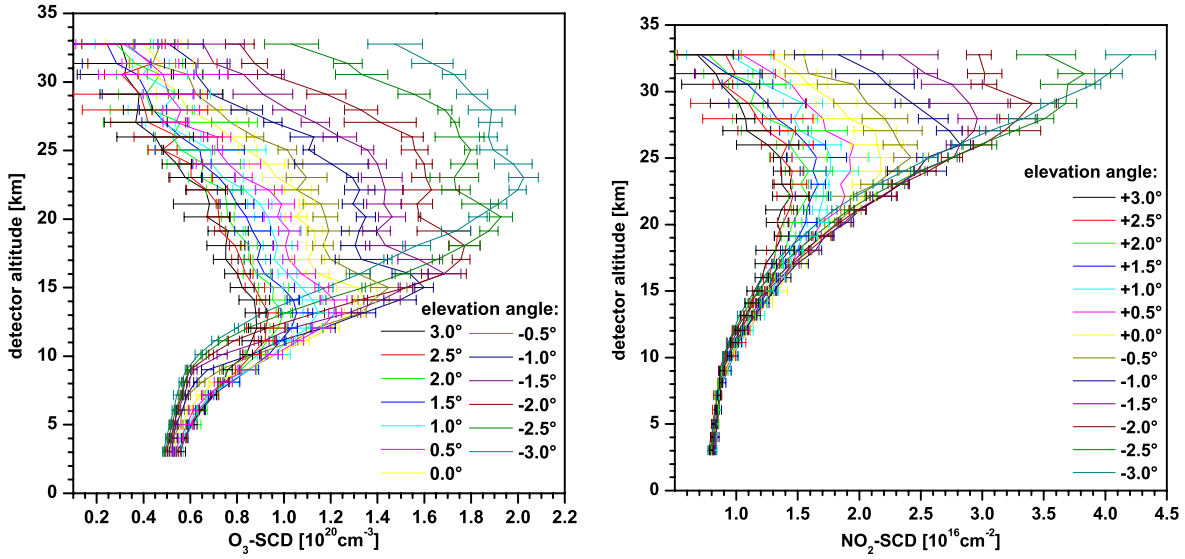

Figure 5.7: Simulated O_3-SCD (left panel) and NO_2-SCD (right panel) vs. detector altitude as a function of elevation angle

angle which also increases the sensitivity of the measurements. However, the increased sensitivity is only important in the case of BrO whose SCDs are close to the detection limit. For all other trace gases, the statistical DOAS error is rather small.

The elevation angle is roughly adjusted on ground prior to the balloon flight. But discrepancies of $\sim 0.5^o$ between the adjusted and actual elevation angle have been observed for all the flights. However, the strong dependence of the measured radiances and trace gas SCDs on elevation angle allows a precise determination of the elevation angle by comparing the measurements and RT simulations, especially for the scanning limb measurements, so that the uncertainty of the elevation angle is very low.

Elevational Oscillations

The limb measurements are affected by oscillations of the gondola around the average elevation angle ϕ_0 which is studied in this subsection. First, the effect of elevational oscillations on the BoxAMF itself is examined for two cases ($\phi_0 = -1.5^o$ in the left panel and $\phi_0 = 0^o$ in the right panel of figure 5.8) for selected detector altitudes (10, 20, and 30 km) and amplitudes ϕ_A between 1^o and 4^o. Qualitatively, two things can be seen. Firstly, the effect is increasing with increasing altitude. For 10 km detector altitude, the width of the BoxAMF is only slightly increasing with increasing ϕ_A, while for 30 km detector altitude, appreciably lower altitudes contribute to the measurements (up to 7 km below the detector for $\phi_0 = -1.5^o$ and $\phi_A = 3^o$. Secondly, the effect is stronger for lower elevation angles. For $\phi_0 = 0^o$, the width of the BoxAMF is increased to ~ 3 km, while it is ~ 7 km for $\phi_0 = -1.5^o$ (in the case of 30 km detector altitude and $\phi_A = 3^o$). Obviously, the effect of elevational oscillations is also strongly increasing with their amplitude ϕ_A. For $\phi_A = 1^o$, the BoxAMF are very close to the still gondola case and increasingly deviate with increasing ϕ_A.

The effect on the actually measured quantities is shown in the figures 5.10 - 5.9. Again, the case of $\phi_0 = -1.5^o$ is shown in the respective left and $\phi_0 = 0^o$ in the right panels. Additionally, the relative deviation of the simulations assuming gondola oscillations ($\phi_A > 0^o$) from those assuming a still gondola (i.e $\phi_A = 0^o$) is plotted vs. detector altitude in the right side of each panel. One qualitative feature is common to all cases: for all quantities the values are lower for detector altitudes below their respective

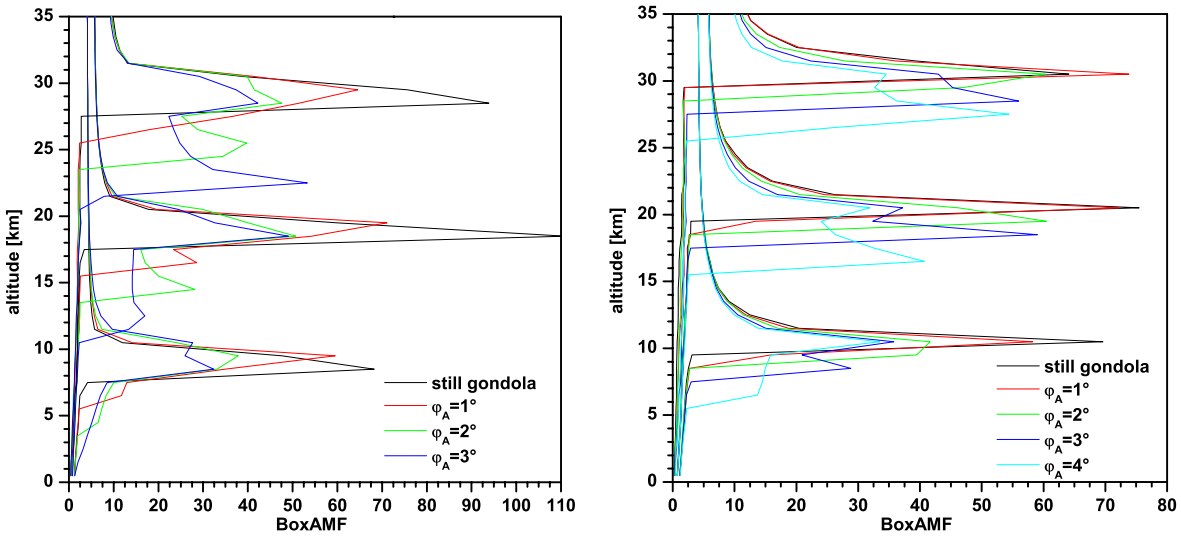

Figure 5.8: RT calculated BoxAMF vs. altitude for 10 km, 20 km, and 30 km detector altitude as a function of elevational oscillation with amplitude ϕ_A for $\phi_0 = -1.5^o$ (left panel) and $\phi_0 = 0^o$ (right panel).

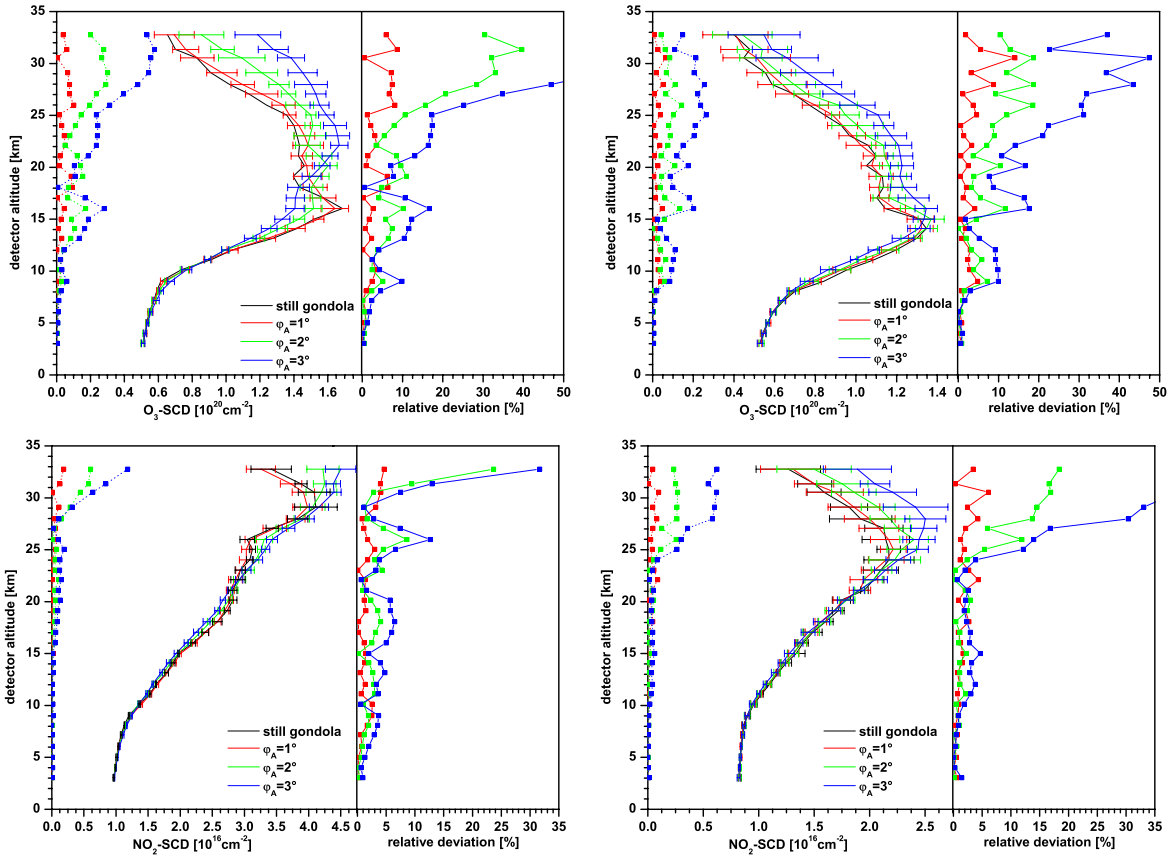

Figure 5.9: Simulated O_3- (upper row) and NO_2- SCDs (lower row) vs. detector altitude as a function of elevational oscillation with amplitude ϕ_A for $\phi_0 = -1.5^o$ (left panels) and $\phi_0 = 0^o$ (right panels) shown in solid lines. Also shown is the absolute (squares and dotted lines) and the relative deviation (squares and solid lines) of the simulations with elevational oscillations from that for a still gondola (i.e. $\phi_A = 0^o$).

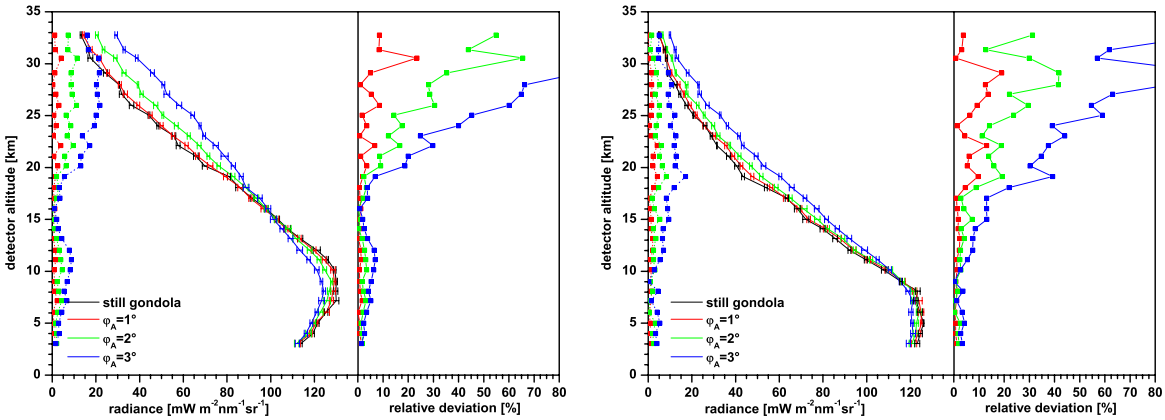

Figure 5.10: RT calculated limb radiance vs. detector altitude as a function of elevational oscillation with amplitude ϕ_A for $\phi_0 = -1.5^o$ (left panel) and $\phi_0 = 0^o$ (right panel) shown in solid lines. Also shown is the absolute (squares and dotted lines) and the relative deviation (squares and solid lines) of the simulations with elevational oscillations from that for a still gondola (i.e. $\phi_A = 0^o$).

maxima while the values are higher for altitudes above the maximum. As already seen for the BoxAMFs, the considered quantities are not strongly affected for $\phi_A = 1^o$. The relative deviations are at most 5 % and much below this value for detector altitudes below ~ 25 km. It can also be seen that the absolute deviations are generally stronger for $\phi_0 = -1.5^o$ compared to $\phi_0 = 0^o$. However, the relative deviations can be smaller for $\phi_0 = -1.5^o$ compared to $\phi_0 = 0^o$ if the absolute values are higher. The radiances are the more sensitive than the SCDs with relative deviations exceeding 100 % for high altitudes and amplitudes. But also the trace gas SCDs can be up to 50 % above those of a still gondola in this case. The NO_2 measurements are only slightly affected at detector altitudes below ~ 25 km but deviations strongly increase when the detector altitudes surpass the NO_2 concentration maximum which is at that altitude. For BrO no simulations have been undertaken, but the qualitative trend should be similar to the case of O_3 as the qualitative shape of the profile is similar.

The lessons learned from these sensitivity studies can be summarized as follows. The sensitivity of the measurements towards trace gas SCDs can be increased by looking at lower elevation angles. However, this also increases the effect of elevational oscillations so that an elevation angle around 0^o is the best compromise. Especially, the NO_2 measurements are affected by this as its maximum is higher up. In the case of BrO, a lower elevation angle might improve the measurements and the effect of elevational oscillations is lower at the altitude of its concentration maximum (i.e. $15 - 20$ km).

5.1.4 Azimuth Angle of the Detector

The effect of azimuthal oscillations of the gondola is examined in this subsection. The azimuth angle of the gondola is stabilized by countermovements of a pivot and measured by onboard instruments. Typically, the azimuth angle is oscillating with amplitudes ranging between 15^o in the beginning and $< 5^o$ around the desired zero position. Only shortly after launch and when the gondola is subject to changing wind directions which usually occur in the tropopause region, the azimuth stabilization is worse with occasional revolutions of the gondola.

The dependence of the quantities of interest (limb radiance, O_3-, and NO_2-SCD is shown in figures 5.11 - 5.13. In the left panels, simulations of the respective quantity are plotted vs. detector altitude for azimuth angles relative to the sun between 5^o and 180^o. In the right panels, simulations of the respective quantity are plotted vs. relative azimuth angle between 0^o and 180^o for several detector

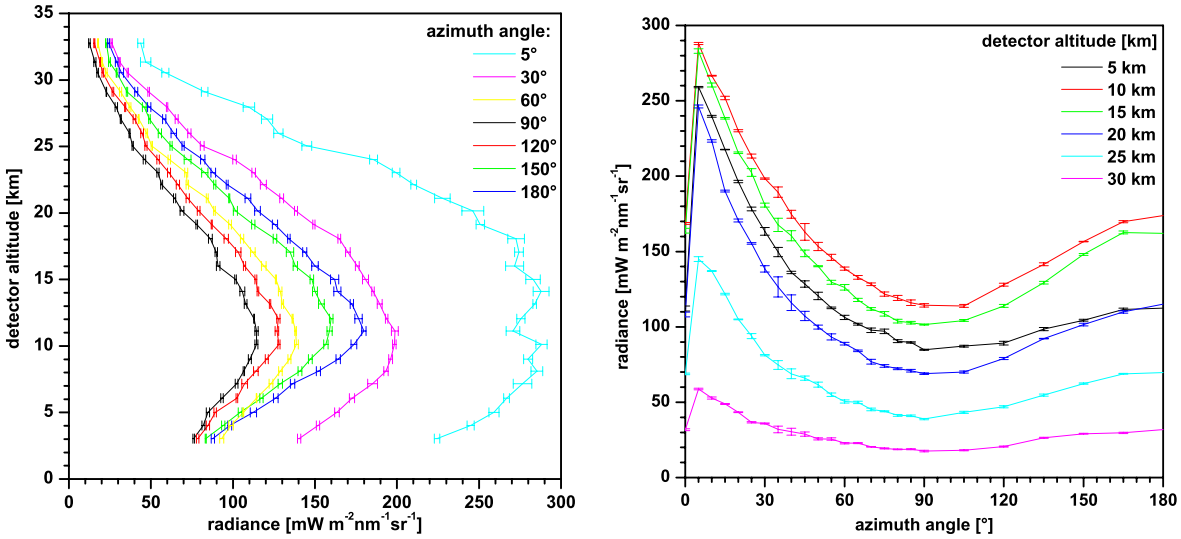

Figure 5.11: Left panel: RT calculated limb radiance vs. detector altitude as function of azimuth angle relative to the sun. Right panel: limb radiance vs. relative azimuth angle for several detector altitudes.

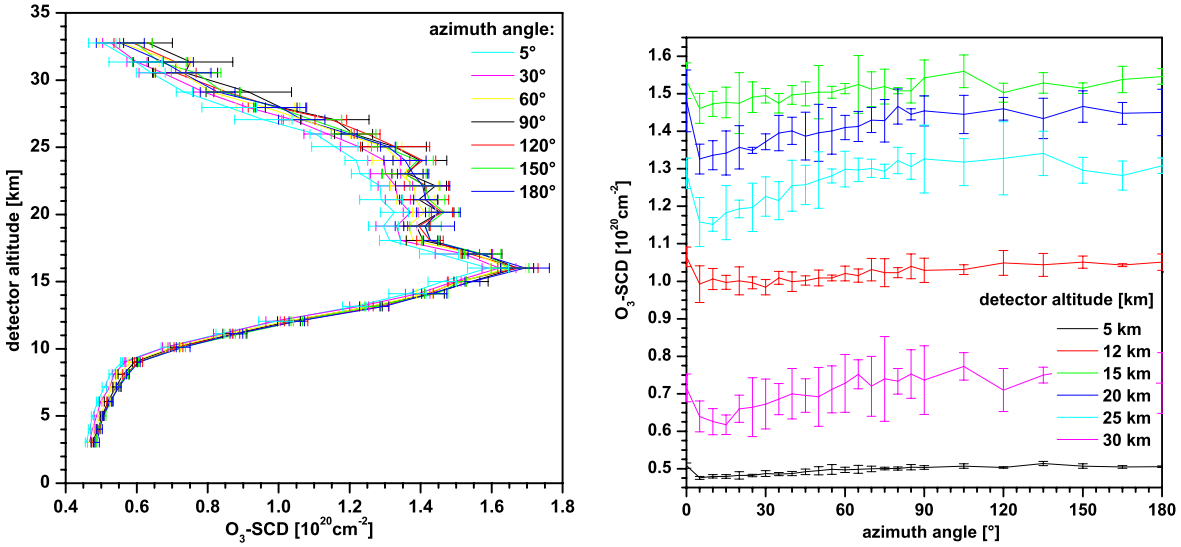

Figure 5.12: Left panel: simulated O_3-SCD vs. detector altitude as function of azimuth angle relative to the sun. Right panel: simulated O_3-SCD vs. relative azimuth angle for several detector altitudes.

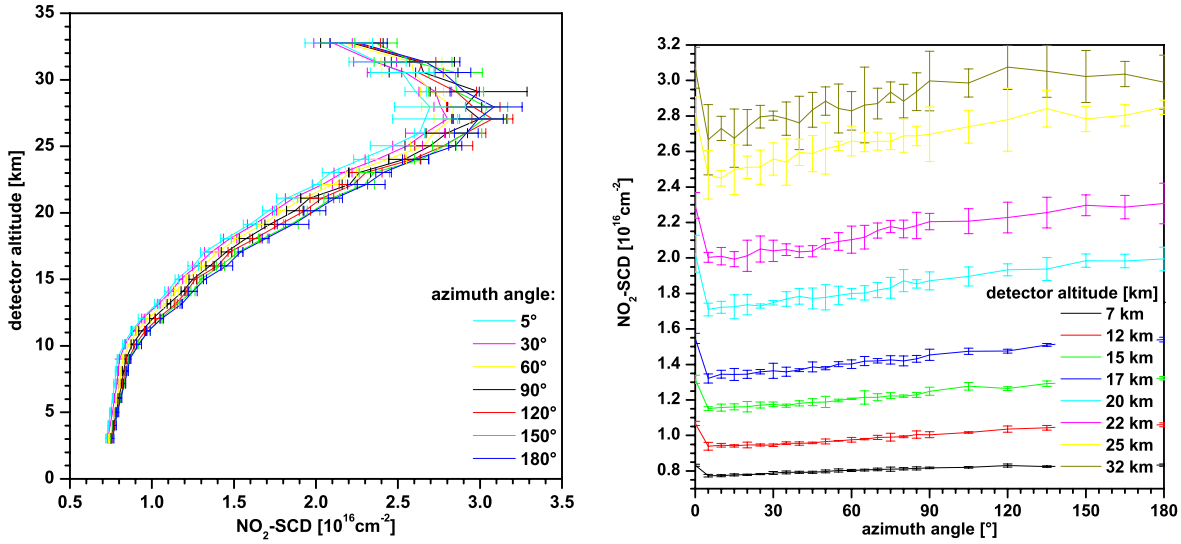

Figure 5.13: Left panel: simulated NO_2-SCD vs. detector altitude as function of azimuth angle relative to the sun. Right panel: simulated NO_2-SCD vs. relative azimuth angle for several detector altitudes.

altitudes.

The RT calculated limb radiances show a strong azimuth dependence. At our viewing direction, i.e. 90^o to the sun, the limb radiances are minimum. This is because the predominant Rayleigh scattering has a minimum at 90^o. The Rayleigh phase function is only one half of the value at 0^o and 180^o scattering angle, respectively, as one polarization axis is not scattered in perpendicular direction. Consequently, the simulated radiances are increasing with increasing deviation from 90^o. The increase of the simulated limb radiance from 90^o to 180^o is monotonically growing from $\sim$ 15 % at 3 km to $\sim$ 93 % at 33 km, where the analyzed radiation is dominated by single Rayleigh scattered photons. With decreasing altitudes multiple and Mie scattered photons increasingly contribute to the analyzed radiation so that the difference between 90^o and 180^o becomes smaller compared to the pure Rayleigh case. The Mie scattering phase function is monotonically decreasing with scattering angle for 0^o to 180^o (for details see next section). From 90^o to 5^o azimuth angle, the RT calculated radiances are strongly increasing by factors between $\sim$ 2.5 and $\sim$ 4. This is because both the Rayleigh and the, especially, the Mie phase function are increasing. The radiances calculated for 0^o are significantly lower than those calculated for 5^o at all altitudes which is believed to be a shortcoming of the RT model as there is no physical reason for this behavior. From this study can be concluded that the number of analyzed photons and, thus, the relative error of the DOAS evaluation of the trace gases can be increased by choosing an azimuth angle around 0^o to the sun. However, this is not practicable from an experimental point of view as there is the danger of pointing directly to the sun which causes the spectra to become oversaturated. Also for azimuth angles around 30^o, the radiance is highly variable with azimuth angle which makes it difficult for the automated measurement routine to determine the right integration time for the measurement. Note that typically 1000 scans are added to one spectrum and only one oversaturated scan makes the entire set useless. So the chosen azimuth angle at the radiance minimum is the better choice in this context. For moderate azimuth oscillations (amplitudes $< 30^o$) around 90^o, the measured limb radiances should only be little affected as the RT calculated radiances are only $0-10$ % (occasionally up to 15 %) higher at 75^o and 105^o.

The azimuth dependance of the simulated trace gas SCDs (see figure 5.12 and 5.13) is comparably low. The simulated trace gas SCDs show an increase with azimuth angle in the $5-180^o$ range. The values simulated for 0^o are, against the general trend, significantly higher than those at 5^o. I assume the RT

calculations around 0^o to be inaccurate as there is no physical reason why the light path should become longer when the telescope is pointing closer to the sun. The difference of the O_3- and NO_2-SCDs, respectively, increase by $\sim 5-16$ % from 5^o to 180^o of azimuth. For the assumed azimuth oscillations of $5-15^o$ the effect is not significant within the uncertainty of the RT calculation. As the values at 90^o lie approximately in the middle of the range, the observed SCDs should be close to the 90^o-values even for 360^o turns of the gondola.

Summarizing the major points of this sensitivity study, it can be concluded that the miniDOAS trace gas measurements are not significantly affected by azimuthal gondola oscillations. The limb radiances are minimum for our viewing geometry, so azimuth movements lead to higher measured radiances. However, for moderate azimuth oscillations ($< 30^o$), the effect is negligible.

5.1.5 Aerosols

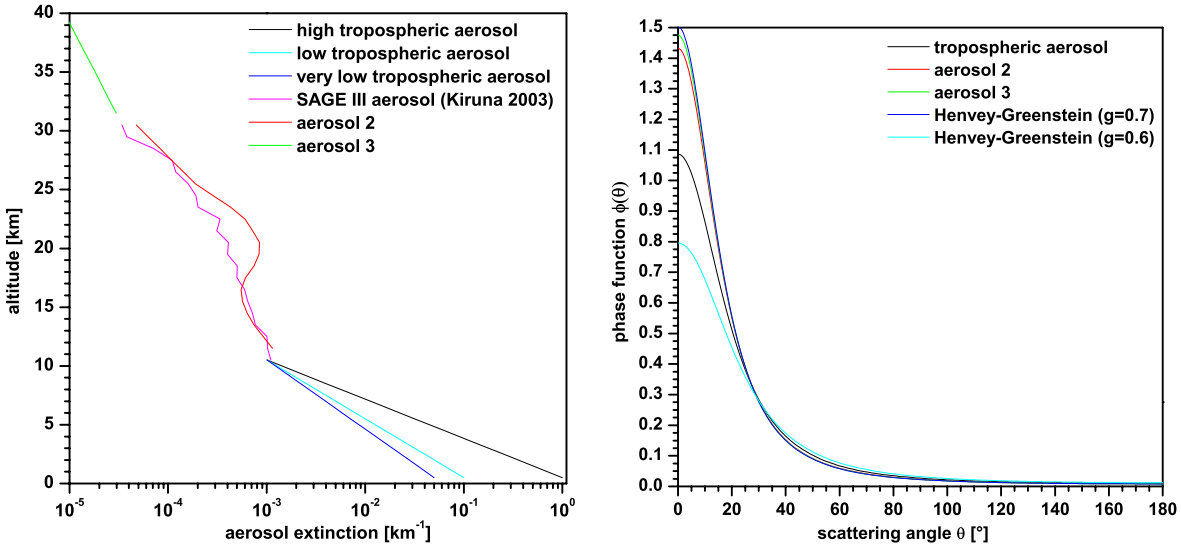

Figure 5.14: Left panel: Aerosol extinction profiles of the scenarios used in this work for 490 nm. Right panel: Aerosol scattering phase functions of the aerosol scenarios shown in the left panel. Also shown are Henvey-Greenstein phase functions with asymmetry parameter $g = 0.6$ (cyan line) and $g = 0.7$ (blue line).

The effect of aerosol scattering on the RT calculations is examined in this subsection. Aerosol are a potential difficulty in the atmospheric radiative transfer as their properties are not precisely known. For stratospheric aerosol extinctions, satellite measurements exist which can be used for the RT modeling. For tropospheric aerosols, however, no measurements for the time of our balloon flights exist. Two parameters are necessary as input for TRACY: an extinction profile and a scattering phase function. Figure 5.14 (left panel) shows the aerosol extinction profiles used in this work. Tropospheric aerosols are highly variable, so several scenarios are modeled. One "high load" scenario with values typical for polluted urban areas and the "low" and "very low load" scenario typical for unpolluted rural areas. For the stratosphere, typical scenarios are assumed (*von Friedeburg*, 2003): "aerosol 2" for the $10-30$ km range and "aerosol 3" above. Alternatively, for the Kiruna 2003 flight aerosol extinction measurements from SAGE III (*Thomason and Taha*, 2003) are available which are very close to the standard profile. The corresponding phase functions are shown in figure 5.14 (right panel). The phase functions are calculated by Mie-theory assuming standard scenarios (*von Friedeburg*, 2003). For comparison, also Henvey-Greenstein phase functions (see equation 3.53) are shown for asymmetry parameters $g = 0.6$

and $g = 0.7$. The phase functions used for the stratospheric aerosols are very close to the Henvey-Greenstein functions with $g = 0.7$. The single scattering albedo ϖ (see equation 3.54) is set to 0.96 for the tropospheric and lower stratospheric aerosol (aerosol 2), and $\varpi = 1$ is assumed for the upper stratospheric aerosol (aerosol 3).

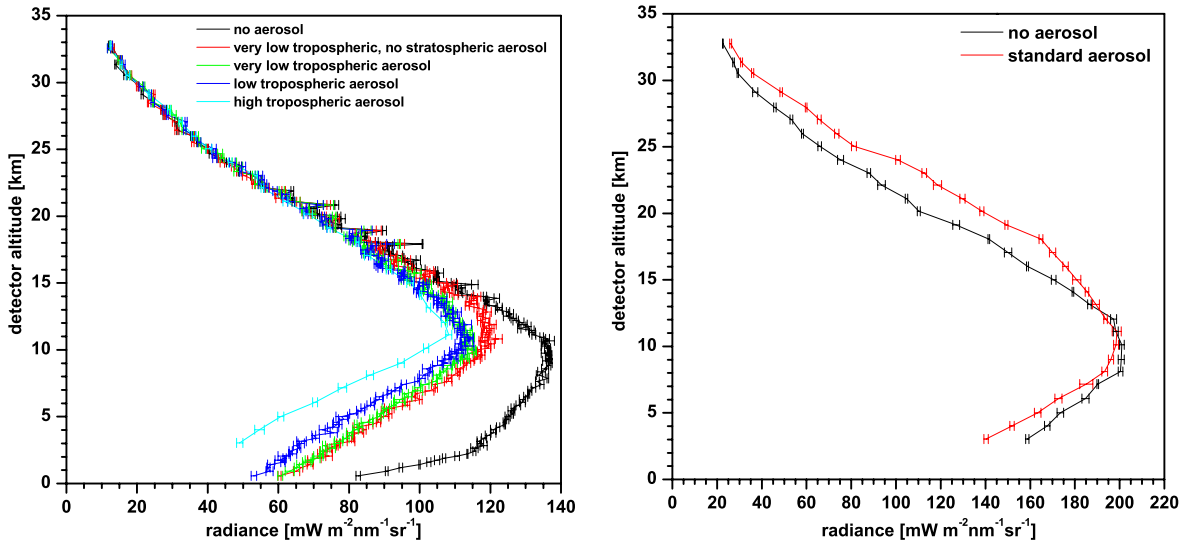

Figure 5.15: RT calculated limb radiances vs. detector altitude for several aerosol scenarios as described in the text for an azimuth angle of 90^o (left panel) and 30^o (right panel) relative to the sun. For the stratosphere, the standard scenarios are used unless otherwise stated.

The effect of tropospheric and stratospheric aerosols on the observed quantities is studied in the following by switching on and off the above described aerosol profiles. RT calculated radiances for several aerosol scenarios are shown in figure 5.15 for an azimuth angle of 90^o (as used for the miniDOAS limb measurements) and 30^o relative to the sun. In the latter case, the limb radiance is increased by additional aerosols at higher altitudes due to fact that more scatterers are available. In the troposphere, the additional aerosol lead to a lower radiance due to absorption and scattering of light out of the light path. At our geometry (i.e. 90^o azimuth angle), additional aerosols always lead to lower limb radiance as the aerosol scattering for angles near 90^o is very unlikely. So aerosols only scatter photons out of the light path but do not lead to additional photons getting scattered into the telescope's field of view compared to pure Rayleigh scattering. Above 15 km the effect of aerosols can be neglected, only in the lower stratosphere, a slight decrease in radiance is observed when aerosols are switched on. In the troposphere, a strong decrease of the radiance is seen with increasing aerosol load.

In the study of how aerosols affect the simulated trace gas SCDs two cases have to be distinguished: Stratospheric absorbers like O_3 and NO_2 (see figure 5.16) and trace gases with maximal abundances in the troposphere (see figure 5.17). As the limb radiances are not significantly affected by stratospheric aerosols, the stratospheric absorbers O_3 and NO_2 are neither. All simulations are basically identical for altitudes above 9 km. Also in the troposphere, the influence of aerosols is very weak. With good eyes can be seen that the the tropospheric SCDs are slightly lower in the "high load" and fairly larger in the "no aerosol" case compared to the "low load" cases. Of course, the influence of tropospheric aerosols is much higher for the tropospheric absorbers. Both the H_2O-SCDs and O_4-ODs are strongly decreasing with increasing aerosol load. Also for stratospheric detector altitudes the simulated SCDs are higher for less tropospheric aerosols as most of the observed absorption is due to photons scattered off the troposphere. The stratospheric aerosols have only a little impact and lead to slightly higher SCDs for

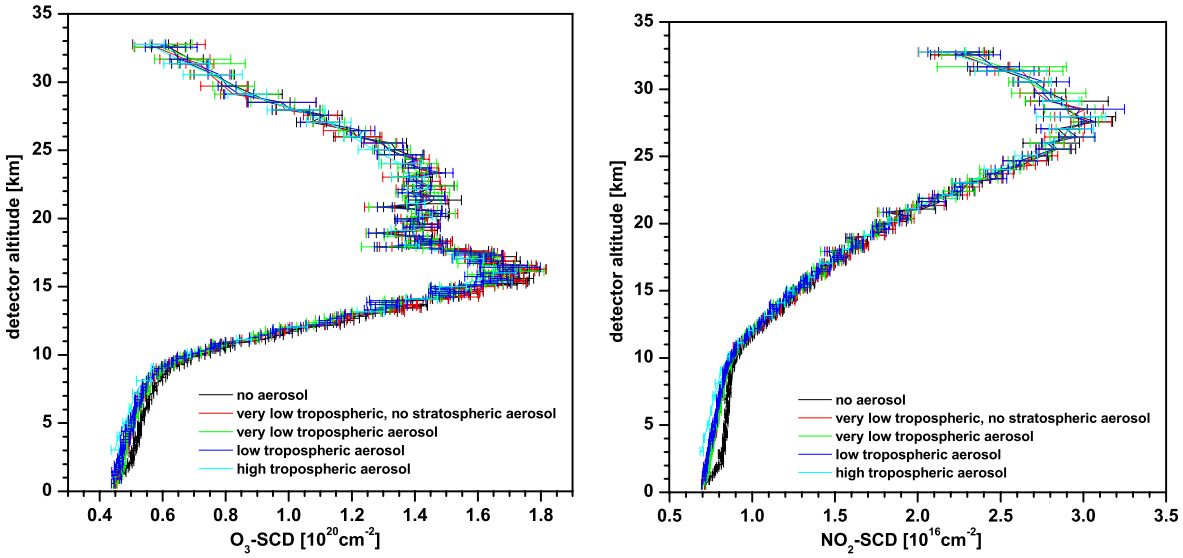

Figure 5.16: Simulated O_3 (left panel), and NO_2-SCDs (right panel) vs. detector altitude for several aerosol scenarios as described in the text. For the stratosphere, the standard scenarios are used unless otherwise stated.

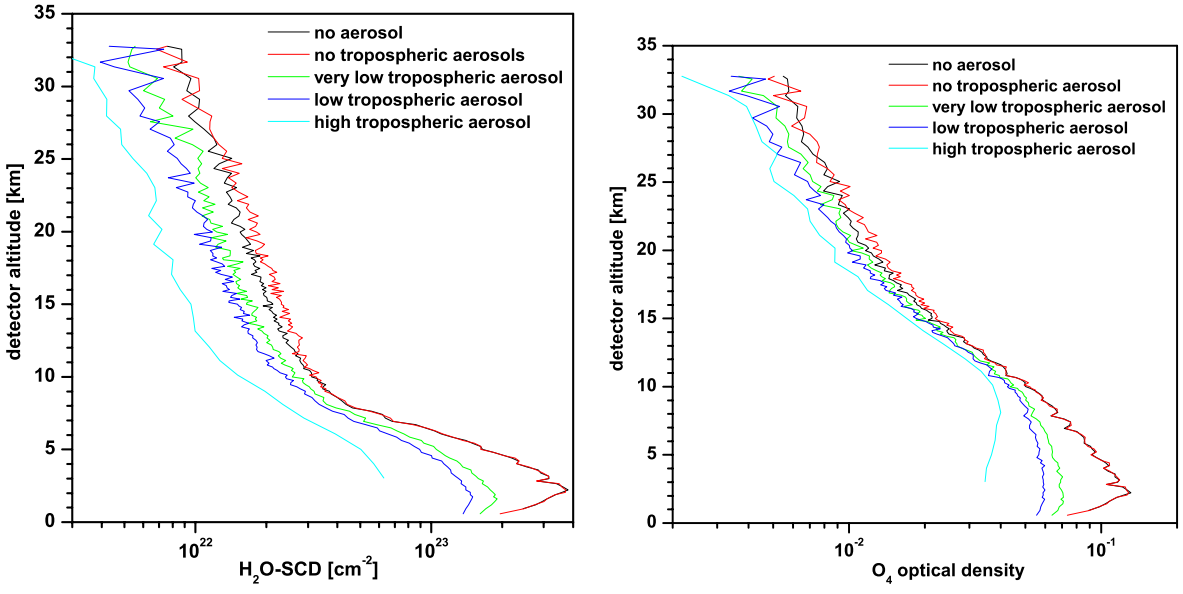

Figure 5.17: Same as figure 5.16 but for H_2O-SCDs (left panel), and O_4-ODs (right panel).

lower stratospheric altitudes, i.e. around $10 - 25$ km, but their effect becomes insignificant for altitudes above.

5.1.6 Scanning Limb Observations

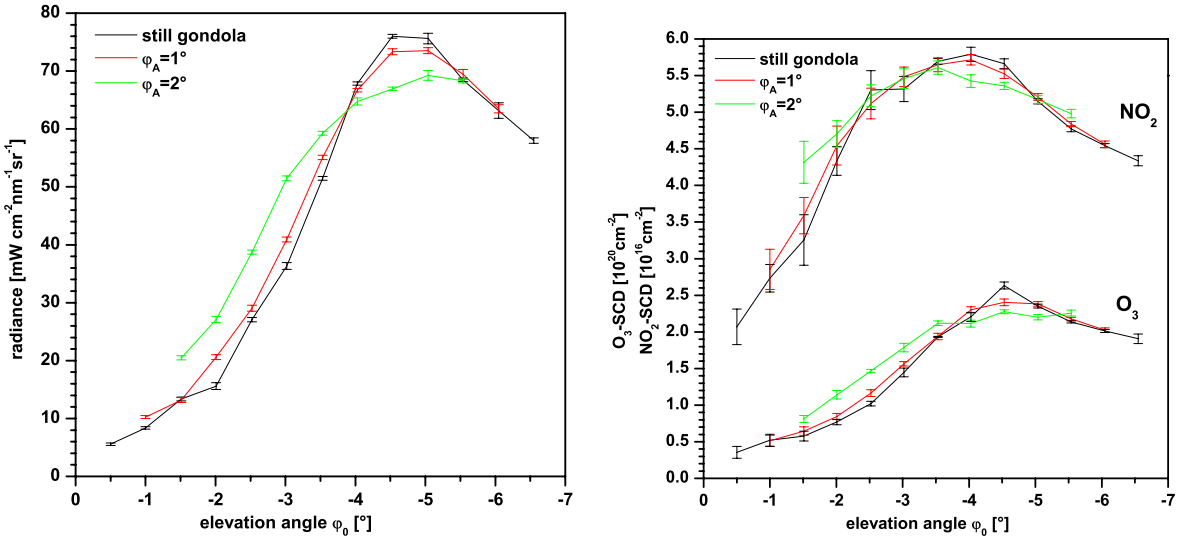

Figure 5.18: Simulated limb radiances (left panel) and O_3- and NO_2- SCDs (right panel) vs. elevation angle ϕ_0 as a function of elevational oscillation ϕ_A between 0^o and 2^o (solid lines) for scanning limb observations.

This section discusses the effect of elevational oscillations on the RT calculations for scanning limb observations at constant float altitude. Generally, the gondola is more stable during float compared to the ascent phase of the flight. Typically, the elevational oscillations have amplitudes between $0.5 - 1.5^o$ and the azimuthal oscillations $< 3^o$. As shown in the previous sections, small azimuthal oscillations and other uncertainties do not seriously affect the results of the TRACY calculations and are not discussed here.

Simulated limb radiances, O_3-, and NO_2- SCDs (right panel) are plotted vs. elevation angle ϕ_0 as a function of elevational oscillation ϕ_A between 0^o and 2^o for a typical scanning limb observation in figure 5.18. The elevational gondola oscillations are treated in a similar manner as in the figures in section 5.1.3. Qualitatively, the results are similar to those obtained for fixed limb measurements during balloon ascent. For an amplitude $\phi_A = 1^o$, the simulations are close to the simulations assuming a still gondola, i.e. $\phi_A = 0^o$ for all three parameters. For an amplitude $\phi_A = 2^o$, significant deviations from the still gondola case are observed. For higher elevations corresponding to tangent heights above the relative maximum of the respective quantity, the simulations are generally higher if gondola oscillations occur compared to a perfectly stable gondola. For tangent heights around and below the maximum, the simulations are below the still gondola case if oscillations are considered, i.e. the maximum is more smeared out and less pronounced in the case of elevational oscillations.

5.1.7 Optimization of the Observation Geometry

One big advantage of scattered light observations is a high degree of freedom of the choice of viewing geometry. As already mentioned in the previous sections, varying the elevation and azimuth angle can

improve (but also worsen) the quality of the limb measurements for a specific parameter. The arguments are summarized here . This section concludes with some remarks how the limb scanning sequence can be improved.

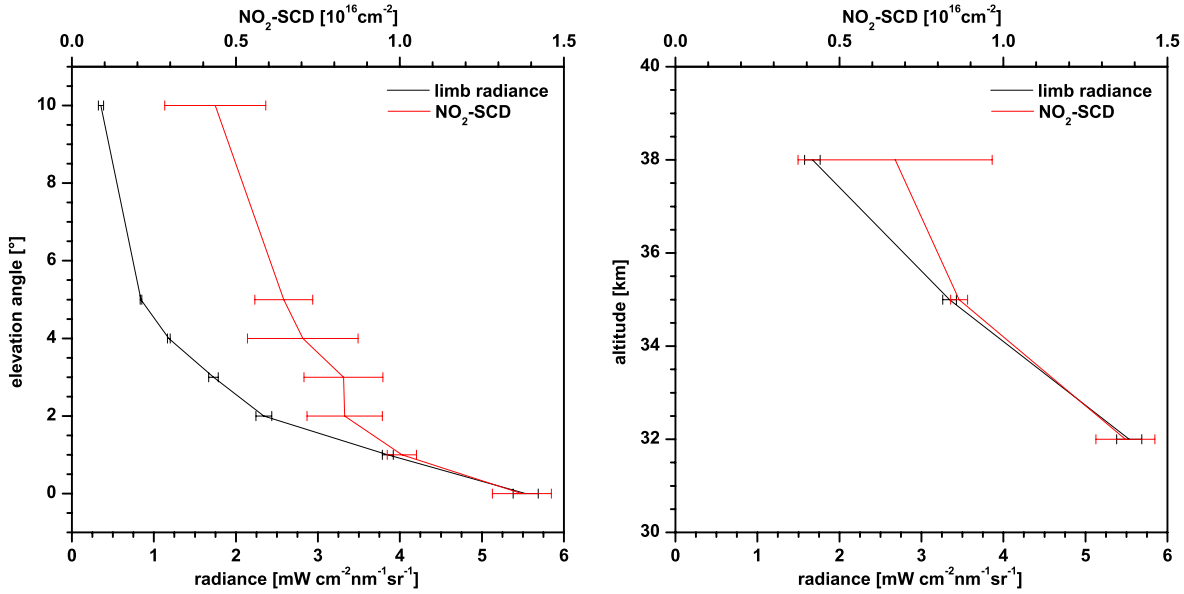

Figure 5.19: Simulated limb radiances (black lines) and NO_2-SCDs (red lines) vs. elevation angle for constant detector altitude of 32 km (left panel) and vs. detector altitude for a constant elevation angle of 0^o (right panel). In both plots, the SZA is 85^o.

For the elevation angle, there is no alternative to the chosen one of 90^o relative to the sun. The biggest argument for this is that the SZA along the line of sight is constant under this condition which is especially important for the limb scan during sunset or sunrise. During day, an azimuth angle of 180^o to the sun could slightly increase the observed limb radiances. Azimuth angles off these relative radiance extrema are not recommendable as the radiance becomes strongly dependant on azimuth angle which might render the automatic saturation leveling more difficult. The sensitivity tests regarding elevation angle have shown that the AMF and, thus, the trace gas SCDs are higher for elevations slightly below the horizon (e.g. for -1.5^o compared to 0^o) while the tangent altitude is still very close to the detector altitude. Especially the sensitivity of the detection of the weak absorber BrO benefits from this. Further decrease in elevation angle leads to tangent heights below the detector, wider BoxAMFs and, thus, worse the conditioning of the profile inversion problem (see the Kiruna 2002 flight, section 6.2.1). However, a lower elevation angle leads to stronger sensitivity of the measurements to elevational gondola oscillations especially affecting the NO_2 observations around the NO_2 concentration maximum between above 25 km. So for the NO_2 measurements, a higher elevation angle of 0^o is favorable. Consequently, the ascent measurements could be optimized by setting the elevation angle to -1.5^o in the beginning up to altitudes of $20 - 25$ km and then switch to 0^o above. After arrival at balloon float altitude (usually around 33 km for a 150000 m^3 balloon), the elevation angle can be further increased to record a solar reference spectrum with minimum absorption. In figure 5.19 (left panel), simulated limb radiances and NO_2-SCDs for positive elevation angles between 0^o and 10^o for 32 km detector altitude and SZA=85^o are plotted. It is seen that the limb radiance is strongly decreasing with elevation angle. NO_2-SCDs are also decreasing with elevation angle. A good compromise would be an elevation angle of $+2^o$ where the NO_2-SCD is by ~ 40 % below that for 0^o elevation. Also O_3-SCDs decrease by ~ 30 %. However, the limb radiance is by a factor of ~ 2.3 smaller compared to 0^o elevation angle which implies that

the measurement time increases by the same factor if the same saturation, i.e. photoelectron noise is desired. Higher elevation angles do not seem useful as the NO_2- SCDs decrease only little while the radiances decrease stronger. Lower trace gas absorption can also be achieved by higher balloon float altitudes. If a 400000 m^3 balloon is used instead of a 150000 m^3 balloon, the float altitude increases from ~ 33 km to ~ 38 km. The resulting limb radiances and NO_2-SCDs are shown in figure 5.19 (right panel).

However, this sequence is difficult to achieve from an experimental standpoint without the possibility to change the elevation from ground by telecommand. In the current version of the instrument without telecommunication, the exact times for the detector movements would have to be programmed before launch which is difficult as experience has shown. A delayed launch or faster than assumed ascent could result in even worse measurements as using a fixed elevation angle.

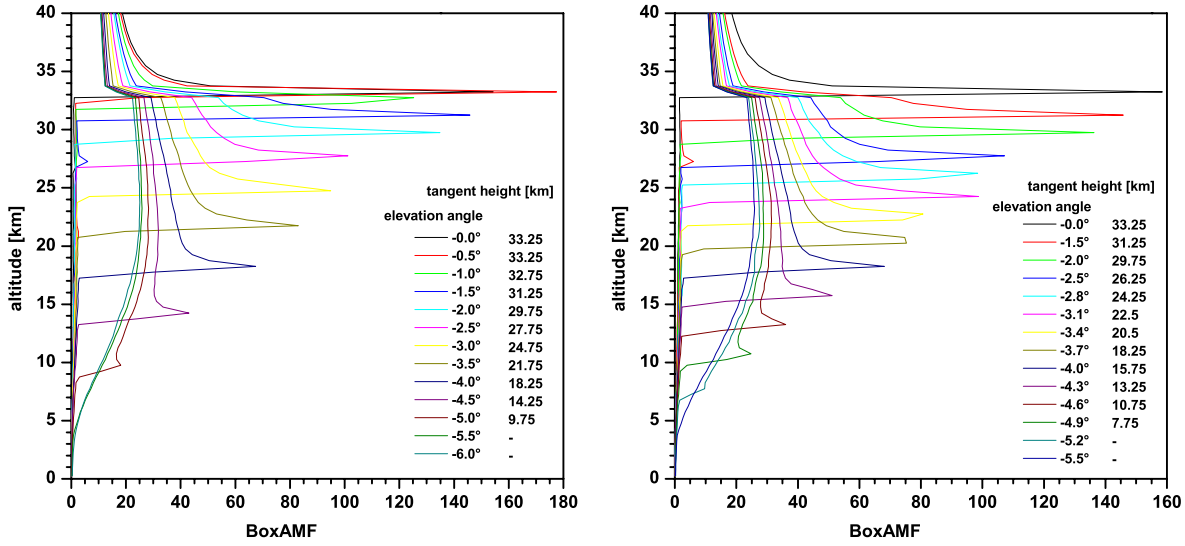

Figure 5.20: RT calculated BoxAMFs vs. altitude as function of elevation angle for the two limbscan sequences described in the text. Also denoted are the approximate tangent heights of each observation given by the maximum BoxAMF.

Now it is discussed how the limb scan sequence can be further improved. For the two scanning limb measurements so far, a constant elevation step of 0.5^o was chosen. The corresponding BoxAMF for constant detector altitude of 33.2 km and 88^o SZA are shown in figure 5.20 (left panel). It can be seen that the tangent height does not change for the first 3 observations. With decreasing elevation, the steps in tangent height are increasing from ~ 1 km to $\sim > 3$ km. So it may be wiser to start the limbscan sequence with a larger step width (e.g. 1.5^o) and decrease it (to 0.3^o) for lower elevations. Step widths $< 0.3^o$ do not seem useful as the unavoidable elevational oscillations are of the same order at best. The resulting BoxAMFs and tangent heights are shown in the right panel of figure 5.20. In this case the steps in tangent height are always around $2-3$ km. However, it is crucial to determine the zero position of the telescope very precisely. In the so far conducted flight, there was an uncertainty of 0.5^o. In this case it might be the better choice to use a constant step width.

5.2 Sensitivity of the Profile Retrieval

5.2.1 Detecting Low Trace Gas Amounts in Front of Large Backgrounds

By looking at the RT calculated BoxAMFs (e.g. figure 5.6), it can be seen that by far the biggest contribution to the measured SCD comes from the altitude layer the detector is actually in with AMF > 50. For altitudes significantly above the detector altitude, the AMF approaches $1/\cos(\mathrm{SZA})$, e.g. values between 4 and 11 for SZA=75^o and 85^o, respectively. For altitudes more than 1 km below the detector, the BoxAMF are comparitively low (typically between 2 and 0.3) but always non-zero. This implies that high trace gas concentrations in the troposphere can dominate the measured SCDs in the stratosphere. This is the case for H_2O and O_4 which both have much lower stratospheric than tropospheric concentrations. But also stratospheric NO_2 measurements can be dominated by high tropospheric contributions in heavily polluted areas. The effect is quantitatively examined here. Another problem arises for measurements of low concentrations below the concentration maximum, e.g. when measuring tropospheric O_3 or BrO , or lower stratospheric NO_2.

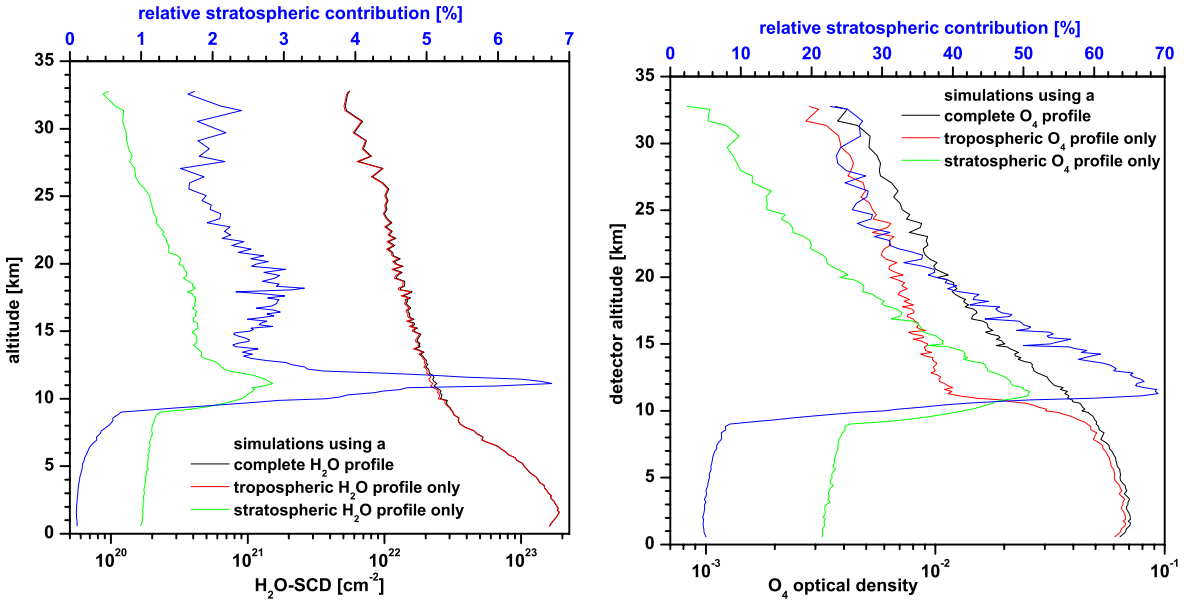

Figure 5.21: Simulated H_2O-SCDs (left panel) and O_4-ODs (right panel) assuming a tropospheric profile (i.e. all values in the respective profiles above 9 km are set to zero, red lines), a stratospheric profile (i.e. all values in the respective profiles below 9 km are set to zero, green lines) and a total profile (black lines). Also shown is the relative contribution of the stratospheric profile to the total SCD/OD (blue lines).

Water vapor has a pronounced maximum at low altitudes with mixing ratios > 1000 ppm on the ground decreasing to ~ 6 ppm in the stratosphere (see figure 6.49). Considering the exponentially with altitude decreasing air density, tropospheric concentrations are exceeding stratospheric concentrations by 4 orders of magnitude. To check the sensitivity of the measurements towards stratospheric H_2O, three simulations are carried out (figure 5.21, right panel): (a) one with the total profile as shown in fig. 6.49, (b) one with all concentrations set to zero at stratospheric altitudes (i.e. above 9 km), and (c) one with all concentrations set to zero at tropospheric altitudes (i.e. below 9 km). This exercise reveals that tropospheric H_2O by far dominates the limb scattered radiation as the simulation using the tropospheric profile is almost identical to the one using the total profile. In fact, the tropospheric SCD exceeds the stratospheric SCD by a factor of 20 in the lower and 60 in the upper stratosphere,

i.e. the stratospheric SCD contributes only by $2-3$ % to the total SCD. This is due the fact that the tropospheric water vapor concentration is by several orders of magnitude (up to 4 for the lowermost troposphere) bigger than the stratospheric one. This affects the stratospheric limb measurements in a way that, even if the BoxAMF of the actual balloon altitude is ~ 100 times bigger than the tropospheric BoxAMF, the measured SCDs are dominated by the tropospheric H_2O concentration.

In the case of O_4, the qualitative picture is similar although the dominance of the tropospheric contributions is not as strong as for H_2O. In figure 5.21 (right panel), a similar exercise as for H_2O is shown. The stratospheric contribution to the total OD ranges between 70 % in the lower and 20 % in the upper stratosphere. Under these condition, a sensitive measurements of the stratospheric profile is possible (see e.g. section 6.5.7).

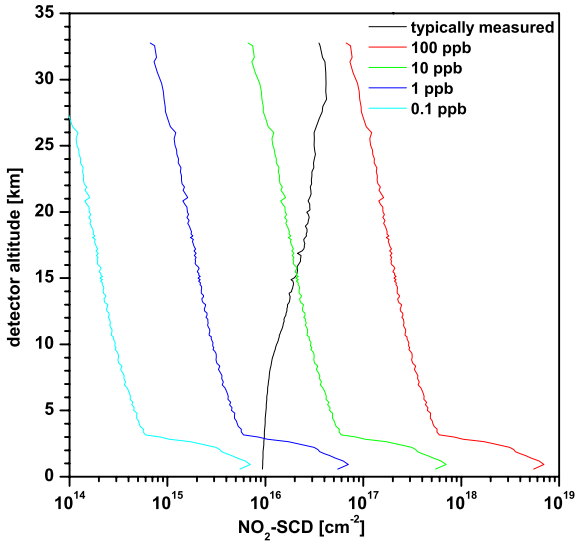

Figure 5.22: Simulated NO_2-SCDs vs. detector altitude assuming an NO_2 mixing ratio in the lowermost altitude layer of 100 ppb (red line), 10 ppb (green line), 1 ppb (blue line), and 0.1 ppb (cyan line). Also shown is an example of measured NO_2-SCDs (black line) from an unpolluted area (Kiruna in northern Sweden).

A third sensitivity study in this context is undertaken for the case of stratospheric NO_2 measurements above polluted areas, i.e. the question whether sensitive stratospheric NO_2 measurements are possible in front of the tropospheric background is tackled. The NO_x abundances in the boundary layer are quite variable with mixing ratios ranging from 0.02 ppb in unpolluted, remote areas to $10-1000$ ppb in heavily-polluted areas (*Seinfeld and Pandis*, 2000). Figure 5.22 shows simulations of NO_2-SCDs assuming NO_2 concentrations ranging from $0.1-100$ ppb in the lowermost altitude layer (i.e. between $0-1$ km and zero everywhere above). Also shown are NO_2-SCDs measured during balloon ascent at Kiruna, i.e. for an unpolluted area. In this case, only stratospheric NO_2 contributes to the observed NO_2-SCDs. By comparing the heavy pollution simulations (i.e. 100 ppb NO_2) to the unpolluted measurements, it can be seen that the stratospheric measurements would be by far dominated by the tropospheric NO_2. A sensitive measurement of stratospheric NO_2 would be difficult if not impossible in this case. However, it should be considered that the limb scattered radiation is collected from quite a big area (several hundred km in diameter), so that the average NO_2 concentration of this area is relevant for the measurements. An average of 100 ppb NO_2 over several hundred km is very high even for industrial centers. For 10 ppb, the (simulated) tropospheric and (measured) stratospheric contribution are of the same order. As has been shown in the case of O_4 the retrieval of stratospheric profiles is possible under such conditions. However, as tropospheric NO_2 concentrations are highly variable (in strict contrast to O_4), variations of the tropospheric NO_2 background during the flight are misinterpreted

as stratospheric profile information so that the retrieved profiles might become very inaccurate in this case. For tropospheric NO_2 concentrations of 1 ppb and less, the tropospheric contribution is much smaller than the stratospheric at higher altitudes so that the measured NO_2-SCDs are not significantly affected. So far, no enhanced NO_2-SCDs were measured at low altitudes for all balloon flights which implies average NO_2 concentrations < 0.1 ppb in the boundary layer.

A similar problem occurs when low trace gas concentrations are to be measured below the concentration maximum. This is especially problematic for NO_2 measurements in the lower stratosphere, but to a lesser degree also for O_3 and BrO measurements at low altitudes. In that case, the measured SCDs are largely determined by the concentrations above the balloon altitude. As the profile information comes, qualitatively speaking, from the difference of the measured SCDs at different altitudes, this profile information has large relative errors as it is given by the difference of two similar but large numbers which is always problematic. In the case of NO_2, the SCD at lower altitudes is given by the large absorption of the solar reference spectrum and the measured (negative) dSCD. Small uncertainties of the latter two quantities yield a large relative error of the retrieved SCD. In the case of O_3 and BrO, this effect is smaller but the relative errors of the retrieved profiles are also maximum for altitudes below the maximum. This effect is discussed more quantitatively section 5.2.4.

5.2.2 Photochemical Effects

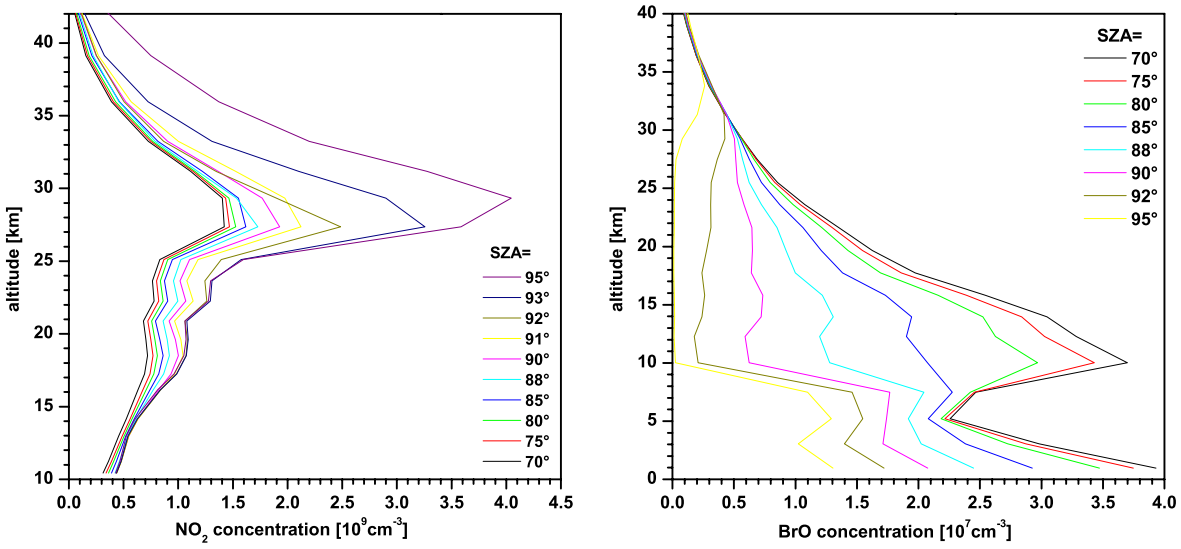

Figure 5.23: Photochemically simulated concentration profiles of NO_2 (left panel) and BrO (right panel) as a function of detector altitude. The profiles are calculated with the LABMOS 1-D model (see section 3.4).

The abundances of radicals like NO_2 and BrO are strongly variable with the incident solar radiation. Thus, their profiles are dependent on the SZA. Photochemical effects can be studied with scanning limb measurements. Here, it is discussed how photochemical changes affect the profile measurements during balloon ascent, and how the profiles of photochemically active radicals can be interpreted.

Figure 5.23 shows photochemically simulated profiles as function of SZA for NO_2 and BrO. The profiles are calculated with the LABMOS 1-D model (see section 3.4 for details on the chemistry models) for the example of the Kiruna 2004 flight. The NO_x amount is initialized with the NO_2 concentrations

measured by the direct sunlight DOAS, while all other species are initialized with SLIMCAT output. Qualitatively, it is seen that the NO_2 concentrations are increasing and the BrO concentrations are decreasing with SZA in the SZA range of interest (SZA were between $> 70^o$ for stratospheric altitudes for all miniDOAS flights and the measurements usually end around SZA=95^o when limb radiances become too low). For more details on the NO_2 and BrO photochemistry see sections 2.3 and 2.4.2, respectively. This implies that the NO_2-SCDs measured during balloon ascent are lower at low altitudes and higher at high altitudes compared to the hypothetical case of a balloon ascent with a constant median SZA. As the contribution of the light below the actual balloon altitude is rather low (BoxAMF are typically < 2 for altitudes more than 1 km below the detector but in the order of 100 at the detector altitude), this means for altitudes around the maximum that the retrieved profile is a good representation of the situation corresponding to the SZA when the balloon passes these altitudes. For altitudes much below the concentration maximum, lower concentrations than present at the time when the balloon passes these altitudes are retrieved because a certain fraction of the observed absorption occurs at altitudes of the NO_2 maximum. Thus, the lower measured SCDs are compensated by too low concentrations at the corresponding altitude. The change of SZA during the flight through the stratosphere is around 7^o corresponding to an NO_2 increase of $5-7$ % at the relevant altitudes for the shown example. Therefore, the distortion of the retrieved profile due to photochemical effects is assumed to be small.

For BrO profile measurements during balloon ascent, the situation is somewhat different, but the conclusions are the same. This is due to the fact that the BrO maximum lies in the lower stratosphere and the concentrations are decreasing with SZA. So the measurements performed around the maximum should not be much affected by the moderately decreasing concentrations for higher altitudes. Also the measurements at higher altitudes are not strongly affected as the photochemical changes are rather low at higher altitudes. This is because the photochemical decline sets in later with increasing altitude. As a consequence, for each altitude the retrieved profile can be seen as a representation of the situation when the balloon (or, more precisely, the tangent height which is approximately the detector height for elevation angles around 0^o) passed the respective altitude level.

5.2.3 Effect of the *a priori* Profile

The Maximum A Posteri (MAP) technique requires the assumption of an a priori profile and a corresponding covariance (see section 3.3). The a priori combines all information that is available about the trace gas profile of interest before the actual measurement is performed. It is, e.g., taken from CTM outputs or other measurements of the trace gas under the respective conditions (e.g. from climatology or nearby satellite measurements). The covariance can be taken, e.g., from climatology. More mathematically, it can also be seen as a parameter determining the relative contribution of the a priori to the retrieved profile. The a priori is necessary because the balloon-borne limb measurements usually contain no profile information about the altitudes above balloon float altitude. So if the measured SCDs were just inverted without assuming a priori values, the retrieved concentrations above would be merely undetermined, which results in extreme oscillations of the values exceeding the actual concentrations by several orders of magnitude. This causes the retrieved concentrations of the altitudes below float (for which the measurements are sensible) to become highly incorrect. Therefore, it is necessary to constrain the values above balloon float by reasonable a priori assumptions. On the other hand, it is desirable that the retrieved profile below balloon float, where the measurements are sensitive, is independent from the a priori. The effect of the a priori and the chosen covariance on the retrieved profile is examined in the following by two sensitivity exercises. First, the a priori is varied for constant covariance, then the covariance is altered for a constant a priori profile.

Figure 5.24 shows the results of the first study for a sample O_3 profile retrieval for the Kiruna, 2003 flight. As a priori profile, the correlative ozone sonde measurements are used. For the test, this profile

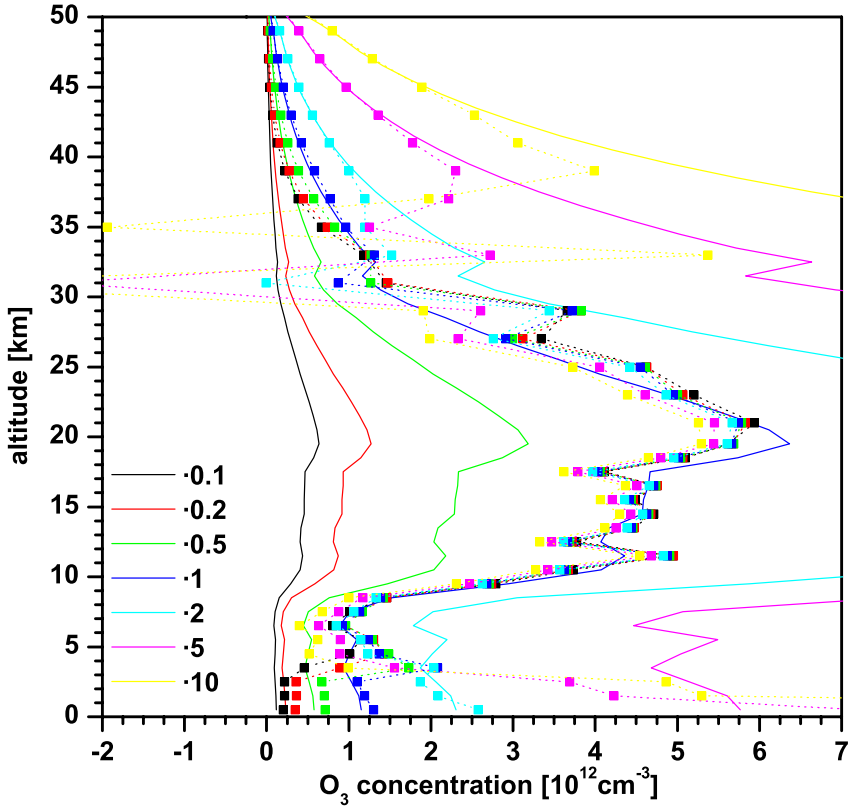

Figure 5.24: Retrieved O_3 profiles (squares and dotted lines) as a function of the used a priori profiles (solid lines). The a priori was multiplied with the stated factors ranging from 0.1 to 10.

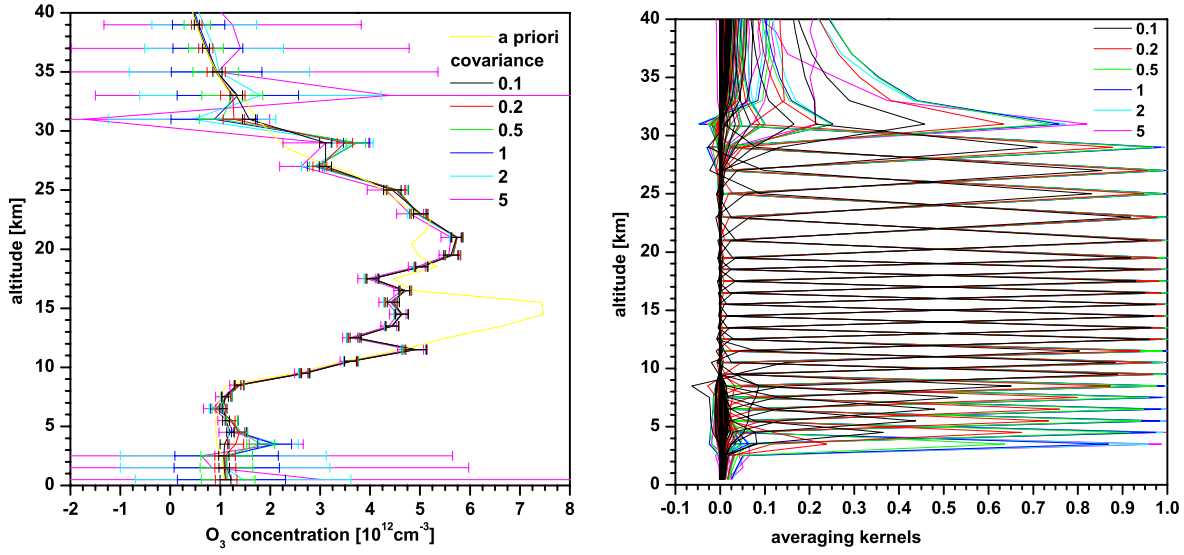

Figure 5.25: Left panel: Retrieved O_3 profiles (solid lines) as a function of the covariance of the a priori. The covariance was set to the a priori times the stated factors between 0.1 and 5. Right panel: Averaging kernels of the profile retrievals shown in the left panel as a function of the covariance of the a priori.

is multiplied with factors between 0.1 and 10. The resulting profiles are used as a priori for the profile retrieval. The covariance is set to 100 %. In the left panel, the retrieved profiles are shown as a function of the used a priori. As there are measurements only between 3 and 30 km, the retrieved profile is only determined by the measurements in this altitude range. This can be seen from the averaging kernels being close to 1. Outside this altitude range, the retrieved profile is mostly determined by the a priori. This is seen in figure 5.24 for altitudes < 3 km and > 30 km. At the transition between the altitude range determined by the measurements and the altitude range determined by the a priori, oscillations can occur for the retrieved profile, especially if there is a mismatch of the a priori and the measurements. In the present test, the concentrations of the a priori profiles multiplied with factors < 2 are definitely larger than in reality. So this mismatch of measured SCDs and a priori is compensated by unrealistically fluctuating retrieved concentrations in the $30 - 35$ km range. This mismatch above 30 km also effects the retrieved values below. The retrieved profiles for the a priori multiplied by 5 and 10 are lower for all altitudes between $3 - 30$ km. For 'real' profile retrievals, the a priori is usually not wrong by a factor of 5 or more, so these two examples can be viewed as absolute worst case scenarios. For the a priori multiplied with factors between 0.1 and 2, the retrieved profiles are not significantly affected for stratospheric altitudes. For tropospheric altitudes, the retrieved concentrations show stronger deviations if the a priori is wrong. In a similar test not shown here, it is found that the retrieved profiles do not change if only the values below 30 km of the a priori profiles are multiplied with factors between 0.1 and 10.

In the second sensitivity test, the same a priori profile is used but its covariance is varied between 0.1 and 5 times of the a priori value, i.e. between 10 % and 500 % relative error. This time, the ozone profile measured one year later at the same location is taken, which is supposed to be close but not identical to the measured situation. The results are shown in figure 5.25. It is found that the retrieved profiles do not significantly deviate in the sensitive altitude range. Above 30 km, oscillations occur for high covariances. The high fluctuations might influence the retrieved concentrations below 30 km, which is seen in the "5"-case by slightly lower values. Decreasing the covariance, decreases the fluctuations but also the averaging kernels (see 5.25 right panel). For (relative) covariances > 1, the averaging kernels are almost 1 in the entire sensitive altitude range between 3 and 30 km. So covariances higher than 1 are usually not necessary. For a relative covariance of 0.1, the averaging kernels are only between 0.3 and 0.95. However, the retrieved profile is not significantly affected by this.

The lessons learned from these two sensitivity exercises can be summarized as follows: the retrieved profiles are not significantly affected by the a priori profile, if its values are reasonably chosen, for altitudes the measurements are sensitive indicated by averaging kernels close to 1. If the a priori is significantly wrong outside this range, the retrieved profile can be affected and/or oscillations can occur. The oscillations can be reduced by choosing a smaller a priori covariance.

5.2.4 Error Analysis

In this subsection, a qualitative discussion of all relevant error sources in the profile retrieval procedure and a quantitative error analysis considering the major uncertainties are given.

Uncertainty of the DOAS Retrieval

The relevant error sources of the DOAS retrieval are discussed in detail in section 3.1.3. Most of the mentioned effects like instrumental noise, Ring and solar I_0 effect, affect the residual, and thus the DOAS retrieval error output by the WinDOAS evaluation tool. This error is used for the profile inversion as SCD error. However, additional systematic errors exist which are not accounted for by the

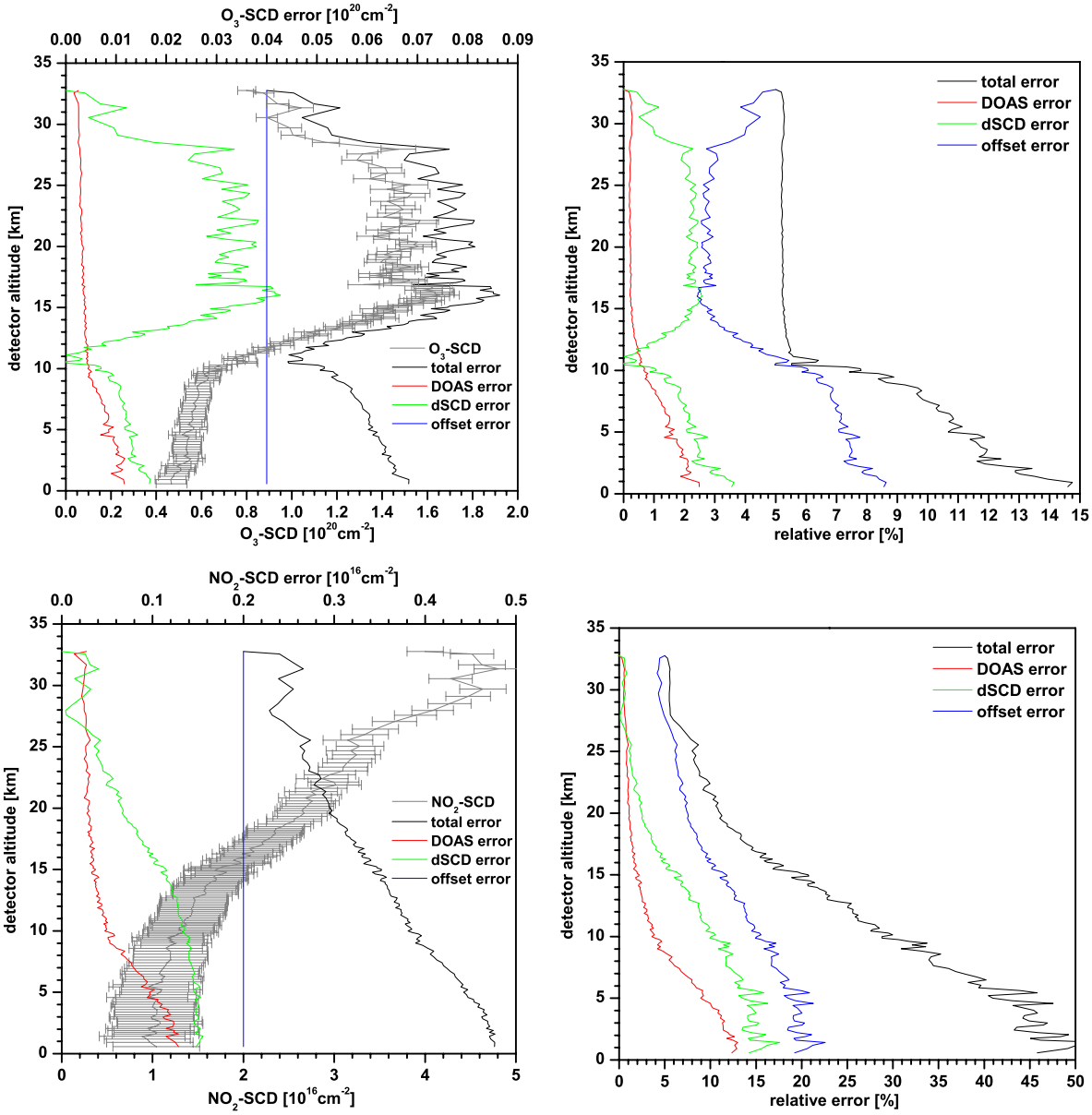

Figure 5.26: Absolute (left panels) and relative errors (right panels) of the DOAS SCD retrieval of O_3 (upper row) and NO_2 (lower row) vs. detector altitude (for a definition of the individual error contributions see text). Also shown in the left panels are the retrieved SCDs and their total errors (as error bars) vs. detector altitude (gray lines).

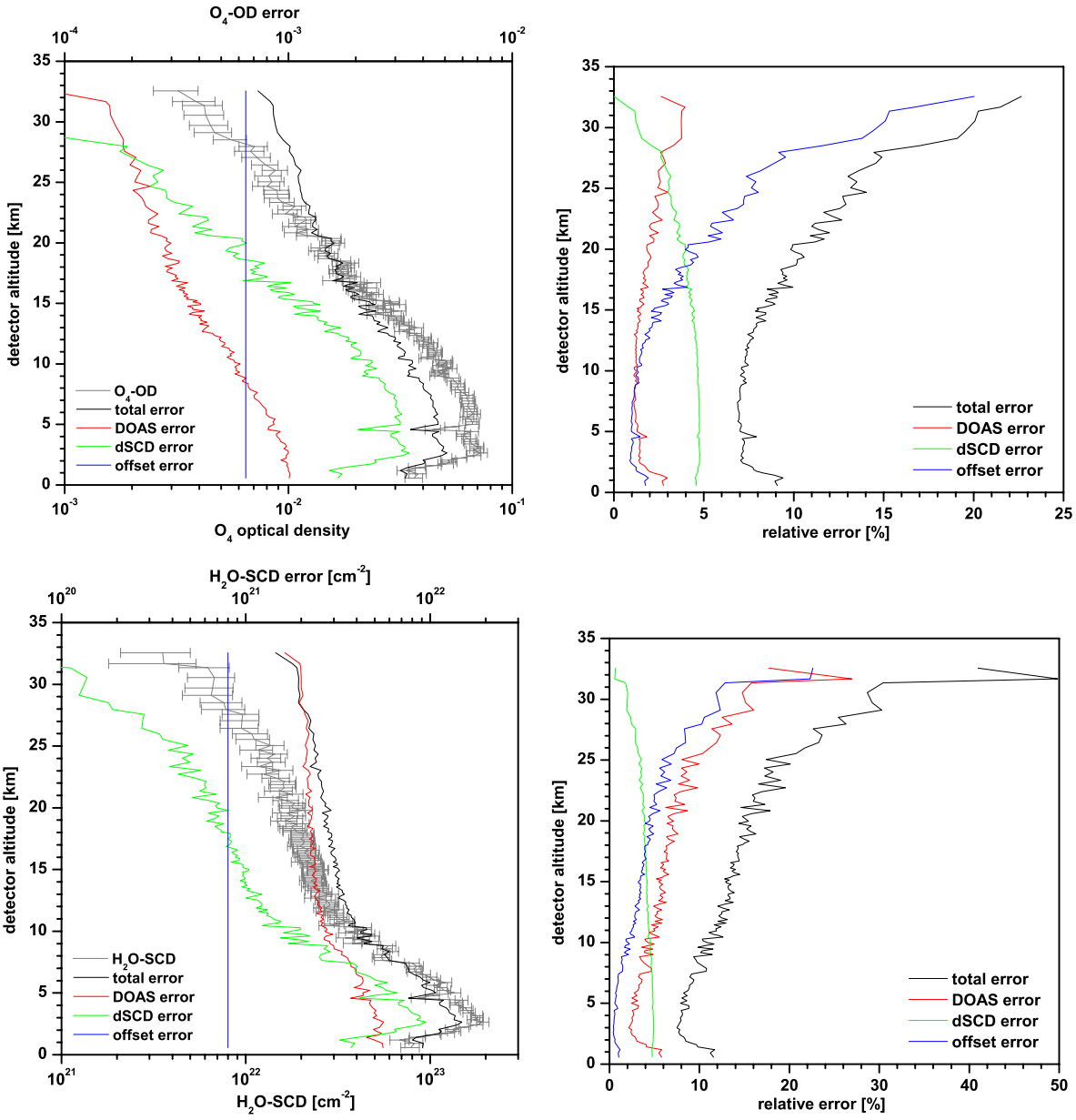

Figure 5.27: Same as figure 5.26 but for an O_4-OD (upper row) and H_2O-SCD retrieval (lower row).

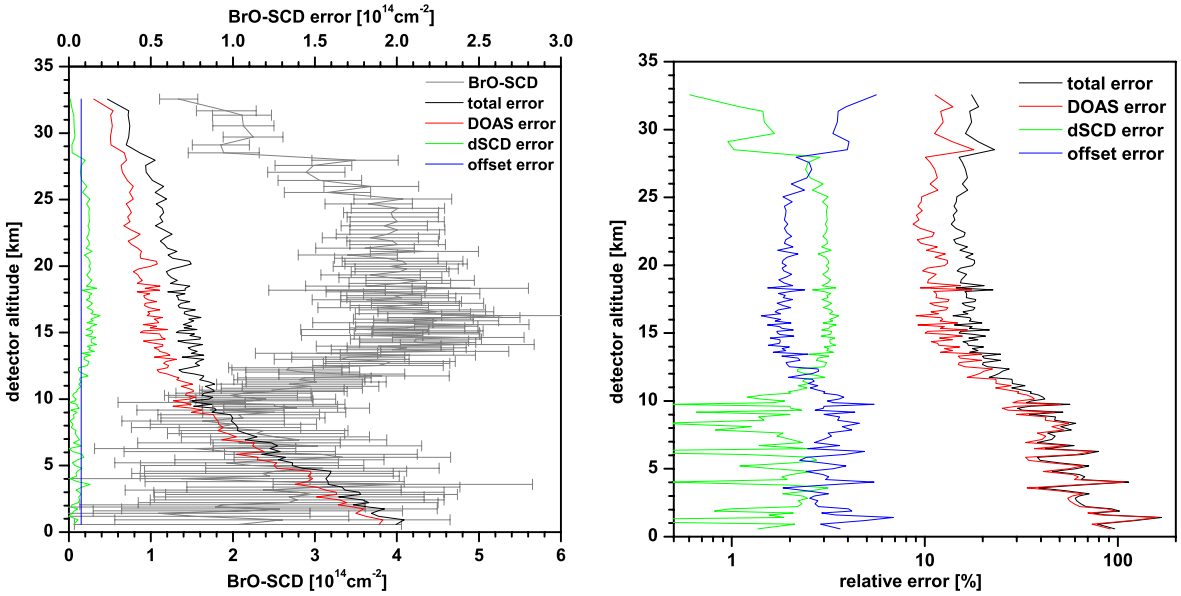

Figure 5.28: Same as figure 5.26 but for a BrO-SCD retrieval.

retrieval error. Errors originating from correlations of the cross sections are difficult (if not impossible) to treat quantitatively with the used software and, thus, not considered in this error analysis. However by carefully checking the DOAS evaluation, this error source can be minimized. Further uncertainties of the DOAS retrieval arise from the cross sections. Their magnitude is determined in laboratory measurements only to a certain precision. Also their temperature dependance gives rise to errors. Assuming a $\sim 10\,\mathrm{K}$ temperature uncertainty, yields ~ 3 % deviation of the O_3 and NO_2 and ~ 5 % of the BrO cross section. Another uncertainty (the largest contribution to the total error in most cases) of the measured SCDs arises from the determination of the trace gas absorption contained in the solar reference spectrum which is added to the retrieved dSCDs to get SCDs (see section 4.4.8). Its uncertainty is estimated to $5-10$ % of its value for O_3, NO_2, and BrO, and > 20 % for H_2O and O_4 as its value is very low in those cases.

The uncertainties of the retrieved trace gas SCDs are discussed in the following for the example of the Kiruna 2004 flight. The following errors are taken into account:

- the DOAS retrieval error as given by the WinDOAS evaluation (further called "DOAS error"),
- the uncertainty of the cross section: 5 % of the retrieved dSCD (further called "dSCD error")
- the uncertainty of the solar reference offset: 5 % of its value for O_3, NO_2, and BrO, and 20 % of its value for H_2O and O_4 (further called "offset error"),
- and the "total error" as the sum of the above contributions

The mentioned error contributions and the total error are plotted for the 5 species vs. detector altitude in figures 5.26 - 5.28. In the left, the absolute values and, in the right, the relative errors are shown. The relative errors are obtained as the ratio of the respective absolute SCD error and the trace gas SCD (and not the dSCD). The major contribution to the total error of the O_3-SCD retrieval is given by the offset error. This contribution is, by definition, constant with altitude and, thus, its contribution to the relative error is maximum in the troposphere where the measured SCDs are minimum. In numbers, its uncertainty ranges between 8.5 % for the lowermost troposphere and 3 % in the stratosphere around the ozone maximum. The DOAS error is comparatively low and also decreases with altitude as the

residuals of the DOAS evaluation strongly decrease with altitude due to the smaller wavelength shift of the measured spectra relative to the solar reference spectrum. Its values are around $2.5 - 1$ % in the troposphere, decreasing to negligible ~ 0.2 % in the stratosphere above 15 km. The dSCD error shows a rather odd altitude dependence with a minimum around 10 km. This is because the retrieved dSCDs are negative in the troposphere and thus their error increases with decreasing altitude. The resulting total error has values of 15 % for the lowermost altitudes decreasing to almost constant values around 5 % above 10 km. In the case of NO_2 , the qualitative picture looks similar, but with higher absolute numbers between 50 % total uncertainty for the lowermost and 5 % for the uppermost spectra for which the NO_2-SCDs are maximum. The major reason for the high errors is the rather unfavorable measurement geometry as the solar reference spectrum is recorded near the NO_2 concentration maximum. This results in a large offset and causes the retrieved dSCDs to become negative for most of the flight. Therefore the dSCD error is increasing with decreasing altitude although the absolute SCDs are decreasing with decreasing altitude. At this point, it might be argued that the dSCD error is somewhat arbitrary as it depends on the chosen solar reference spectrum. Taking e.g. the lowermost spectrum as reference would yield positive dSCDs throughout the flight and, thus, dSCD errors increasing with altitude. However, the determination of the offset of this spectrum is not easily possible as it requires the excact knowledge of the entire stratospheric and tropospheric NO_2 concentration profile. As the offset is usually determined by comparison with a stratospheric profile composed from direct sunlight DOAS measurements and CTM output above, the tropospheric SCDs have a higher uncertainty due to the temperature and other uncertainties of the cross section so the chosen estimation of the error is logical. Additionally, the DOAS error is increasing with decreasing with altitude for the same reasons as stated for O_3. Its relative contributions range from 12 % near the ground to < 1 % above 20 km. In the case of BrO, the relative contributions of the individual error sources are somewhat different. The total error of the BrO-SCD (see figure 5.28) is dominated by the DOAS retrieval error which lies around $10 - 20$ % for most of the stratosphere, i.e. above 12 km. Below, the error is dramatically increasing due to a larger residual caused by an increasing spectral shift and the decreasing UV skylight. Therfore the BrO-dSCDs fall below the detection limit for altitudes < 10 km. The solar reference offset, which can be determined rather precisely using SLIMCAT CTM output, only causes a minor error contribution as well as the uncertainty of the cross section. Their added contributions cause a relative uncertainty of ~ 5 %. This results in a total error of $15-25$ % for the BrO-SCD for altitudes above 12 km. The altitude dependence of the error contributions for the tropospheric absorbers H_2O and O_4 (see figure 5.27) is completely different compared to the afore discussed stratospheric trace gases. The SCDs decrease by more than an order of magnitude from the lowermost to the uppermost spectra. This causes individual contributions to be predominant in the troposphere but almost negligible in the upper stratosphere and vice versa. In the troposphere, the most important error contribution is caused by the uncertainties of the cross section (dSCD error) with almost 5 %. The relative dSCD error is decreasing to < 1 % in the upper stratosphere. The opposite altitude dependence is observed for the offset error. In numbers, the offset error is around $1 - 2$ % in the troposphere and increasing for the uppermost spectra to 20 %, i.e the assumed uncertainty of the offset as the SCD is almost equal to the offset value at high altitudes. The DOAS error is really small for the O_4-SCD retrieval with relative errors between $1 - 4$ %. For the H_2O retrieval, the DOAS errors are somewhat larger with $2 - 5$ % in the troposphere increasing to 15 % in the upper stratosphere. Note that the DOAS error in our definition is not the relative error of the DOAS retrieval, as the former is defined as σ/SCD and the latter as $\sigma/dSCD$ with the DOAS retrieval error σ.

Uncertainty of the RT Calculation

As discussed in the first section of this chapter, the RT calculations have large uncertainties which affect the BoxAMF used for profile inversion. Firstly, as a Monte-Carlo model is used, the calculated BoxAMF

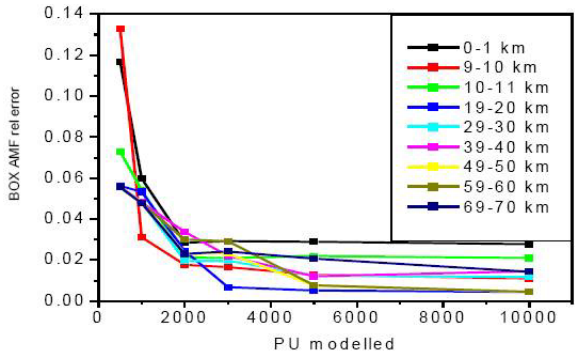

Figure 5.29: Relative error of the RT calculated BoxAMF vs. number of modeled Photon Units (PU) as function of altitude (adopted from (*von Friedeburg*, 2003)).

are subject to statistical fluctuation. Their effect can be minimized by simulating more photons which improves the statistics. *von Friedeburg* (2003) calculated the relative errors of the BoxAMFs as function of modeled photons and altitude (see figure 5.29) for the following geometry: 10 km detector altitude, -4^o elevation angle, 90^o azimuth angle relative to the sun and circular half aperture angle of 0.5^o. The relative errors of the BoxAMF is smaller than 4 % at all altitude levels if more than 2000 modeled photons contribute to the calculations. Generally, the relative error is decreasing with altitude. For the RT calculations used in this work, usually 10000 photons are modeled. So the relative errors are assumed to be < 2 % for the relevant altitudes above 10 km.

Also systematic effects arising from uncertainties of the observation geometry, aerosol profiles etc. (see section 5.1) affect the accuracy of the calculated BoxAMF. However, no error is assumed for the BoxAMF in the following quantitative error analysis.

Error of the Retrieved Profile

The error of the profile retrieval is calculated according to equation 3.65 based on the DOAS retrieval error and the assumed a priori covariance. This error contribution is further called "retrieval error". As shown above, neither the a priori and nor its covariance significantly affect the profiles in the altitudes of interest, so the statistical profile retrieval error is determined by the statistical DOAS retrieval error. Additionally, the above mentioned systematic effects affect the accuracy of the retrieved profiles and have to be treated separately. The effect of the uncertainty of the cross section (dSCD error) and the solar reference offset (offset error) can be accounted for by calculating two sets of SCDs one with and the other without considering the respective uncertainty. The difference of the profiles retrieved with these SCDs is a measure of the impact of the respective error on the retrieved profile.

A quantitative analysis of these effects is shown in figures 5.30 and 5.31 for example profile inversions of O_3, NO_2, BrO, and O_4. Qualitatively, the altitude dependence of the individual error contributions is similar for the retrieved profiles and measured SCDs. For the O_3 profile inversion, the total relative error is rather small and also constant throughout the stratosphere with values around $5-6$ % in the $11-30$ km altitude range. The most dominant contributions are the systematical uncertainties (dSCD and offset errors), the statistical retrieval error is < 1 % in the mentioned altitude range. For altitudes below, the relative offset error is strongly increasing as the absolute concentrations are decreasing causing total uncertainties up to 50 % at 7 km. For lower altitudes, the measurements are no more sensitive to O_3 indicated by averaging kernels $\ll 1$ and, hence, the retrieved profiles are mostly determined by the a priori. So these altitudes are not considered in the plotted profiles and error analysis. For the NO_2 profile inversion, the qualitative picture is similar, but the absolute numbers of relative errors are

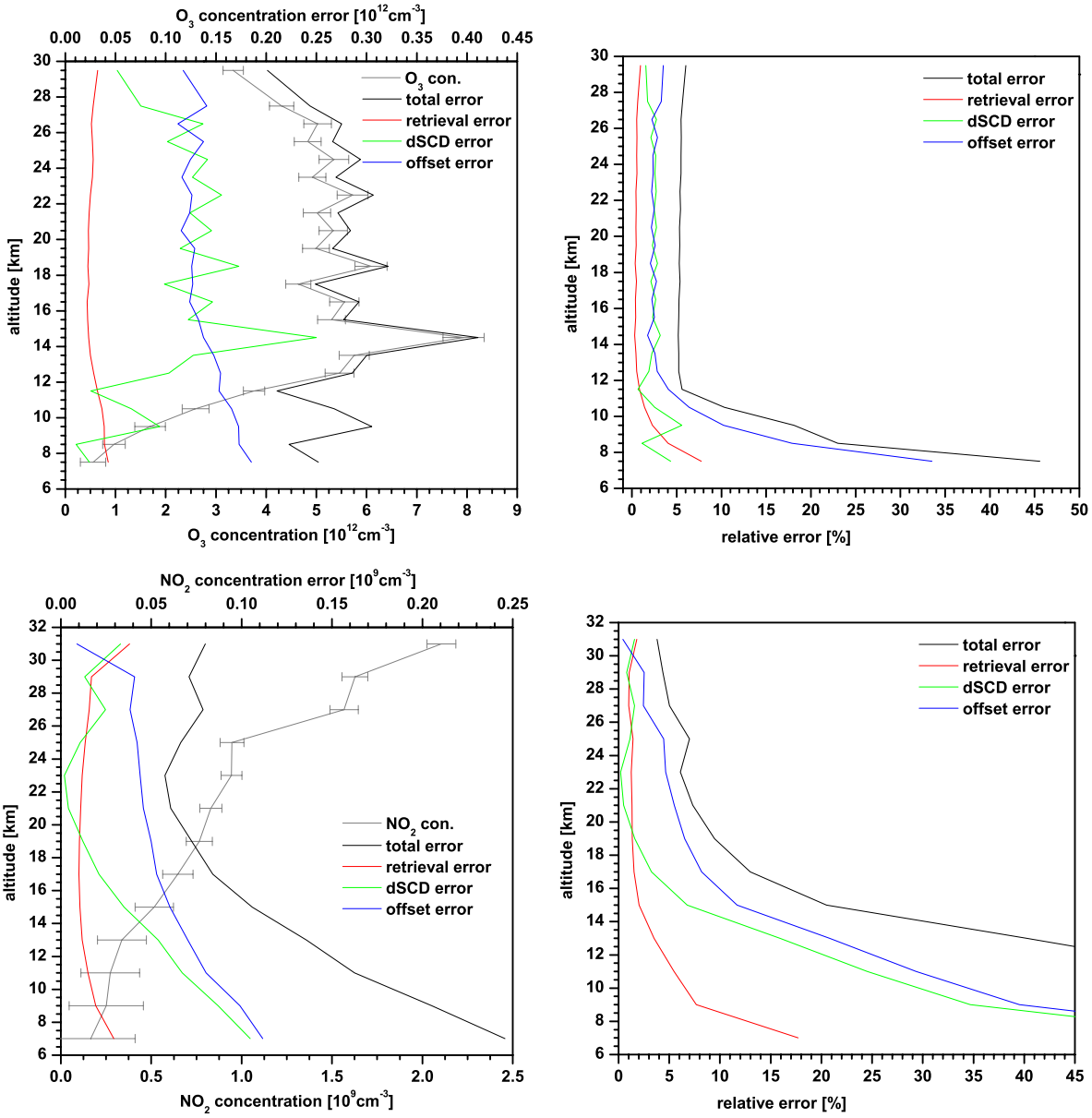

Figure 5.30: Absolute (left panels) and relative errors (right panels) of the retrieved O_3 (upper row) and NO_2 (lower row) profile vs. altitude (for a definition of the individual error contributions see text). Also shown in the left panels are the retrieved profiles and their total errors as error bars vs. altitude (gray lines).

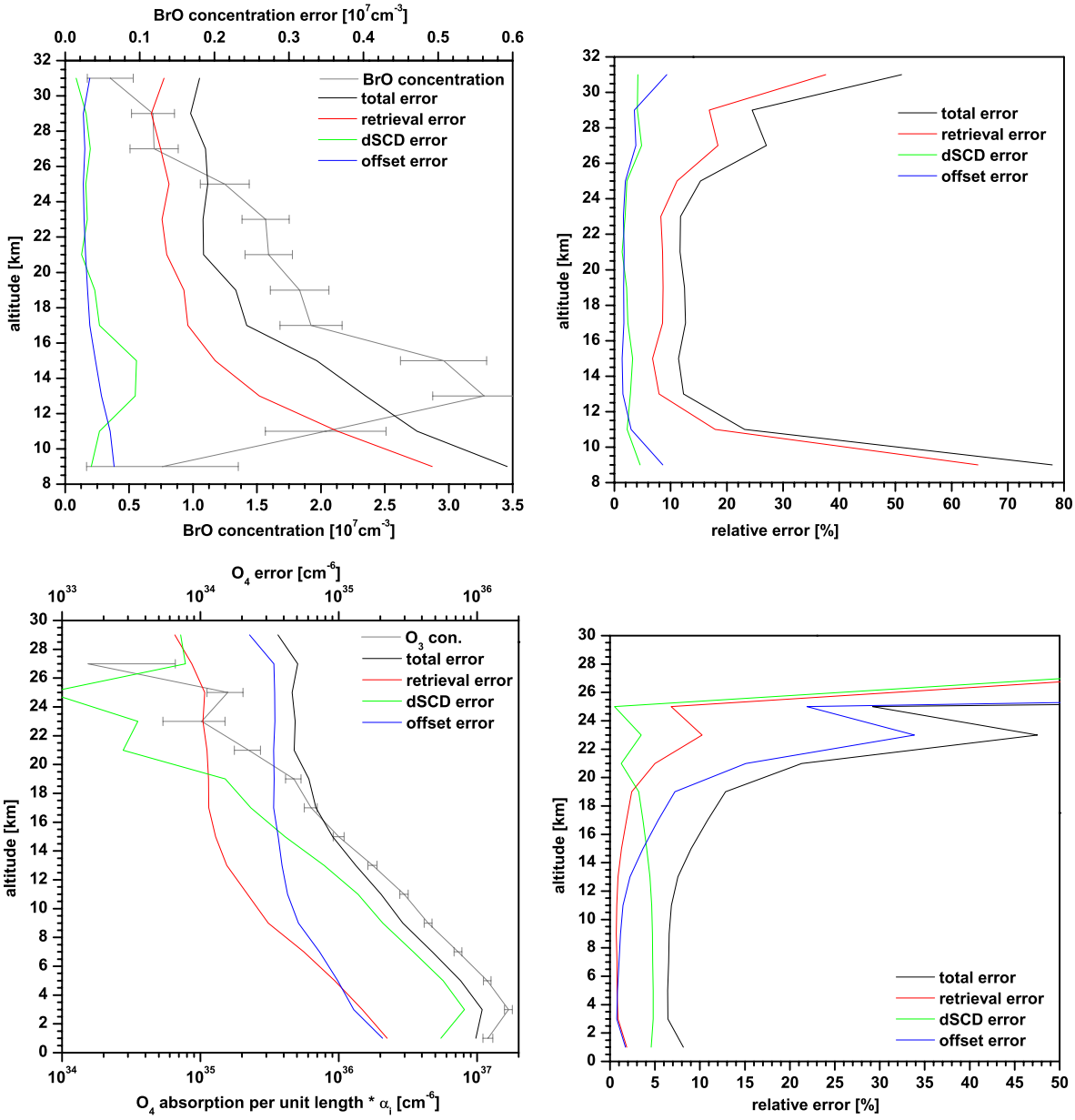

Figure 5.31: Same as figure 5.30 but for a BrO (upper row) and O_4 (lower row) profile retrieval.

higher. In the upper stratosphere (above ~ 19 km in this case) where appreciable NO_2 concentrations are measured, the total errors are < 10 % which is sensitivity comparable to that of O_3. With decreasing altitude, the systematical uncertainties are strongly increasing, e.g. for the $14 - 16$ km layer, a total error of 20 % is found, but its value is exceeding 100 % for the lowermost considered altitude layer (i.e. $6 - 8$ km). The error of the BrO retrieval is dominated by the retrieval error originating from the statistical error of the DOAS retrieval. The total relative error is around $10 - 15$ % in the $12 - 26$ km range, i.e. for altitudes with appreciable BrO concentrations. Above, the relative errors are increasing as the BrO concentrations are further decreasing. For altitudes below 12 km, the total error is significantly increasing due to the poor signal to noise ration (decreasing BrO concentrations, but increasing residuals due to low light and instrumental instabilities). Totally opposite is the situation for the profile inversion of the (mostly) tropospheric absorber O_4. In the troposphere and lower stratosphere up to 15 km, the most dominant error contribution is given by the systematic DOAS uncertainty (dSCD error). The assumed 5 % dSCD error yield ~ 5 % error of the retrieved profile as the total SCD is predominantly given by the dSCD. The offset and also the statistical retrieval error do not play an important role at low altitudes. Above 15 km, the offset, and thus its error, becomes the most important contribution. With exponentially decreasing O_4 concentrations, the relative error is dramatically increasing, and the measurements become mostly insensitive to O_4 above ~ 22 km, indicated by highly fluctuating retrieved O_4 absorptions with relative errors > 50 % and by decreasing averaging kernels.

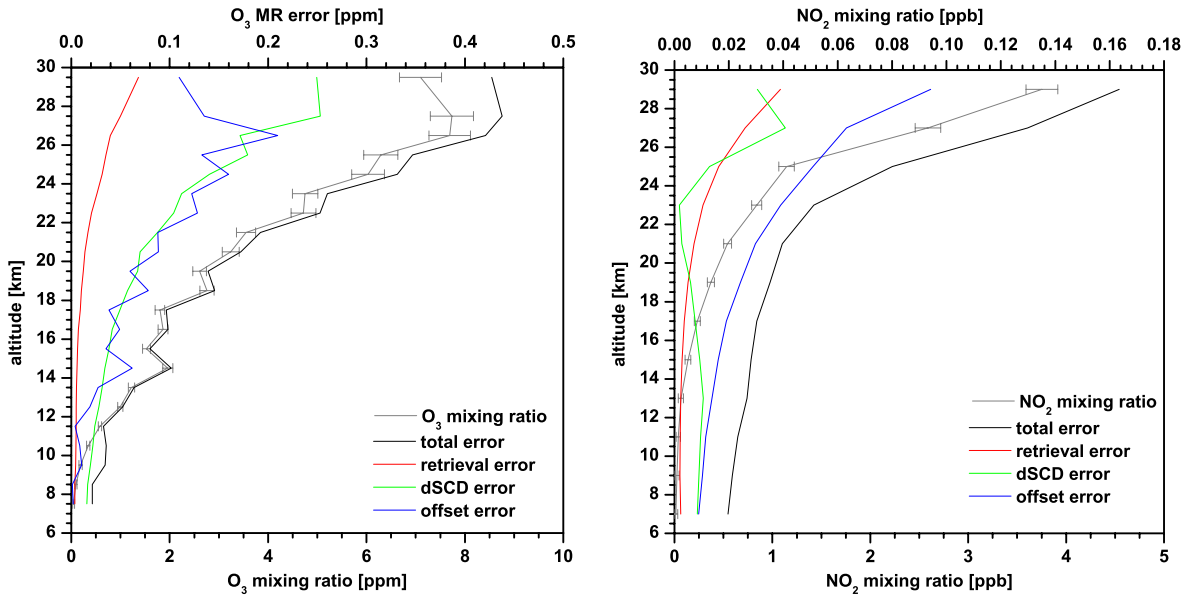

Figure 5.32: Absolute errors of the retrieved O_3 (upper row) and NO_2 (lower row) mixing ratio profile vs. altitude (for a definition of the individual error contributions see text). Also shown in the left panels are the retrieved mixing ratio profiles and their total errors as error bars vs. altitude (gray lines).

Finally, O_3, NO_2, and BrO concentration profiles are converted to mixing ratio (MR) and errors on the mixing ratio scale are estimated. Therefore, the retrieved concentrations (con) at each altitude layer are divided by the layer's average air density N (i.e. air molecules per volume V) obtained from the pressure and temperature measurements under the assumption of the ideal gas equation:

$$N = \frac{p\,V}{k_B\,T},\ (k_B = 1.38 \cdot 10^{-23}\,\mathrm{J/K}) \tag{5.2}$$

$$MR = \frac{con}{N}. \tag{5.3}$$

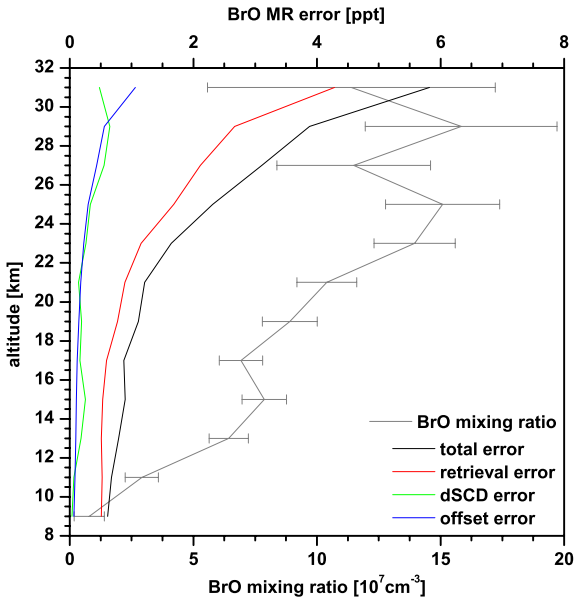

Figure 5.33: Same as figure 5.32, but for a BrO mixing ratio profile.

From this definition, it is clear that the relative errors are the same on the concentration and mixing ratio scale. However, as the air density N is decreasing exponentially with altitude and the measurement uncertainties are approximately constant on a concentration scale for most of the stratosphere for the mentioned trace gases, the mixing ratio error is usually larger at higher altitudes. For O_3 the estimated total error is ~ 0.1 ppm in the lower and ~ 0.4 ppm in the upper stratosphere for the simulated case. For NO_2 total errors are between $0.02 - 0.04$ ppb below 20 km and ~ 0.16 ppb at 30 km. However, the mixing ratios are also increasing in the same way in both cases so that the relative errors are constant (for O_3) and even decreasing with altitude (for NO_2), as shown before. For BrO, the mixing ratios are approximately constant above ~ 22 km in the simulated case while the concentrations are, consequently, strongly decreasing in that altitude range. Therefore, the total mixing ratio uncertainty also increases with altitude with numbers between ~ 1 ppt below 20 km and ~ 5 ppt around 30 km.

Chapter 6

Results and Discussion

6.1 Flights and Observations

Table 6.1 gives an overview about the 5 miniDOAS flights undertaken so far. 4 of them were performed at high-latitudes (1 in summer and 3 in winter) and 1 flight at mid-latitudes fall conditions. Also given is the configuration of the instrument and the observation modes (for a description see previous chapter, i.e. section 4.3) applied during the flight. During the first flight of the Kiruna 2003 campaign (i.e. the flight on March, 4), the sealing of the spectrometers was leaking, causing some humidity to enter the spectrometers during balloon ascent. Although the instrument worked well during the flight and the retrieved trace gas data looks reasonable, some intriguing features are observed in the DOAS analysis which are most likely due to water contamination on the detector. Considering this uncertainty, the results are not discussed here. The results obtained during the other 4 flights are presented in detail in the following sections. The measured quantities are compared to correlative measurements by other instruments and to simulations with the RTM TRACY. For clarification please note the following. Although always denoted in the figure captions which instrument the respective results are obtained with, two abbreviations are used for the in-figure legends: the term 'measurements' alone always refers to miniDOAS limb measurements, and the term 'DOAS' alone stands for the larger direct sunlight DOAS spectrometer.

6.2 The LPMA/miniDOAS Flight from Kiruna, August $18/19^{th}$, 2002

6.2.1 Flight Conditions

The first application of the miniDOAS instrument took place at high-latitudes aboard the LPMA gondola. Like all high-latitudes flights, it was launched from Esrange near Kiruna in northern Sweden. Esrange is a satellite, rocket and balloon research facility operated by the 'Swedish Space Corporation' (SSC[1]) and the balloon launches are performed by a cooperation of SSC and the French 'Centre Nationale des Etudes Spatiales' (CNES[2]). Esrange is situated at 67.9^o northern latitude and 21.1^o eastern longitude. The flight took place on August $18/19^{th}$, i.e. at the end of summer at the time of

[1] for more details see their website http://www.ssc.se
[2] for more details see their website http://www.cnes.fr

Table 6.1: Compendium of balloon-borne miniDOAS measurements

Date Time (UT)	Location	Geophys. Cond. SZA range	Instrument	Observation Mode
Aug. 18/19, 2002 15:15 - 2:38	Kiruna 67.9^{o}N, 21.1^{o}E	high-lat. sum. 69.75^o – 94.4^o 94.6 – 88.1^o	LPMA/ miniDOAS	nadir fixed limb
March 4, 2003 12:55 - 15:25	Kiruna 67.9^{o}N, 21.1^{o}E	high-lat. spring 77.6^o – 88.8^o	LPMA/DOAS miniDOAS	nadir fixed limb
March 23, 2003 14:47 - 17:35	Kiruna 67.9^{o}N, 21.1^{o}E	high-lat. spring 78.9^o – 94.7^o	LPMA/DOAS miniDOAS	nadir fixed limb during ascent scanning limb at float
Oct., 9, 2003 15:39 - 17:09	Aire-sur-l'Adour 43.7^{o}N, 0.25^{o}W	mid-lat fall 66^o – 88^o	LPMA/DOAS miniDOAS	nadir fixed limb
March, 24, 2004 13:55 - 17:35	Kiruna 67.9^{o}N, 21.1^{o}E	high-lat. spring 72^o – 98^o	LPMA/DOAS miniDOAS mk.2	fixed limb during ascent scanning limb at float
November, 2004 [1]	Teresina, Brazil 5.1^{o}S, 42.8^{o}W	tropics –	LPMA/DOAS miniDOAS mk.2	direct sunlight

[1] flight canceled, only groundbased measurements exist

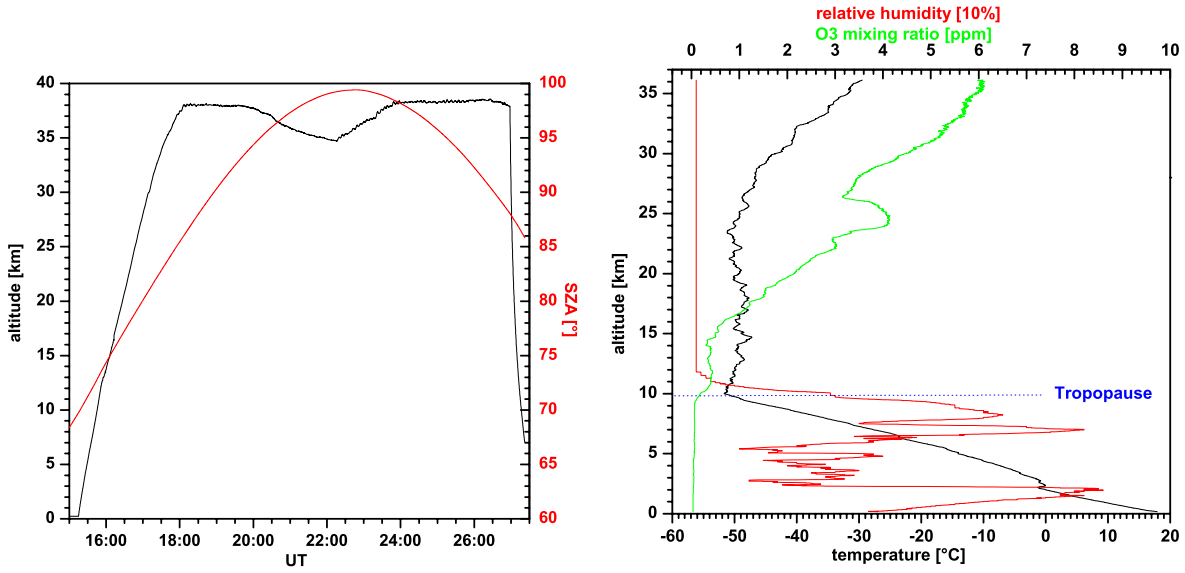

Figure 6.1: Left panel: altitude (black line) and Solar Zenith Angle (SZA, red line) vs. Universal Time (UT). Note that times $> 24\,\mathrm{hours}$ refer to August 19^{th}). Right panel: results from the ozone sonde launched from Esrange on August 18^{th}. Shown are the temperature (black line), relative humidity (red line), and the ozone mixing ratio (green line). The approximate height of the tropopause ($\sim 10\,\mathrm{km}$) is shown in blue dots.

the 'turn-around' between stratospheric summer and winter circulation, i.e. from easterly to westerly winds. During the turn-around, the stratospheric dynamics are characterized by very weak winds from arbitrary directions, i.e. no direction is preferred. As a result, the gondola landed only ~ 150 km away from the Esrange base. The altitude profile of the flight together with the Solar Zenith Angle (SZA) are shown in figure 6.1 (left panel). The gondola was launched at 15:15 UT at SZA=69.8^o. After ~ 2 h50 min, around 18:05 UT at SZA=85.9^o, the float altitude of ~ 38 km was reached. The balloon remained at this constant altitude until ~ 20 UT corresponding to an SZA of 94.5^o. Afterwards, the balloon descended to an altitude of ~ 35 km at 22:15 UT due to cooling of the helium in the absence of sunlight. After ballast was dropped, the balloon ascended again and the float altitude of 38.2 km was reached again at 0 UT at SZA=98.1^o so that the sunrise measurements could be performed at a constant balloon altitude. At 2:58 UT and SZA=88.1^o, the gondola was cut and landed ~ 150 km south of the base. In figure 6.1 (right panel), the results of the ozone sonde, launched ~ 3 h after the LPMA-balloon from Esrange, are shown. Plotted are temperature, O_3 mixing ratio and relative humidity vs. altitude. From these measurements, the tropopause height is determined to ~ 10 km. From the relative humidity profile it can be assumed that there was a cloud layer around 2 km and a second one between $7 - 9$ km.

6.2.2 Instrument Performance

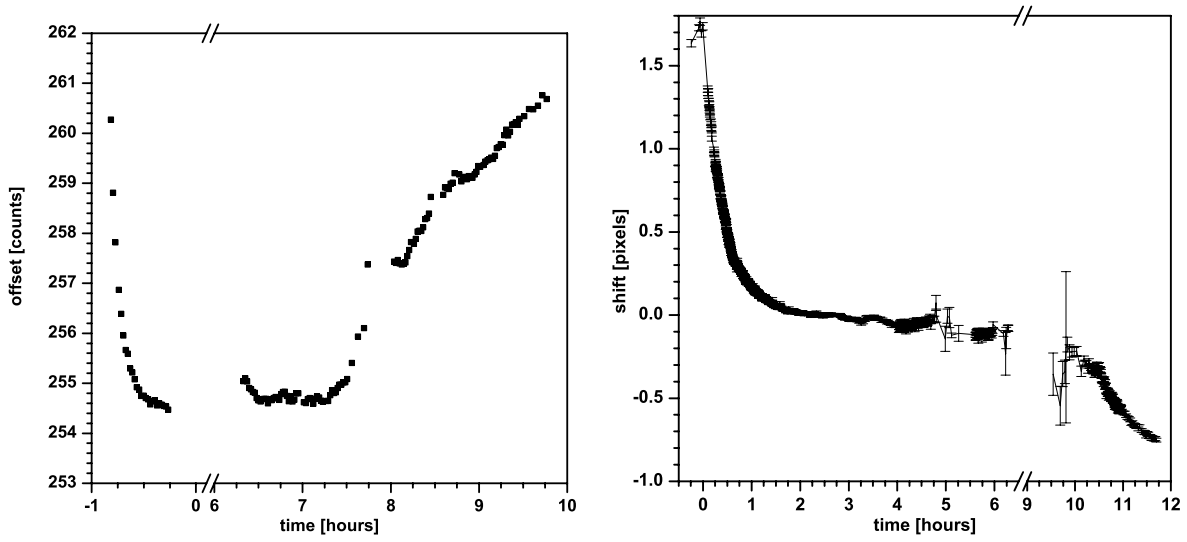

Figure 6.2: Left panel: electronic offset level (as a proxy for the spectrograph temperature) as function of time ($t = 0$ marks the launch time of the balloon). Right panel: spectral shift of the spectra relative to the solar reference recorded at float at $t = 2.75$ h.

Being the first flight, it was interesting to see how well and stably the instrument operated under 'real', i.e. stratospheric, conditions. From the software side, the instrument performed as expected. During this flight, the XDOAS package (*Grassi*, 2002) under Linux was used for the only time. The automatic saturation level determination recorded more than 1000 well saturated spectra before sunset. After the radiance became too low (around SZA$\approx 95^o$), the instrument switched into the 'night mode' measuring dark current and electronic offset spectra. At sunset, i.e. when the intensity exceeded a certain level, it switched again into nominal measurement mode for sunset measurements. Some few spectra were lost due to communication problems. The reason for this abnormalities remains unclear being one of the reasons why the use of XDOAS was discontinued. Another important issue is the optical stability of the instrument. It can be checked by looking at the spectral shift of the measured spectra relative to a

solar reference spectrum shown in figure 6.2 (right panel). The solar reference spectrum was recorded around 18 UT shortly after the float altitude of ~ 38 km was reached. The relative shift is maximum for the spectra recorded at ground level and decreases with decreasing altitude difference and, thus, pressure difference between the two spectra. ~ 1 h after the launch, i.e. at an altitude of ~ 20 km and a pressure of ~ 60 hPa, the relative shift drops below 0.1 pixels and remains below this value until the end of the sunset ~ 3 h later. This is an indication that the temperature stabilization worked well up to this point (~ 6 h after the launch). After sunset, the relative shift is ~ 0.25 pixels and increases to ~ 0.75 pixels indicating that the temperature stabilization was not perfect anymore. The temperature inside the spectrograph can also be checked by looking at the electronic offset. The electronic offset recorded before the launch and during night at balloon float is shown in figure 6.2 (left panel). After ~ 15 min, a constant offset value and, thus, temperature is reached. The same offset value is measured for the first hour after sunset indicating that the temperature stabilization was very good for about 7.5 h. Afterwards, the offset values increase by 6 counts during the next 2.5 h. This increase corresponds, roughly estimated, to a 1 K decrease in temperature of the spectrograph. This can be explained by the fact that all the liquid water was either frozen or evaporated by then. The frozen ice does not remain at a constant temperature of 0^oC but cools down as the surrounding temperature was around -25^oC at float altitude. The residuals of the DOAS fit in the O_3 retrieval region ($490 - 520$ nm) are around $1 \cdot 10^{-3}$ for the ascent and $2 \cdot 10^{-3}$ during sunset and sunrise.

As the stepper motor was not yet implemented for this first flight, the limb telescope was kept at a constant elevation angle of $\sim -3^o$ and azimuth angle of 90^o to the sun. This elevation angle was chosen because the limb radiances are very low for 0^o elevation at 38 km. However, this elevation angle was not a really wise choice as the measurements become more sensitive to elevational oscillations of the gondola and the BoxAMF are smeared out over a wider altitude range. Thus, the profile inversion problem is worse conditioned compared to an elevation angle around 0^o which was, consequently, chosen for all the following flights.

6.2.3 O_3 measurements

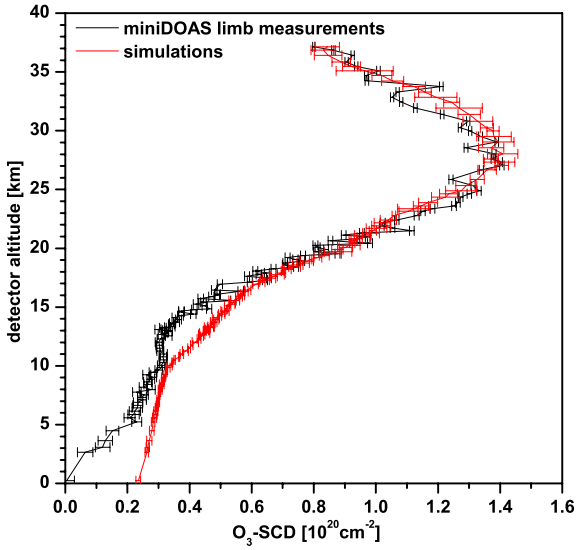

Figure 6.3: Comparison of measured (black line) and simulated (red line) O_3-SCDs during balloon ascent vs. detector altitude (=balloon altitude).

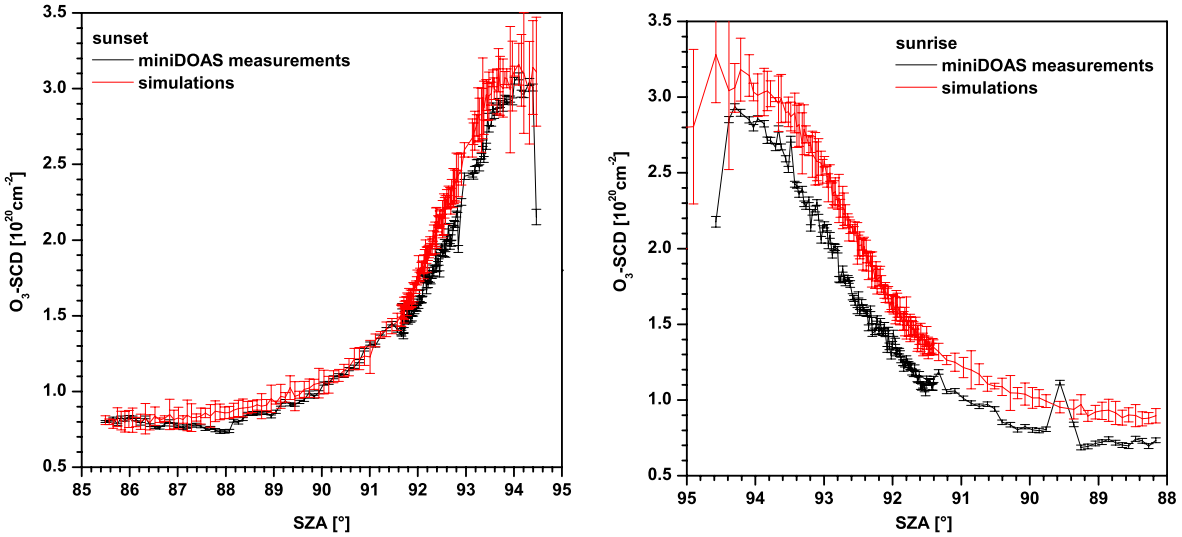

Figure 6.4: Comparison of measured (black line) and simulated (red line) O_3-SCDs at balloon float during sunset (left panel) and sunrise (right panel) vs. local SZA.

Firstly, a comparison between measured and simulated O_3-SCDs is discussed. For the simulations, the O_3-profile measured by an ECC ozone sonde launched ~ 3 h after the LPMA-balloon from Esrange is used for altitudes < 36 km. For altitudes above, the O_3-concentrations are obtained from close-by SCIAMACHY measurements (*von Savigny, pers. comm.*). As the DOAS evaluation with a convolved Kurucz spectrum as Fraunhofer reference does not work for this flight, the unknown offset of the measured dSCDs due to the O_3 absorption contained in the solar reference is determined by comparing the measured and simulated SCDs. A value of $8 \cdot 10^{19}\,\mathrm{cm}^{-2}$ is found. For the ascent measurements (see figure 6.3), a rather good agreement between the measured and simulated O_3-SCDs is observed for balloon altitudes above 15 km. For lower altitudes, the agreement is worse. An explanation could be tropospheric clouds which are not considered in the simulations or a wrongly assumed tropospheric aerosol load. During sunset (see figure 6.4, left panel), the measured and simulated SCDs match quite well over the entire observed SZA range of $85.5^o - 94.5^o$. During sunrise (see figure 6.4, right panel), the measured SCDs are systematically lower than the simulated ones, however, the qualitative trend is the same. The O_3-profile used for the simulations was measured ~ 7 h earlier which could explain the discrepancies.

Secondly, the simulated BoxAMFs and the measured SCDs are used to obtain a vertical profile. BoxAMFs for several balloon altitudes are shown in figure 6.5 (left panel). It can be seen that the individual BoxAMF generally have a rather broad maximum. For detector altitudes up to 18 km, the maximum is reached in the box the balloon is actually in. With increasing altitude the maxima become broader, i.e. more underlying boxes contribute to the observed light path. This means that the troposphere (i.e. the altitude layers up to 10 km) significantly contributes to the observed light path. As the troposphere is more difficult to model due to the existence of clouds (which are not considered in the present simulations) this could be an explanation for the observed discrepancies between the measured and simulated SCDs. Starting with the BoxAMF for 21 km, a maximum forms at the layer of the tangent height. The tangent height is defined in this case as the lowermost layer which can be 'directly' seen by the telescope, i.e. without multiple scattering. This maximum increases with increasing balloon altitude but the altitude layers between the tangent and detector height (~ 7 km) still significantly contribute to the observed light path. It can also be seen that the maximum of the BoxAMF corresponding of the 'highest' available spectrum recorded around 37 km lies in the $29 - 30$ km layer, which means that hardly any profile information about the altitudes above 30 km is contained in the measurements. The

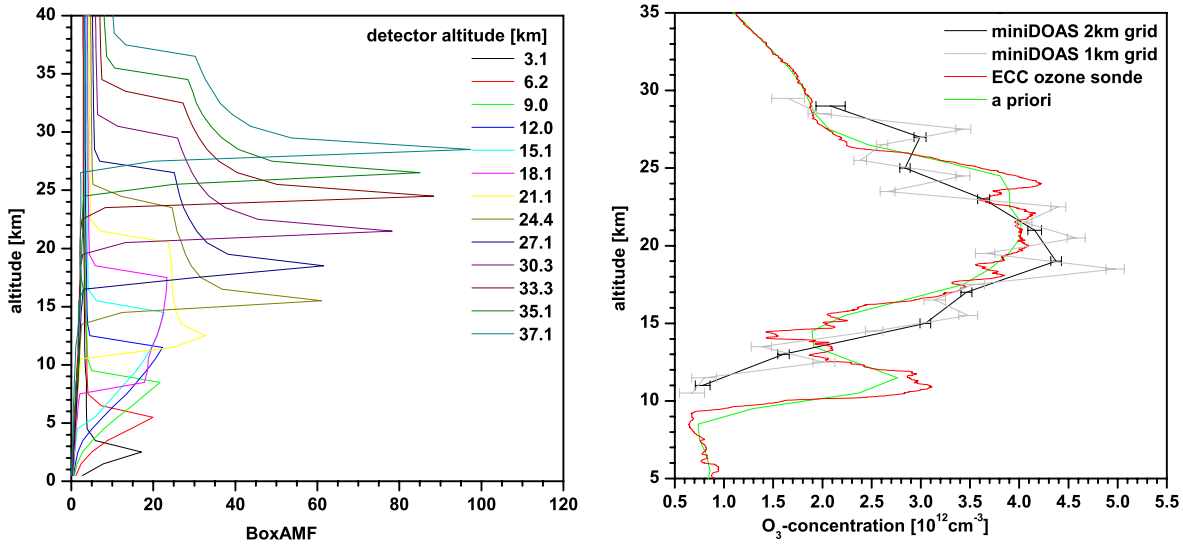

Figure 6.5: Left panel: RT calculated BoxAMFs vs. altitude for selected detector altitudes during balloon ascent. Right panel: miniDOAS O_3-profiles retrieved on a $2\,\mathrm{km}$ grid (black line) and $1\,\mathrm{km}$ grid (gray line) compared to the measurements from the ECC ozone sonde launched $\sim 3\,\mathrm{h}$ after the LPMA balloon (red line). Also shown is the a priori profile (green line) used for the retrieval.

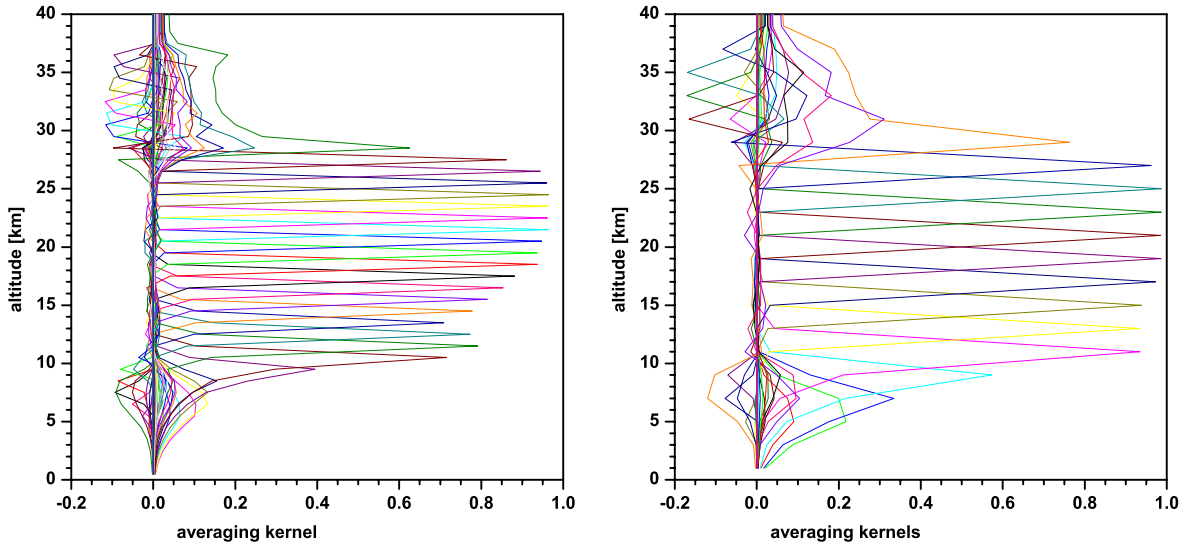

Figure 6.6: Averaging kernels for the profile retrievals shown in fig. 6.5 on a $1\,\mathrm{km}$ grid (left panel) and a $2\,\mathrm{km}$ grid (right panel), respectively.

RT calculated BoxAMF for all altitudes are inverted according to the methods described in section 3.3. The results are shown in figure 6.5 (right panel). Two profile retrievals have been performed on a 1 km and 2 km grid, respectively. The averaging kernels for both retrievals are shown in figure 6.6. The profile retrieved on a 1 km grid looks very noisy. Additionally, the averaging kernels do not reach 1 for most altitudes which means that this grid size is too narrow. The profile retrieved on a 2 km grid looks much smoother. However, the agreement with the ozone sonde profile is rather poor. There are several reasons for this. Firstly, the elevation angle, which strongly affects the measured SCDs and the tangent height of the observations, is not exactly known. This uncertainty might be the reason for the shift of the respective maxima of the two profiles. Secondly, the broad maxima of the BoxAMF cause the profile inversion problem to be worse conditioned compared to the case of a detector elevation angle around 0^o (see the next sections). For altitudes below $\sim$ 15 km, the BoxAMF show no pronounced maximum which causes a rather poor vertical sensitivity at these altitudes.

Summarizing the results from this flight leads to the conclusion that the chosen elevation angle of 3^o below the horizon was a rather unwise choice. Consequently, elevation angles around 0^o were chosen for all further miniDOAS fixed limb measurements.

6.3 The LPMA/DOAS/miniDOAS Flight from Kiruna, March 23^{rd}, 2003

6.3.1 Flight Conditions

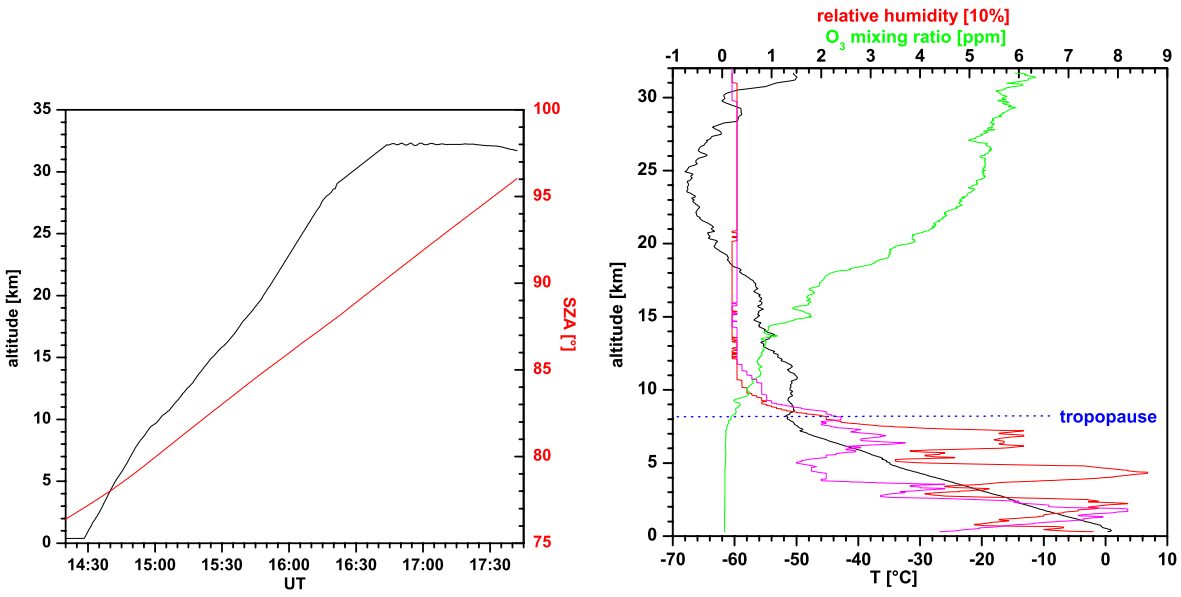

Figure 6.7: Left panel: Altitude profile of the LPMA/DOAS balloon (black line) and Solar Zenith Angle (SZA) vs. Universal Time (UT). Right panel: results of the ozone sonde launched $\sim$ 3 h after the LPMA/DOAS gondola. Shown are the temperature (black line), O_3-mixing ratio (green line), and the relative humitity (red line). For comparison, the relative humidity measured by a meteo sonde launched $\sim$ 3.5 h before the LPMA-balloon is also shown (magenta line). The approx. height of the tropopause ($\sim$ 8 km) is given with blue dots.

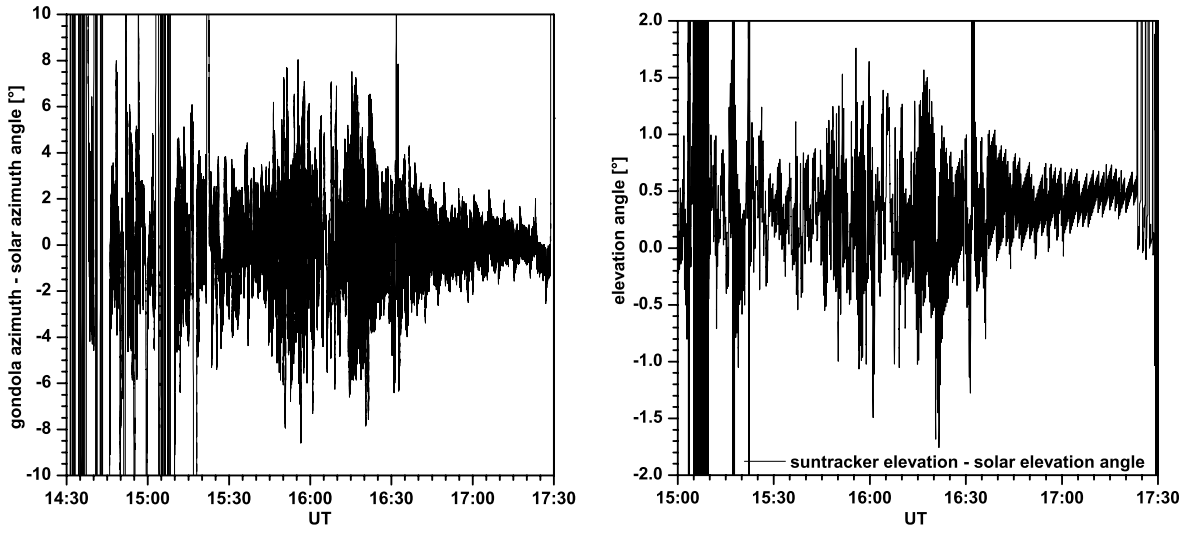

Figure 6.8: Azimuth angle of the gondola minus solar azimuth angle (left panel) and elevation angle of the suntracker minus solar elevation angle (right panel), respectively, vs. time.

The second flight of the Kiruna campaign was launched on March 23^{rd}, 2003 at 14:28 UT and SZA=77^o. The altitude profile and the corresponding SZA are shown in figure 6.7 (left panel). After 2 h15 min ascent, the float altitude of $\sim$ 32 km was reached at 16:43 UT and SZA=90.2^o. After $\sim$ 1 h at float, the balloon was cut at 17:41 UT and SZA=96^o. The results of the ozone sounding by an ECC sonde launched at 17:38 UT, i.e. $\sim$ 3 h after the LPMA/DOAS balloon, is shown in figure 6.7 (right panel). From the temperature profile, the tropopause height is estimated to 8 km. The relative humidity profile has several maxima around 2 km, 4 km, and 6 − 7 km which might be due to cloud layers. For comparison also a humidity profile measured by a meteo sonde launched in the morning at 10:56 UT, i.e. $\sim$ 3.5 h before the LPMA/DOAS-balloon, is shown. In this sounding, the humidity only has a maximum around 2 km which shows that the cloud cover was highly variable on that day.

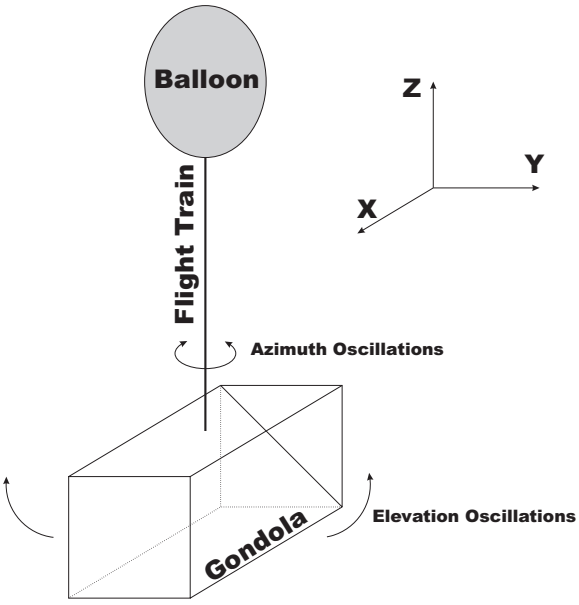

Figure 6.9: Sketch of the gondola movements.

An important aspect for limb measurements is the stability of the gondola. The gondola movements can be described with respect to three axes. It can perform rotational oscillations with respect to the z-axis given by the flight train of the balloon. These azimuthal movements are slowed by controlled countermovements of the pivot (azimuth stabilization). The gondola can also swing along the flight train in x- and y-direction. These elevational oscillations cannot be stabilized.

The absolute azimuth angle of the LPMA-gondola relative to the Earth (e.g. 0^o corresponds to North, 90^o to East etc.) is recorded by onboard instrumentation. Subtracting the local solar azimuth angle yields the azimuth angle of the gondola relative to the sun. This quantity vs. time is plotted in figure 6.8 (left panel). In the troposphere and especially in the tropopause region, the gondola was quite unstable in azimuth. Above $\sim 10\,\mathrm{km}$ (i.e. after 15:10 UT), the azimuth stabilization was very well with amplitudes of $6 - 15^o$ decreasing to $< 3^o$ towards the end of the flight. As shown in section 5.1.4, azimuth oscillations of this magnitude do not significantly affect the measurements or RT calculations.

As the sensitivity tests have shown (see section 5.1.3), the measurements are much more sensitive to elevational gondola movements. Unfortunately, the elevation of the LPMA gondola is not directly measured by onboard sensors. The only existing data about the gondola's elevational position is given by the suntracker's elevation angle. Assuming that the suntracker is perfectly locked to the sun, i.e. always pointing to the same point of the solar disk, the gondola's elevation angle can be obtained by subtracting the actual solar elevation given by 90^o-SZA from the suntracker's elevation angle. This quantity is plotted vs. time in figure 6.8 (right panel). Note that the miniDOAS limb telescope is pointing at an angle of $\sim 90^o$ relative to the sun and, thus, also relative to the suntracker so that the shown quantity does not directly give the elevational oscillation of the limb measurements. However, it can be assumed that the elevation angle of the detector is qualitatively the same. Also note that the plotted data only gives the elevation angle of the gondola, when the suntracker is locked to the sun. Before 15:10 UT, this was not the case most of the time, so no information about the elevation is available for tropospheric altitudes. Afterwards, the elevation oscillations had amplitudes of $0.5 - 1.5^o$ between $10 - 18\,\mathrm{km}$, increasing to amplitudes of $2 - 3^o$ between $18 - 28\,\mathrm{km}$, and again decreasing to 1^o for the beginning and $< 0.5^o$ at the end of the float phase. However, for the following RT calculations during ascent, it is assumed that the telescope is constantly pointing to an azimuth angle of $+90^o$ relative to the sun and to an elevation angle of 0.5 above the horizon.

6.3.2 Instrument Performance

The spectral shift and the residuals of the DOAS evaluation of O_3 and NO_2 vs. detector altitude in the $490 - 520\,\mathrm{nm}$ and $400 - 450\,\mathrm{nm}$ wavelength range, respectively, are shown in figure 6.10 . The residuals of the O_3 retrieval are pretty constant with altitude ranging between $1.1 \cdot 10^{-3}$ at low and $0.8 \cdot 10^{-3}$ at high altitudes. In the NO_2 region, the residuals are decreasing from $1.6 \cdot 10^{-3}$ at low altitudes to $0.7 \cdot 10^{-3}$. This behavior is mainly due to the lower limb radiances at low altitudes.

6.3.3 Absolute Limb Radiance Measurements

The evaluation of the measurements with regard to absolute limb radiances is done in the same way as described in section 6.5.3. In this section, only a discussion of the results is given.

The resulting calibration coefficient as function of wavelength is shown in figure 6.12. The sensitivity of the instrument is increasing between 350 and 400 nm. It is almost constant between 400 and 490 nm. In the $490 - 530\,\mathrm{nm}$ interval, the sensitivity is highly variable with a sharp maximum near 510 nm.

A comparison between measured and RT calculated limb radiances during balloon ascent is shown in figure 6.13 (left panel) for 360 nm and 490 nm. Measurements for altitudes $< 11\,\mathrm{km}$ are rejected because

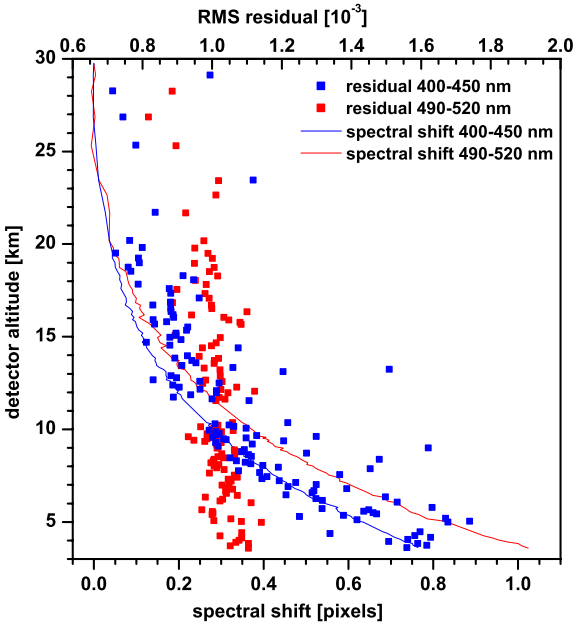

Figure 6.10: RMS residual of the DOAS retrieval of NO_2 ($400 - 450$ nm, blue squares) and O_3 ($490 - 520$ nm, red squares), and spectral shift of the spectra relative to the solar reference spectrum (blue and red line, respectively) vs. detector altitude.

the gondola was unstable. An uncertainty of the radiometric calibration of 10 % and 5 % is assumed for the radiometric calibration at 360 nm and 490 nm, respectively. Note that the measurements at 360 nm are corrected as described in section 6.5.3. The match between measurements and simulations is excellent for all (stratospheric) altitudes at 490 nm, and also for altitudes > 18 km at 360 nm. Below 18 km, the measured radiances are systematically higher than the simulated ones. The reason for this is still unclear. It is suspected that the TRACY RT calculations become incorrect for an increasing fraction of multiple scattered photons.

A comparison between measured and RT simulated limb radiance for the limb-scanning measurements at float altitude is shown in figure 6.13 (right panel) for 490 nm. The limb scans start at an elevation angle of 0.5^o above the horizon and decrease to 5.5^o below the horizon with 0.5^o step width. The altitudes given in the figure are rough geometrical estimates of the tangent height of the observation. Note that an exact knowledge of the tangent height is not necessary as the only input needed for the TRACY RT calculation is the detector position and viewing direction relative to the sun. Again, the RT simulations match very well with the measurements. Only for the first limb-scanning sequence a discrepancy is observed for the 15.5 km data point.

6.3.4 O_3 Results

In a first step, the slant column densities of ozone (O_3-SCD) are inferred from the measured spectra, and compared with the same parameter simulated by Tracy RT calculations. As input either the O_3 profile simultaneously measured on board by an Electro Chemical Cell (ECC), or by a stand-alone ECC O_3 Sonde, ~ 3 h launched after the LPMA/DOAS gondola is used. Figure 6.15 (left panel) reveals that the measured and simulated O_3-SCDs compare reasonably well, however only for the simulations using the ozone profile measured by the ECC Sonde aboard (blue line in fig. 6.15). Conversely taking the O_3 profile in the simulation measured by the stand-alone ECC Sonde (~ 3 h launched after the LPMA/DOAS payload), larger O_3 concentrations are obtained in the $12 - 21$ km height range with a

Figure 6.11: Illumination situation around the earth terminator as seen from the International Space Station (ISS).

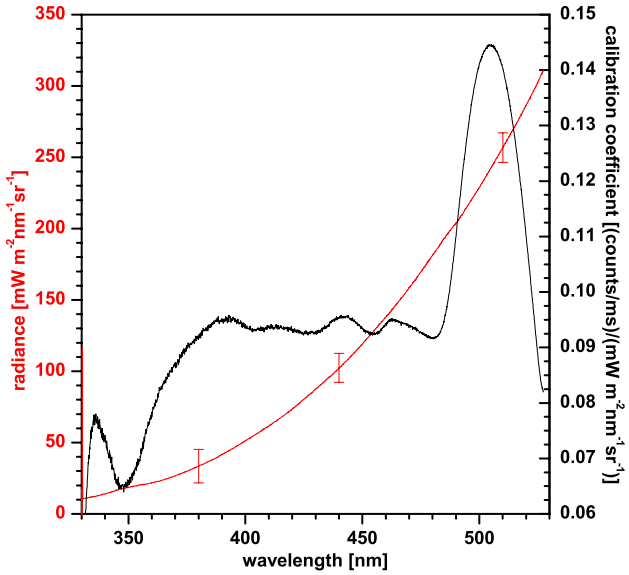

Figure 6.12: Output of the Bremen Ulbricht Sphere used for the absolute radiance calibration (red line), and determined calibration coefficient (i.e. wavelength dependant sensitivity, see section 6.5.3 for its definition) (black line).

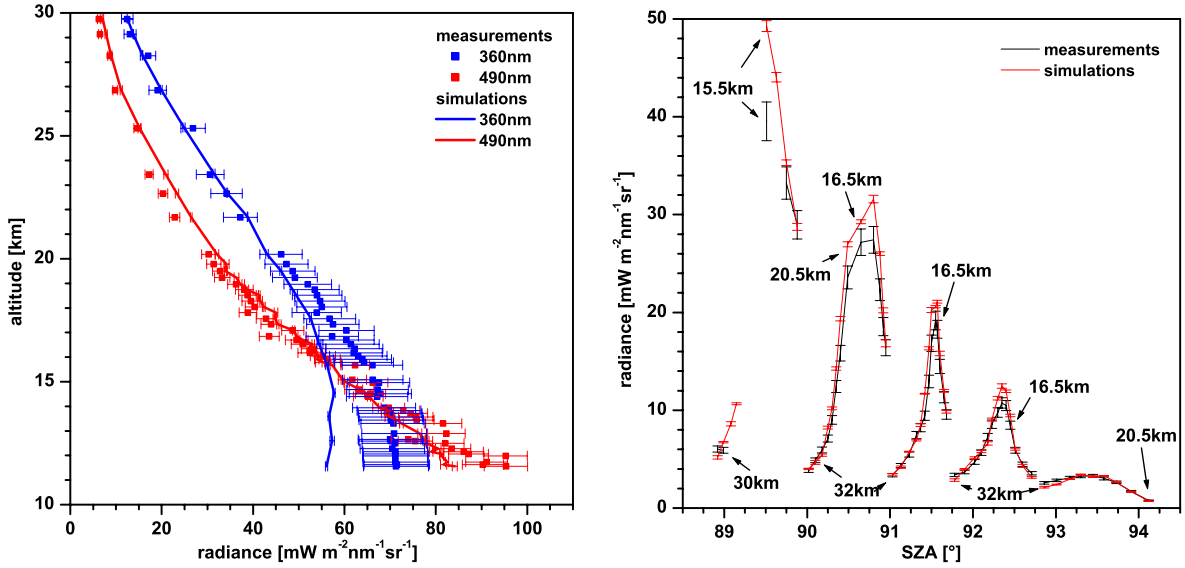

Figure 6.13: Left Panel: Comparison of measured and RT calculated limb radiances vs. detector altitude for ascent for $360\,\mathrm{nm}$ (in blue) and $490\,\mathrm{nm}$ (in red). Right panel: measured (black lines) and simulated (red lines) limb radiances vs. local SZA for balloon float in limb scanning mode for $490\,\mathrm{nm}$. The altitude labels denote the calculated tangent heights of the respective observation.

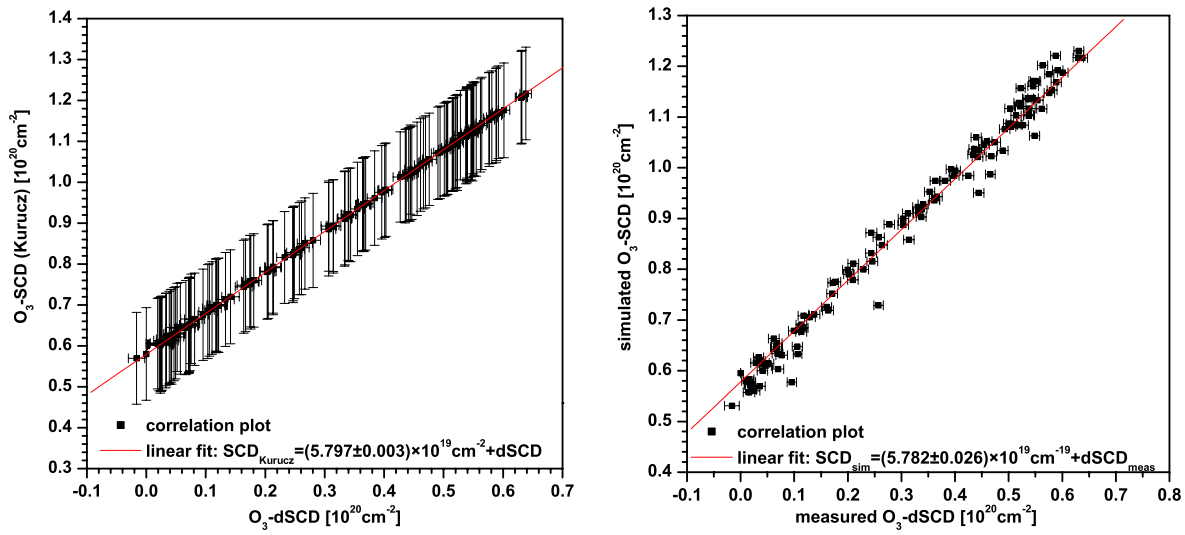

Figure 6.14: Determination of the O_3 absorption of the solar reference spectrum. Left panel: retrieved O_3-SCDs with convolved Kurucz spectrum as solar reference vs. O_3-dSCDs with self recorded solar reference (black squares) and linear fit (red line) of the correlation plot. Right panel: simulated O_3-SCDs vs. measured O_3-dSCDs (black squares) and linear fit (red line) of the correlation plot.

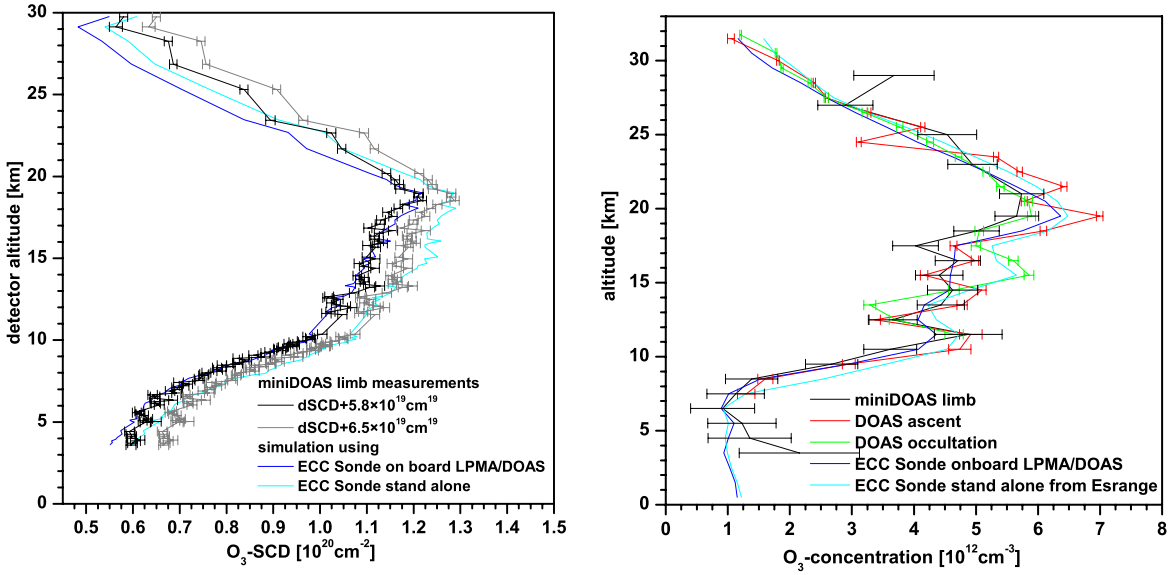

Figure 6.15: Left panel: comparison of measured and simulated O_3-SCDs in the UV and visible spectral range. For the simulations the two O_3 profile measured by the ECC Ozone Sondes (see right panel) are used. Right panel: Comparison of retrieved O_3 profiles from miniDOAS limb measurements during balloon ascent (black line), direct sunlight DOAS measurements during balloon ascent (red line), and two ECC Ozone Sondes one on board the LPMA/DOAS gondola (blue line) and one stand alone (green line).

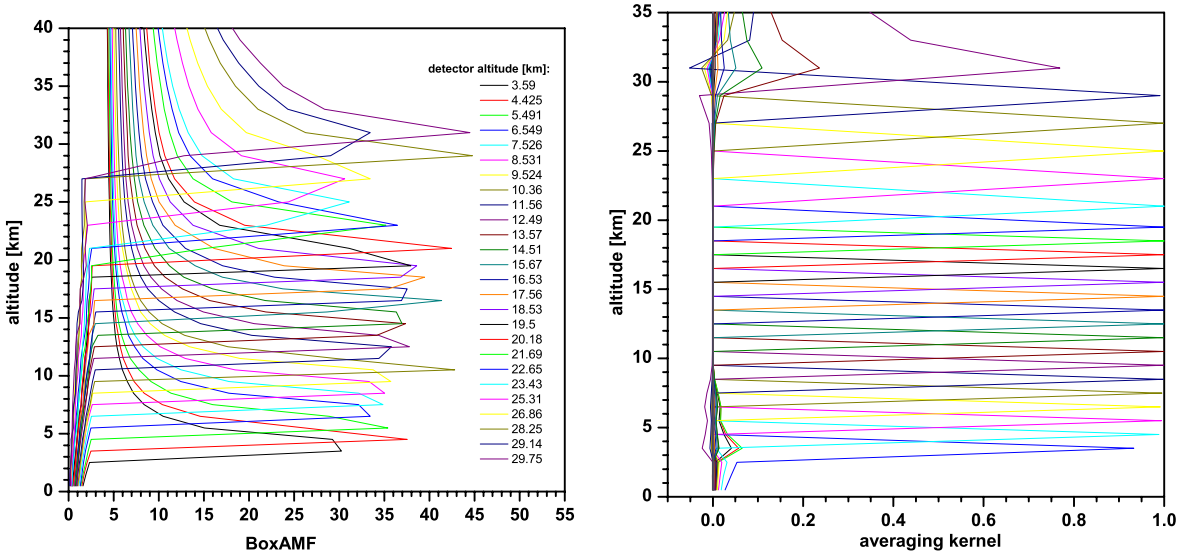

Figure 6.16: Left panel: RT calculated BoxAMF as a function of altitude. Right panel: averaging kernels of the profile inversion shown in fig. 6.15.

corresponding overestimation in the simulated O_3 -SCDs (green line in fig. 6.15). This comparison clearly demonstrates the quality of the limb O_3 measurements and its sensitivity towards the shape and O_3 concentration of the profile. A major uncertainty of the measured SCDs is given by the solar reference offset to be added to the DOAS retrieved dSCDs. Two methods for the determination of this offset value are used and compared in figure 6.14. The first possibility is to use the high resolution Kurucz spectrum convolved to the instrumental resolution as solar reference for a DOAS evaluation of the measured spectra. As the Kurucz spectrum contains no atmospheric absorption features, the DOAS fit yields the absolute SCD in this case. However, the retrieval error is much higher compared to using a self-recorded solar reference due to improperly removed Fraunhofer structures. This can be seen when comparing the error bars in figure 6.14 (left panel) for the two DOAS evaluations. Despite the large errors of the Kurucz-fit, its correlation with the DOAS results using the self-recorded reference is excellent. A linear fit of the correlation yields a value of $5.797 \cdot 10^{19}\,\mathrm{cm}^{-2}$ for the solar reference offset. The second way to determine the offset is via a correlation of the measured dSCDs to the RT simulated SCDs shown in the right panel of the mentioned figure. The correlation is also very good and yields an offset value of $5.782 \cdot 10^{19}\,\mathrm{cm}^{-2}$ which agrees excellently with the offset determined by the Kurucz fit within their uncertainties. For the following profile retrieval, an offset of $5.8 \cdot 10^{19}\,\mathrm{cm}^{-2}$ is used. To estimate the error arising from the offset uncertainty, a second profile is retrieved with an offset value of $6.5 \cdot 10^{19}\,\mathrm{cm}^{-2}$ and the difference of the two profiles is added to the profile retrieval error (for details on the error calculation, see section 5.2.4). As can be seen in figure 6.15 (left panel), adding $6.5 \cdot 10^{19}\,\mathrm{cm}^{-2}$ to the measured dSCDs yields an SCD-profile which matches well the simulations using the stand-alone ECC-sonde as input. Note that the error bars shown in that figure only include the statistical DOAS error but no systematical DOAS error arising from uncertainties of the cross section or the offset determination.

In a second step, the measured O_3-SCDs are mathematically inverted into an O_3 profile (see fig. 6.15, right panel), using RT simulated Box Air Mass Factors (BoxAMF, see fig. 6.16, left panel) for each observation, and the inversion routines described in section 3.3. Overall, a good agreement is found between the inferred limb O_3 profile and the simultaneously measured O_3 profiles either from the aboard ECC sonde or from the direct sun DOAS observations indicating the feasibility of the balloon-borne limb method. The large sensitivity for upper tropospheric and lower stratospheric trace gas detection is also indicated by the averaging kernels (see fig. 6.16, right panel) which attain a value close to unity within the $4 - 30\,\mathrm{km}$ height range on a 1 km altitude grid below 20 km and 2 km above 20 km. The lower altitude resolution above 20 km is chosen because there are much less measurement points due to the lower limb radiances in this altitude range (~ 100 measurements in the $3.5 - 20\,\mathrm{km}$ range vs. ~ 10 measurements in the $20 - 30\,\mathrm{km}$ range).

6.3.5 NO_2 Results

The NO_2 profile retrieval is done in the same way as for O_3. The NO_2 absorption of the solar reference is done by a correlation of the measured NO_2-dSCDs with simulated NO_2-SCDs using the direct sunlight DOAS profile (see figure 6.17, left panel). A value of $2.28 \cdot 10^{16}\,\mathrm{cm}^{-2}$ is found and added to the measured dSCDs. Using this offset value, the measured SCDs compare excellently to the RT simulated SCDs (see figure 6.17, right panel). An uncertainty of 5 % is assumed for this offset value and used for the calculation of the error of the retrieved profile arising from this uncertainty (for details of the error calculation, see section 5.2.4). No systematical cross section uncertainty is assumed for this comparison as the same cross sections are used by both methods (i.e. miniDOAS limb and solar occultation DOAS).

Fig. 6.18 (left panel) shows a comparison of the NO_2 profiles for the balloon ascent inferred from miniDOAS limb (black line) and direct sunlight DOAS (red line) measurements. Generally, the two profiles compare excellently, especially from 20 km down to 7 km. Above 20 km the two profiles show

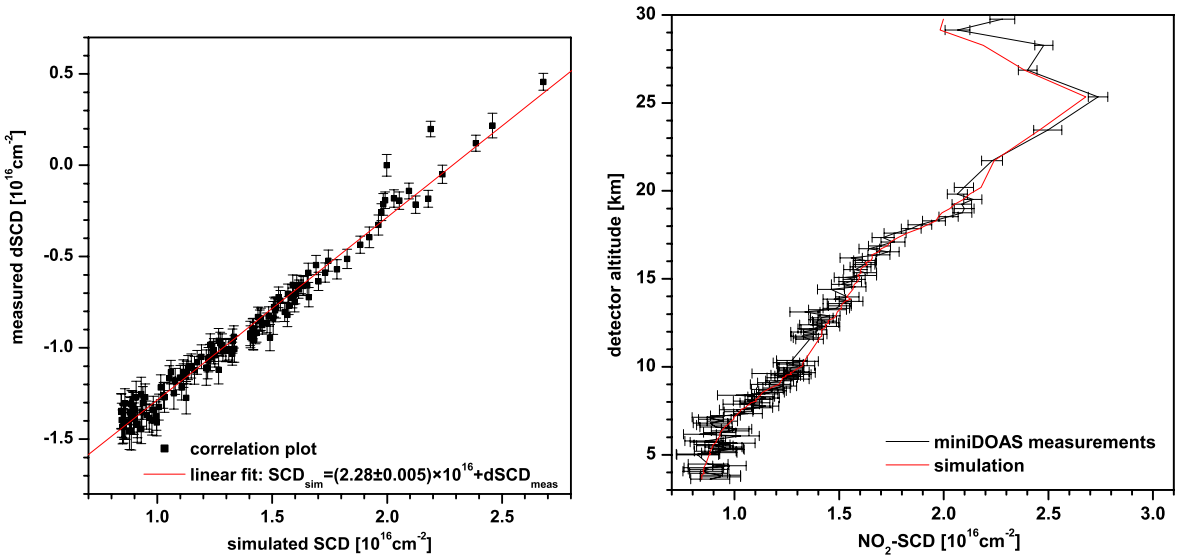

Figure 6.17: Left panel: Determination of the NO_2 absorption of the solar reference spectrum. Shown are the measured NO_2-dSCDs vs. simulated NO_2-SCDs (black squares) and a linear fit (red line) of the correlation plot. Right panel: Comparison of the measured NO_2-SCDs (black line) and simulated NO_2-SCDs (red line) using the DOAS ascent profile as input.

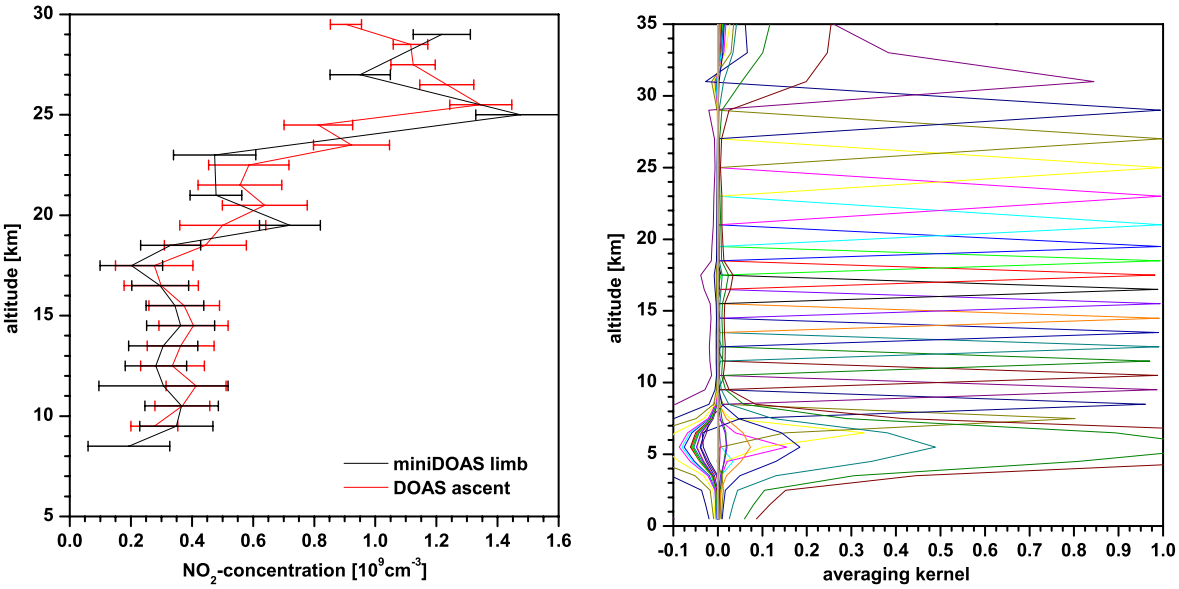

Figure 6.18: Left panel: comparison of retrieved NO_2 profiles from miniDOAS limb measurements (black line) and direct sunlight DOAS measurements during balloon ascent (red line). Right panel: averaging kernels for the shown miniDOAS profile retrieval.

some discrepancies which may be due to the low numbers of limb measurements which cause some fluctuations in the miniDOAS profile. However, this finding demonstrates the equally large sensitivity of the balloon-borne ascent limb measurement compared to the solar occultation technique. It is a result of the trade of the larger sensitivity of the direct sunlight measurement (i.e. lower residual/error of the DOAS evaluation) compared to the limb spectroscopy due to the much higher number of analyzed photons, and the higher air mass factors of the limb measurements (up to ~ 50 in the limb case for the altitude layer the balloon is in vs. $1/\cos(\mathrm{SZA}) \approx 6$ for SZA$\approx 80^o$ in the direct sunlight case) and, thus, the better conditioning of the inversion problem.

6.3.6 O_4 Results

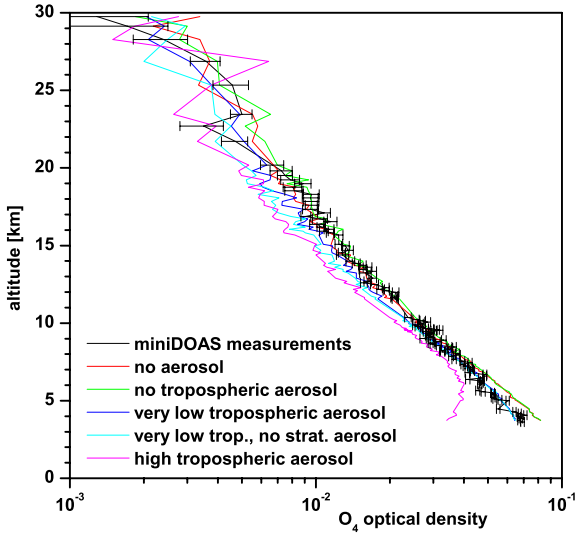

Figure 6.19: Measured O_4 optical densities (OD, black lines) compared to simulations (colored lines) using different tropospheric aerosol scenarios (left panel). For details of the aerosol scenarios see section 5.1.5.

For the O_2-O_2 dimer (O_4), the absorption cross section σ is not known. The only available experimental data from literature is the pair absorption cross section α which is defined as the O_4 absorbance per unit length (ε) over the O_2 concentration squared:

$$\alpha(T) = \frac{\varepsilon(T)}{[\mathrm{O_2}]^2} = \sigma \cdot K_{eq}(T), \tag{6.1}$$

where σ is the (unknown) O_4 absorption cross section and K_{eq} is the (also unknown) O_4 equilibrium constant. It is assumed that σ is independent of temperature (*Johnston et al.*, 1984) and, thus, the T-dependance of α arises only from the T-dependance of K_{eq}. As the band shapes do not change with T and p, and the T-dependence is rather weak (about 11 % for $\Delta T = 50\,\mathrm{K}$) (*Pfeilsticker et al.*, 2001), the O_4 pair absorption cross section measured by *Hermans* (2002) at room temperature is used for the DOAS evaluation.

O_2 has a constant mixing ratio of $\sim$ 21 % up to very high altitudes ($> 60\,\mathrm{km}$). Accordingly, the O_2 concentration $[O_2]$ can be calculated by $[O_2] = 0.2094 \cdot p/(k \cdot T)$. As the concentration of O_4 is proportional to the known O_2 concentration squared, the O_4 measurements can be used to investigate the length of the light path through the atmosphere. In our case, the RT modeled BoxAMFs are multiplied with a squared O_2 concentration profile (see figure 6.20, left panel) and multiplied by the peak

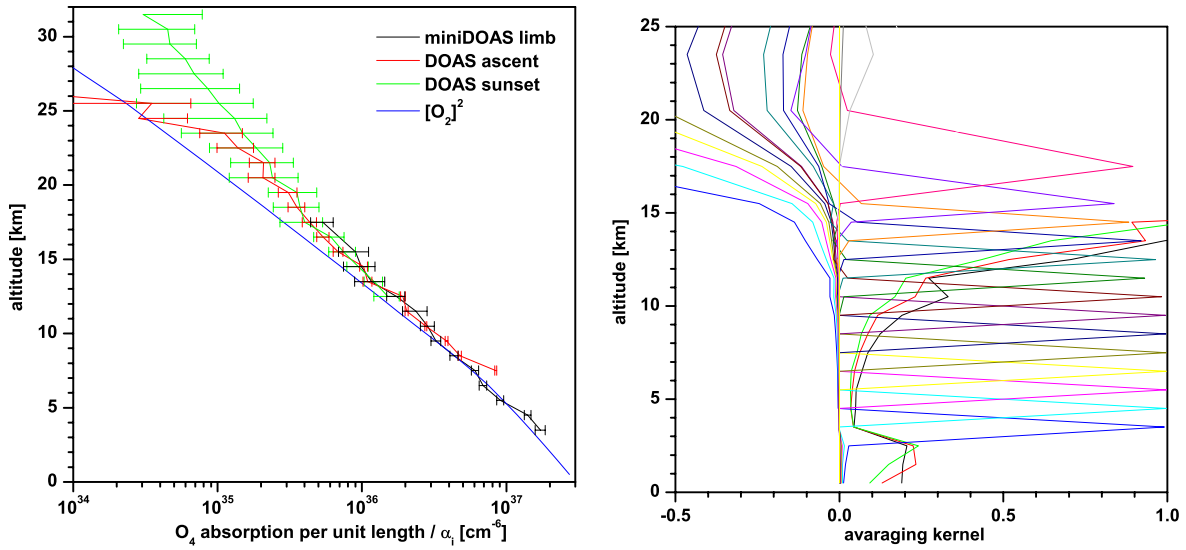

Figure 6.20: Left panel: O_4 absorption profile retrieved from miniDOAS limb measurements (black line) compared to the profiles retrieved from direct sunlight DOAS measurements during balloon ascent (red line) and solar occultation (green line). Shown is the O_4 absorption per unit length multiplied by the peak O_4 collision pair absorption cross section α_i. For comparison, the O_2-concentration squared ($[O_2]^2$, blue line) is shown. Right panel: Corresponding averaging kernels for the miniDOAS O_4 profile retrieval.

O_4 collision pair absorption cross section α_i of the O_4 absorption band used for the DOAS evaluation. This quantity can be compared to the measured O_4 optical densities (OD). In a second step, the calculated BoxAMFs are used to retrieve a vertical O_4 absorption profile. Dividing the retrieved O_4 absorption per unit length for each altitude layer by α_i yields the O_2-concentration squared. As the O_4 concentration decreases exponentially with altitude, the O_4 measurements are especially sensitive to the troposphere while their sensitivity decreases with altitude.

Figure 6.19 shows a comparison of the measured O_4 ODs as a function of detector height compared to simulations of the same quantity for several aerosol scenarios as described in section 5.1.5. It can be seen that stratospheric aerosol does not affect the O_4 ODs significantly (e.g. by comparing the red and green lines or the blue and cyan lines, respectively). Tropospheric aerosol, however, significantly shortens the light path at lower altitudes. The plot reveals that assuming a high tropospheric aerosol load (magenta line) leads to smaller than measured O_4-ODs while not considering any tropospheric aerosol in the simulation (green line) yields larger than measured O_4-ODs in the troposphere. A profile inversion of the O_4 measurements in the above mentioned units and the corresponding averaging kernels are shown in figure 6.20. Note that the shown errors only include the statistical DOAS error but no systematical effects. From the averaging kernels it can be seen that the measurements are only sensitive up to an altitude of 18 km due to the very low O_4 concentrations higher up. In the 3-18 km range, the miniDOAS profile compares well with the profiles obtained from direct sunlight DOAS measurements during ascent and solar occultation. The profile retrieved from miniDOAS O_4 measurements also compares very well to the calculated $[O_2]^2$ profile up to 14 km. For higher altitudes, the measurements show higher values, most likely due to the temperature dependence of the O_4 absorption cross section which is not accounted for. But also the decreasing with altitude sensitivity might be an explanation for the increasing discrepancies.

6.3.7 Scanning Limb Measurements

The scanning limb observations are discussed in more detail for the Kiruna 2004 flight (see section 6.5.10), so only a brief discussion of the results is given here. The limb scans for this flight cover an elevation angle between $+0.5^o$ and -5.5^o. For the corresponding tangent heights see table 6.3.7.

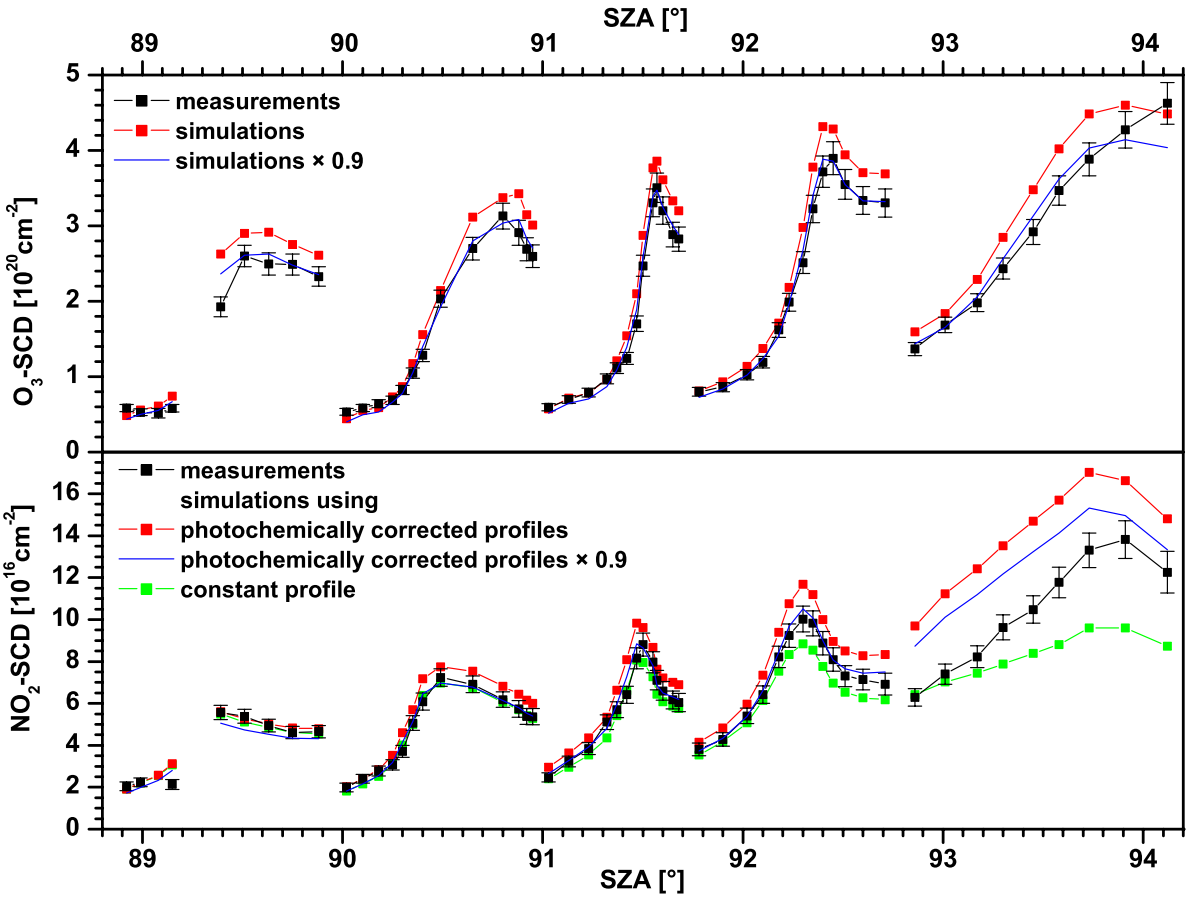

Figure 6.21: Measured (black squares) and simulated (colored squares) O_3- (upper panel) and NO_2- SCDs (lower panel) for scanning limb measurements at balloon float. For the NO_2- SCD simulation, photochemically corrected profiles (red squares) are used (for details see text). For comparison a simulation using a constant profile obtained from DOAS ascent measurements is shown by green squares. Also shown are the simulated O_3- and NO_2- SCDs multiplied by a factor of 0.9 (blue lines).

The measured O_3- and NO_2-SCDs are compared to RT simulations using the same profile as for the simulations of the respective SCDs during ascent. For NO_2, additionally, photochemically scaled profiles are used as input for the simulation. The comparison is shown in figure 6.21. For the O_3-SCDs, the picture looks somewhat different compared to the Kiruna 2004 flight: measured and simulated O_3-SCDs match very well for high tangent heights, while the simulated SCDs are systematically larger for tangent heights below 21 km; for the Kiruna 2004 flight, the opposite is found. For this flight, the elevational gondola oscillations were small ($1 - 0.5^o$) during float which explains the good coincidence at high tangent heights. There are two possible explanations for the mismatch at low tangent altitudes: either the ozone profile is different with lower concentrations compared to that observed during balloon ascent or the RT calculated BoxAMF are slightly too large. For the NO_2-SCD comparison of the first 4 limb scans using the photochemically scaled profiles as input for the simulation, the qualitative

Table 6.2: Tangent height of the scanning limb observations as a function of detector elevation angle. The tangent heights are given by the altitude layer with maximum BoxAMF.

elevation	tangent height
$+0.50^o$	$32.0 - 33.0$ km
-0.00^o	$32.0 - 33.0$ km
-0.50^o	$32.0 - 33.0$ km
-1.00^o	$31.0 - 32.0$ km
-1.51^o	$30.0 - 31.0$ km
-2.01^o	$28.5 - 29.0$ km
-2.52^o	$26.0 - 26.5$ km
-3.02^o	$23.5 - 24.0$ km
-3.53^o	$20.5 - 21.0$ km
-4.03^o	$16.5 - 17.0$ km
-4.53^o	$13.0 - 13.5$ km
-5.04^o	–
-5.54^o	–

picture looks the same as for O_3. Multiplying both the simulated O_3- and NO_2-SCDs by a factor of 0.9 (shown by blue lines in the figure) results in values almost identical to the measurements. This gives rise to the assumption that the RT calculated BoxAMFs are slightly too large (i.e. by 10 %) under these unfavorable conditions with very low sun and very slant light paths through the atmosphere, and that the photochemical increase in NO_2 concentration is handled correctly by the chemistry model. Future limb scan measurements with lower SZA have to show wether these discrepancies, which are not observed for the ascent measurements, is typical for the geometry, i.e. for elevation angles $< 0^o$ or due to the high SZA. For the last limb scan, the simulated NO_2-SCDs are systematically higher than measured, also similar to the case of O_3. It is also seen that the simulations using a constant profile obtained from the direct sunlight DOAS measurements during balloon ascent for SZA in the range of $80 - 88.5^o$ become incorrect with increasing SZA. This comparison nicely demonstrates the feasibility to obtain time-dependant profile information of photochemically active radicals by limb scanning observations and gives confidence into the validity of the applied chemical calculations in the SZA range of $88 - 92.5^o$.

In the next step, vertical profiles are inferred from the measured SCDs and the RT calculated BoxAMF using the same algorithm as for the ascent profile retrieval. The problem is that only very few measurements exist. The differences in tangent altitude between consecutive scans are between < 1 km for the first to < 4 km for the last measurement points. Therefore, the profile retrieval is tested on a 2 km and a 3 km grid for O_3 and NO_2 in figures 6.22 and 6.23, respectively. The O_3 profile retrieved on a 2 km grid has very odd averaging kernels and large covariances and is not shown here. The averaging kernels of the NO_2 retrieval on a 2 km grid are much smaller than 1 with a width wider than the grid size for altitudes below 25 km indicating a lower vertical resolution there. The averaging kernels at these altitudes also imply that the retrieved profile points are not independent. Above 23 km, the averaging kernels indicate a vertical resolution of 2 km. However, the retrieved profiles are also very noisy at these altitudes. So a resolution of 2 km is considered too fine for the given measurement geometry and uncertainties. On a 3 km grid, the both the retrieved O_3 and NO_2 profiles are smoother. The averaging kernels are close to 1 for the $16 - 34$ km altitude range indicating a vertical resolution of 3 km there. Below, the averaging kernels decrease very quickly indication a low sensitivity of the measurements. However, the retrieved O_3 profiles have somewhat smaller concentrations than the ozone sonde profile, a fact already discussed for the SCD comparison above. Also the NO_2 profiles are smaller than the

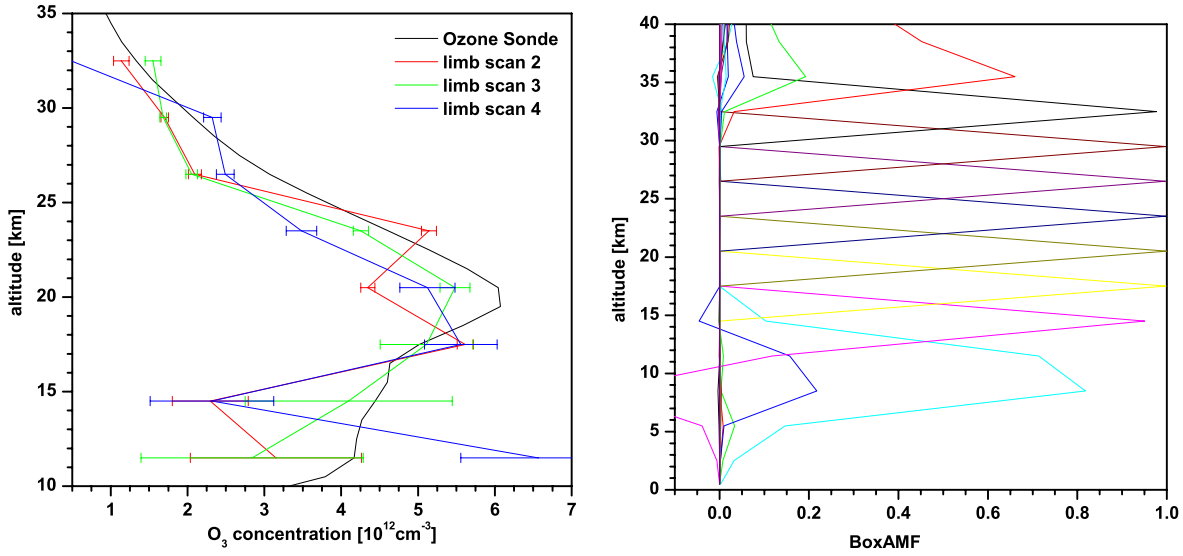

Figure 6.22: Left Panel: Retrieved O_3 profiles from scanning limb measurements on a 3 km grid. Right Panel: Averaging kernels for the profile retrieval of limbscan 2 shown in the left panel.

chemically modeled concentrations.

Summarizing the experience gained from this retrieval exercise, it seems to be possible to retrieve O_3 and NO_2 profiles from scanning limb measurements with 3 km vertical resolution between 15 km and float altitude, However, with rather hight uncertainties due to the low number of measurements. Therefore, in order to validate the RT model or the photochemical calculations, a comparison of measured and simulated SCDs without the additional uncertainties of the retrieval are more useful.

6.3.8 Nadir Measurements

In nadir geometry, the detector telescope is pointing straight downwards to the surface at an elevation angle of -90^o. In this observation mode, the measured SCDs are not sensitive to gondola movements as the azimuth angle is meaningless for -90^o elevation angle and the elevational oscillations are rather small. Figure 6.24 shows a comparison of measured and simulated O_3-SCDs for the miniDOAS nadir observations. The SCDs are plotted vs. SZA which is increasing almost linear with time. Note that all data for SZA$< 90^o$ correspond to the balloon ascent while all data for SZA$> 90^o$ were recorded during balloon float. The agreement of measured and simulated SCDs is good. Some discrepancies are observed at higher altitudes. It should be noted that this need not be a problem of the RT calculations but might be due to changing O_3 concentrations observed during the balloon flight (see figure 6.15, right panel, which shows slightly different O_3 profiles measured by the two sondes or the DOAS during ascent and occultation). For high SZA, i.e. $> 92^o$, the RT modelling becomes increasingly difficult as only very few of the modeled photons actually hit the sun, i.e. contribute to the calculation which results in rather poor statistics and noisy BoxAMFs.

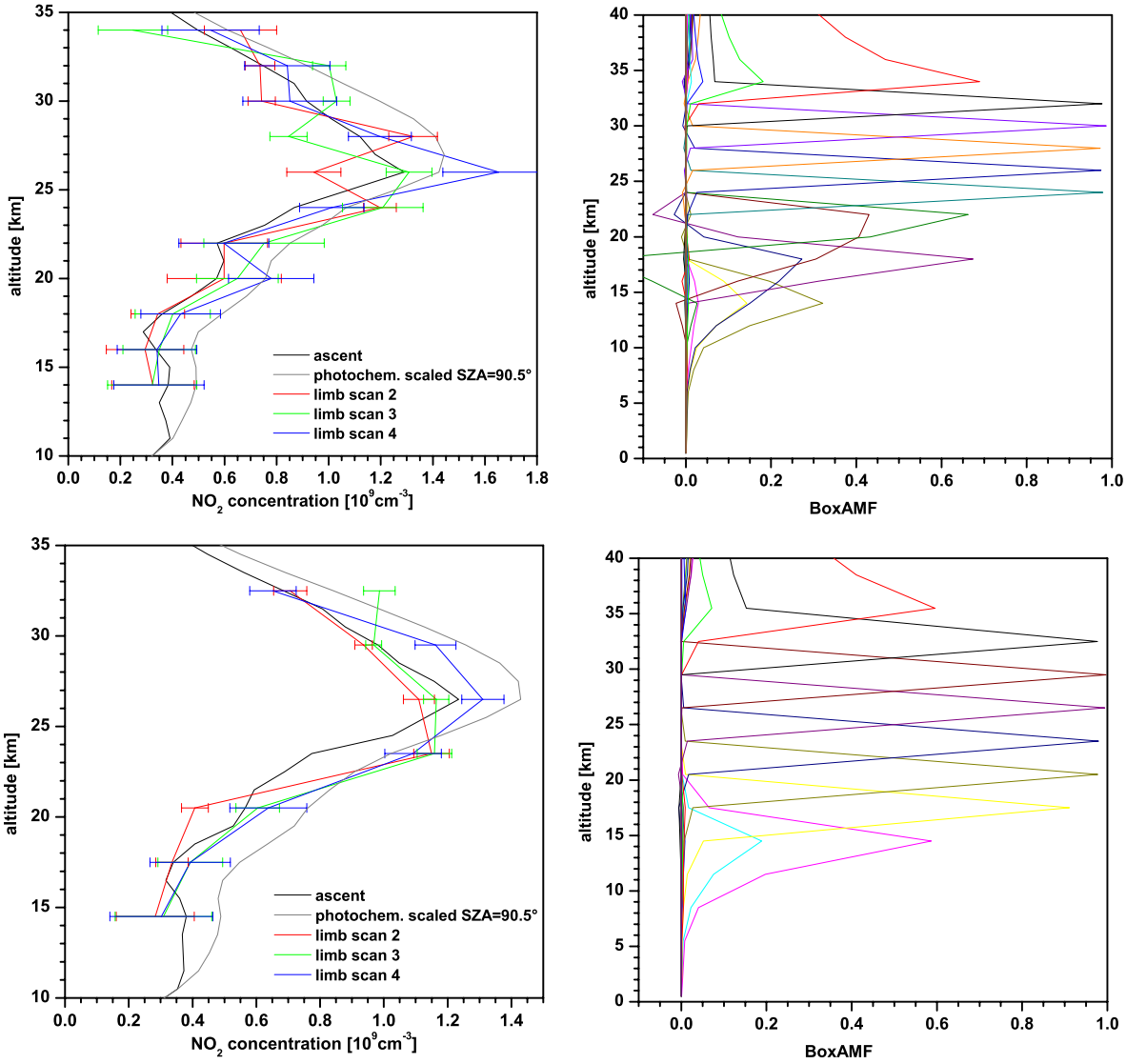

Figure 6.23: Left Panels: Retrieved NO_2 profiles from scanning limb measurements on a $2\,\mathrm{km}$ and $3\,\mathrm{km}$ grid (upper and lower row, respectively). Right Panels: Averaging kernels for the profile retrieval of limbscan 2 shown in the left panels. The corresponding SZA intervals of limbscans $2-4$ are $90-91^o$, $91-91.7^o$, and $91.8-92.8^o$, respectively.

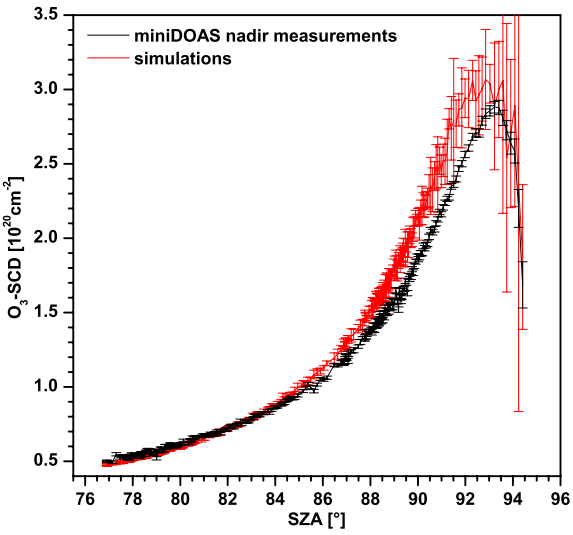

Figure 6.24: Comparison of measured and simulated O_3-SCDs in nadir geometry vs. local SZA.

6.4 The LPMA/DOAS/miniDOAS Flight from Aire-sur-l'Adour, October 9^{th}, 2003

6.4.1 Flight Conditions

The flight from Aire-sur-l'Adour was the, so far, only miniDOAS flight at mid-latitudes. It was launched on October 9^{th}, 2003 from the CNES balloon division headquarter situated at 43.7^o northern latitude and 0.25^o western longitude. The flight profile of the flight is shown in figure 6.25, left panel. The launch was at 14:55 UT at SZA=65^o . After 1 h37 min of ascent, the float altitude of $\sim$ 33 km was reached at 16:32 UT at SZA=80.8^o, approx. half an hour earlier than initially planned. After about half an hour at float (at 17:08 UT and SZA=87.5^o), the balloon had to be cut because it approached the densely populated area of Toulouse, $\sim$ 30 min earlier than initially planned. So, unfortunately, we missed the sunset and also the limb scanning measurements which were supposed to commence automatically at 17:10 UT. To determine the right time to switch into limb scanning mode is always problematic since it is solely based on the calculated trajectory.

Figure 6.25, right panel, shows the results of the ozone sonde launched at 16:13 UT, i.e. $\sim$ 1.5 h after the LPMA/DOAS balloon, from the base in Aire-sur-l'Adour. From the measured temperature, O_3, and humidity profile, the tropopause height is determined to $\sim$ 14 km. From the relative humidity profile, it can be assumed that there were clouds around 1.5 km and 9 km.

In figure 6.26 (left panel) the gondola's azimuth angle minus the solar azimuth angle is plotted vs. time. This quantity should be zero for a perfectly azimuth stabilized gondola. However, it can be seen that the azimuth stabilization completely failed during the first $\sim$ 40 min, i.e. up to an altitude of $\sim$ 16 km. Afterwards, the gondola stabilized with azimuthal oscillations with an amplitude of $6 - 10^o$ during ascent and decreasing to $\sim 3^o$ during balloon float. The period time of the oscillations is typically in the order of 20 s. As described in more detail in section 6.3.1, the gondola's elevation angle is examined by looking at the suntracker's elevation minus the solar elevation angle. This quantity is plotted vs. time in figure 6.26 (right panel). It can be seen that the gondola movements were stronger during ascent with amplitudes up to 5^o. As for the azimuthal oscillation, the period time of the elevational oscillation is $\sim 20\,s$ which is in the order of the typical integration time for 500 co-added scans. Note that even if it were possible to integrate over exactly one (or several) full periods the obtained spectrum, and

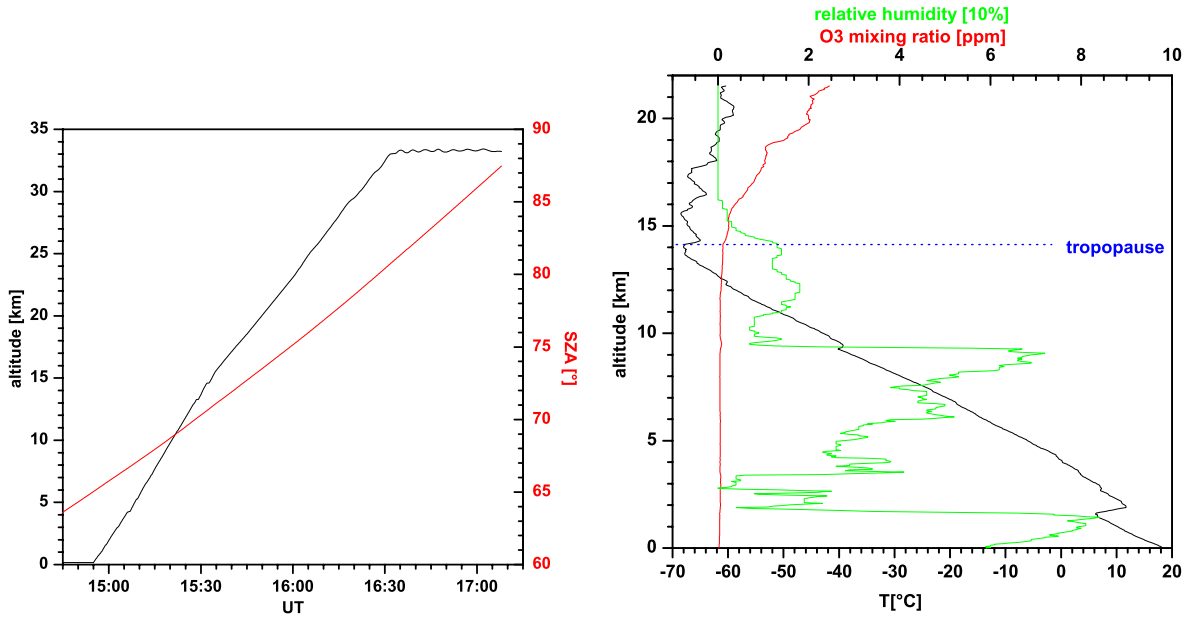

Figure 6.25: Left panel: Altitude profile of the LPMA/DOAS balloon (black line) and Solar Zenith Angle (SZA) vs. time. Left panel: Results of the ozone sonde launched $\sim 1.5\,\mathrm{h}$ after the LPMA/DOAS gondola. Shown is the temperature (black line), O_3 mixing ratio (red line), and relative humidity (green line). The approx. height of the tropopause ($\sim 14\,\mathrm{km}$) is shown with blue dots).

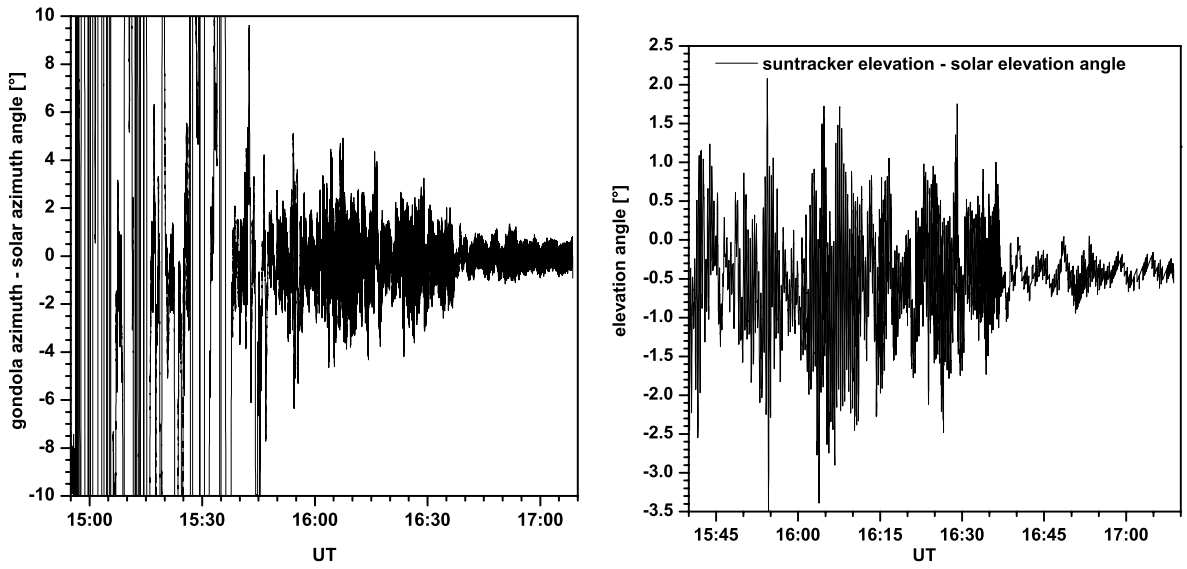

Figure 6.26: Azimuth angle of the gondola minus solar azimuth angle (left panel) and elevation angle of the suntracker minus solar elevation angle (right panel), respectively, vs. time.

thus trace gas absorption, would be different compared to a perfectly stable gondola as the radiative transfer is highly nonlinear. This effect of gondola instability is discussed quantitatively in 5.1.3. In the following it is assumed that the limb telescope is always pointing to a constant elevation angle of -0.5^o to the horizon and an azimuth angle of 90^o to the sun.

6.4.2 Instrument Performance

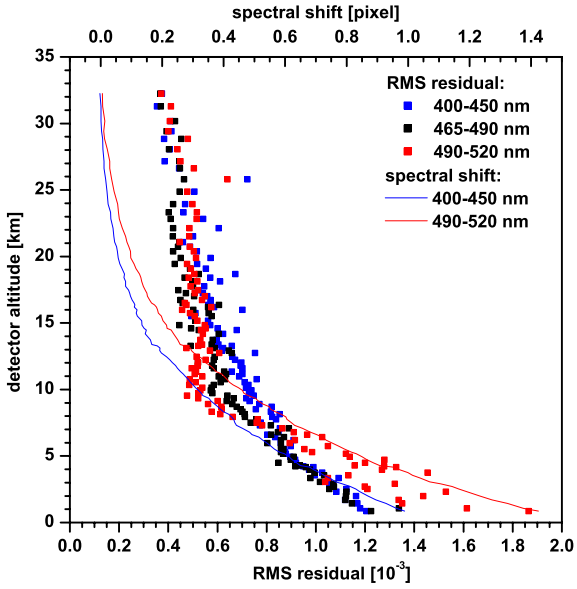

Figure 6.27: RMS residual of the DOAS retrieval of NO_2 ($400-450$ nm, blue squares), O_4 ($465-490$ nm, black squares), and O_3 ($490-520$ nm, red squares), and spectral shift of the spectra relative to the solar reference spectrum (blue and red line, respectively) vs. detector altitude.

The stability of the optical imaging is checked by looking at the RMS residual of the DOAS retrieval and the spectral shift of the measured spectra relative to the solar reference spectrum recorded at float altitude (33.1 km and SZA=81^o). These quantities vs. balloon altitude are plotted in figure 6.27. The spectral shift decreases from values of 1 pixel and 1.4 pixels in the $400-450$ nm and $490-520$ nm wavelength range, respectively, for altitudes near ground level to zero with increasing balloon altitude. Consequently, the residuals are higher for lower altitudes where the spectral shift is largest. The RMS residuals decrease from values of $1.2 \cdot 10^{-3}$ and $1.8 \cdot 10^{-3}$ in the $400-450$ nm and $490-520$ nm wavelength range, respectively, to values around $0.4 \cdot 10^{-3}$ at balloon float altitude. The high residuals in the O_3 retrieval region ($490-520$ nm) are not only due to the higher spectral shift but also due to the imperfectly removed water vapor absorptions because of the high tropospheric H_2O content. This significantly affects the quality of the O_3 DOAS retrieval at altitudes below 9 km. For altitudes above 9 km, where the H_2O absorption strongly decreases, the RMS residuals decrease to values around $0.5-0.6 \cdot 10^{-3}$ which is very close to the limit given by the photo-electron shot noise. In the $400-450$ nm region, the residuals are slightly higher because of the lower number of analyzed photons. All in all, the residuals are reasonably small for a detection of the mentioned trace gases.

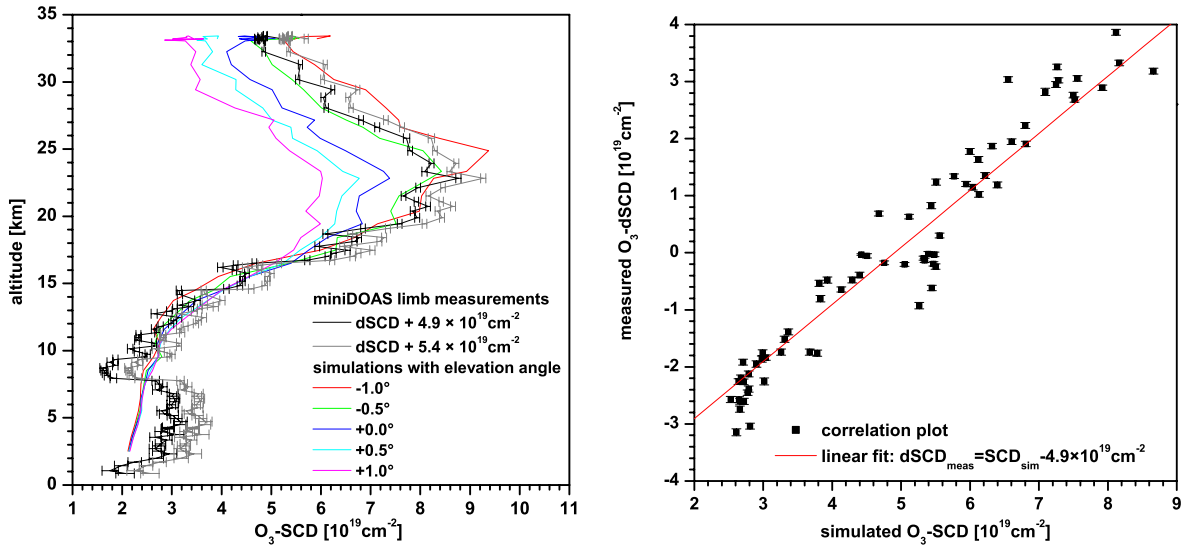

Figure 6.28: Left panel: measured O_3-SCDs (black and gray line, respectively) vs. detector altitude compared to several simulations for several elevation angles (colored lines) are shown. Right panel: measured O_3-dSCDs vs. simulated O_3-SCDs (black squares) and a linear fit of the correlation plot (red line).

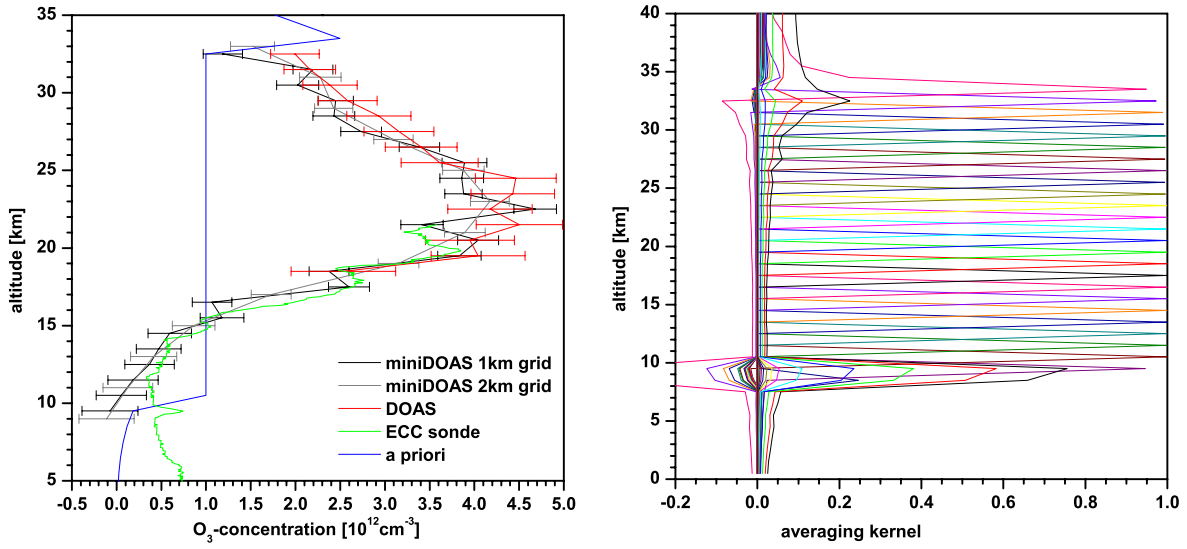

Figure 6.29: Left panel: O_3-profiles retrieved on a $1\,\mathrm{km}$ (black line) and $2\,\mathrm{km}$ grid (gray line), respectively, compared to the profiles measured by the direct sunlight DOAS (red line) and an ECC sonde (green line) launched $\sim 1.5\,\mathrm{h}$ after the LPMA-balloon. Also shown is the a priori profile (blue line) used for the retrieval. Right panel: Averaging kernels for the profile retrieval on a $1\,\mathrm{km}$ grid.

6.4.3 O_3 Results

The measured O_3-SCDs are compared to RT simulated values in figure 6.28 (left panel). Several simulation runs with elevation angles between -1^o and $+1^o$ are performed to determine the exact angle which was roughly adjusted to 0^o on the ground. As input for the simulation, a profile composed from ozone sonde measurements ($0 - 22$ km), DOAS ascent measurements ($22 - 33$ km) and typical values above is used. It can be seen that the best matching between the measured and simulated SCDs is achieved for an elevation angle of -0.5^o (green line). This value together with the azimuth angle of 90^o to the sun is used for the profile retrieval. The O_3 absorption of the solar reference spectrum is determined from the correlation of measured dSCDs and simulated SCDs (see figure 6.28, right panel). A value of $4.9{\cdot}10^{19}$ cm^{-2} is found and added to the measured dSCDs (black line). The uncertainty of this offset is assumed as 10 %, so a second SCD profile is used for the profile inversion with $5.4{\cdot}10^{19}$ cm^{-2} added to the measured dSCDs (gray line). As the measured O_3-SCDs for altitudes below 9 km are affected by the strong and not perfectly removed H_2O absorptions also present in the $490 - 520$ nm region, they are deleted for the profile inversion and only SCDs above 9 km are considered.

The O_3-concentration profiles retrieved on a 1 km (black line) and 2 km grid (gray line), respectively, are shown in figure 6.29 (left panel) together with the profiles obtained from the direct sunlight DOAS (red line) and an ECC sonde (green line) launched ~ 1.5 h after the LPMA/DOAS-balloon. The miniDOAS profile with 1 km resolution compares very nicely to the ozone sonde profile in the $11 - 22$ km range, e.g. the maxima at 17 km and 20 km can be seen. Below 11 km, the miniDOAS measurements are somewhat lower which can be explained by the existing difficulties in tropospheric RT modeling. Additionally, the gondola was rather unstable below 16 km with strong azimuthal oscillations and even revolutions. The comparison to the DOAS profile is also quite good over the entire altitude range within the error bars (for details about the DOAS profile retrieval and error calculation see *Butz et al.* (2005)). The a priori profile used for the retrieval is also shown in the figure and its covariance is set to 100 %. The rather odd shape of the a priori is due to the fact that its values have been set to a constant value between 10 km and 33 km. This little exercise demonstrate the retrieved profile's independence of the a priori in this altitude range, only above and below typical O_3-concentrations are used to stabilize the inversion. The averaging kernels of the retrieval (shown in figure 6.29, right panel) behave very well in the entire region of interest, i.e. $9 - 33$ km, with values close to 1. The profile retrieved on a 2 km altitude grid is also shown (gray line), although a broader grid does not seem to be necessary given the shown retrieval on the 1 km grid. The error bars in the plot are the sum of the (rather small) profile inversion error originating from the DOAS retrieval error which is very small in the case of O_3, and the much bigger contribution originating from the uncertainty of the solar reference offset. Assuming $0.25{\cdot}10^{19}$ cm^{-2}, i.e. 10 % (see above), for its uncertainty leads to a pretty constant uncertainty in the retrieved profiles decreasing from $0.25{\cdot}10^{12}$ cm^{-3} at lower to $0.1{\cdot}10^{12}$ cm^{-3} at higher altitudes. Considering the low tropospheric O_3 concentrations, this uncertainty is in the order of $40 - 100$ % for altitudes below 15 km but decreasing to $4 - 7$ % at higher altitudes (17-33 km) with much higher O_3 concentrations.

6.4.4 NO_2 Results

The measured NO_2-SCDs and an RT simulation of the same quantity is shown in figure 6.30 (right panel). Again, the determination of the solar reference offset to be added to the retrieved dSCD values is the biggest uncertainty. The particular problem for this flight is that DOAS measurements are only available for altitudes above 18 km up to 33 km. So for all other altitude levels, SLIMCAT NO_2 concentrations scaled to the DOAS profile are used. A value of $4{\cdot}10^{16}$ cm^{-2} is added to the measured dSCDs. The so obtained NO_2 -SCDs (black line) match quite nicely for altitudes up to ~ 20 km with the simulation (red line). However, at higher altitudes the measured values are higher

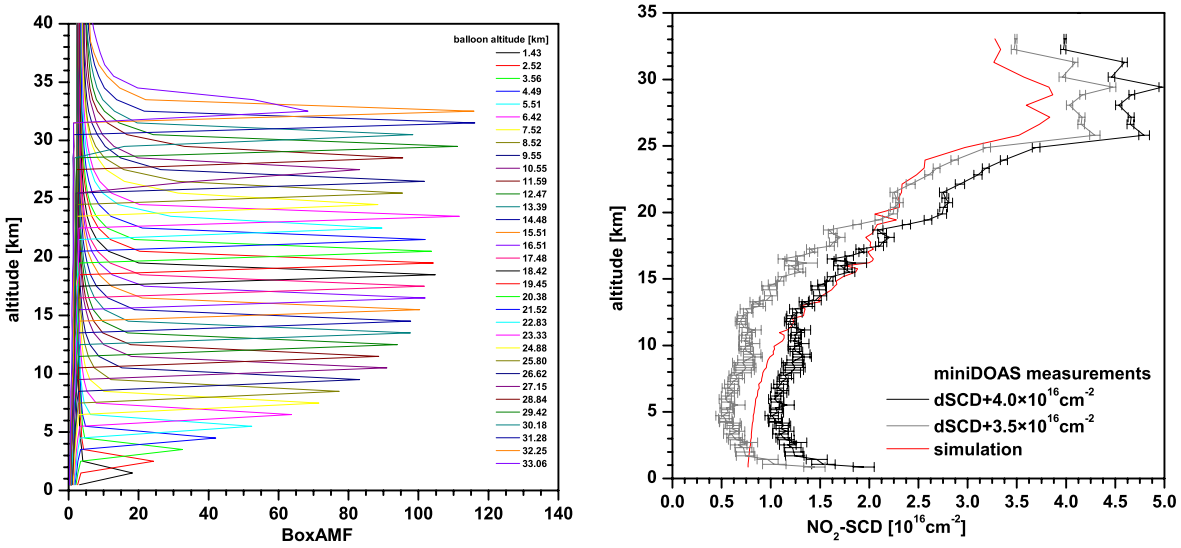

Figure 6.30: Left panel: Box Air Mass Factors (BoxAMF) for selected altitudes during balloon ascent. Right panel: measured NO_2-SCDs for two solar reference offsets (black and gray line, respectively) compared to RT simulated NO_2-SCDs using the DOAS ascent profile as input.

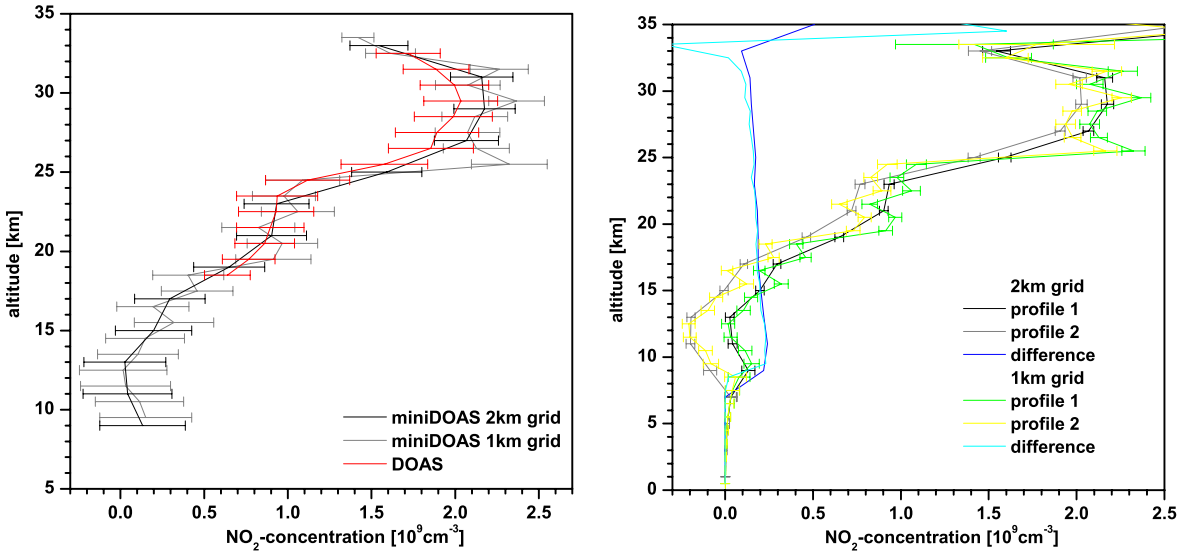

Figure 6.31: Left panel: NO_2 concentration profiles retrieved from miniDOAS limb measurements on a 2 km grid (black line) and on 1 km grid (green line), respectively, and direct sunlight DOAS measurements (red line) during balloon ascent. Right panel: NO_2 using different solar reference offsets ($4{\cdot}10^{16}$ cm^{-2} (profile 1), and $3.5{\cdot}10^{16}$ cm^{-2} (profile 2), respectively) retrieved on a 2 km grid (black and gray lines) and on a 2 km grid (green and yellow lines), respectively. Also shown is the difference of the respective profiles (blue and cyan lines).

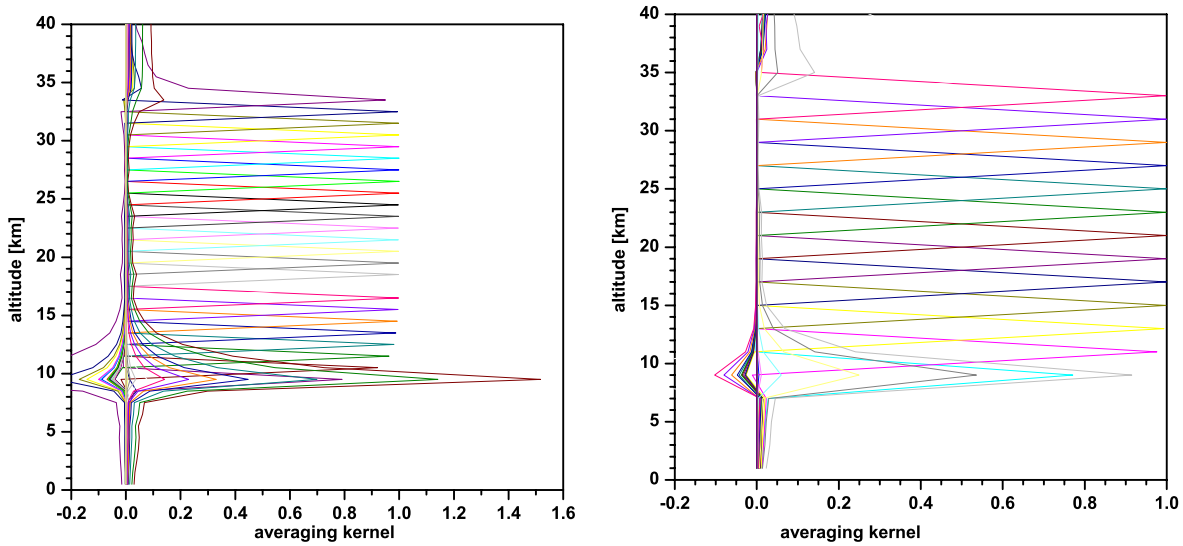

Figure 6.32: Averaging kernels for the profile retrievals shown in fig. 6.31 (right panel) on a 1 km grid (left panel) and a 2 km grid (right panel), respectively.

than the simulated ones. A possible reason are the rather strong elevational oscillations of the gondola with amplitudes of $3 - 4^o$ for the respective phase of the flight (see figure 6.26, right panel) which can lead to significantly higher NO_2-dSCDs compared to a still gondola. A second SCD profile with $3.5 \cdot 10^{16}\,\mathrm{cm}^{-2}$ added to the measured dSCDs (gray line) is also shown in figure 6.30 (right panel). These SCD values are much below the simulated ones for altitudes below 20 km but in agreement with the simulations between 20 and 25 km. It cannot really be judged, which of the two SCD offset values is the real one so the uncertainty of the SCD measurements is estimated to the difference of the two profiles, i.e. $0.5 \cdot 10^{16}\,\mathrm{cm}^{-2}$. As for the DOAS retrieval for both measurement techniques (i.e. miniDOAS limb and direct sunlight DOAS), the same NO_2 cross sections are used, no systematical cross section error is assumed for the error calculation of the following profile retrieval.

Another specific problem for the NO_2 profile retrieval for this flight are the low BoxAMF at low altitudes (i.e. below $\sim$ 8 km) compared to those above 10 km (see figure 6.30, left panel). This makes the measurements rather insensitive at those altitudes and including the measurements below 9 km only leads to an odd behavior of the averaging kernels (i.e. values $\gg 1$) for these altitudes, so all measured SCDs below 9 km are excluded for the profile inversion. The NO_2 concentration profiles retrieved on a 2 km grid (black line) and 1 km grid (gray line), are shown in figure 6.31 (left panel). As a priori profile, the same profile used for the simulation (i.e. NO_2 concentrations from the DOAS measurements where available and adjusted SLIMCAT values everywhere else) is used. The covariance of the a priori is set to 100 % to ensure the independence of the retrieved profile from it. From the averaging kernels (see figure 6.32), it can be seen that the measurements are sensitive to NO_2 between 10 and 34 km both on a 1 km and 2 km grid as the values are 1 in this altitude range (except for the $10 - 15$ km range of the 1 km grid retrieval where the averaging kernels are between $0.9 - 1$). However, the profile retrieved on the 1 km grid is rather noisy, especially at altitudes above 25 km, i.e. near the NO_2 concentration maximum, which is attributed to elevational gondola movements. These fluctuations are averaged out in the 2 km case so that this profile is favored. The obtained miniDOAS profiles match very well within the error bars with the NO_2 profile obtained from direct sunlight DOAS measurements during balloon ascent (red line). Only in the $25 - 32$ km range, the miniDOAS concentrations are significantly larger which can be explained by the already mentioned effect of the elevational gondola oscillation leading to higher measured NO_2-SCDs in this altitude range. The effect of the uncertainty of the determination of the NO_2 absorption of the solar reference spectrum is investigated by performing another profile

inversion with a second set of SCDs with an offset value by $0.5 \cdot 10^{16}\,\mathrm{cm}^{-2}$ smaller (see above). The results are visualized in figure 6.31 (right panel). It can be seen that the difference in the SCD offset leads to a rather constant difference between the two obtained concentration profiles (bluish lines) with values decreasing from $0.25 \cdot 10^{9}\,\mathrm{cm}^{-3}$ at low altitudes to $0.1 \cdot 10^{9}\,\mathrm{cm}^{-3}$ at high altitudes both on the 1 km and 2 km grid. This difference is added to the error of the profile retrieval itself, i.e. originating from the NO_2 DOAS retrieval error which is shown by the error bars in figure 6.31 (right panel), and included in the error bars of the profiles plotted in 6.31 (left panel). This error contribution dominates the total error by far which can easily be seen when comparing the error bars of the profiles in the left and right panel.

6.5 The LPMA/DOAS/miniDOAS Flight from Kiruna, March 24^{th}, 2004

6.5.1 Flight Conditions

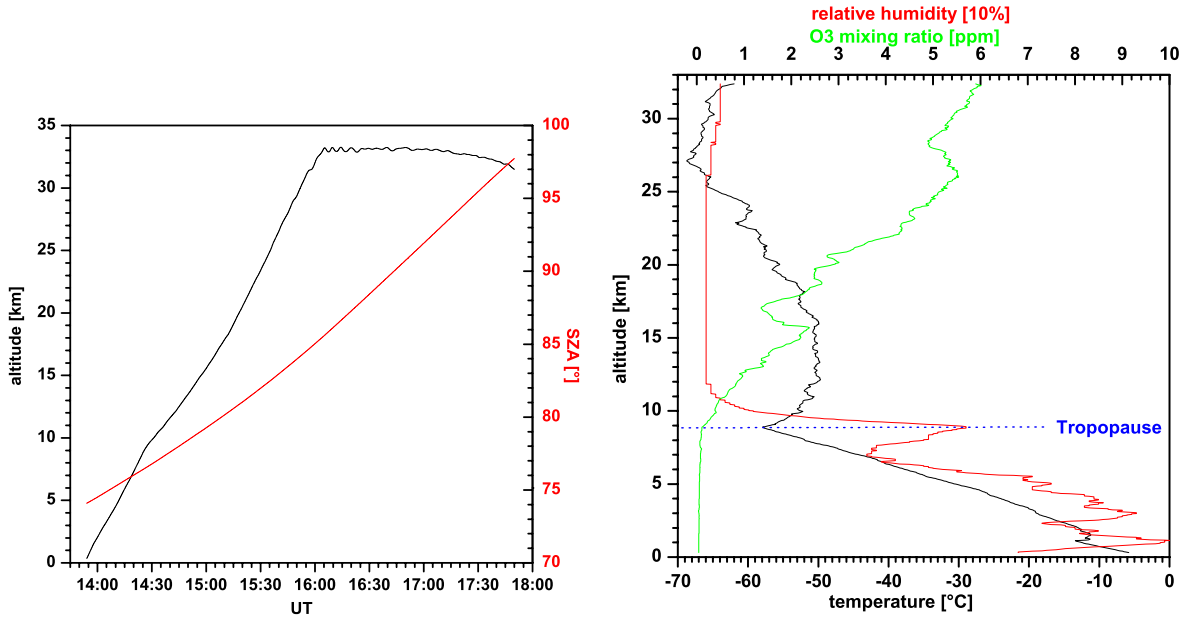

Figure 6.33: Left panel: Altitude profile of the LPMA/DOAS balloon (black line) and Solar Zenith Angle (SZA) vs. Universal Time (UT). Right panel: results of the ozone sonde launched from Esrange ~ 1 h after the LPMA/DOAS gondola. Shown are the temperature (black line), O_3-mixing ratio (green line), and the relative humidity (red line). The approx. height of the tropopause (~ 8.9 km) is given with blue dots.

The flight was launched on March 24^{th}, 2004 at 13:54 UT and SZA=74.1^o. The altitude profile of the flight and the corresponding SZA are shown in figure 6.33 (left panel). After 2 h10 min ascent, the float altitude of $\sim$ 33 km was reached at 16:05 UT and SZA=85.6^o. After $\sim 1\frac{3}{4}$h at float, the balloon was cut at 17:50 UT and SZA=97.7^o. The results of the ozone sounding by an ECC sonde launched at 14:58 UT, i.e. $\sim$ 1 h after the LPMA/DOAS balloon, is shown in figure 6.33 (right panel). From the temperature profile, the tropopause height is estimated to $\sim$ 8.9 km. The relative humidity reaches almost 100 % around 1 km which might be due to clouds.

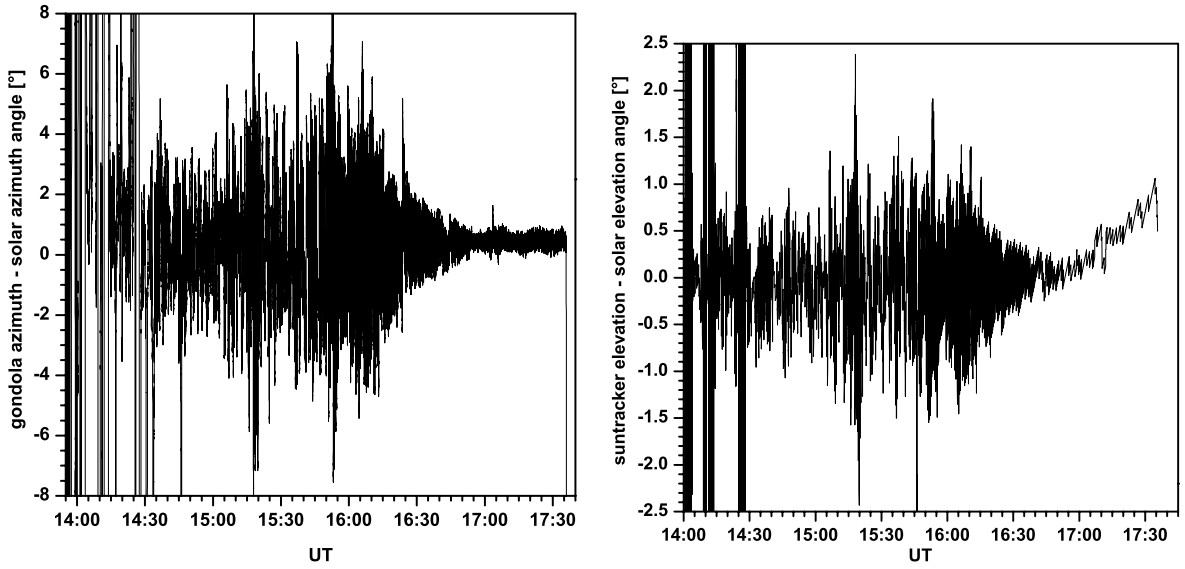

Figure 6.34: Azimuth angle of the gondola minus solar azimuth angle (left panel) and elevation angle of the suntracker minus solar elevation angle (right panel) vs. time.

The elevational and azimuthal position of the gondola relative to the sun is shown in figure 6.34. It can be seen that the azimuth oscillation had an amplitude between $6 - 10^o$ during ascent and in the beginning of the float phase. During float the gondola movements slowed to $1 - 2^o$ in the last hour of the flight. The same trend can be seen in the elevational oscillations with amplitudes around 1^o during the beginning of the ascent increasing to $2 - 3^o$ later on, i.e. between 15:10-16:20 UT or altitudes above ~ 19 km and the first 15 min of float. In the course of the float phase, the gondola's elevational oscillations slowed to amplitudes $< 0.5^o$ during the last hour of the flight.

6.5.2 Instrument Performance

As can be seen in figure 6.35 (right panel), the residuals achieved in the DOAS evaluations are lower than in the previous flights thanks to a higher light sensitivity which allows for co-adding 1000 scans per spectrum and a lower spectral shift due to the pressure stabilization (see also section 4.1.2 for details on the miniDOAS mk.2 applied for the first time in this flight). This allows for the first time for the detection of BrO. The residuals in the UV are generally higher in the UV, especially at low altitudes, mostly because of the much lower limb radiances under these conditions leading to rather poorly saturated spectra (i.e. a saturation level of ~ 15 % in the troposphere compared to ~ 50 % in the stratosphere in the BrO retrieval range of $347 - 359$ nm) which can be seen in figure 6.35 (left panel).

6.5.3 Absolute Limb Radiance Measurements

The instrument is absolutely radiometrically calibrated shortly before the balloon flight with an absolutely calibrated Ulbricht sphere. For experimental details about the calibration of both the source and the instrument, see section 4.5. Here, the results of the calibration measurements and the limb radiance measurements during the balloon flight are reported.

For the absolute radiometric calibration in the "field" shortly prior to the actual balloon flight, spectra with the Ulbricht sphere as source are recorded at different integration times (between 3 and 19 ms)

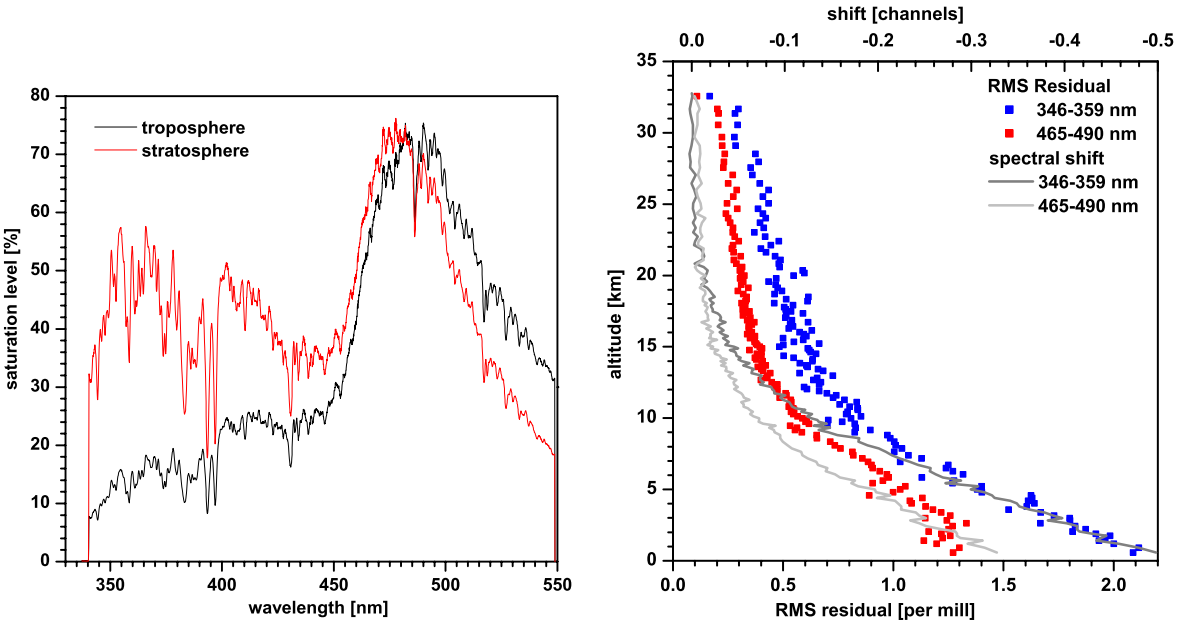

Figure 6.35: Left panel: saturation levels vs. wavelength for a tropospheric spectrum (black line) recorded in 6.49 km altitude and the stratospheric spectrum (red line) recorded in 32.77 km altitude used as Fraunhofer reference. Right panel: spectral shift (gray lines) and residual of the DOAS evaluations (colored squares) in the UV and visible spectral range with and without halogen lamp correction.

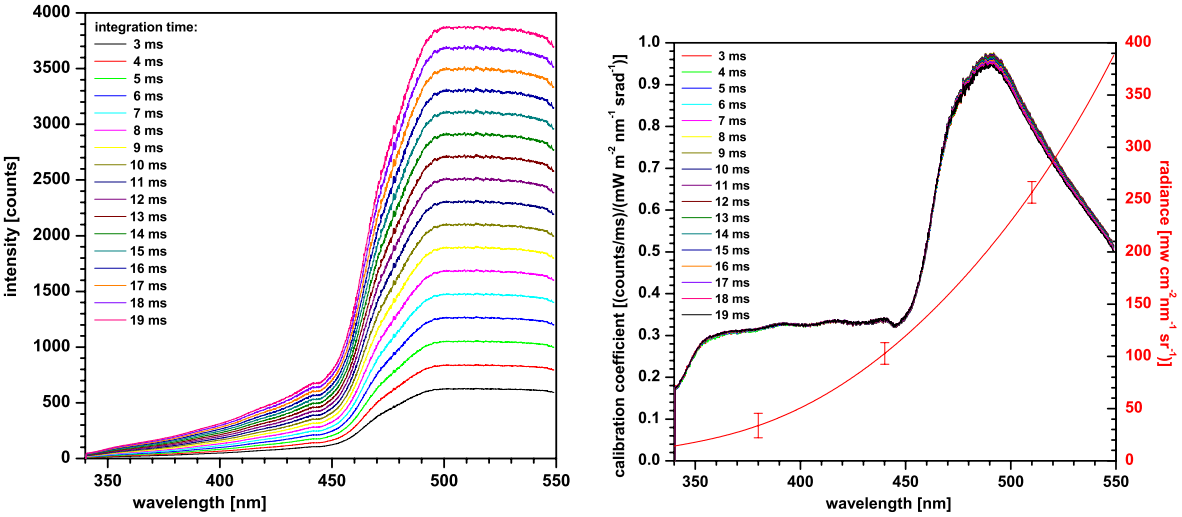

Figure 6.36: Left panel: measured intensity vs. wavelength as a function of integration time per scan for the calibration source. Right panel: calibration coefficient defined as the quotient of count rate per ms and radiance vs. wavelength as a function of integration time (colored lines). Also shown is the output radiance of the calibration source vs. wavelength (red line).

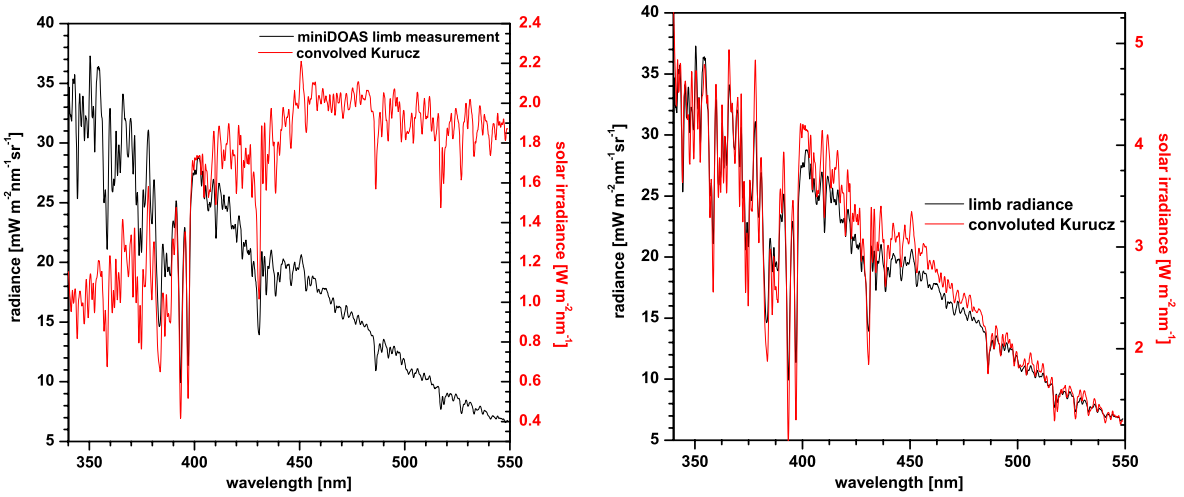

Figure 6.37: Left panel: measured radiance vs. wavelength (black line) for a spectrum recorded at balloon float (32.8 km, SZA=85.4^o, 90^o azimuth and -1.5^o elevation angle) and absolutely calibrated Kurucz spectrum convolved with the instrument's slit function (red line). Right panel: zoom of the plot shown in the left panel into a narrower wavelength interval.

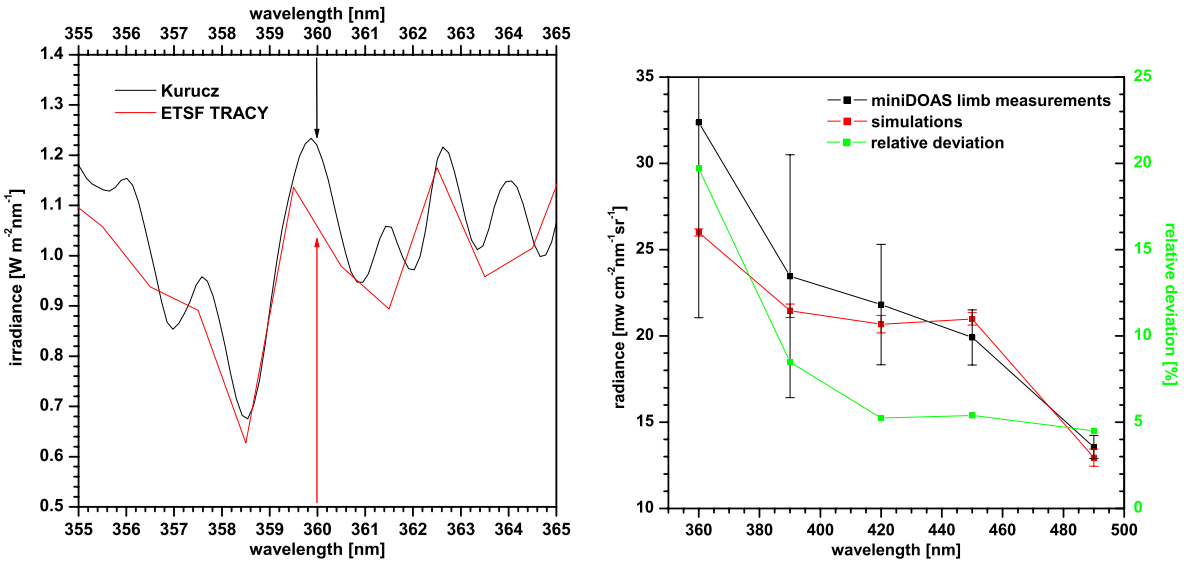

Figure 6.38: Left panel: Absolutely calibrated Kurucz spectrum convolved with the instrument's slit function (black line) compared to the extra-terrestrial solar function (ETSF) used by TRACY. Right panel: Limb radiance measured at several wavelengths (black squares) compared to TRACY simulations of the same quantity (red squares) for the spectrum shown in figure 6.37. Also shown is the relative deviation of the radiance values vs. wavelength (green squares).

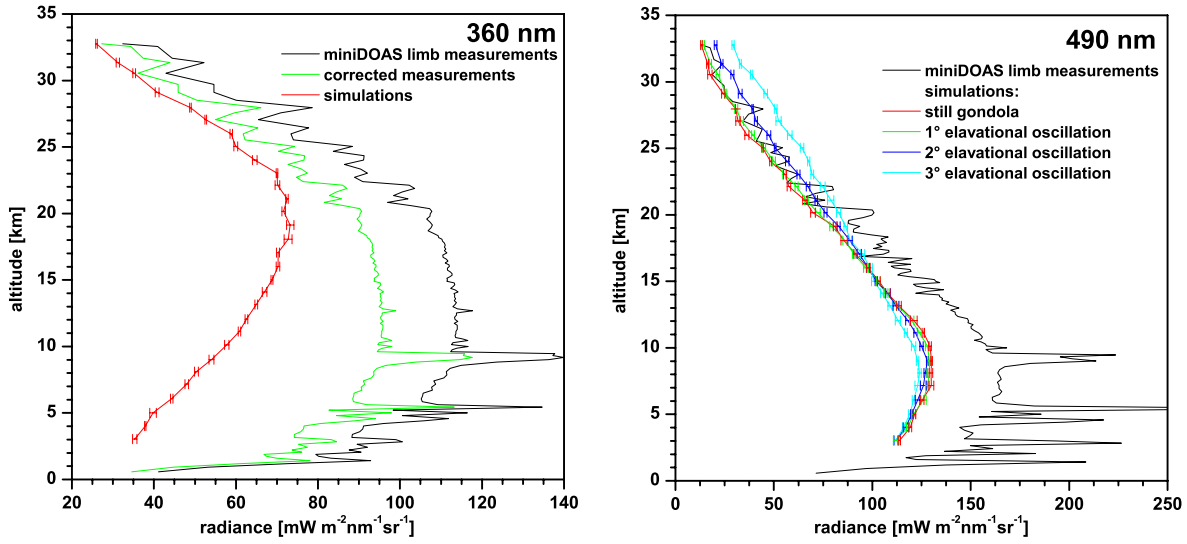

Figure 6.39: Left panel: Measured limb radiance at 360 nm vs. altitude with (green line) and without correction (black line). For details about the applied correction see text. Also shown are TRACY RT simulations of the same quantity (red line). Right panel: Measured limb radiance at 490 nm vs. altitude (black line) compared to RT simulated radiances assuming different elevational oscillations of the detector (colored lines).

resulting in different saturation levels of the measured spectra (see figure 6.36, left panel). The obtained count rates (i.e. counts per ms) are divided by the output radiance of the source $I(\lambda)$ to obtain a calibration coefficient $c(\lambda)$:

$$c(\lambda) = \frac{\text{count rate}}{I(\lambda)} \quad \left[\frac{\text{counts/ms}}{\text{mW cm}^{-2}\ \text{nm}^{-1}\ \text{sr}^{-1}}\right]. \tag{6.2}$$

$c(\lambda)$ is thus a measure for the sensitivity of the spectrometer towards radiation. It is plotted vs. wavelength in figure 6.36, right panel) as a function of integration time. The sensitivity is almost constant in $350-450$ nm, strongly increasing by a factor of >3 from $450-490$ nm reaching a maximum near 490 nm. From $490-550$ nm it is again decreasing by a factor of ~ 2. Comparing the absolute values of $c(\lambda)$ obtained for this flight to those from Kiruna 2003 (see figure , it can be seen that the new instrument has a sensitivity higher by a factor of ~ 7 at 500 nm and ~ 3.5 at 400 nm. The values of $c(\lambda)$ obtained at different wavelengths deviate by ~ 3 % due to the detector non-linearity. For the radiometric calibration of the spectra of the actual balloon flight, the calibration coefficient obtained for the highest saturation (i.e. recorded with 19 ms integration time) is used. The uncertainty of the output radiance of the calibration source ranges between 4 % at 510 nm and 380 nm (for details see section 4.5) which directly affects the accuracy of the absolute calibration of the instrument by the same relative error. One disadvantage of the used calibration source is that the wavelength dependence of its radiance output (see figure 6.36, right panel, red line) is totally different from that of the typical limb radiance (see figure 6.37, left panel). While the lamp's radiance is strongly increasing from the blue to the red end of the observed wavelength interval, the limb radiance shows the opposite trend. Considering the instrumental sensitivity also increasing to higher wavelengths, this results in lamp spectra with very poor saturations at lower wavelengths (e.g. 3 % at 360 nm) for full saturation around 500 nm. For limb radiances, especially at higher altitudes, the recorded spectra have a comparatively equal saturation over the entire observed wavelength interval (see figure 6.35, left panel). This means that the achieved saturations are considerably different for the calibration and the actual atmospheric measurements which means that the that the detector non-linearities (around 3 %, see section 4.2.2)

affect the accuracy of the radiometric calibration. Adding this error to the uncertainty of the absolute calibration of the source leads to a total relative error of the miniDOAS radiometric calibration of ranging between 5 % at 490 nm and 35 % at 360 nm.

For the comparison of measured and RT simulated limb radiances, a precise wavelength calibration is crucial. The wavelength calibration of the measurement is performed by a fit of a spectrum measured at balloon float to a Kurucz spectrum convolved with the instrumental slit function using the WinDOAS calibration tool. For details of this procedure see section 4.4.1. A comparison of the so wavelength calibrated measured spectrum to the convolved Kurucz spectrum is shown in figure 6.37. In the right panel, it can be seen that the wavelength calibration is very accurate as the Fraunhofer lines appear at the same wavelengths. The qualitative trend of the measured limb radiance compared to the solar irradiance can be explained as follows: the solar irradiance is moderately increasing by a factor of ~ 2 from the blue to the red end of the observed wavelength interval. As the Rayleigh scattering strongly decreases with wavelength (i.e. it is proportional to λ^{-4} the observed limb radiance is consequently also decreasing with wavelength for the shown spectrum recorded at balloon float where Rayleigh scattering is the dominating effect. As the solar spectrum is highly structured, the actual irradiance value at a given wavelength is strongly dependant on the spectral resolution of the observation. Therefore, it is crucial that the solar irradiance spectrum used as input for the RT calculation has the same resolution as the instrument to be compared with. Figure 6.38 shows a comparison of the Extra-Terrestrial Solar Function (ETSF) used by TRACY and an absolutely calibrated Kurucz spectrum (*Kurucz et al.*, 1984) convolved to the instrumental resolution for wavelengths around 360 nm. It can be seen that the resolution of the TRACY ETSF is much wider than that of the miniDOAS instrument. This results in the Fraunhofer lines to be much more smeared out in the TRACY spectrum compared to the miniDOAS measurements which results in strong deviations between the irradiance value used by TRACY (red arrow) and that the miniDOAS instrument "sees" (black arrow). Therefore, all TRACY simulations are multiplied with the ratio of Kurucz and ETSF irradiance at the wavelength of interest. As a consequence, the TRACY RT calculations are based on the Kurucz solar irradiance.

Figure 6.38 shows a comparison of measured and TRACY simulated radiances as a function of wavelength for a spectrum recorded at balloon float (32.8 km, SZA=85.4^o, 90^o azimuth and -1.5^o elevation angle). It can be seen that the relative deviation of the two radiance values is below 5 % for wavelengths above 420 nm and increasing for lower wavelengths to $\sim$ 20 % at 360 nm. This is in agreement with the uncertainty of the absolute calibration assumed to 5 % at 490 nm and 35 % at 360 nm. The RT under these conditions are comparatively simple as most photons ($\sim$ 80 %) are single Rayleigh scattered and Mie-scattering on aerosols plays a minor role ($<$ 10 %). Therefore, the RT simulated radiances are assumed to be pretty accurate under these conditions and, thus, used to check the miniDOAS radiometric calibration at low wavelengths. The TRACY simulations yield a radiance ratio of $I(360\,\text{nm})/I(490\,\text{nm}) = 1.84$. This is a reasonable value as the following simple estimation shows: The relative solar irradiance calculated from the convolved Kurucz spectrum shown in figure 6.37 for the two wavelengths is $E(360\,\text{nm})/E(490\,\text{nm}) = 0.58$. The relative probability for Rayleigh scattering is $(490\,\text{nm}/360\,\text{nm})^4 = 3.432$ which yields a radiance ratio of $I(360\,\text{nm})/I(490\,\text{nm}) = 1.99$ assuming solely Rayleigh scattering. Therefore, the radiance measurements at 360 nm are multiplied by a correction factor of setting which sets the ratio $I(360\,\text{nm})/I(490\,\text{nm})$ to 1.84.

Figure 6.39 shows the limb radiances measured during balloon ascent vs. detector altitude. It can be seen that the uncorrected measurements at 360 nm (left panel) are significantly higher than the simulated values. After the above described correction is applied, the measured radiances are close to the simulations for high altitudes. However for altitudes below 20 km the measured radiances are significantly higher than simulated. For $\lambda = 490$ nm, the picture looks similar. At higher altitudes (above $\sim$ 14 km), measured and simulated radiances match quite nicely. The fluctuations of the measured radiances are most likely due to gondola instabilities. The radiance measurements are especially

sensitive to elevational oscillations but also to strong azimuthal oscillations (see section 5.1). Therefore, additional simulations considering elevational oscillations with amplitudes between 1^o and 3^o are carried out. It can be seen that the observed radiances lie between the simulations assuming a still and a with 3^o oscillating gondola for altitudes above ~ 20 km. Below 20 km, elevational fluctuations should have a smaller effect on the radiance according to the RT simulations. Also the azimuthal oscillations with an amplitude of at most 15^o does not significantly affect the simulated radiance. However, the fluctuations of the measurements become higher. Below 16 km, the measured radiances are significantly higher (by > 20 %) than simulated. It should be noted that the measurements below 13 km have appreciable contributions from the troposphere, which is more difficult to RT model due to the presence of clouds which are not considered in the presented RT simulations. Additionally, the gondola is much more unstable in the troposphere and especially around the tropopause which was around 9 km. Strong azimuthal oscillations and revolutions lead to significantly higher radiance as the telescopes looks into a radiance minimum given a still gondola. For an azimuth angle of 0^o, simulated radiances are about twice as high as for the azimuth angle of 90^o assumed in the actually shown simulations.

Summarizing the above results, it is found that the measurements and the TRACY RT simulations match very well for higher altitudes. As the TRACY simulations at 360 km begin to deviate from the measurements at higher altitudes compared to 490 km, I assume that the increasing significance of multiple scattering causes the RT simulations to become increasingly incorrect.

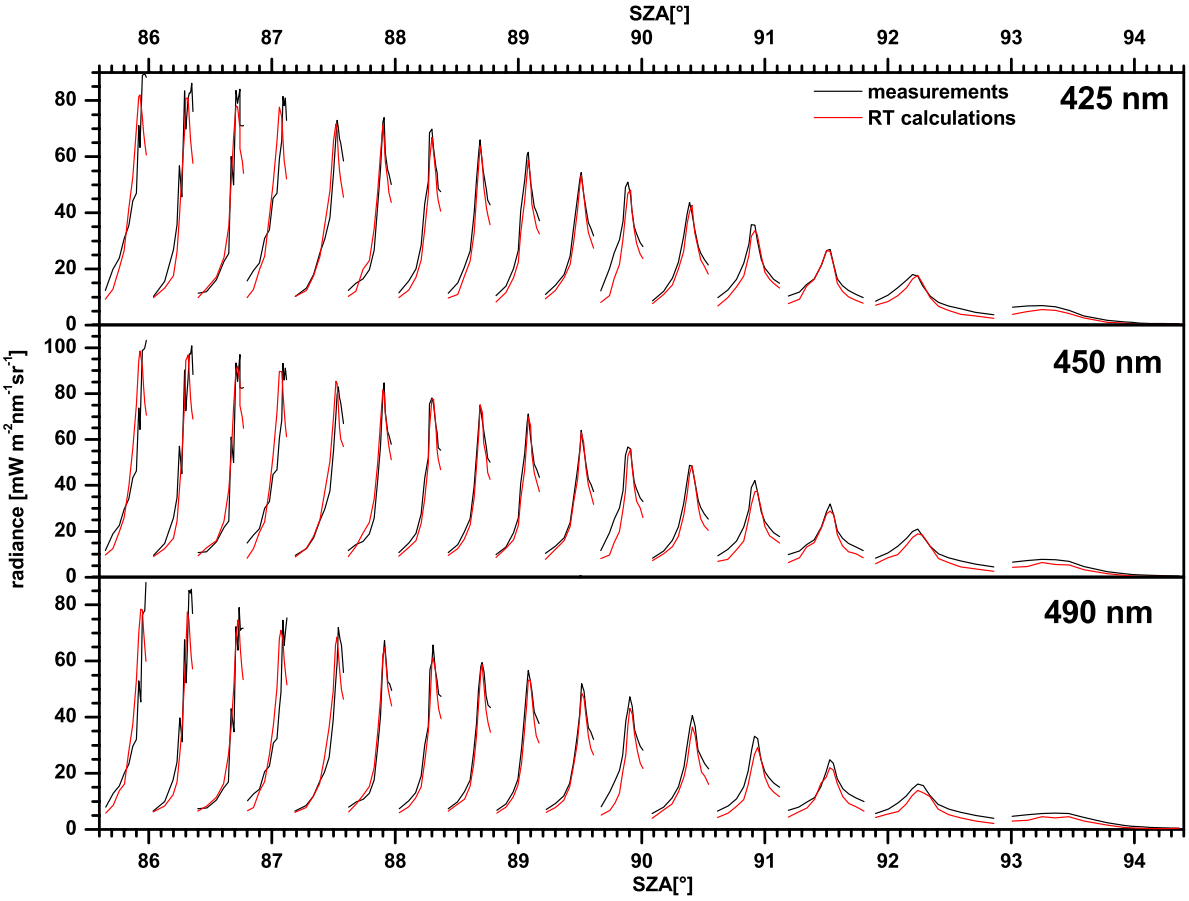

Figure 6.40: Comparison of measured (black lines) and RT calculated radiances vs. SZA for scanning limb measurements during balloon float at 425 nm (upper panel), 450 nm (middle panel), and 490 nm (lower panel).

Now, the limb radiances obtained during scanning limb measurements at balloon float (~ 33 km altitude) for SZAs between 85.6^o and 96.5^o are discussed. Each limb scan covers an elevation angle range of $0.5 - 6.5^o$ below the horizon with a step width of 0.5^o. The tangent heights corresponding to each observation are shown in table 6.5.10.

Figure 6.40 shows a comparison of measured and RT calculated limb radiances for scanning limb measurements. Qualitatively, a very good coincidence for the considered wavelengths between 425 and 490 nm is found. For the first limb scans obtained for $86.6 - 89.5^o$, the deviations are larger caused by stronger elevational gondola oscillations with amplitudes of $1 - 1.5^o$. This results in a rather noisy trend of the measured radiances. As shown in section 5.1.3, amplitudes $> 1^o$ significantly affect the observed limb radiances. For SZA $> 89.5^o$, the gondola oscillations slowed to amplitudes $< 0.5^o$ which are not considered to affect the measured radiances. The azimuthal gondola oscillations have amplitudes between 4^o for the first limb scans and 1^o for the limb scans corresponding to SZA $> 89.5^o$. These small oscillations are not expected to significantly affect the measured radiances. For the limb scans corresponding to SZA $> 90^o$, the RT calculated limb radiances are systematically lower by $10 - 20$ % than measured at all considered wavelengths. An explanation might be a systematic error of the instrument's absolute calibration. Additionally, the uncertainties of the RT calculations are increasing due to the lower number of modeled photons and, thus, increasing statistical error. This can also be seen in the calculated BoxAMF becoming noisier with increasing SZA.

6.5.4 O_3 Results

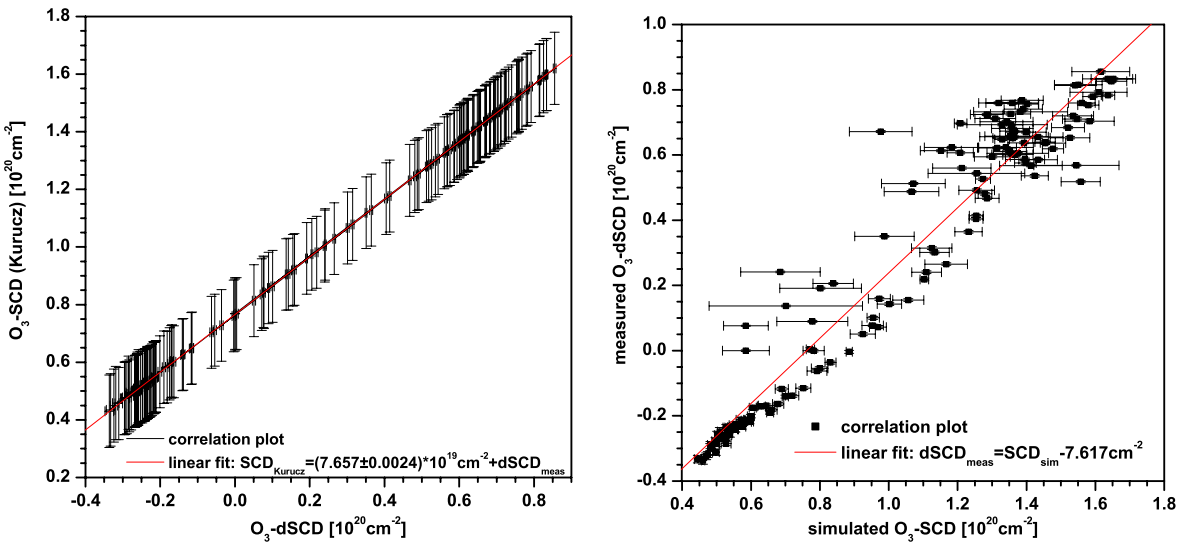

Figure 6.41: Determination of the O_3 absorption of the solar reference spectrum. Left panel: retrieved O_3-SCDs with convolved Kurucz spectrum as solar reference vs. O_3-dSCDs with self recorded solar reference (black squares) and linear fit (red line) of the correlation plot. Right panel: simulated O_3-SCDs vs. measured O_3-dSCDs (black squares) and linear fit (red line) of the correlation plot.

As the DOAS method only gives differential Slant Column Densities (dSCD), i.e. the difference of the O_3 absorbance of the evaluated spectrum and the Fraunhofer reference spectrum, this so-called Fraunhofer offset has to be determined separately. That for, the measured spectra are evaluated with a Kurucz extraterrestrial solar spectrum convolved to the instrument's resolution as reference. This DOAS evaluation shows much higher residuals (RMS residual of $12 \cdot 10^{-3}$ vs. $0.3 \cdot 10^{-3}$ for the self

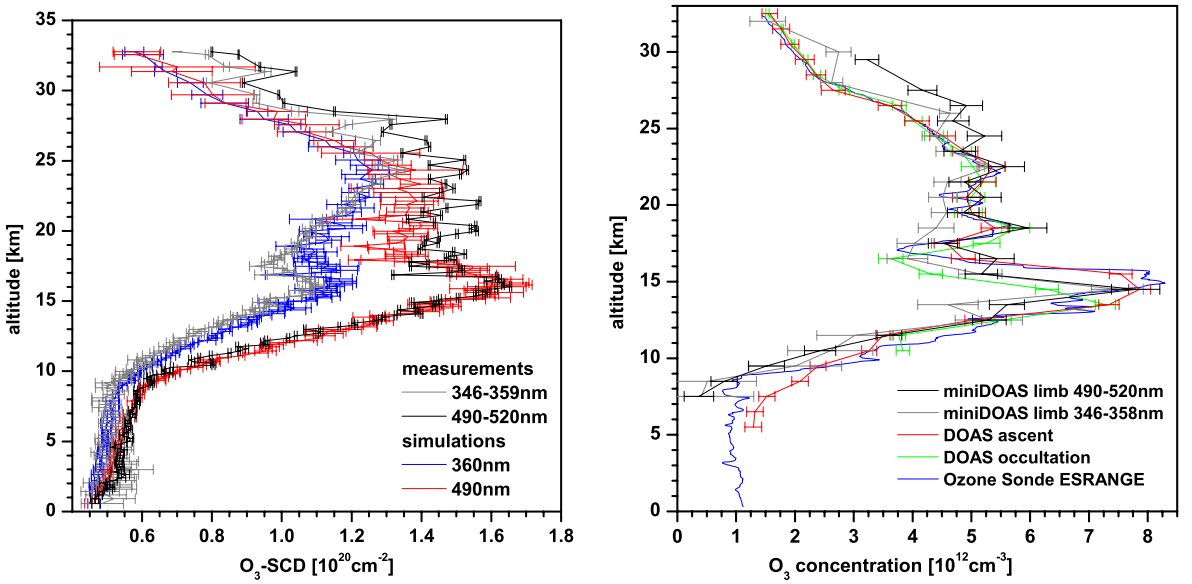

Figure 6.42: Left panel: comparison of measured and simulated O_3-SCD's in the UV and visible spectral range. For the simulations the O_3 profile measured by the ECC Ozone Sonde (see right panel) is used. Right panel: Comparison of retrieved O_3 profiles from miniDOAS limb measurements during balloon ascent in the visible (black line) and UV spectral range (gray line), and direct sunlight DOAS measurements during balloon ascent (red line) and solar occultation (green line). Also shown is the profile from an ECC Ozone Sonde launched $\sim 1\,\mathrm{h}$ after the LPMA/DOAS gondola.

recorded reference). Nevertheless, both SCD trends correlate very well and all structures seen in the precise DOAS evaluation with the self recorded solar reference can also be seen in the case of the Kurucz reference. A linear fit of the correlation plot gives a value of $(7.657 \pm 0.0024) \cdot 10^{19}\,\mathrm{cm}^{-2}$ for the Fraunhofer offset (see fig. 6.41, left panel). In the right panel of the figure a correlation plot of measured dSCDs and simulated SCDs is shown. A linear fit yields an offset value of $7.617 \cdot 10^{19}\,\mathrm{cm}^{-2}$. For the following profile retrieval, a value of $7.6 \cdot 10^{19}\,\mathrm{cm}^{-2}$ is added to the measured dSCD. In figure 6.42 (right panel), the resulting SCDs are shown in comparison to an RT simulation using the ozone sonde profile as input. Except for some deviations above 25 km arising from strong gondola oscillations, both sets of SCDs agree very well. For comparison and as a test of the RT calculations, O_3 is also evaluated in the UV. It is performed in the $346 - 359\,\mathrm{nm}$ wavelength range with the same references used for the evaluation of BrO except that only one O_3 temperature ($T = 223\,\mathrm{K}$) is used. Again, the measured and simulated O_3-SCDs compare very well if a proper value for the Fraunhofer offset ($7 \cdot 10^{19}\,\mathrm{cm}^{-2}$) is added to the measured dSCDs. This underlines the validity of the radiative transfer calculations in the UV.

Figure 6.42 shows a comparison of the retrieved profiles from the miniDOAS measurements in the UV and visible spectral range as well as the O_3 profiles obtained from the direct sunlight DOAS during balloon ascent and solar occultation and the ECC sonde. Generally, a good agreement is found between the profiles. Only above 25 km, the miniDOAS values are higher than the ones from the otherwise measured profiles. This is most likely due to the strong oscillations of the gondola in this part of the flight which results in strong fluctuations of the measured O_3-SCD's and, thus, the obtained O_3 concentration values above 25 km so that these values are not shown. In the UV, the measurements are affected less by these gondola movements so that the retrieved profile is rather smooth up to 30 km.

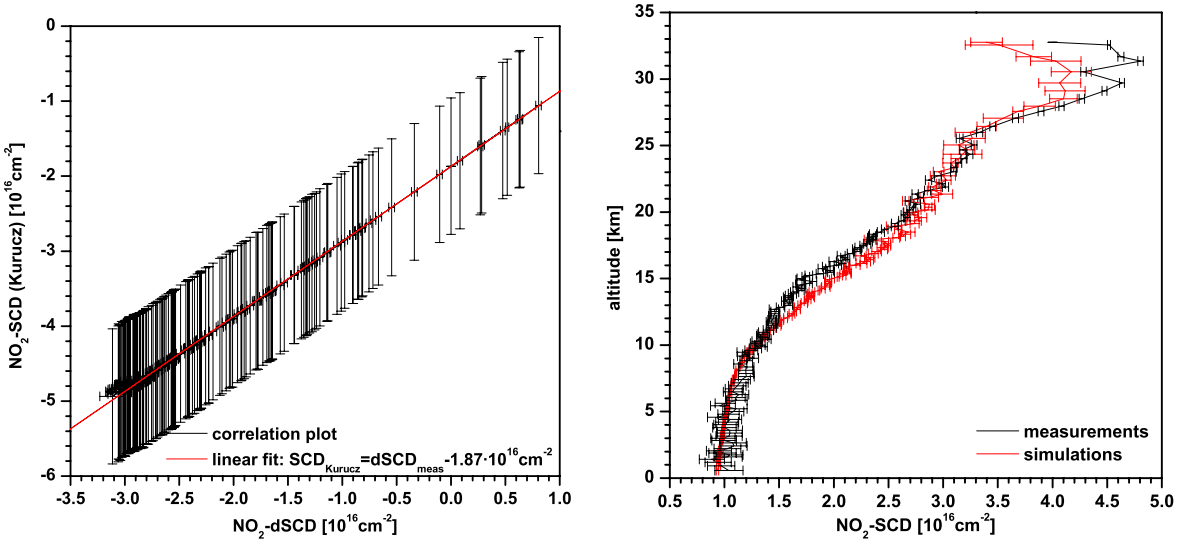

Figure 6.43: Left panel: same as fig. 6.41 (right panel) but for an NO_2 DOAS evaluation. Right panel: Comparison of measured and simulated NO_2-SCDs. For the simulation the NO_2 profile measured by direct sunlight DOAS during balloon ascent (see figure 6.44, left panel) is used.

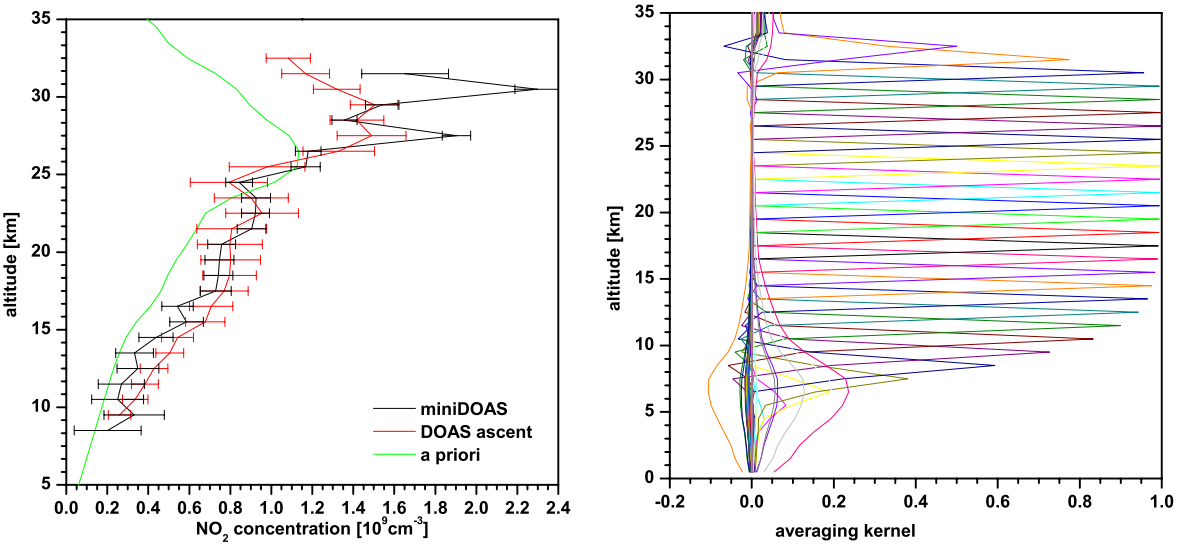

Figure 6.44: Left panel: Comparison of retrieved NO_2 profiles from miniDOAS limb measurements during balloon ascent for 1 km grid size (black line), and direct sunlight DOAS measurements during balloon ascent (red line). Also shown is the a priori used for the profile inversion. Right panel: Averaging kernels of the miniDOAS profile retrieval shown in the left panel.

6.5.5 NO_2 Results

The the steps in the NO_2 profile retrieval are basically the same as in the case of O_3. A particular problem, however, is the determination of the Fraunhofer offset. The method of using a convolved Kurucz spectrum as refernce is not possible which can be seen in fig. 6.43. Again, the correlation between the SCD values obtained with the Kurucz and the self-recorded solar reference is excellent, despite the high residual of the Kurucz fit. But the results of the Kurucz fit are definitely wrong as they are all negative. This means that there must be a systematic, constant offset that is found by the DOAS fit in all spectra. Changing the spectral region of the NO_2 DOAS evaluation results in totally different values for this offset. It is difficult to find a reason for this behavior as the NO_2 optical density in the Kurucz DOAS evaluations are generally much lower than the residual, i.e. the NO_2 absorption cannot be seen with the eye.

In order to be able to retrieve a profile, despite that, the Fraunhofer offset is determined by comparing the measured and simulated SCDs (fig. 6.43). This comparison yields a value for the offset of $4 \cdot 10^{16}\,\mathrm{cm}^{-2}$. An uncertainty of 5 % is assumed dor this value, so a second profile retrieval is performed with $3.8 \cdot 10^{16}\,\mathrm{cm}^{-2}$. The NO_2- SCD measurements are affected by elevational oscillations of the gondola above 25 km which leads to significantly larger measured SCDs than simulated.

The NO_2 concentration profile retrieved an a 1 km is shown in figure 6.44 (left panel) compared to a profile inferred from direct sunlight DOAS measurements during balloon ascent. The averaging kernels of the miniDOAS profile retrieval are shown in the right panel. The difference of the retrieved profiles with $4 \cdot 10^{16}\,\mathrm{cm}^{-2}$ and $3.8 \cdot 10^{16}\,\mathrm{cm}^{-2}$ offset is added to the error of the profile retrieval to account for the uncertainty of the determination of the solar reference offset. From the averaging kernels it can be seen that the miniDOAS limb measurements are sensitive to NO_2 for altitudes between 7 and 32 km with averaging kernels reaching 1 for the $15 - 30$ km range. For altitudes below 15 km the averaging kernels are monotonically decreasing to values of ~ 0.6 at the $8 - 9$ km layer and ~ 0.4 at the $7 - 8$ km layer indicating the decreasing sensitivity with decreasing altitude. For altitudes between 7 and 27 km the profiles inferred from the two measurement techniques match within the respective error bars. For altitudes above 27 km the miniDOAS profile shows much higher concentrations compared to the DOAS profile which is due to the too high SCDs measured at these altitudes due to the elevational gondola oscillations. So the values for these altitudes are believed to be unrealistic. The local SZA for both measurements is between 76.8^o and 85.4^o at 10 km and float altitude (~ 33 km).

6.5.6 BrO Results

As the determination of the Fraunhofer offset by a Kurucz fit is not possible for a small absorber like BrO, it is taken from the RT simulations. As input the BrO profile measured with the direct sunlight DOAS spectrometer is used between 10 and 30 km. Outside this altitude range the output of the SLIMCAT model for SZA=85.4^o, which is the SZA of the solar reference spectrum, is used. The model output is very reliable for altitudes above 30 km which are input for the determination of the Fraunhofer offset and the photochemical changes are small for SZA>90 at these altitudes. Its value is found to be $1.6 \cdot 10^{14}\,\mathrm{cm}^{-2}$. Fig. 6.45 (left panel) shows a comparison of the modeled and simulated BrO-SCD's. Between 10 km and 23 km they agree quite well. Below 10 km the agreement becomes poorer which can be explained by the high uncertainties of the DOAS evaluation due to the high residuals causing the SCDs to be below the detection limit assumed as twice the DOAS fit error. These high residuals for low altitudes are a result of the poorly saturated spectra in the UV because of the low UV radiance and the spectral shift of the spectra because of instrumental instability (see fig. 6.35). With increasing altitude the residuals become lower and the obtained SCDs become more reliable with less fluctuations. Above 23 km the gondola instabilities, which affect strongly the miniDOAS measurements but also slightly

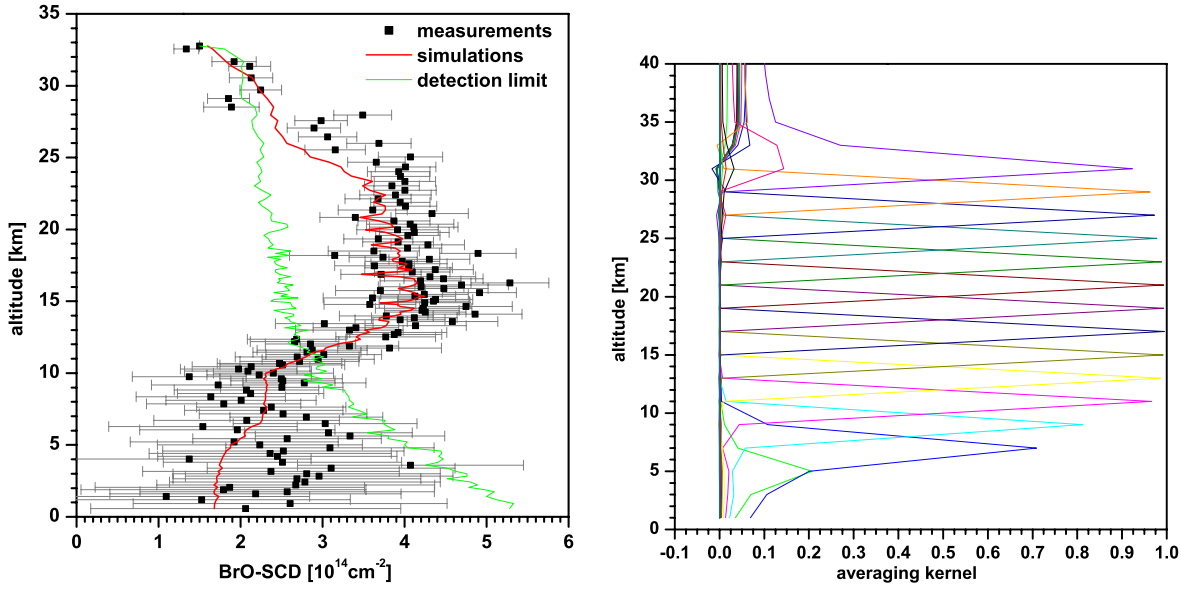

Figure 6.45: Left panel: comparison of measured (black line) and simulated (red line) BrO-SCDs. For the simulations the BrO profile measured by the direct sunlight DOAS spectrograph (see right panel) is used. Also shown is the detection limit (green line) given by twice the DOAS retrieval error. Right panel: averaging kernels for the BrO profile retrieval shown in figure 6.46.

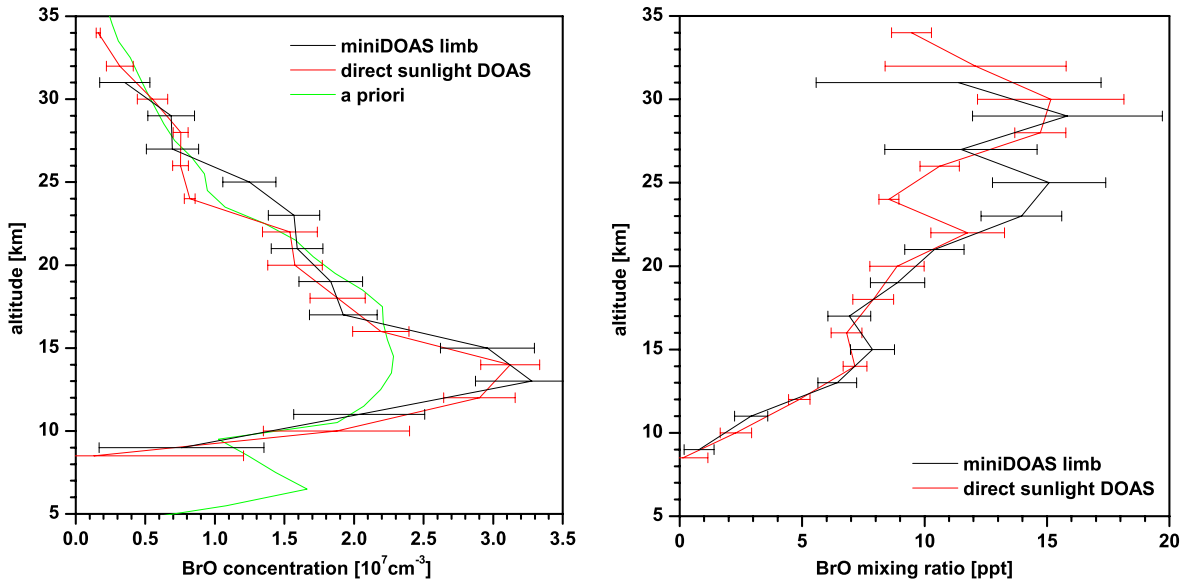

Figure 6.46: Comparison of retrieved BrO profiles from miniDOAS limb measurements during balloon ascent (black lines), and direct sunlight DOAS measurements during balloon ascent (red lines). The left panel shows concentration and the right panel mixing ratio profiles. Also shown is the a priori profile (green line) used for the retrieval.

the direct sunlight measurements, are an explanation for the discrepancy between the simulated and measured SCD values.

Fig. 6.46 shows the retrieved profile of the miniDOAS limb and the direct sunlight DOAS measurements during balloon ascent. Because of the high fluctuations of the miniDOAS BrO-SCDs an altitude grid of 2 km is chosen. On this grid a smooth profile is obtained and the averaging kernels are close to 1 for $10 - 32$ km of altitude. The miniDOAS BrO profile compares well with the DOAS profile in the $11 - 23$ km range. Above 23 km the two profiles show some discrepancies that have already been discussed for the SCD comparison. As in the case of NO_2 profile retrieval, the much higher uncertainties of the miniDOAS limb measured BrO-SCDs compared to the SCDs of the direct sunlight DOAS measurements are compensated by the better conditioning of the inversion problem (i.e. BoxAMFs with sharp maximum at the detector altitude) so that both profiles have similar uncertainties. The error arising from the uncertainty of the Fraunhofer reference offset (assumed to $0.1 \cdot 10^{14}\,\mathrm{cm}^{-2}$) is only a minor contribution (~ 20 %) of the shown total error. Its effect on the shown profile is only around 2 %. The total uncertainty of the retrieved profile lies between ~ 12 % in the $12 - 26$ km range and significantly higher below and above as concentrations are much lower. For more details on the error calculations see section 5.2.4. As discussed in section 5.2.2, the effect of the photochemical changes of the BrO concentration during balloon ascent on the retrieved profile is assumed as small. The SZA ranges from 76.5^o at 9 km, 79^o at 15 km where the maximum concentrations are found, and 85.4^o at float altitude of ~ 33 km. As the limb measurements are very sensitive to the concentrations at the actual detector altitude, the retrieved profile is assumed to represent the situation of the time the BrO maximum is observed, i.e. SZA $\approx 79^o$. The retrieved mixing ratios of ~ 10 ppt around 20 km and ~ 15 ppt around 25 km are in reasonable agreement with the current understanding of stratospheric bromine chemistry and previous DOAS balloon measurements at the same place and conditions (compare e.g. *Harder et al.* (1998); *Fitzenberger* (2000)).

6.5.7 O_4 Results

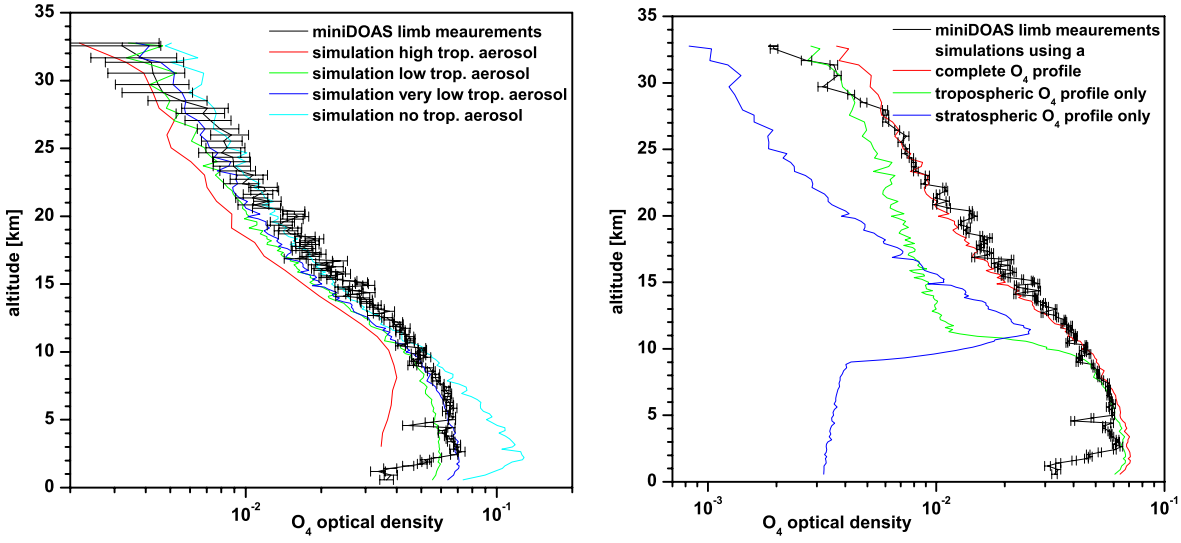

Figure 6.47: Measured O_4-ODs (black lines) compared to simulations (colored lines) using different tropospheric aerosol scenarios (left panel) and O_4 profiles (right panel). For details of the aerosol scenarios see section 5.1.5. Right panel: For the tropospheric O_4 profile (green line) the O_4 concentration is set to 0 for all altitudes above 9 km while for the stratospheric profile (blue line) all values ≤ 9 km are set to 0.

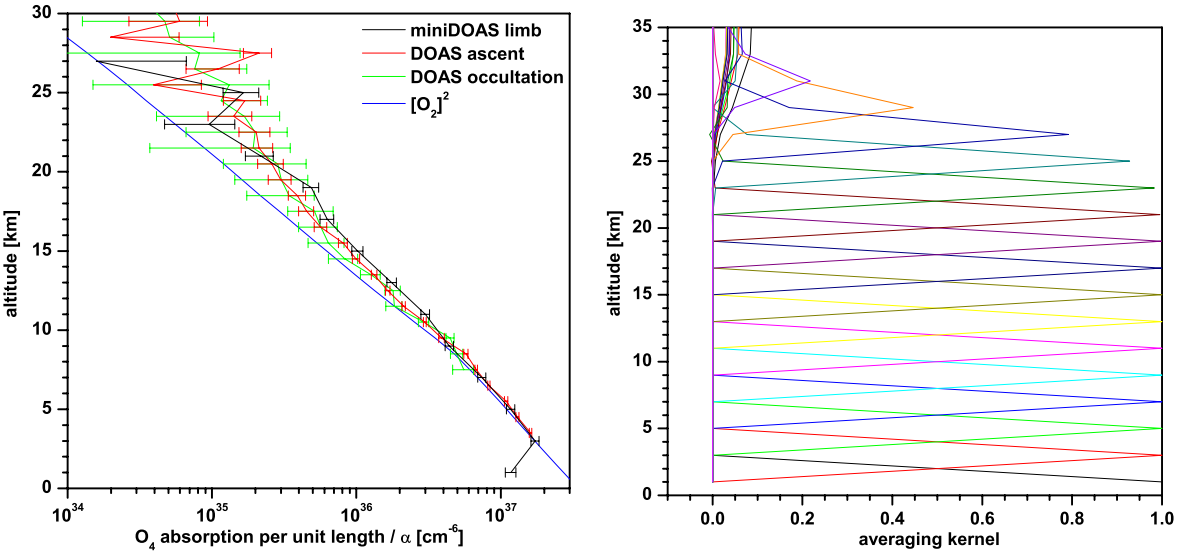

Figure 6.48: Left panel: O_4-profile retrieved from miniDOAS limb measurements (black line) compared to the profiles retrieved from direct sunlight DOAS measurements during balloon ascent (red line) and solar occultation (green line), respectively. Shown is the O_4 absorption per unit length multiplied by the peak O_4 collision pair absorption cross section α_i. For comparison, the O_2-concentration squared ($[O_2]^2$, blue line) is shown. Right panel: Averaging kernels for the miniDOAS O_4 profile retrieval shown in the left panel.

As the O_4-SCDs are especially sensitive to the tropospheric light path (because the O_4 concentration decreases exponentially with altitude), and the tropospheric light path is - in contrast to the stratospheric light path - very sensitive to the aerosol load, the O_4 measurements can be used to investigate the tropospheric aerosol loads (*Wagner et al.*, 2002, 2004). Figure 6.47 (left panel)[3] shows a comparison of measured and simulated O_4-ODs for several tropospheric aerosol scenarios as described in section 5.1.5. It can be seen that the O_4-ODs agree best with the simulation using very low tropospheric aerosol load (blue line). This aerosol load is quite reasonable for a remote and, thus, rather unpolluted area like northern Scandinavia. It can be seen that the simulations with high aerosol load (red line) - a scenario typical for heavily polluted areas - do not match the measurements as well as the simulations without any tropospheric aerosols (cyan line). This underlines the validity of the TRACY treatment of aerosol scattering. For altitudes below 5 km some, and for altitudes below 2.5 km all, measured SCDs are considerably smaller than the simulated ones. A reason for this can be clouds which are not considered in the RT calculations but can significantly shorten the range of sight and thus decrease the BoxAMF and O_4-OD. The biggest uncertainty of the miniDOAS measurements is the O_4 absorption contained in the Fraunhofer reference spectrum. A number of $3.2 \cdot 10^{-3}$ is found and added to the measured differential optical densities. However, the impact of the Fraunhofer offset is negligible in the troposphere as O_4-ODs reach values around $8 \cdot 10^{-2}$. In another exercise, the sensitivity of the measurements towards the O_4 concentration for different balloon altitudes is studied. Therefore, the O_4 profile is split into a tropospheric profile (i.e. all values for altitudes > 9 km are set to 0) and a stratospheric one (consequently, all values for altitudes ≤ 9 km are set to 0). The simulations using these two profiles compared to a simulation using the entire O_4 profile and to the measurements is shown in figure 6.47 (right panel). The green and blue lines, show the contribution of the tropospheric and stratospheric profile, respectively, to the total simulated OD (red line). In the troposphere (i.e. below 9 km), the stratosphere only contributes by ~ 5 % to the total O_4-OD. In the lower stratosphere, stratospheric and tropospheric values contribute equally to the measured OD but the stratospheric contributions

[3]For a definition of the quantities used in this section see section 6.3.6

drops to $\sim$ 10 % around 30 km as the O_4-concentration decreases exponentially with altitude, while the tropospheric BoxAMFs decrease only little with increasing balloon altitude. This means that the sensitivity of the measurements decreases with altitude.

The measured O_4-ODs are inverted and the resulting vertical optical densities are divided by the height of each layer using the same algorithm as in the case of all the other trace gases. This results in a vertical profile of the O_4 absorption per unit length. This profile is divided by the peak O_4 collision pair cross section α_i of the respective O_4 absorption band used for the DOAS evaluation. Because of the definition of σ the result of this procedure is not the O_4 concentration but the O_2-concentration squared ($[O_2]^2 = 0.2094 \cdot p/(k_B \cdot T)$). Figure 6.48 (left panel) shows a comparison of the retrieved profiles from miniDOAS limb and direct sunlight DOAS measurements and also $[O_2]^2$. The errors are calculated as described in section 5.2.4. From the averaging kernels (figure 6.48, right panel), it can be seen that the measurements are sensitive up to 27 km so the retrieved profile is shown only up to this altitude. Except for the value at 1 km which os most likely affected by clouds, the measured profiles compare quite well within the error bars. While the calculated $[O_2]^2$ compares quite nicely to the measured profiles up to 11 km, the measured profiles have increasingly higher values with increasing altitude. An explanation for this is the non-accounting temperature dependence. As the O_4 cross section increases with decreasing temperature, the measured O_4 optical densities are systematically too low as the atmospheric temperatures were below 0^oC and the used O_4 cross section was recorded at room temperature. Another possible explanation might be the decreasing sensitivity of the measurements of both methods to O_4 with increasing altitude due to the increasing effect of tropospheric O_4 to the measured O_4-ODs in the case of the limb measurements, and the very low O_4-ODs for higher altitudes in the direct sunlight case. Also the uncertainty of the Fraunhofer offset of the O_4-OD might be a reason for the observed discrepancies as it affects the lower ODs measured at high altitudes more than the much higher ODs measured at lower altitudes.

6.5.8 H_2O Results

The water vapor mixing ratio is derived from the dew point profile measured by the Ozone Sonde launched from Esrange $\sim$ 2 h after the LPMA/DOAS payload. From the dew point θ_D one can approximately calculate the H_2O partial pressure p_{H_2O} for every altitude using Magnus' Formula:

$$p_{H_2O} = C_1 \cdot \exp\left(\frac{C_2 \cdot \theta_D}{C_3 + \theta_D}\right);$$

$$\text{where } C_1 = 610.78\,\text{Pa};\ C_2 = 17.84362;\ C_3 = 245.425^oC; (\theta_D < 0^oC). \tag{6.3}$$

Dividing this result by the actual pressure which is also measured by the Ozone Sonde gives the H_2O mixing ratio (see fig. 6.49 left panel). With the air density derived from the measured temperature and pressure profile one can derive a concentration profile (see fig. 6.49 right panel). As the water vapor measurements of the Ozone Sonde get less accurate with increasing altitude, a constant mixing ratio of 6 ppm is assumed for altitudes above 28 km. However, these uncertainties in the stratospheric water vapor profile don't affect the quality of the simulations (see below).

In figure 6.50 comparisons of measured and simulated H_2O-SCDs are shown. In the left panel a comparison of the measurements to simulations using the same H_2O concentration profile but different tropospheric aerosol scenarios as described in section 5.1.5. The results are very similar to the case of O_4, as the water vapor concentration is also maximum on the ground and strongly decreases with increasing altitude. For high tropospheric aerosol loads the simulated H_2O-SCDs (red line) are much below the measured ones (black line). Assuming no tropospheric aerosol in the simulation, the simulated H_2O-SCDs (cyan lines) are much above the measured ones especially at low altitudes (below

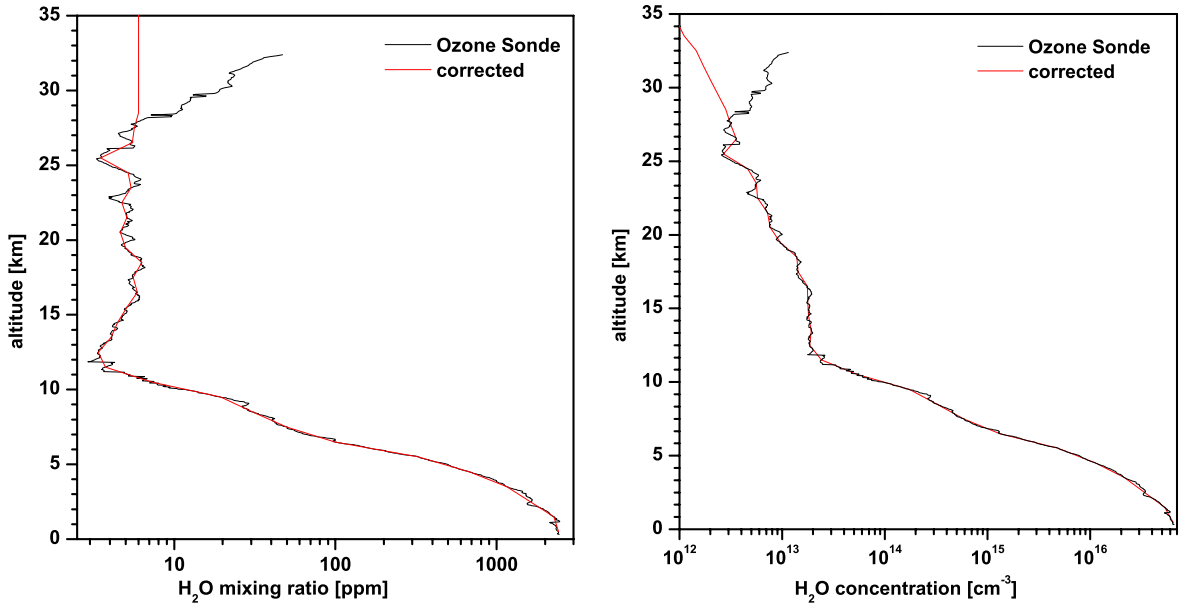

Figure 6.49: Water vapor mixing ratio (left panel) and concentration (right panel) profile obtained from the Ozone Sonde relative humidity measurements. The raw measurements are plotted in red and the profile actually used for the simulation in black.

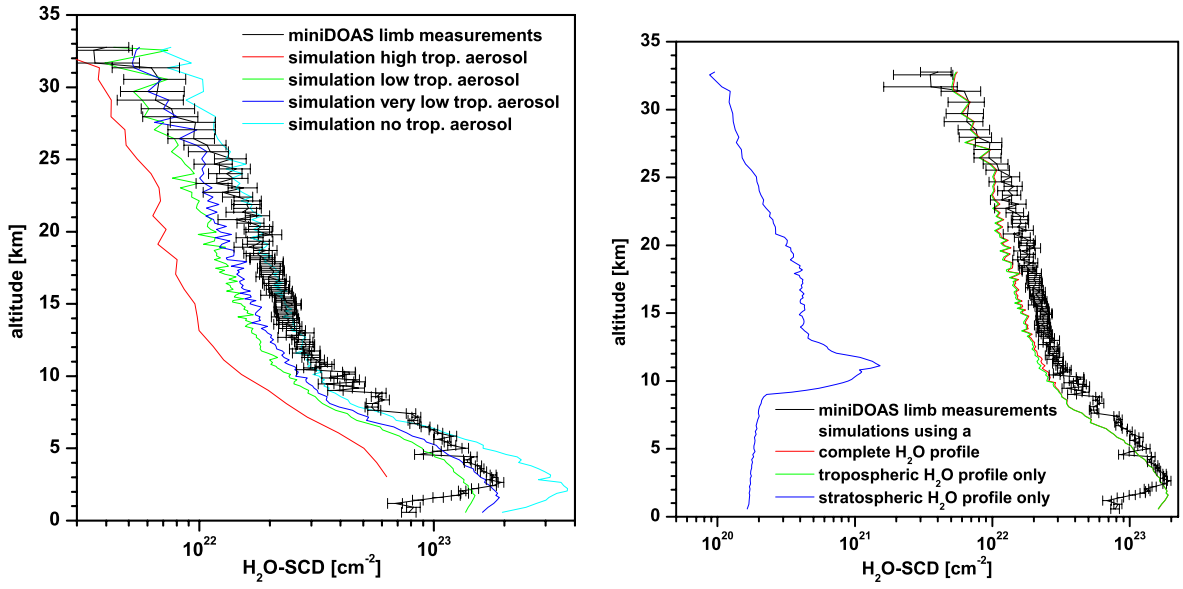

Figure 6.50: Left panel: Comparison of measured (black line) and simulated (colored lines) H_2O-SCDs for several tropospheric aerosol scenarios. Right panel: Comparison of measured (black line) and simulated (red line) H_2O-SCDs. For the simulation of tropospheric water vapor (green line), all values in the H_2O-profile above $9\,\mathrm{km}$ are set to zero, and for the stratospheric simulation (blue line), all values below $9\,\mathrm{km}$ are set to zero.

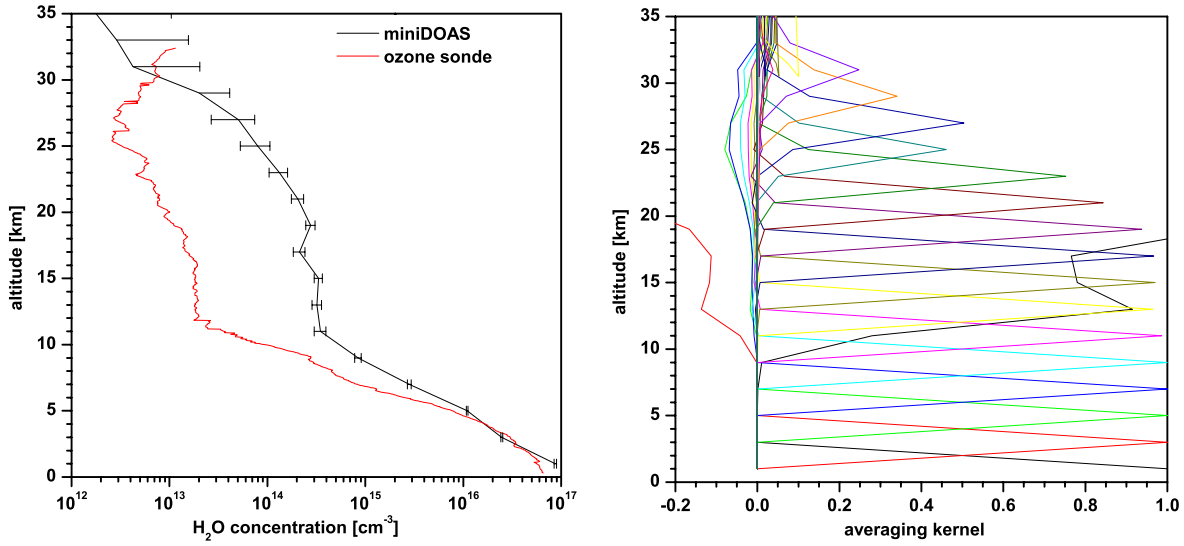

Figure 6.51: Left panel: H_2O concentration profile inferred from miniDOAS limb measurements (black line) and ozone sonde measurements (red line). Right panel: Averaging kernels for the miniDOAS profile inversion.

$\sim 6\,\mathrm{km}$). As in the case of O_4, the best match between measurements and simulations in the troposphere is found for the very low aerosol load scenario (blue line). As already discussed in section 5.2.1, the miniDOAS limb measurements are totally insensitive to stratospheric water vapor. This can be seen in 6.50, right panel). It is obvious that small stratospheric contributions to the total SCDs in the order of $10^{20} - 10^{21}\,\mathrm{cm}^{-2}$ cannot be sensitively measured as the typical DOAS error of the H_2O evaluation is $> 10^{21}\,\mathrm{cm}^{-2}$. Also the uncertainty of the solar reference offset is of this order of magnitude. Under these conditions, the comparison between measured and simulated SCDs is very good above $\sim 7\,\mathrm{km}$. The good qualitative agreement between the measured and simulated SCD demonstrates that the RT calculations are very accurate also for altitude layers that are not directly seen by the telescope but only by multiple scattered photons. However, the simulated H_2O-SCDs are generally higher than the measured ones above 7 km. There are several potential reasons for this discrepancy: as always when comparing SCDs, there is the uncertainty of the trace gas amount in the reference spectrum which is obtained from the simulations for the uppermost measurements. However, the effect of the offset which is assumed as $4 \cdot 10^{21}\,\mathrm{cm}^{-2}$ is small for lower altitudes where the measured dSCDs are several $10^{22}\,\mathrm{cm}^{-2}$. Another reason is the fact that the tropospheric water vapor concentration as well as the cloud cover is highly variable spatially and temporally so that the conditions seen from the gondola can be different than the one measured by the ozone sonde. Also the lowermost measurements (below 2.5 km) might be affected by clouds. As clouds largely shorten the light path in the altitude levels the balloon is actually in, the measured SCDs are much lower than the simulated ones since no clouds are considered in the RT calculations. But also the gondola movements which are rather strong shortly after launch might be an explanation for the observed discrepancies.

A profile inversion is shown in figure 6.51. From the averaging kernels (right panel), it can be seen that the retrieval is independent from the a priori profile up to 20 km. In the troposphere, the obtained H_2O concentrations are reasonable and match quite well with the values measured by the ozone sonde up to 5 km. In the stratosphere, however, the retrieved concentrations show huge discrepancies which is due to the afore discussed fact that the stratospheric water vapor contributes by at most 5 % to the total SCD. Considering the uncertainties in both the measurement and the RT calculations it is clear that the limb observations are not sensitive to the small stratospheric H_2O concentrations in front of the large tropospheric background.

6.5.9 Upper Limits of Stratospheric IO

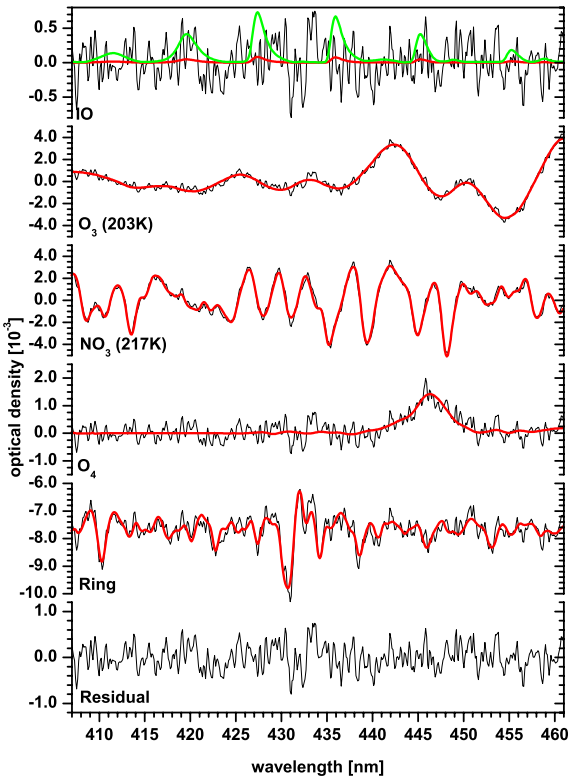

Figure 6.52: Sample DOAS evaluation in the $407 - 461\,\mathrm{nm}$ range for a limb observation during balloon ascent ($15.5\,\mathrm{km}$ altitude, -1.5^o elevation angle, 90^o azimuth angle, and 79.2^o SZA) using a Fraunhofer reference spectrum recorded at $32.77\,\mathrm{km}$ altitude, -1.5^o elevation angle, 90^o azimuth angle, and 85.4^o SZA. Shown is the optical density of the absorbance of the trace gases and Ring cross section (red lines) and the latter plus the residual structure (black lines). Also shown is the RT simulated IO optical density (green line) assuming a constant IO mixing ratio of $0.5\,\mathrm{ppt}$.

The measured spectra are also searched for IO absorption. No IO significantly above the detection limit given as twice the DOAS evaluation error as calculated by the WinDOAS tool is found. Several fit regions in the $400 - 465\,\mathrm{nm}$ range have been tested. The results presented in this section are obtained in the $407 - 461\,\mathrm{nm}$ interval and the same cross sections as for the NO_2 evaluation are used. Additionally, an IO cross section measured by *Hönninger* (1999) at $T = 295\,\mathrm{K}$ and $p = 10\,\mathrm{mbar}$ with $0.085 - 0.095\,\mathrm{nm}$ resolution, convolved with the miniDOAS slit function, is used. A sample DOAS evaluation for a stratospheric spectrum measured at $15.5\,\mathrm{km}$ is shown in figure 6.52 (for details see figure caption).

The question discussed in the following is how much IO can reside in the atmosphere without being detected by the miniDOAS instrument with the given residuals, i.e. which IO upper limits can be inferred from the measurements. Therefore RT simulations of IO-dSCDs are performed. The key problem is that the limb scatter measurements are also sensitive to the IO concentrations below and above the detector altitude, so the shape of the IO profile plays a role. As no IO profile measurements exist, a constant mixing ratio is assumed. Figure 6.53 shows simulated IO-dSCDs for assumed IO mixing ratios between 0.1 and 1 ppt. Also shown are the retrieved IO-dSCDs which are always below the detection limit indicated by the $2-\sigma$ DOAS error. In the lower stratosphere up to $18\,\mathrm{km}$, the inferred

detection limit corresponds to IO mixing ratios < 0.2 ppt. With increasing altitude, the concentrations corresponding to constant mixing ratio are decreasing due to decreasing air density and, thus, the inferred upper limits are increasing, e.g. to 0.3 ppt at 22 km, 0.5 ppt at 26 km and 1 ppt at 30 km, because the DOAS residuals are almost constant with altitude. For altitudes below 10 km, the obtained upper limits increase due to the strongly increasing residuals caused by the spectral shift of the optical imaging and the decreasing simulated dSCDs due to decreasing BoxAMFs because of lower SZAs. Note that the numbers are only rough estimations based on the assumption of constant IO mixing ratio. For other profile shapes, e.g. decreasing mixing ratio with decreasing altitude, the upper limits are higher. Also the exact determination of the detection limit of a DOAS evaluation is problematic. For the used definition of twice the DOAS error (see equation 3.24), the residual is assumed to consist of white noise. If systematic structures with widths > 1 pixel are present, the detection limit might be higher. Also correlations of the cross sections might cause the DOAS fit to retrieve wrong dSCDs for trace gases at the detection limit. In a similar study by *Bösch et al.* (2003) about IO upper limits inferred from solar occultation measurements, fake IO is retrieved by the DOAS fit if the center-to-limb darkening effect is not properly corrected for. However, this effect does not occur for limb scattering observation as always all the light from the entire solar disk contributes to the skylight.

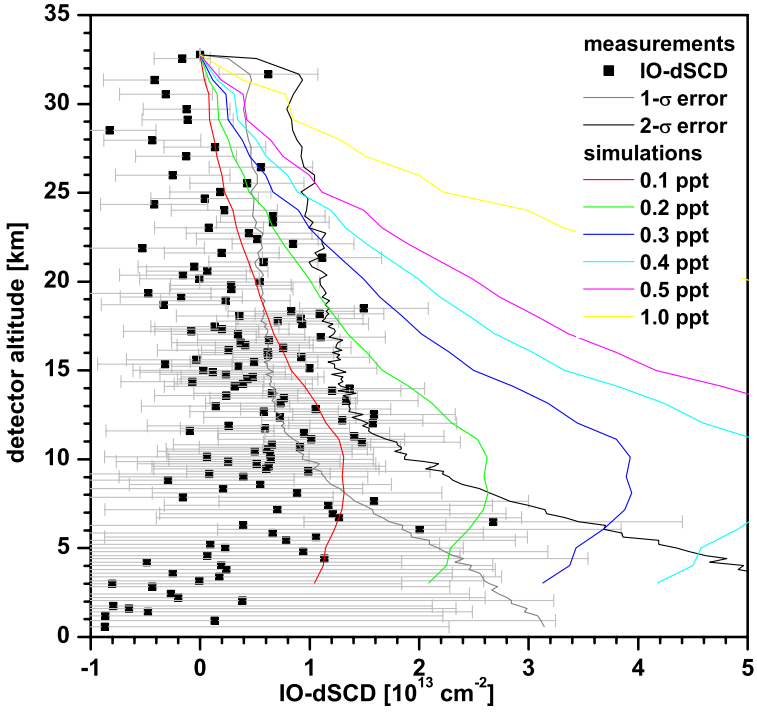

Figure 6.53: Measured (black squares, gray error bars) and simulated (colored lines) IO-dSCDs vs. detector altitude. For the simulation, constant atmospheric IO mixing ratios between 0.1 and 1 ppt are assumed. Also shown is the $1-\sigma$ DOAS error (gray line) and the theoretical detection limit given as twice that value ($2-\sigma$ error, black line).

A further test to obtain an upper limit is performed by looking directly at the DOAS evaluation itself. Therefore, the optical density of the IO absorption assuming a constant IO mixing ratio of 0.5 ppt is simulated. It is shown in figure 6.52 by a green line together with the residual. It is clearly seen that an IO absorption of this optical density should be detected by the DOAS fit. *Stutz and Platt* (1996) pointed out that a DOAS fit is able to detect optical densities below what is visible by the eye. Hence, the detection limits as given by the above mentioned formula seem reasonable.

The estimated upper limits are in reasonable agreement with previous studies. Direct sunlight observation at large air masses either from Kitt peak (*Wennberg et al.*, 1997) find upper limits of the total atmospheric I_y column of 0.2 $(+0.2/-0.1)$ ppt. Balloon-borne SAOZ measurements (*Pundt et al.*, 1998) yield an upper limit of IO of 0.2 ± 0.1 ppt for the lower stratosphere. The lowest upper limits are reported by *Bösch et al.* (2003) inferred from solar occultation DOAS balloon measurements. The lowest values are 0.10 ppt, 0.07 ppt, and 0.06 ppt for 20, 15 and 12.5 km, respectively. Somewhat contradictory to these studies, *Wittrock et al.* (2000) report that stratospheric IO could occasionally have been as large as $0.65 - 0.8$ (± 0.2) ppt.

6.5.10 Scanning Limb Measurements

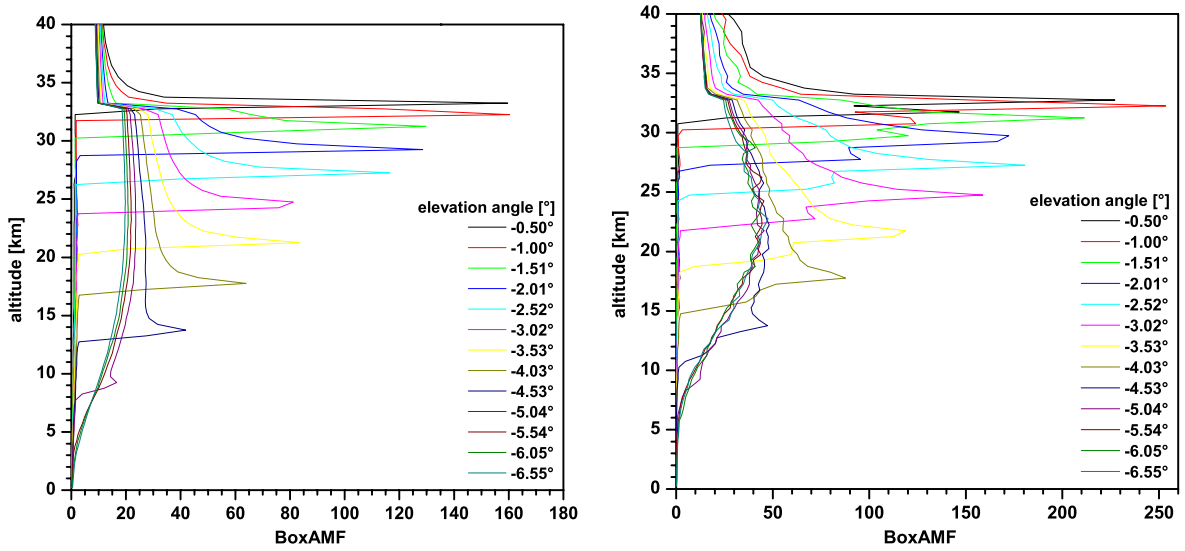

Figure 6.54: RT calculated BoxAMF vs. altitude as a function of detector elevation angle for the 1^{st} (left panel) and the 14^{th} (right panel) limb scan, corresponding an SZA range of $85.6 - 86.0^o$ and $91.2 - 91.8^o$, respectively.

This section discusses the trace gas information obtained from scanning limb observations at balloon float ($\sim$ 33 km altitude) for SZAs between 85.6^o and 96.5^o. Each limb scan covers an elevation angle range of $0.5 - 6.5^o$ below the horizon with a step width of 0.5^o. The corresponding tangent altitudes defined as the altitude layer with maximum BoxAMF are shown in table 6.5.10. The BoxAMF for the 1^{st} and 14^{th} limb scan, corresponding to an SZA range of $85.6 - 86.0^o$ and $91.2 - 91.8^o$, respectively, are shown in figure 6.54. Obviously, the tangent altitudes decrease with decreasing elevation angle. The distances between the tangent heights for one observation to the next is increasing with decreasing elevation angle for constant step width. The definition of a tangent heights becomes more and more difficult with decreasing elevation angle as the maxima become less pronounced. For elevation angles $< -5^o$, no maxima are seen and the BoxAMF do not significantly change with further decreasing elevation angle. For a more detailed discussion of the BoxAMF for scanning limb geometry see also section 5.1.6.

The primary objective of the scanning limb measurements is to obtain time-dependant profile information of photochemically active radicals like NO_2. To study the sensitivity of the measurements towards photochemical changes, the validity of the TRACY RT calculations is examined by comparing measured and simulated SCDs of the photochemically stable species O_3, O_4, and H_2O. In a second step,

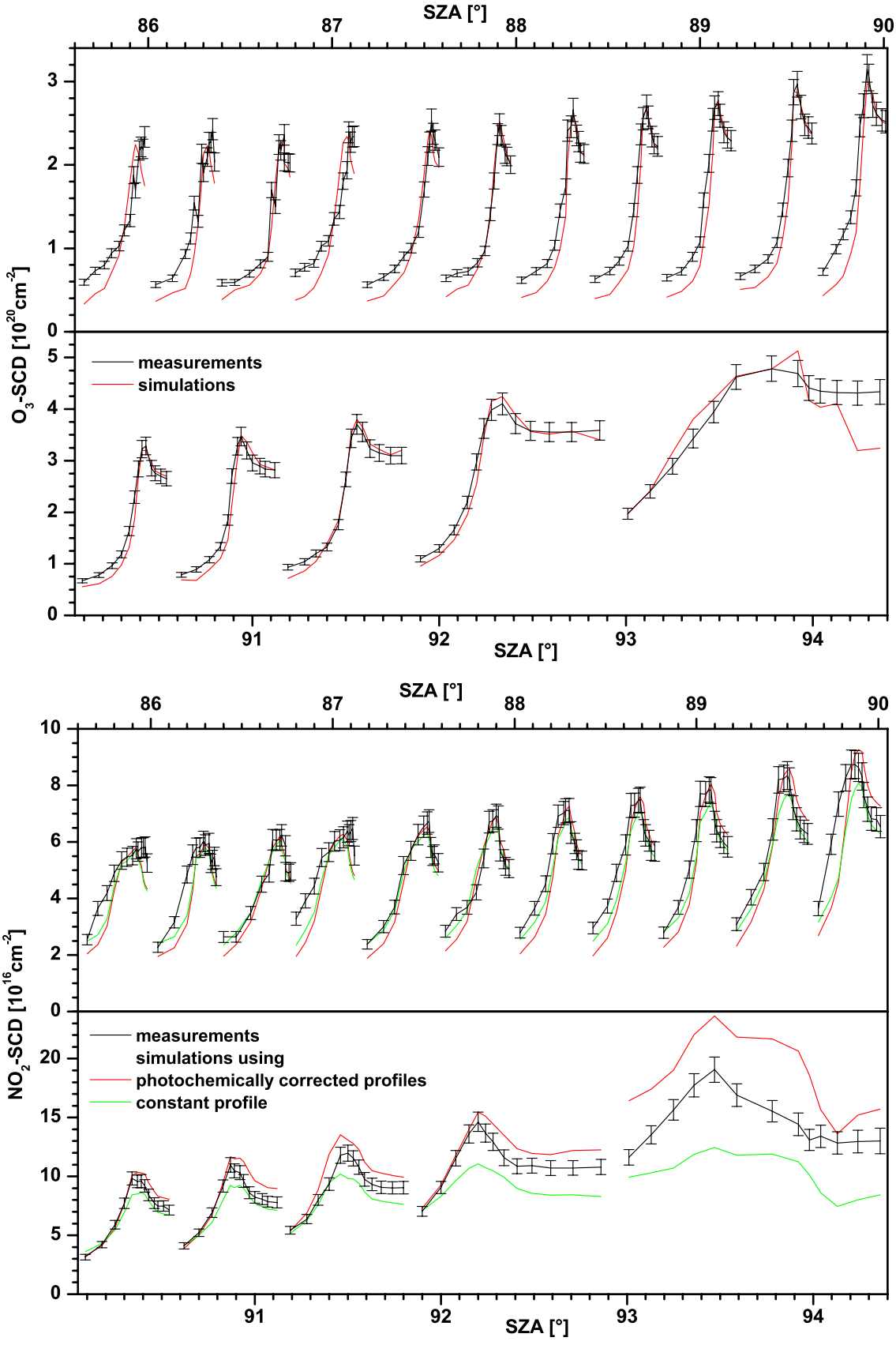

Figure 6.55: Measured (black lines) and simulated (red and green lines) O_3- (upper panel) and NO_2-SCDs (lower panel) for scanning limb measurements at balloon float. For the NO_2- SCD simulation, photochemically corrected profiles (red lines) are used (for details see text). For comparison a simulation using a constant profile obtained from DOAS ascent measurements is shown with green lines.

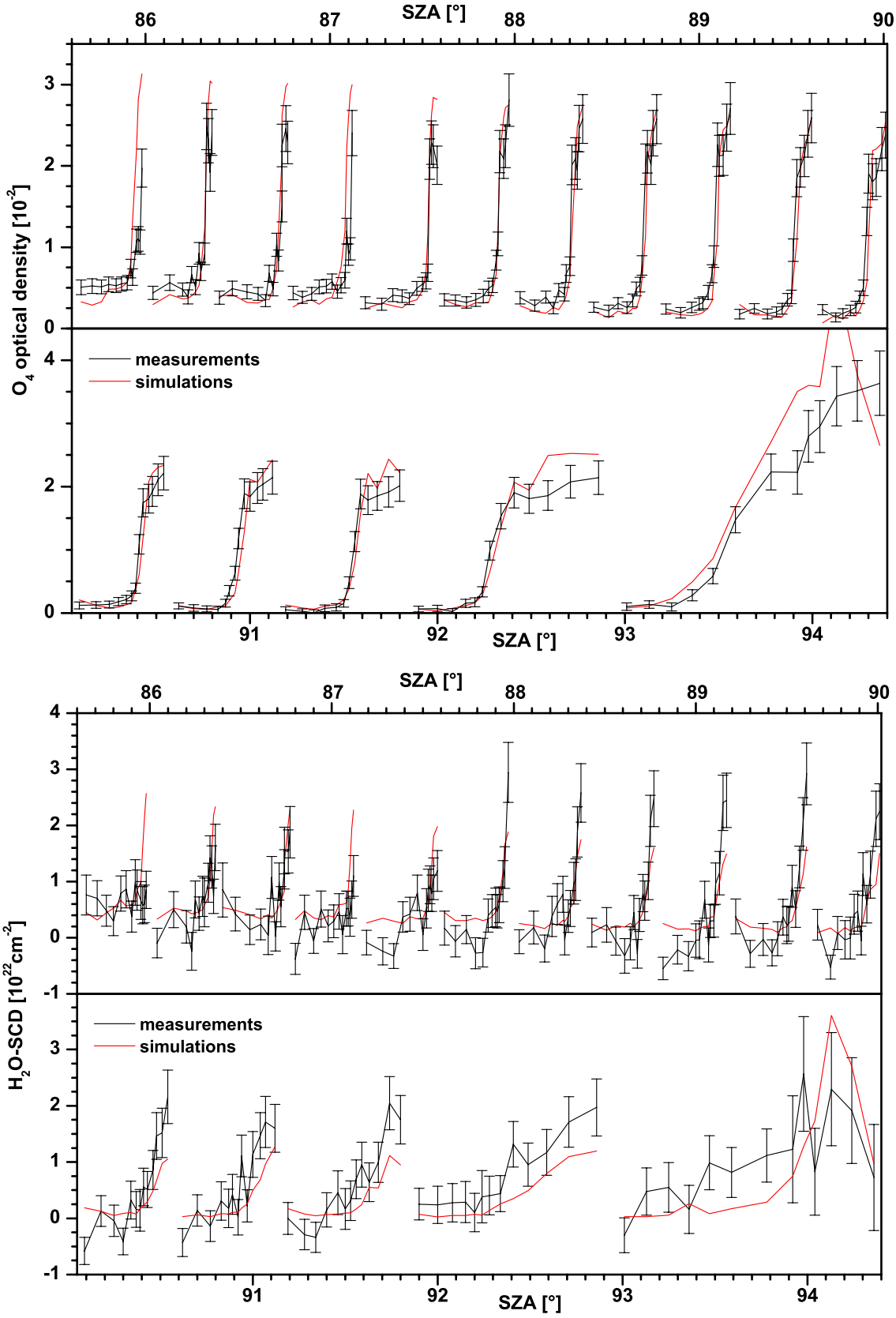

Figure 6.56: Measured (black lines) and simulated (red lines) O_4-ODs (upper panel) and H_2O-SCDs (lower panel) for scanning limb measurements at balloon float.

Table 6.3: Tangent height of the scanning limb observations as a function of detector elevation angle. The tangent heights are given by the altitude layer with maximum BoxAMF.

elevation	tangent height
-0.50^o	$33.0 - 33.5$ km
-1.00^o	$32.0 - 32.5$ km
-1.51^o	$31.0 - 31.5$ km
-2.01^o	$29.0 - 29.5$ km
-2.52^o	$27.0 - 27.5$ km
-3.02^o	$24.5 - 25.0$ km
-3.53^o	$21.0 - 21.5$ km
-4.03^o	$17.5 - 18.0$ km
-4.53^o	$13.5 - 14.0$ km
-5.04^o	$9.0 - 9.5$ km
-5.54^o	–
-6.05^o	–
-6.55^o	–

photochemically scaled NO_2 profiles are used to simulate NO_2- SCDs being compared to the measurements. To account for the photochemistry, for each observation a profile corresponding to the SZA at the balloon's position is calculated. Therefore, NO_2 profiles as function of SZA are calculated using the 1-D box model LABMOS (see section 3.4.2). The qualitative trend of the NO_2 profiles with time is discussed in section 5.2.2.

The inferred trace gas SCDs are shown in figures 6.55 and 6.56. First, the results of the photochemically stable species are discussed. It can be seen for all trace gases that the first limb scans (for SZA $< 88^o$) are affected by the strong elevational gondola oscillations with amplitudes of $3-1.5^o$ resulting in fluctuations of the SCDs. Additionally, the measured O_3- SCDs for the highest elevation angles and, thus tangent heights, are higher than the simulated ones. As the gondola oscillations slowed down to amplitudes $< 1^o$ with increasing time, i.e. for SZA $> 90^o$, the deviations at high tangent heights become smaller. For lower tangent heights (~ 21 km and lower), the agreement of measured and simulated SCDs is generally excellent for all limb scans. For the last shown limb scan (SZA$>93^o$), the analyzed radiance is very low which affects the accuracy of both the measurements and the simulations so that the agreement becomes worse. Also for the tropospheric absorber O_4, the measured and simulated optical densities agree well within the error bars giving confidence in the RT calculations even under the hard to model situation of SZA $> 90^o$. For water vapor, the measurements are rather noisy with large errors because of the low H_2O absorbance as most water vapor resides at the lowermost altitudes where the BoxAMF are very small. However, a good qualitative agreement between measurements and simulation is observed.

Now, the results for the photochemically active radical NO_2 are discussed. The NO_2 concentrations are increasing with SZA, abd the strongest increase is observed for SZA$>90^o$. This is seen in figure 6.55 (lower panel) showing measured and simulated NO_2-SCDs. Two simulations are carried out, one using the constant NO_2 profile inferred from DOAS measurements during balloon ascent for SZA$=77-85^o$ and a second one using photochemically modeled profiles. Similar to the O_3-SCD comparison, the first 11 limb scans (corresponding to SZA$<90^o$ show some deviations of measured and simulated NO_2-SCDs caused by rather strong elevational gondola deviations. Also the photochemical growth of NO_2 concentrations is rather small being seen by the almost matching of the green and red lines in the figure. For limb scans $12-15$, i.e. SZA$=90.1-92.9^o$, simulations and measurements agree better, however, only if the photochemically modeled profiles are used for the simulations. Hence, the increase

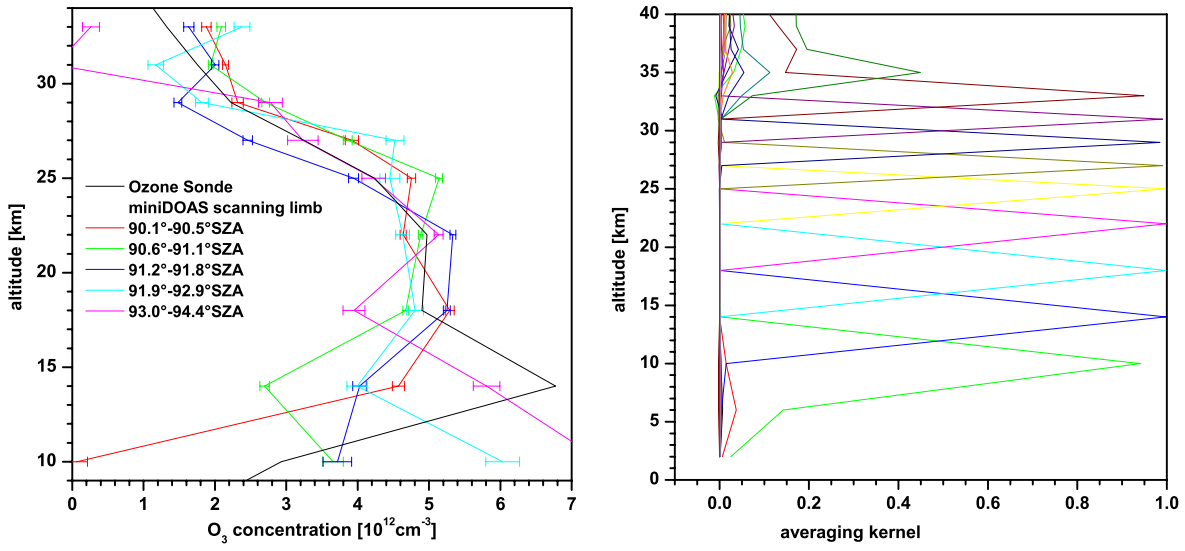

Figure 6.57: O_3 profiles retrieved from scanning limb observations (left panel) and averaging kernels for the profile inversion corresponding to SZA=$90.6 - 91.1^o$ (right panel).

of NO_2 concentrations with SZA is clearly seen in the miniDOAS scanning limb measurements.

In a last step, vertical profiles are obtained from the scanning limb measurements for O_3 and NO_2. As the first limb scans are affected by strong gondola instabilities only the limb scans $12-16$, i.e. SZA$> 90^o$ are considered. The altitude grid is chosen to 4 km below 24 km and 2 km above owing to the lower sensitivity at lower altitudes due to increasing steps of tangent altitude and lower sensitivity of the measurements due to broader maxima of the BoxAMF. The shown error bars only include the retrieval error obtained from the statistical DOAS error but no systematical effects. The retrieved O_3 profiles are shown in figure 6.57 (left panel) together with the Ozone Sonde profile smoothed to the same altitude grid. Qualitatively, a fair agreement between the miniDOAS and Ozone Sonde profiles is found above 18 km, while deviations increase with decreasing altitude. The averaging kernels (see figure 6.57, right panel) indicate a sensitivity of the measurements between 8 and 34 km on the chosen altitude grid. It should be noted that the averaging kernels corresponding to the other profile inversions (not shown here) are very similar but getting slightly worse with increasing SZA. The obtained NO_2 profiles are shown in figure 6.58 for 4 limb scans between 90^o and 93^o SZA and compared to LABMOS model outputs for a median SZA of each limb scan. Additionally, the constant DOAS ascent NO_2 profile, which is used as a priori for all miniDOAS retrievals, is shown for comparison. The retrieved profiles match well the photochemically modeled profiles for all 4 limb scans. Especially around the NO_2 concentration maximum (i.e. in the $26 - 34$ km range), the match is excellent, while deviations are stronger below as concentrations are lower and the sensitivity of the measurements decrease. However, a rather strong deviation is observed at 29 km for the 3^{rd} shown limb scan (lower left panel) indicating a rather strong sensitivity of the profile retrieval to even small deviations of individual measurements. The averaging kernels (see figure 6.59) indicate a sensitivity of the measurements to NO_2 between 12 and 34 km on the chosen altitude grid. To summarize it can be said that the observed overall good matching increases our confidence in the quality of miniDOAS scanning limb measurements and the validity of the applied RT and photochemical modeling. Additionally, this comparison demonstrates the feasibility to obtain time-dependent profile information of radicals as function of SZA by scanning limb measurements.

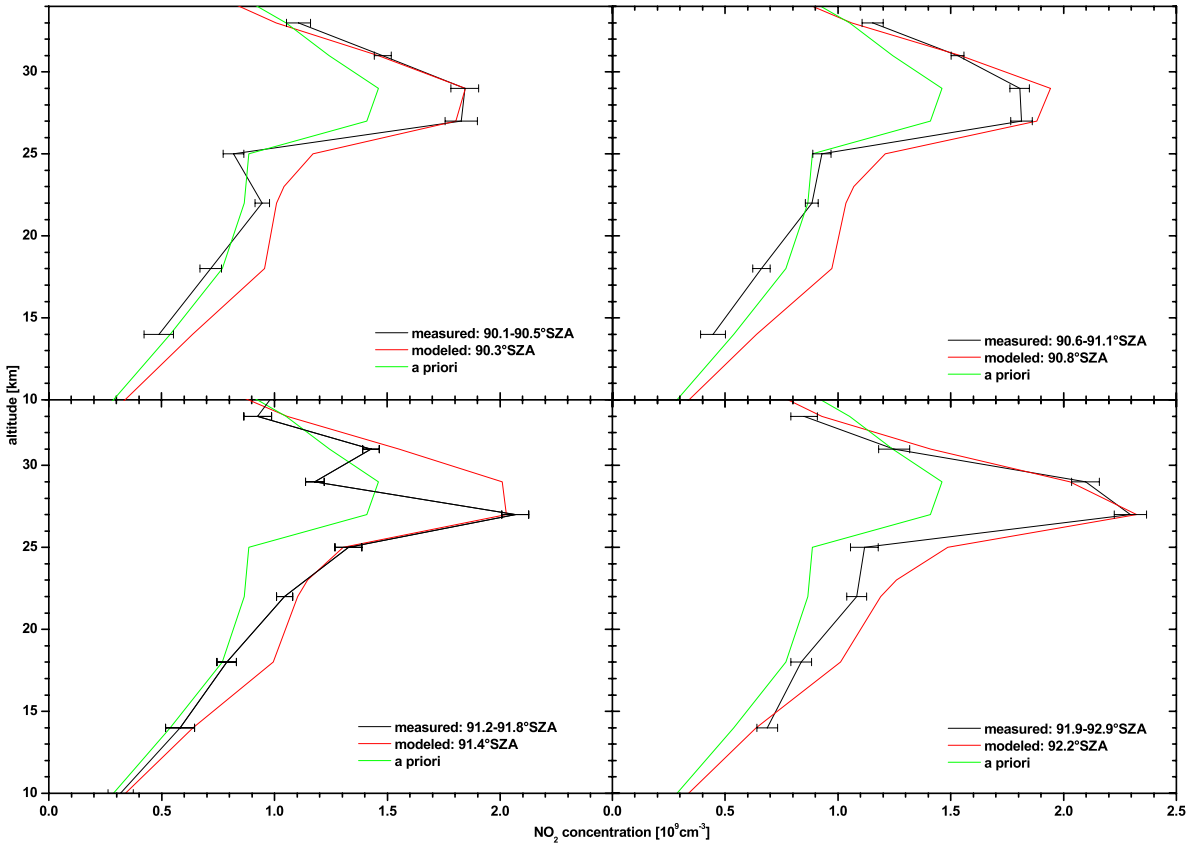

Figure 6.58: NO_2 profiles retrieved from scanning limb observations (black lines) compared to photochemically scaled profiles (red lines) and the constant profile inferred from DOAS measurements during balloon ascent (SZA=$76 - 85^o$).

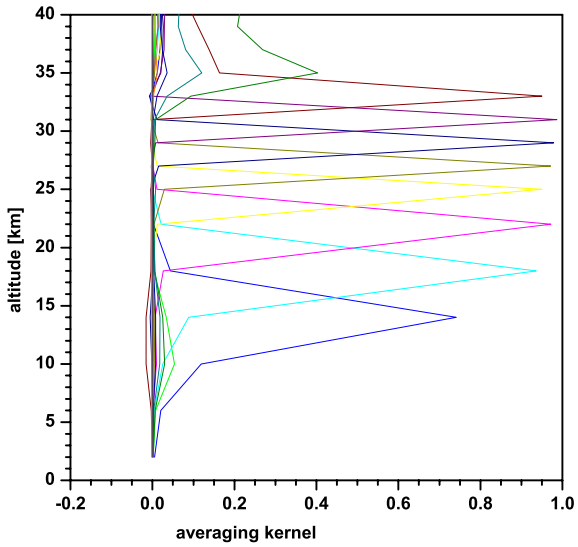

Figure 6.59: Averaging kernels for the NO_2 profile retrieval shown in figure 6.58, upper right panel (SZA=$90.6 - 91.1^o$).

6.6 The Tropical Large Balloon Campaign in Teresina, Brazil, November/December 2004

In the framework of Envisat validation, a campaign dedicated to launch for the first time large balloons inside the Inner Tropical Convergence zone (ITC) was organized. Three miniDOAS flights aboard the LPMA/DOAS, LPMA/IASI, and MIPAS-B2 balloon gondolas, respectively, were planned. Unfortunately, none of the flights took place due to operational reasons. However, several new applications of the miniDOAS instrument were tested and are briefly described in this section.

6.6.1 Direct Sunlight Measurements

In order to validate the absolute radiance measurements of SCIAMACHY in the wavelength region above 650 nm not covered by our "large" DOAS (*Gurlit et al.*, 2004), a broad band spectrometer covering a wavelength region of $178 - 873$ nm at moderate resolution was absolutely calibrated and tested during ground based sunrise and sunset measurements.

Instrumental

For the planned LPMA/DOAS flight, the nadir channel of the miniDOAS instrument was replaced by a direct sunlight spectrometer. The only difference of the direct sunlight configuration compared to the limb/nadir configuration is that the telescopes are replaced by a cosine corrector. A cosine corrector by Ocean Optics (*Ocean Optics*, 2004)) is placed directly in front of the light intake of the glass fiber bundle. The fiber is put behind the LPMA suntracker seeing the same light as the two telescopes of the large DOAS. An Ocean Optics USB2000 spectrometer covering the $178 - 873$ nm wavelength region at a resolution of ~ 3 nm FWHM, corresponding to a sampling of ~ 3 pixels per FWHM, is used. This wavelength range allows the DOAS retrieval of O_3, NO_2, H_2O, O_4, and O_2.

Absolute Radiometric Calibration

The instrument is absolutely calibrated in order to measure the solar irradiance. The calibration procedure is described in detail in *Gurlit et al.* (2004). Here, some results from the calibration measurements are discussed.

For the calibration, two light sources are used: a collimator providing a parallel light beam with the same aperture angle as the sun (therefore this source is also called "sun simulator"), and a National Institute of Standards and Technology (NIST) FEL 1000W irradiance standard Quartz Tungsten Halogen (QTH) lamp (serial number F-455).

The advantage of the collimator's parallel light is its high homogeneity. Hence, the output intensity is independent of the distance between the source and the detector. However, its output power is rather low so that rather long integration times of the order of 30 min are necessary to achieve a reasonable S/N ratio. Additionally, the source is only indirectly calibrated for absolute irradiance by transfer measurements (see *Gurlit et al.* (2004) for details) which causes additional uncertainties. For the actual absolute calibration, the NIST-lamp is used whose output power is much larger. However, it is a point source which implies that its intensity is decreasing quadratically with the distance between lamp and detector R. So this distance has to be determined very precisely to know exactly the light intensity at the detector position. The R^2-law is only valid for sufficiently large R, i.e. when the lamp can be viewed as a point. This is checked by a series of measurements for variable R ranging between 2.6

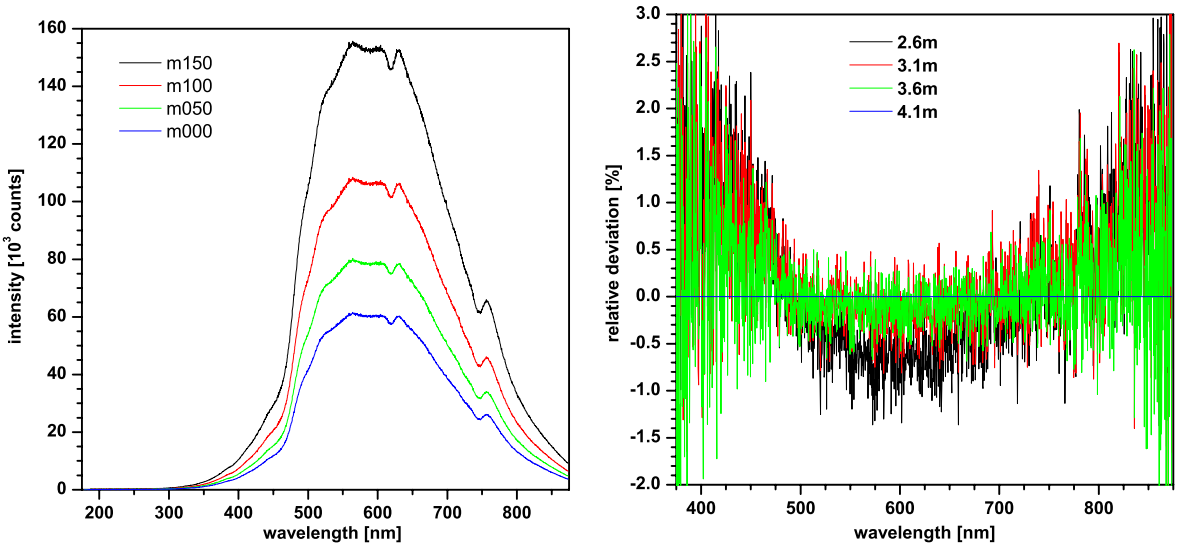

Figure 6.60: Left panel: Measured intensity vs. wavelength as a function of the distance between calibration lamp and detector R. Right panel: relative deviation of the intensity times R^2 from that for $R = 4.1\,\mathrm{m}$ as a function of R.

and 4.1 m. The measured intensities (with 5 s integration time and 50 co-added scans, shown in figure 6.60, left panel) are multiplied by R^2. This should result ideally in the same values for each R. This is checked by calculating the relative deviation of the individual measurements from the value obtained for $R = 4.1\,\mathrm{m}$ (shown in figure 6.60, right panel). For wavelengths $< 375\,\mathrm{nm}$, the relative deviations are very high due to the very low observed intensities. In the $475 - 775\,\mathrm{nm}$ range the deviations are below 1 % for the measurements at $R = 3.1\,\mathrm{m}$ and 3.6 m and getting larger towards both ends of the shown wavelength range as the measured intensities decrease. For $R = 2.6\,\mathrm{m}$, the values are systematically lower. An explanation might be a deviation from the R^2-law. But also detector non-linearities might explain this behavior as the saturation levels of the measured spectra are significantly lower for larger detector distances. Note that the non-linearity correction (see section 4.2.2) was switched on during this measurement. With the correction switched off, the deviations are significantly larger. All in all, this measurement demonstrates a good reproducibility of the calibration measurements. Unfortunately, the calibration measurements were not completed by the time the actual balloon flight was canceled, so that no absolute irradiance information exists for the ground-based sunset and sunrise measurements and, thus, the calibration of the miniDOAS and DOAS cannot be directly compared.

The Sunset Observation on November 24^{th}, 2004

The trace gas retrieval of the miniDOAS direct sunlight measurements are compared with the measurements of the same quantities performed with the large DOAS in the same observation geometry (see figure 6.61). Generally a good agreement is found for the broad-band absorbers O_3 and O_4. For the highly structured absorbers NO_2 the miniDOAS measurement have rather low optical densities as the resolution is rather poor. Also big uncertainties are introduced by the convolution of the high resolution literature cross section du to the low sampling ratio of the detector. Also the H_2O measurement agree only qualitatively. The quantitative discrepancies might be explained by differences in the used cross sections and also the afore mentioned effects of poor resolution and sampling. However, it should be noted that the primary objective of the spectrograph is the measurement of solar irradiance at balloon float altitude. Therefore only the major trace gas absorptions have to be removed out of the spectra, while a sensitive detection of weakly absorbing trace gases is not necessary. The presented RMS resid-

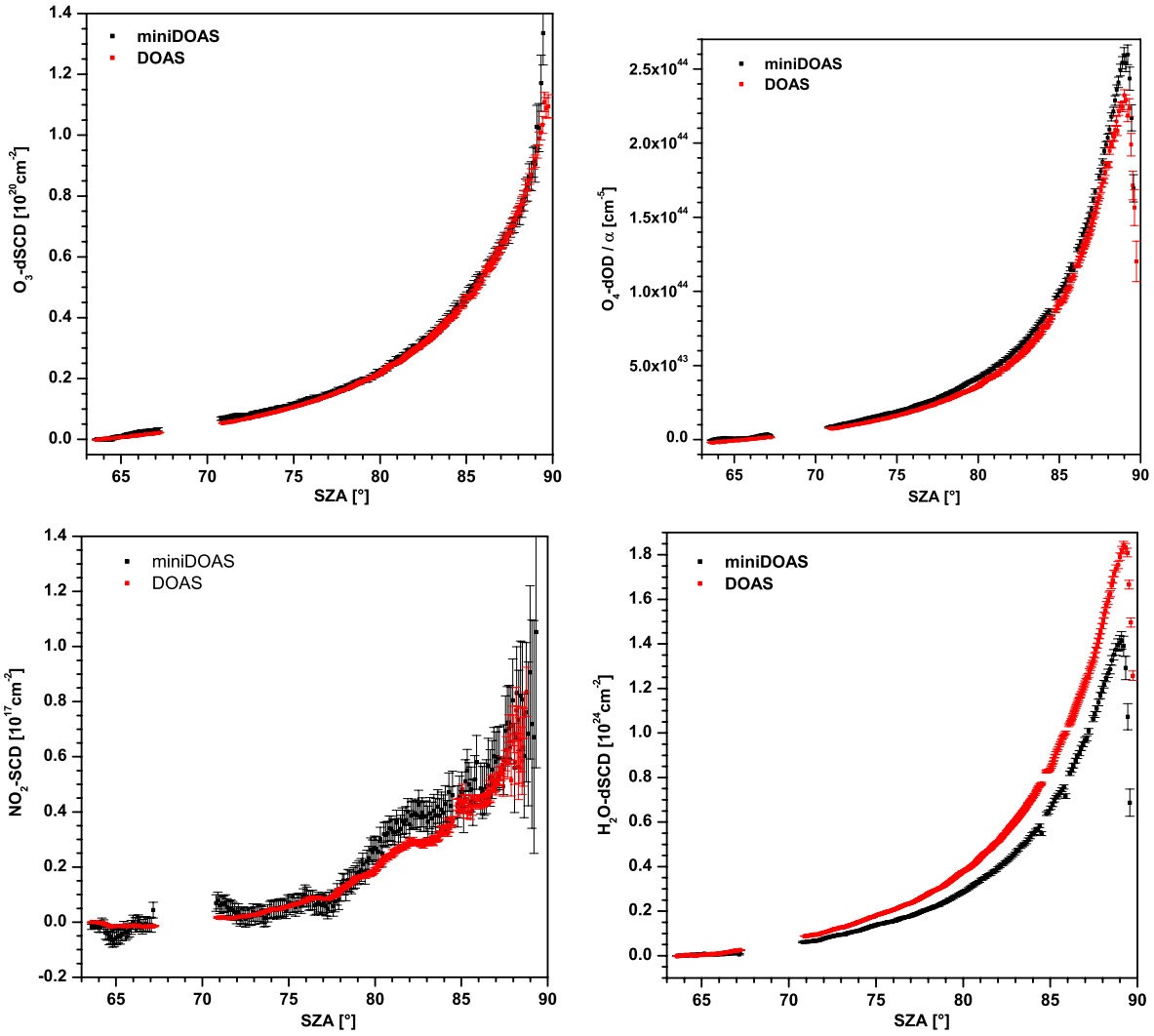

Figure 6.61: O_3-dSCD (upper left panel), O_4 differential Optical Density (dOD) divided by α (upper right panel), H_2O-dSCD (lower left panel) and NO_2-dSCD (lower right panel) vs. SZA retrieved from miniDOAS (black squares) and DOAS (red squares) direct sun measurements.

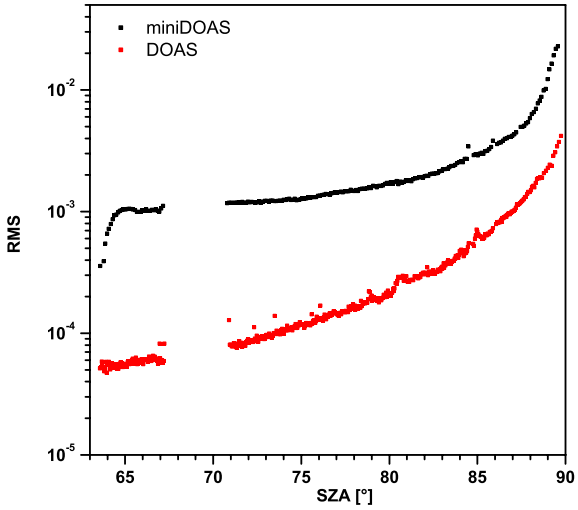

Figure 6.62: RMS residuals of the O_3 DOAS retrieval of the miniDOAS (black squares) and DOAS (red squares) measurements shown in figure 6.61.

uals (figure 6.62) show that this is possible even under the condition of very high water concentrations. The rather good agreement of the O_4 measurements show that the detection of broad band absorbers is reasonable, so that the determination of the total air mass along the line of sight by O_4 or O_2 observations is assumed to be possible. The determination of the total air mass (either by measurements or RT simulations) is crucial for the calculation of a top-of-the-atmosphere irradiance from the measured irradiance "inside" the atmosphere.

6.6.2 Application of the miniDOAS Instrument on the MIPAS-B2 Gondola

So far, the miniDOAS instrument has only been flown on the LPMA balloon payload. Due to its compact design and its automated measurement routine, the miniDOAS instrument can be easily installed on other balloon gondolas. In this section, the planned measurements aboard the azimuth controlled MIPAS-B2 payload are briefly described. Descriptions of the MIPAS-B2 spectrometer and gondola can be found in (*Friedl-Vallon et al.*, 2004) and on their website[4].

Instrumental

The instrument can be installed on the MIPAS-B2 gondola without problems. As there is no connection to the onboard power supply available, the miniDOAS is equipped with own batteries. Two 14.4 V Lithium batteries with deep discharge protection wired in series are used. Their capacity of 13 Ah each should allow for 50 h of measurements assuming a current of 0.3 A at 28.8 V. Even if the capacity decreases due to the low ambient temperatures during the balloon flight, the batteries' capacity is enough for the typical flight duration incl. countdown of max. 20 h.

Planned Scanning Limb and Nadir Measurements

Due to its optimization for solar occultation measurements, the LPMA/DOAS gondola typically arrives at float altitudes at rather high solar zenith angles (typically $> 85^o$). This leaves only very little time for

[4]http://www-imk.fzk.de/asf/mipas-b/mipas-b.htm

limb scanning measurements at float. Additionally, these measurements are very difficult to interpret as radiative transfer calculations under low sun conditions, especially around SZA=90^o, are notoriously problematic.

The MIPAS-B2 instrument analyzes thermic emission of the earth in the infra-red spectral region and is, thus, independent of the sun. For the flight in Teresina, a launch at 2 h a.m. local time, i.e. an ascent during night and arrival at float altitude before sunrise, was planned. Then, at least 5 h, if possible even longer until sunset $\sim$ 12 h later, at float was planned. This flight profile gives the possibility of extensive limb profiling measurements during sunrise and also under high sun conditions, i.e. with higher limb radiances. However, some constraints apply. The MIPAS-B2 instrument performs several limb scans in different viewing geometries, i.e. under several angles to the sun. This means that the whole gondola and, thus, also the miniDOAS limb telescope are rotated after every scan. A MIPAS limb scanning sequence typically takes 30 min. As the miniDOAS limb scanning measurements are automatic, they cannot be synchronized with the MIPAS limb scans. This means that every miniDOAS limb scanning sequence has to be significantly shorter than 30 min to ensure that at least one complete scan is perfomed before the gondola is rotated. So the measurement routine is programmed that way that every scan takes $\sim$ 15 min. At low tangent heights, this should allow for adding 1000 scans which is the minimum for the detection of BrO. Additionally, the limb scanning sequence itself, i.e. the angular step size, has been optimized as discussed in section 5.1.7. The mentioned exact determination of the telescope's zero position is easy on the MIPAS gondola as the elevation of the gondola is monitored by onboard instrumentation.

Another objective of the miniDOAS instrument is the direct validation of the absolute nadir radiances measured by SCIAMACHY with balloon-borne measurements. This asks for a direct satellite overpass or, as a direct overpass is very difficult to achieve, temporal and spatial as close as possible measurements. As the LPMA/DOAS gondola is preferably launched in the afternoon to allow for daylight ascent and sunset measurements, this goal could not yet be achieved. The launch time and trajectory of the MIPAS-B2 gondola is usually planned in a way to get a close ENVISAT match, so close-by miniDOAS balloon and SCIAMACHY satellite nadir measurements could be achieved and compared.

Chapter 7

Conclusions

7.1 Summary

In the framework of this thesis, a new balloon-borne DOAS instrument ('miniDOAS') was developed with a special emphasis put on small size, low weight and power consumption, but also a stable optical imaging. While compact design offers the possibility of versatile applications, optical stability is crucial for the detection of weak absorbers like BrO.

The miniDOAS instrument has been thoroughly characterized in the laboratory. In its typical configuration, the miniDOAS consists of 2 independent spectrometer channels analyzing skylight in limb and nadir geometry in the $330-550\,\mathrm{nm}$ wavelength range at a resolution of $0.8-1.0\,\mathrm{nm}$ with a sampling ratio of $8-10\,^{\mathrm{pixels}}/_{\mathrm{FWHM}}$. This wavelength range allows the detection of the atmospheric trace gases O_3, NO_2, BrO, H_2O, O_4 and, potentially, OClO, IO, OIO, and CH_2O. Its size is $26\times26\times31\,\mathrm{cm}^3$, its weight $\sim 7\,\mathrm{kg}$, and its power consumption $\sim 7.5\,\mathrm{W}$. The spectrometers are kept at a constant temperature of $0^o\,\mathrm{C}$ by a water-ice mixture. The temperature stabilization lasts for $\sim 8\,\mathrm{h}$ under flight condition which is longer than the usual flight duration. The spectrometers are also pressure stabilized by a vacuum sealed aluminum housing that can keep pressures $< 1\,\mathrm{mbar}$ for several days. The instrumental noise causes an RMS of $6.8\cdot10^{-3}$ for a single scan. During balloon flight, typically 1000 scans are co-added, worth $20-100\,\mathrm{s}$ integration time, corresponding to an RMS residual of $0.24\cdot10^{-3}$.

The new instrument has been tested during 5 balloon-flights aboard the LPMA/DOAS balloon payload. The measured quantities are skylight radiances and, after DOAS analysis, trace gas column densities along the line of sight. The measured limb radiances are compared to RT calculations of the same quantity using the novel Monte Carlo radiative transfer model TRACY developed by *von Friedeburg* (2003). The trace gas information retrieved from the miniDOAS measurements is compared to correlative profile measurements by other sensors deployed on the LPMA/DOAS gondola (ECC ozone sonde, direct sunlight DOAS) and stand alone in-situ sensors (ECC ozone sonde). Additional instrumentation aboard the LPMA/DOAS and the stand-alone ozone sonde provide measurements of the key atmospheric parameters like temperature-, pressure- and humidity-profiles. This offers the unique possibility to validate each step of the novel technique of atmospheric trace gas profiling by limb scatter measurements individually. The RT model's output can be validated on the radiance level. Additionally, the RT calculated trace gas SCDs can be compared to simulations of the same quantity using the measured profiles and atmospheric parameters as input. In a final step, the measured SCDs are inverted using the MAP inversion technique which allows a detailed study of the profile retrieval and its sensitivities.

The accuracy of the absolute radiance calibration is between 35 % in the UV (390 nm) and 5 % in the

visible range (500 nm). Measured and RT calculated radiances in scanning limb geometry at balloon float match well for the observed high SZA between 85^o and 94^o, a situation still very hard to model. For fixed limb observations during balloon ascent, the measurements agree well for tangent altitudes above ~ 10 km at 490 nm and ~ 15 km at 360 nm. This is interpreted as that measurements and calculations agree well for conditions where the RT is dominated by single Rayleigh scattering. With increasing significance of multiple scattering the measured and modeled radiances diverge.

For vertical O_3 and NO_2 profiles, the accuracy is $5-10$ % for altitudes around the relative maximum, but much higher for altitudes below. Averaging kernels indicate a height resolution of 1 km. For BrO profiles the uncertainties are slightly higher ($15-25$ %) at stratospheric altitudes due to the much lower observed BrO optical densities. The height resolution is 2 km as indicated by the averaging kernels. Measured and simulated SCDs of the tropospheric absorbers O_4 and H_2O coincide well for the entire observed altitude range, i.e. also for measurements in the stratosphere where the observed SCDs are dominated by multiply scattered photons from the troposphere indicating the proper treatment of this situation by the TRACY RT calculations. Comparison of measured and simulated O_4-SCDs also yield information about tropospheric aerosol loads. Vertical O_4 absorption profiles can be inferred in the troposphere and lower stratosphere with strongly decreasing sensitivity above 20 km due to the exponentially with altitude decreasing concentrations. H_2O concentrations can only be inferred in the troposphere. In the stratosphere, concentrations are too low (over 4 orders of magnitude lower than on the ground) to be sensitively measured before the large tropospheric background. In fact, stratospheric water vapor only contributes by ~ 3 % to the measured SCDs for stratospheric detector altitudes at 490 nm.

During balloon float phase, scanning limb measurements are performed with constant detector altitude but variable elevation angle, i.e. tangent altitude of the observation. A fair agreement between measured and RT simulated O_3- and NO_2-SCDs is found for the considered SZA range of $85 - 95^o$. The lower sensitivity of the measurements due to lower limb radiances at high SZA are compensated by increasing light paths and, thus, increasing SCDs. Vertical O_3 and NO_2 profiles can be retrieved with $2-4$ km altitude resolution. The increasing NO_2 concentrations with increasing SZA due to NO_x photochemistry is observed. So scanning limb observations provide time-dependant profile information which is especially interesting for studies of the combined photochemistry of the radicals NO_2, BrO and, possibly, OClO.

7.2 Outlook

The instrument's compact design and automated measurement routines allow the versatile application on different platforms and viewing geometries. During the Teresina campaign, several new possibilities were tested. They include direct sunlight observations using the parallel sunlight beam provided by the LPMA suntracker. With a wavelength range covering $200 - 870$ nm, these measurements can provide absolute solar irradiance information at wavelengths not covered by the other sensors onboard which is not only important for satellite validation (e.g. SCIAMACHY on Envisat) but also to validate the currently available solar irradiance information e.g. from (*Kurucz et al.*, 1984) or SOLSPEC (*Thuillier et al.*, 1997, 1998a,b)). The LPMA/DOAS gondola offers unique possibilities for the validation of the instrument. However, its flight trajectory is optimized for solar occultation measurements meaning high solar zenith angles of $70 - 95^o$. Especially the scanning limb measurements are limited to SZA between 85^o and 95^o. These conditions are difficult to RT model and suffer from low limb radiances, especially for SZA $> 90^o$. The LPMA/IASI and MIPAS-B2 balloon payloads observe IR emission and are, thus, independent of the solar position. Therfore, their trajectory usually has longer times at float during daytime. This offers the possibility for extensive scanning limb measurements also under high sun conditions which largely simplify the RT calculations, provide larger limb radiances and lower residual

trace gas absorptions of the solar reference spectrum which reduces the errors of the measurements due to incorrect determination of the solar reference offset. The higher radiances allow to co-add more scans per observation at every elevation angle which decreases the residuals and, thus, would allow to detect weak absorbers like BrO or, potentially OClO by scanning limb measurements. Limb scanning observations allow to retrieve time-dependent profile information being especially interesting for studying photochemical changes of radicals like NO_2, BrO, and OClO. The combined photochemistry of the mentioned radicals is subject of most recent research. Additionally, the flight trajectory of the mentioned balloon gondolas can be planned to achieve a direct satellite overpass so that nadir radiances measured by miniDOAS and e.g. SCIAMACHY/Envisat can be directly compared. A validation of nadir radiances is very difficult, if not impossible, for measurements not performed at the identical time and position due to the high temporal and spacial variability of the cloud cover and ground albedo which the nadir radiances are directly proportional to. Another advantage of the MIPAS-B2 over the LPMA/DOAS payload is the availability of additional onboard sensors providing exact knowledge of the gondola's position relative to the sun and earth, i.e. the exact azimuth and elevation angle of the detector. This removes all uncertainties of the RT calculations arising from missing pointing information. All the three discussed applications (direct sun observations on LPMA/DOAS, and scanning limb and nadir measurements on LPMA/IASI and MIPAS-B2) were planned for the recent tropical large balloons campaign at Teresina but were canceled for operational reasons. However, they are planned to happen during the backup campaign at the same place in June 2005. For this campaign, also fixed limb measurements aboard LPMA/DOAS are planned with the scientific objective to obtain new information about O_3, NO_2, BrO and, potentially, IO, OIO, or CH_2O concentrations in the tropical UT/LS[1]. This is highly interesting information for global stratospheric chemistry as most of the transport from the troposphere to the stratosphere occurs in this region. Hence, these measurements could provide new insights on the source strength of ozone depleting species in the stratosphere by transport from the troposphere.

Another possible application of a revised miniDOAS instrument is the stand-alone operation. However, this would require additional instrumentation providing exact information of the detector's position (e.g. by GPS) and azimuth and elevation angle (e.g. as aboard MIPAS-B2). Another thinkable solution would be to use a high detector aperture (360^o azimuth and $> 30^o$ elevation range) to allow direct sun observations throughout the entire flight without the necessity of an active suntracker. This can be achieved, e.g., by a design similar to that deployed by the SAOZ balloon payload, i.e. a cone-shaped mirror reflecting the sunlight onto the detector. This would not eliminate the problem of contamination of the observed solar irradiance by scattered light, an effect believed to be manageable for SAOZ measurements of O_3, NO_2, or BrO, but the sensitivity could be improved thanks to a more stable optical imaging due to temperature and pressure stabilization.

Another possible platform for the miniDOAS instrument are stratospheric research aircrafts like Geophysica. So far, a comparable instrument in multi-axis-geometry (AMAX-DOAS (*Heue et al.*, 2005)) is employed on the DLR Falcon providing interesting information about tropospheric NO_2 columns. With scanning limb observations, profile information of the mentioned trace gases and also of BrO can be inferred for altitudes below the airplane's flight altitude (e.g. 20 km for the Geophysica).

Also the existing observation modes can be improved by further instrumental tuning. One possibility is to attach a Peltier cooling directly to the detector. This would not only allow lower detector temperatures, a feature fairly unnecessary in the UV/vis spectral range as the noise originating from the dark current is already immeasurably small at 0^o C, but also a higher stability of the detector temperature. Temperature instabilities are believed to be the major reason for the still existing spectral shift and, thus, enhanced residuals at lower altitudes after the elimination of pressure fluctuations by evacuation

[1]Upper Troposphere and Lower Stratosphere

of the spectrometers. Also the application of additional sensors providing the detector's exact azimuth and elevation angle would largely simplify the interpretation of the limb scatter measurements and increase the accuracy of the retrieved vertical profiles. Another idea is to extend the wavelength range into the near-IR region. O_2-SCD measurements might provide more exact information about the light path of the observations and, thus, more details about the aerosol load. Stratospheric water vapor measurements also improve in the IR due to the lower contribution of photons coming from the troposphere via multiple scattering. E.g. at 950 nm, the contribution of double-scattered radiation is smaller by a factor of $\sim 2^4 = 16$ compared to 490 nm.

Appendix A

Technical Manual

A.1 Profile Retrieval

WinDOAS	performs DOAS evaluation and retrieves dSCDs from measured spectra
JUL_DATE.EXE	calculates the sun's position for a given time and geolocation
interpol.m	creates atmosphere files for TRACY
matrix.m	creates matrix.txt for TRACY
trin.exe	creates profile.txt for TRACY
3DRTSim.exe	the actual TRACY executable
SRManager.exe	calls TRACY with several profile files
amf_fw.m	calculates SCDs from a vertical profiles and RT modeled BoxAMF
amf_inv.m	inverts the AMF matrix and retrieves the vertical profile from measured SCDs

A.1.1 RT Modeling

In this section, the parameters and files that are necessary for the RT modeling with TRACY are described. The main input file of TRACY is called by default 'profile.txt'. It contains information about the trace gas and aerosol profiles to be considered, the detector position and its viewing geometry, and atmospheric parameters like ground and cloud albedo, and cloud coverage. And it tells TRACY what to do, i.e. how many photons to model and in which mode to run. Another important input file is 'matrix.txt' which contains the geolocation of every measurement. Additionally, several files containing information about the atmospheric conditions are necessary and have to be created for every balloon flight. For a description of the format of the individual input files, also see the TRACY user manual (*von Friedeburg*, 2004).

All the relevant atmospheric parameters like pressure, temperature and air density vs. altitude are provided by LPMA in a file with extension '.MTB'. From this file, a file with the columns altitude, air density, temperature and pressure is created called, accordingly, 'LPMA??.ATp' (?? stands for the flight number). Vertical profiles of the trace gases of interest and aerosol extinction coefficient also have to be given. From these files, the MATLAB program 'interpol.m' interpolates the atmospheric profiles on the grid given in the file 'grid.txt'. The names of the trace gas and aerosol extinction files have to be given in the 'profile.txt' file while the air density, temperature and pressure have default names. Note that the information in the latter three files is redundant as the air density can be calculated from pressure and temperature using the ideal gas equation, so TRACY only uses the values of the file 'AirDen.Dat'.

Also note that the air density file has to be called 'AirDen.Dat' and not 'AirDen.txt' as written in the TRACY user manual.

The dSCDs are retrieved from the measured spectra using WinDOAS and the trace gas content of the solar reference spectrum has to be determined using one of the methods described in section 4.4.8. This gives a file with the measured SCDs and their uncertainties vs. time as output. For every measurement, the position of the detector, its viewing direction and the sun's position has to be calculated. For the LPMA/DOAS flights, LPMA provides a file 'LPMA??.ysg' that gives the gondola's geolocation, i.e. latitude, longitude and altitude vs. time typically in steps of 1 or 10 s . This information can be used to calculate the sun's position, i.e. the Solar Zenith Angle (SZA) and Solar Azimuth angle (SAz). All this information is saved in a file, usually called 'LPMA??.pos'. Note that times in the HH:MM:SS format can neither be read nor handled by MATLAB, so they have to be changed into numerical format (fraction of the day, e.g. 12 p.m. corresponds to 0.5). This can be done, e.g., with ORIGIN. The file with numerical time is usually called 'LPMA??.nos'. This file together with a file containing the times of the measurements are the input for the MATLAB program 'matrix.m' which calculates the file 'matrix.txt' that can be directly used as input for TRACY. As TRACY can only handle several detector positions in one profile.txt but only one observation geometry, i.e. elevation angle, the situation is more tricky in case of scanning limb measurements. In this case, the elevation angle of each observation has to be added as sixth column in the 'matrix.txt' file. With the program 'trin.exe' (called with the parameter '-limbscan', for more details try 'trin -help'), an individual profile-file for every single measurement can be created from this matrix-file and a 'skeleton profile-file' in which the numbers from the matrix-file are written. The TRACY input program 'trin' must also be used if TRACY is run under Linux which is possible using the Windows emulator 'wine'. As TRACY crashes after the simulation of $\sim$ 50000 photons, it is practically impossible to work through a complete matrix-file. But if TRACY is called anew after every single simulation, it runs stably. 'trin' also creates a bash-script 'aufruf.scr' which calls TRACY for all the created profile-files. Under Windows, the program 'SRManager.exe' can be used to call TRACY. In case of a crash, it automatically restarts TRACY at the last worked line of the matrix-file. However, this only works if the automatic error report sending service under Windows is turned off. If this service is turned on, a dialog box appears after every crash of TRACY and the program waits until 'okay' is pressed. In order to know in which line of the 'matrix' file to restart the calculation, TRACY always writes the line number of the matrix-file it is currently working on into a file called 'status.txt'. Note that when TRACY is called (i.e. without using 'SRManager'), it always starts working at the line number of the matrix-file as written in the profile-file plus the number contained in the file 'status.txt' which can be quite confusing. However, when 'SRManager' is called, 'status.txt' is set to 0 and, consequently, TRACY starts working at the line of the matrix given in 'profiles.txt'. The profile-files to be worked on have to be written into the file 'SRList.txt'. This file is also created by 'trin'. The important output files of TRACY are the two files by default called 'AMF.txt' and 'BOX.txt'. Beside many other information, 'AMF.txt' contains the simulated radiances and trace gas SCDs that can be directly compared to the respective measured quantities. The 'BOX.txt' contains the modeled Box Air Mass Factors (BoxAMFs) that are used for the profile retrieval.

A.1.2 Profile Inversion

The profile inversion is performed according to the Maximum a posteri algorithm as described in *Rodgers* (2000) chapter 4. This algorithm is implemented in the MATLAB program 'amf_inv.m'. It requires the RT modeled BoxAMFs (file '*.AMF'), the measured SCDs and their uncertainties (file '*.SCD') and an a priori profile ('*.VCD') for the desired trace gas profile as input. Note that the unit of the '*.VCD'-file is not [cm^{-2}] but [cm^{-3}], so it gives trace gas concentrations (i.e. VCD divided by 10000 cm) rather than a Vertical Column Density (VCD). The altitude grid of the three files ('AMF', 'SCD' and 'VCD')

have to match, i.e. for every line in the SCD-file there has to be one line with BoxAMF in the AMF-file. The grid of the VCD-file has to be the same as that of the lines of the BoxAMF. The output of 'amf_inv.m' is the retrieved profile '*_out.VCD' and the averaging kernels ('*.AVK') of the retrieval. The covariance matrix of the measured SCDs is calculated from the given measurement uncertainties by creating a diagonal matrix with the measurement errors squared as elements. The covariance of the a priori profile is calculated from the profile itself. Therefore, the parameter *error* in the 'amf_inv.m' code can be set. It gives the relative error, i.e. a value of 1 means that the covariance is identical to the a priori profile values squared. Additionally, the altitude gridding can be manipulated in the 'matrix.m' code by setting the parameters *alt* and *grid*. The program assumes the input BoxAMFs and VCD on a 1 km grid (if the BoxAMF are calculated on a different grid, the program code has to be adjusted). The output grid is also 1 km for grid points $\leq alt$ while the grid size is *grid* for grid points $> alt$. The parameter *grid* has to be an integer ≥ 1 since several BoxAMFs can be added to get a broader grid but a finer grid spacing can only be achieved by recalculating the BoxAMFs with TRACY.

The MATLAB program 'amf_fw' can be used to generate simulated SCDs that can be directly compared with the measured values. Therefore, the modeled BoxAMFs (file '*.AMF') and a vertical profile (file '*.VCD') are used. The output is a file ('*_out.SCD') containing a simulated SCD for each observation contained in the AMF-file.

Publications

Parts of this work have been published in the following article:

- Weidner, F., H. Bösch, H. Bovensmann, J.P. Burrows, A. Butz, C. Camy-Peyret, M. Dorf, K. Gerilowski, W. Gurlit, U. Platt, C. von Friedeburg, T. Wagner, and K. Pfeilsticker, Balloon-borne Limb profiling of UV/vis skylight radiances, O_3, NO_2 and BrO: technical set-up and validation of the method, *Atmos. Chem. Phys. Disc.*, **4**, 7631-7665, 2004.

Contributions have been made to the following articles:

- Sioris, C.E., C.S. Haley, C.A. McLinden, C. von Savigny, I.C. McDade, J.C. McConnell, W.F.J. Evans, N.D. Lloyd, E.J. Llewellyn, K.V. Chance, T.P. Kurosu, D. Murtagh, U. Frisk and K. Pfeilsticker, H. Bösch, F. Weidner, K. Strong, J. Stegman, and G. Megie, Stratospheric profiles of nitrogen dioxide observed by OSIRIS on the Odin satellite, *J. Geophys. Res.*, **108**, 4215, 2003.
- W. Gurlit, H. Bösch, H. Bovensmann, J.P. Burrows, A. Butz, C. Camy-Peyret, M. Dorf, K. Gerilowski, A. Lindner, S. Noel, U. Platt, F. Weidner, and K. Pfeilsticker, The UV-A and visible solar irradiance spectrum: Inter-comparison of absolutely calibrated, spectrally medium resolved solar irradiance spectra and from balloon- and satellite-borne measurements, *Atmos. Chem. Phys. Disc.*, **4**, 8439-8469, 2004.

Bibliography

Albritton, D. L., A. L. Schmeltekopf, and R. N. Zare, An Introduction to the Least-Squares Fitting of Spectroscopic Data, in *Molecular Spectroscopy: Modern Research*, edited by R. K. Narahari and M. W. Weldon, Academic Press, Orlando, Florida, USA, 1976.

Alicke, B., K. Hebestreit, U. Platt, J. Carpenter, and T. Sturges, Measurements of iodine oxide in the midlatitudes, *Ann. Geophys.*, **16**, 1998.

Alicke, B., K. Hebestreit, J. Stutz, and U. Platt, Iodine oxide in the marine boundary layer, *Nature*, **397**, 572–573, 1999.

Aliwell, S. R., et al., Analysis for BrO in Zenith-sky spectra: An intercomparision exercise for analysis improvement, *J. Geophys. Res.*, **107**, 10.1029/2001JD000,329, 2002.

Allan, B., J. C. Plane, and G. McFiggans, Observations of OIO in the remote marine boundary layer, *Geophys. Res. Lett.*, **28**, 1945–1948, 2001.

Amoruso, A., L. Crescentini, G. Fiocco, and M. Volpe, New measurements of the NO_2 absorption cross section in the 440-460 nm region and estimates of the NO_2-N_2O_4 equilibrium constant, *J. Geophys. Res.*, **98**, 1993.

Andreae, M., et al., Methyl halide emissions from savanna fires in southern Africa, *J. Geophys. Res.*, **101**, 23,603–23,614, 1996.

Bates, D. R., and M. Nicolet, Atmospheric hydrogen, *Publ. Astron. Soc. Pac.*, **62**, 106–110, 1950.

Bauer, N., Charakterisierung des DOAS-Ballon-Spektrographen zur Bestimmung stratosphärischer Spurenstoffe, Diploma thesis, Institut für Umweltphysik, Universität Heidelberg, 1997.

Berthet, G., J.-B. Renard, C. Brogniez, C. Robert, M. Chartier, and M. Pirre, Analysis of OBrO, IO, and OIO absorption signature, in UV-Visible spectra measured at night and sunrise by stratospheric balloon-borne instruments, *J. Geophys. Res.*, **108**, 4161, 2003.

Bösch, H., Studies of Stratospheric Nitrogen and Iodine Chemistry with Balloon Borne DOAS Measurements, Dissertation, Institut für Umweltphysik, Universität Heidelberg, 2002.

Bösch, H., C. Camy-Peyret, M. Chipperfield, R. Fitzenberger, H. Harder, C. Schiller, M. Schneider, T. Trautmann, and K. Pfeilsticker, Inter comparison of measured and modeled stratospheric UV/vis actinic fluxes at large solar zenith angles, *Geophys. Res. Lett.*, **28**, 1179–1182, 2001.

Bösch, H., C. Camy-Peyret, M. P. Chipperfield, R. Fitzenberger, H. Harder, U. Platt, and K. Pfeilsticker, Upper limits of stratospheric IO and OIO inferred from center-to-limb-darkening-corrected balloon-borne solar occultation visible spectra: Implications for total gaseous iodine and stratospheric ozone, *J. Geophys. Res.*, **108**, 4455, 2003.

Brasseur, G., and S. Solomon, *Aeronomy of the middle atmosphere*, D. Reidel Publ., Dordrecht, Boston, Lancaster, Tokyo, 1986.

Brewer, A. W., Evidence for a world circulation provided by the measurements of helium and water vapour distribution in the stratosphere, *Q.J.R. Meteorol. Soc.*, **75**, 351–363, 1949.

Buchwitz, M., V. Rozanov, and J. Burrows, Development of a correlated k-distribution band model scheme for the radiative transfer program GOMETRAN/SCIATRAN for retrieval of atmospheric constituents from SCIAMACHY/ENVISAT-1 data, in *European Symposium on Remote Sensing*, vol. 3495, pp. 171–186, Barcelona, Spain, 1998.

Burkholder, J., and R. Talukdar, Temperature dependence of the ozone absorption cross section over the wavelength range 410 to 760 nm, *Geophys. Res. Lett.*, **21**, 581–584, 1994.

Burrows, J., E. Hölzle, A. Goede, H. Visser, and W. Fricke, SCIAMACHY - Scanning Imaging Absorption Spectrometer for Atmospheric Chartography, *Acta Astronautica*, **35**, 445, 1995.

Burrows, J., U. Platt, K. Chance, M. Vountas, V. Rozanov, A. Richter, H. Haug, and L. Marquard, *Study of the Ring Effect*, European Space Agency, Noordivijk, The Netherlands, 1996.

Burrows, J., et al., The Global Ozone Monitoring Experiment (GOME): Mission Concept and First Scientific Results, *J. Atmos. Sci.*, **56**, 151–175, 1999a.

Burrows, J. P., A. Dehn, B. Deters, S. Himmelmann, A. Richter, S. Voigt, and J. Orphal, Atmospheric remote-sensing reference data from GOME: 2. temperature-dependent absorption cross sections of O_3 in the 231-794 nm range, *J. Quant. Spec. and Rad. Transf.*, **61**, 509–517, 1999b.

Bussemer, M., Der Ring-Effekt: Ursachen und Einfluß auf die spektroskopische Messung stratosphärischer Spurenstoffe, Diploma thesis, Institut für Umweltphysik, Universität Heidelberg, 1993.

Butler, J., A. Montzka, A. Clarke, J. Lobert, and J. Elkins, Growth and distribution of halons in the atmosphere, *J. Geophys. Res.*, **103**, 1503–1511, 2000.

Butz, A., et al., Inter-comparison of Stratospheric O_3 and NO_2 profiles by balloon-borne UV/vis and near-IR solar occultation and ENVISAT/SCIAMACHY limb measurements, *Atmos. Chem. Phys. (in prep.)*, 2005.

Camy-Peyret, C., C. Flaud, A. Perrin, C. Rinsland, A. Goldmann, and F. Murcray, Strotospheric N_2O_5, CH_4 and N_2O profiles from IR solar occultation spectra, *J. Atmos. Chem.*, **16**, 31–40, 1993.

Camy-Peyret, C., P. Jeseck, T. Hawat, G. Durry, S. Payan, G. Berube, L. Rochette, and D. Huguenin, The LPMA Balloon-Borne FTIR Spectrometer: Remote Sensing of Atmospheric Constituents, *Proceedings of the 12th ESA Symposium on Rocket and Balloon Programmes and Related Research, Lillehammer, Norway*, pp. 323–328, 1995.

Camy-Peyret, C., P. Jeseck, T. Hawat, G. Durry, S. Payan, G. Berube, L. Rochette, and D. Huguenin, Recent results obtained with the LPMA and DOAS balloon-borne instruments during the ILAS, SABINE and THESEO campains, *Proceedings of the 14th ESA Symposium on Rocket and Balloon Programmes and Related Research, Potsdam, Germany*, pp. 341–345, 1999.

Canty, T., et al., Nighttime OClO in the winter Arctic vortex, *J. Geophys. Res.*, **110**, D01,301, 2005.

Carlotti, M., Global fit approach to the analysis of limb-scanning atmospheric measurements, *Appl. Opt.*, **27**, 3250–3254, 1988.

Carslaw, K., B. Luo, S. Clegg, T. Peter, P. Brimblecombe, and P. Crutzen, Stratospheric aerosol growth and HNO_3 gas phase depletion from coupled HNO_3 and water uptake by liquid particles, *Geophys. Res. Lett.*, **25**, 2479–2482, 1994.

Chance, K., and R. Spurr, Ring effect studies; Rayleigh scattering, including molecular parameters for rotational Raman scattering and the Fraunhofer spectrum, *Appl. Opt.*, **36**, 5224–5230, 1997.

Chapman, S., On ozone and atomic oxygen in the upper atmosphere, *Philos. Mag.*, **10**, 369–383, 1930.

Chipperfield, M., Multiannual simulations with a three-dimensional chemical transport model, *J. Geophys. Res.*, **104**, 1781–1805, 1999.

Chipperfield, M., and J. Pyle, Model sensitivity studies of Arctic ozone depletion, *J. Geophys. Res.*, **103**, 28,389–28,403, 1998.

Clark, H., R. H. A. Billingham, and H. Pumphrey, Cirrus and water vapor in the tropical tropopause layer observed by Upper Atmosphere Research Satellite (UARS), *J. Geophys. Res.*, **108(D24)**, 4751, 2003.

Coheur, P.-F., S. Fally, M. Carleer, C. Clerbaux, R. Colin, A. Jenouvrier, M.-F. Merienne, C. Hermans, and A. Vandaele, New Water Vapor Line Parameters in the 26000-13000 cm^{-1} region, *JQRST*, pp. 493–510, 2002.

Cornu, A., Observation de la limit ultraviolett du spectre solaire a diverse altitudes, *C. R. Acad. Sci.*, **89**, 1879.

Cox, R., W. Bloss, and R. Jones, OIO and the atmospheric cycle of iodine, *Geophys. Res. Lett.*, **26**, 1857–1860, 1999.

Crutzen, P., and F. Arnold, Nitric acid cloud formation in the cold Antarctic stratosphere: a major cause for the springtime ozone hole, *Nature*, **324**, 651–655, 1986.

Crutzen, P. J., The influence of nitrogen oxide on the atmospheric ozone content, *Q.J.R. Meteorol. Soc.*, **96**, 320–327, 1970.

Dahlbeck, A., and K. Stammes, A new spherical model for computing the radiation field available for photolysis and heating at twilight, *Planet. Space Sci.*, **39**, 671–683, 1991.

David, C., S. Becki, S. Godin, G. Mégie, and M. Chipperfield, Polar stratospheric clouds climatology over Dumont d'Urville between 1989 and 1993 and the influence of volcanic aerosols on their formation, *J. Geophys. Res.*, **103**, 22,163–22,180, 1998.

Davidson, J., C. Cantrell, A. McDaniel, R. Shetter, S. Madronich, and J. Calvert, Visible-ultraviolet absorption cross section for NO_2 as a function of temperature dependence, *J. Geophys. Res.*, **93**, 1988.

Davis, D., J. Crawford, S. Liu, S. McKeen, A. Bandy, D. Thornton, F. Rowland, and D. Blake, Potential impact of iodine on tropospheric levels of ozone and other critical oxidants, *J. Geophys. Res.*, **101**, 2135–2147, 1996.

DeMore, W. B., S. P. Sander, C. J. Howard, A. R. Ravishankara, D. M. Golden, C. E. Kolb, R. F. Hampson, M. J. Kurylo, and M. J. Molina, Chemical Kinetics and Photochemical Data for Use in Stratospheric Modeling No. 12, *Jet Propulsion Laboratory, Pasadena, Publication 97-4*, 1997.

Deshler, T., M. Hervig, D. Hofmann, J. Rosen, and J. Liley, Thirty years of in-situ stratospheric aerosol size distribution measurements from Laramie, Wyoming (41^{o}N), using balloon-borne instruments, *J. Geophys. Res.*, pp. 4167–4179, 2003.

Dessler, A., E. Weinstock, E. Hintsa, J. Anderson, C. Webster, R. May, J. Elkins, and G. Dutton, An examination of the total hydrogen budget of the lower stratosphere, *Geophys. Res. Lett.*, **21**, 2563–2566, 1994.

Dobber, M., Absolute radiometric calibration calibration of the SCIAMACHY PFM, *TNSCIA1000TP/190 issue 1*, 1999.

Dorf, M., et al., Balloon-borne stratospheric BrO measurements: Intercomparison with ENVISAT/SCIAMACHY BrO limb profiles, *Atmos. Chem. Phys. (in prep.)*, 2005.

Dufour, G., et al., 4D comparison method to study NO_y partitioning in summer polar stratosphere. Influence of aerosol burden., *Atmos. Chem. Phys.*, **5**, 919–926, 2005.

Erle, F., Untersuchungen zur Halogenaktivierung der winterlichen Stratosphäre anhand flugzeuggestützter spektroskopischer Messungen, Ph.d. thesis, IUP Heidelberg, Heidelberg, 1999.

Erle, F., A. Grendel, D. Perner, U. Platt, and K. Pfeilsticker, Evidence of heterogeneous bromine chemistry on cold stratospheric sulphate aerosols, *Geophys. Res. Lett.*, **25**, 4329–4332, 1998.

Fahey, D., et al., The detection of large HNO_3 containing particles in the winter Arctic stratosphere, *Science*, **291**, 1026–1031, 2001.

Farman, J., B. Gardiner, and J. Shanklin, Large losses of total ozone in Antarctica reveal seasonal ClO_x/NO_x interaction, *Nature*, **315**, 207–210, 1985.

Fayt, C., and M. van Roozendael, WinDOAS 2.1. Software User Manual, *technical report*, 2001, see http://www.oma.be/BIRA-IASB/Molecules/BrO/WinDOAS-SUM-210b.pdf.

Ferlemann, F., N. Bauer, H. Harder, H. Osterkamp, D. Perner, U. Platt, M. Schneider, P. Vradelis, and K. Pfeilsticker, A new DOAS-instrument for stratospheric balloon-borne trace gas studies, *Appl. Opt.*, **39**, 2377–2386, 2000.

Ferlemann, F., et al., Stratospheric BrO profiles measured at different latitudes and seasons: Instrument description, spectral analysis and profile retrieval, *Geophys. Res. Lett.*, **25**, 3847–3850, 1998.

Fitzenberger, R., Investigation of the stratospheric inorganic bromine budget for 1996-2000: balloon-borne measurements and model comparisons, Ph.D. thesis, University of Heidelberg, 2000.

Fitzenberger, R., H. Bösch, C. Camy-Peyret, M. Chipperfield, H. Harder, U. Platt, B.-M. Sinnhuber, T. Wagner, and K. Pfeilsticker, First profile measurement of tropospheric BrO, *Geophys. Res. Lett.*, **27**, 2921–2924, 2000.

Fitzenberger, R., et al., Balloon-Borne DOAS Measurements for the Validation of SCIAMACHY UV/Vis Data Products, *Proceedings of the 15th ESA Symposium on European Rocket and Balloon Programmes and Related Research at Biarritz, France*, 2003.

Fleischmann, O., M. Hartmann, J. Orphal, and J. Burrows, UV absorption cross sections of BrO for stratospheric temperatures (203-293K) recorded by a Time-resolved Rapid Scan FTS method, 2000, for details see: http://www.iup.physik.uni-bremen.de/gruppen/molspec/bro2_page.html.

Frank, H., Ein Strahlungstransportmodell zur Interpretation von spektroskopischen Spurenstoffmessungen in der Erdatmosphäre, Diploma thesis, University of Heidelberg, 1991.

Fraser, P., D. Oram, C. Reeves, and S. Penkett, Southern hemispheric halon trends (1978-1998) and global halon emissions, *J. Geophys. Res.*, **104**, 15,985–15,999, 1999.

Frieß, U., T. Wagner, I. Pundt, K. Pfeilsticker, and U. Platt, Spectroscopic Measurements of Tropospheric Iodine Oxide at Neumeyer Station, Antarctica, *Geophys. Res. Lett.*, **28**, 1941–1944, 2001.

Friedl-Vallon, F., G. Maucher, A. Kleinert, A. Lengel, C. Keim, H. Oelhaf, H. Fischer, M. Seefeldner, and O. Trieschmann, Design and characterization of the balloon-borne Michelson Interferometer for Passive Atmospheric Sounding, *Appl. Opt.*, **43**, 3335–3355, 2004.

Funk, O., Photon Pathlength Distributions for Cloudy Skies: Oxygen A-Band Measurements and Radiative Transfer Model Calculations, Dissertation, Institut für Umweltphysik, Universität Heidelberg, 2000.

Gerilowski, K., Estimation of the absolute value of the ESM Diffuser BRDF from NASA sphere measurements from Optec-5, *IFE-SCIA-KG-200440128_ESM_BRDF_correction draft 1.3*, 2004.

Gomer, T., T. Brauers, F. Heintz, J. Stutz, and U. Platt, MFC version 1.98 user manual, *technical report*, University of Heidelberg, 1995.

Grainger, J., and J. Ring, Anomalous Fraunhofer line profiles, *Nature*, **193**, 762, 1962.

Grassi, L., XDoas - User Manual, *technical report*, 2002.

Gurlit, W., K. Gerilowski, and J. Burrows, SCIAMACHY solar irradiance validation using radiometric calibration of balloonborne, airbourne and ground-based spectrometers, *ESA SP-531*, 2003.

Gurlit, W., et al., The UV-A and visible solar irradiance spectrum: Inter-comparison of absolutely calibrated, spectrally medium resolved solar irradiance spectra from balloon- and satellite-borne measurements, *Atmos. Chem. Phys. Discuss.*, **4**, 8439–8469, 2004.

Haley, C., et al., Retrieval of stratospheric O_3 and NO_2 profiles from Odin Optical Spectrograph and Infrared Imager System (OSIRIS) limb-scattered sunlight measurements, *J. Geophys. Res.*, **109**, 16,303–16,321, 2004.

Hall, B., et al., Halocarbons and other atmospheric trace species, in *Climate Monitoring and Diagnostics Laboratory: Summary Report No. 26, 2000-2001*, pp. 106–135, NOAA/Climate Monitoring and Diagnostics Laboratory, Boulder, Colorado, 2002, edited by D.B. King and R.C. Schnell.

Hansen, D., and K. Mauersberger, The vapor pressure of HNO_3-H_2O solutions, *J. Phys. Chem.*, **92**, 6167–6170, 1988.

Harder, H., et al., Stratospheric BrO profiles measured at different latitudes and seasons: Atmospheric observations, *Geophys. Res. Lett.*, **25**, 3843–3846, 1998.

Harder, H., et al., Comparison of measured and modeled stratospheric BrO: Implications for the total amount of stratospheric bromine, *Geophys. Res. Lett.*, **27**, 3695–3698, 2000.

Harder, J. W., J. W. Brault, P. V. Johnston, and G. H. Mount, Temperature-Dependent NO_2 Cross Sections at High Spectral Resolution, *J. Geophys. Res.*, **102**, 3861–3879, 1997.

Hartley, W., On the absorption of solar rays by atmospheric ozone, *J. Chem. Soc.*, **39**, 111, 1881.

Hartmann, D., J. Holton, and Q.Fu, The heat balance of the tropical tropopause cirrus and stratospheric dehydration, *Geophys. Res. Lett.*, **28**, 1969–1973, 2001.

Harwood, M., and R. Jones, Temperature dependent ultraviolett-visible absorption cross sections of NO_2 and N_2O_4: low temperature mesurements of the equilibrium constant for 2 $NO_2 \longleftrightarrow N_2O_4$, *J. Geophys. Res.*, **99**, 22,955–22,964, 1994.

Haug, H., Raman-Streuung von Sonnenlicht in der Erdatmosphäre, diploma thesis, Institut für Umweltphysik, Ruprecht-Karls-Universität Heidelberg, 1996, d467.

Hausmann, M., U. Brandenburger, T. Brauers, and H.-P. Dorn, Detection of tropospheric OH radicals by long-path differential-optical-absorption spectroscopy: Experimantal setup, accuracy, and precision, *J. Geophys. Res.*, **102**, 16,011–16,022, 1997.

Hausmann, M., U. Brandenburger, T. Brauers, and H.-P. Dorn, Simple Monte Carlo methods to estimate the spectra evaluation error in differential-optical-absorption spectroscopy, *Appl. Opt.*, **38**, 462–475, 1999.

Hawat, T., C. Camy-Peyret, and R. Torguet, Description and performance of a balloon-borne heliostat for solar absorption measurements, *Proceedings of the 12th ESA Symposium on Rocket and Balloon Programmes and Related Research, Lillehammer, Norway*, 1995.

Hebestreit, K., Halogen Oxides in the Mid-Latitudinal Planetary Boundary Layer, Ph.d. thesis, IUP Heidelberg, 2001.

Henvey, L., and J. Greenstein, Diffuse radiation in the Galaxy, *Astrophys. Journal*, **93**, 70–83, 1941.

Hermans, private communication, 2002, for details see: http://www.oma.be/BIRA-IASB/Scientific/Topics/lower/LaboBase/acvd/O4Info.html.

Heue, K.-P., et al., Validation of SCIAMACHY tropospheric NO2-columns with AMAXDOAS measurements , *Atmos. Chem. Phys.*, **5**, 1039–1051, 2005.

Himmelmann, S., J. Orphal, H. Bovensmann, A. Richter, A. Ladstätter-Weissenmayer, and J. Burrows, First Observation of the OIO Molecule by Time-Resolved Flash-Photolysis Absorption-Spectroscopy, *Chem. Phys. Lett.*, **251**, 330, 1996.

Hoffmann, T., C. O'Dowd, and J. Seinfeld, IO homogeneous nucleation: An explanation for coastal new particle formation, *Geophys. Res. Lett.*, **28**, 1949–1952, 2001.

Holton, J., and A. Gettelmann, Horizontal transport and the dehydration of the stratosphere, *Geophys. Res. Lett.*, **28**, 2799–2802, 2001.

Hönninger, G., Referenzspektren reaktiver Halogenverbindungen für DOAS-Messungen, Diploma thesis, University of Heidelberg, 1999.

Hönninger, G., I. Pundt, T. Wagner, and U. Platt, MAX-DOAS: An Advanced Instrument for studying Tropospheric Chemistry, *Geophys. Res. Abs.*, **2**, 2000.

Hönninger, G., C. von Friedeburg, and U. Platt, Multi Axis Differential Optical Absorption Spectroscopy (MAX-DOAS), *Atmos. Chem. Phys.*, **4**, 231–254, 2004.

Hoskins, B., Toward a PV-Θ-view of the general circulation, *Tellus*, **43 AB**, 27–35, 1991.

Huppert, R., Theoretische und experimentelle Untersuchungen zum solaren I_0 Effekt, Diploma thesis, IUP Heidelberg, 2000.

Ingham, T., M. Cameron, and J. Crowley, Photodissociation of IO (355 nm) and OIO (532 nm): Quantum Yields for O(^{3}P) and I(^{2}P$_J$) Production, *J. of Phys. Chem. A*, **104**, 8001–8010, 2000.

Johnston, H., M. Paige, and F. Yao, Oxygen Absorption Cross Sections in the Herzberg Continuum and between 206 and 327 K, *J. Geophys. Res.*, **89**, 11,661–11,665, 1984.

Johnston, H. S., Reduction of stratospheric ozone by nitrogen oxide catalysts from supersonic transport exhaust, *Science*, **173**, 517–522, 1971.

Johnston, P., Making UV/Vis cross sections, reference Fraunhofer and synthetic spectra, 1996, unpublished manuscript.

Kirmse, B., A. Delon, and R. Jost, NO_2 absorption cross section and its temperature dependence, *J. Geophys. Res.*, **102**, 1997.

Kraus, S., DOASIS - DOAS Intelligent System, 2004, see http://www.iup.uni-heidelberg.de/bugtracker/projects/doasis/.

Kurucz, R., I. Furenhild, J. Brault, and L. Testermann, Solar flux atlas from 296 to 1300 nm, *National Solar Observatory Atlas No. 1*, 1984.

Kylling, A., UVspec: a program package for calculation of diffuse and direct UV and visible intensities and fluxes, 1995, available at: ftp://kaja.gi.alaska.edu/pub/arve.

Lary, D., and J. Pyle, Diffuse radiation, twilight and photochemistry, *J. Atmos. Chem*, pp. 373–392, 1991.

Lefèvre, F., G. Brasseur, I. Folkins, A. Smith, and P. Simon, Chemistry of the 1991-1992 stratospheric winter: Three-dimensional model simulations, *J. Geophys. Res.*, **99**, 8183–8195, 1994.

Lefèvre, F., F. Figarol, K. Carslaw, and T. Peter, The 1997 Arctic ozone depletion quantified from three-dimensional model simulations, *Geophys. Res. Lett.*, **23**, 2424–2428, 1998.

Llewellyn, E., et al., The OSIRIS instrument on the Odin spacecraft, *Can. J. Phys.*, **82**, 411–422, 2004.

Loewenstein, M., et al., New observations of the NO_y/N_2O correlation in the lower stratosphere, *Science*, **283**, 1993.

Lohberger, F., Imaging Spectroscopy of Atmospheric Trace Gases, Diplomarbeit, IUP Heidelberg, 2003.

London, J., Proceedings of the NATO Advanced Institute on the Atmospheric Ozone (Portugal), U.S. Dept. of Transportation, FAA - Washington, D.C., USA - No. FAA-EE-80-20, 1980.

Marquard, L., T. Wagner, and U. Platt, Improved Air Mass Factor Concepts for Scattered Radiation Differential Optical Absorption Spectroscopy of Atmospheric Species, *J. Geophys. Res.*, **105**, 1315–1327, 2000.

Marquard, L. C., Modellierung des Strahlungstransports in der Erdatmosphäre, Ph.D. thesis, Institut für Umweltphysik, Ruprecht-Karls-Universität Heidelberg, 1998.

McCormick, M., H. Steele, P. Hamill, W. Chu, and T. Swissler, Polar Stratospheric Cloud sightings by SAM II, *J. Atmos. Sci.*, **39**, 1387–1397, 1982.

McElroy, C., Stratospheric nitrogen dioxide concentrations as determined from limb brightness measurements made on June 17th 1983, *J. Geophys. Res.*, **93**, 7075–7083, 1988.

McElroy, M., R. Salawitch, C. Wofsy, and J. Logan, Reductions of Antarctic ozone due to synergistic interactions of chlorine and bromine, *Nature*, **321**, 759–762, 1986.

Meeus, J., *Astronomische Algorithmen*, Johann Ambrosius Barth Verlag, Heidelberg, 1992.

Michelsen, H., G. Manney, M. Gunson, and R. Zander, Correlations of stratospheric abundances of NO_y,O_3, N_2O and CH_4 derived from ATMOS measurements, *J. Geophys. Res.*, **103**, 28,347–28,359, 1998.

Misra, A., and P. Marshall, Computational investigations of iodine oxides, *J. Phys. Chem.*, **102**, 9056–9060, 1998.

Molina, L. T., and M. J. Molina, Production of Cl_2O_2 from the self reaction of the ClO radical, *J. Phys. Chem.*, **91**, 433, 1987.

Molina, L. T., and F. S. Rowland, Stratospheric sink for chlorofluromethanes: chlorine atom catalyzed destruction of ozone, *Nature*, **249**, 820–822, 1974.

Montzka, S., J. Butler, B. Hall, D. Mondell, and J. Elkins, A decline in tropospheric organic bromine, *Geophys. Res. Lett.*, **30**, 1826–1829, 2003.

Morgner, A., Ein objektorientiertes 3D-Monte-Carlo-Strahlungstransportmodell, Diploma thesis, IUP Heidelberg, Heidelberg, 2003.

Motzka, S., J. Butler, B. Hall, D. Mondeel, and J. Elkins, A decline in tropospheric organic bromine, *Geophys. Res. Lett.*, **30**, 1826–1829, 2003.

Murphy, D., and D. Thompson, Halogen ions and NO^+ in the mass spectra of aerosols in the upper troposphere and lower stratosphere, *Geophys. Res. Lett.*, **27**, 3217–3220, 2000.

Murphy, D., D. Thompson, and A. Middlebrook, Bromine, iodine, and chlorine in single aerosol particles at Cape Grim, *Geophys. Res. Lett.*, **24**, 3197–3200, 1997.

Murtagh, D., et al., An overview of the Odin atmospheric mission, *Can. J. Phys.*, **80**, 309–319, 2002.

Newman, P., J. Gleason, R. McPeters, and R. Stolarski, Anomalously low ozone over the Arctic, *Geophys. Res. Lett.*, **24**, 2689–2692, 1997.

Nicolet, M., On the Molecular Scattering in the Terrestrial Atmosphere: An Empirical Formula for its Calculation in the Homosphere, *Planet. Space Sci.*, **32**, 1467–1468, 1984.

Ocean Optics, Product Catalog, 2004.

Oltsman, S., and D. Hofmann, The increase in lower-stratospheric water vapor at a mid-latitude Northern Hemisphere site from 1981 to 1994, *Nature*, **374**, 146–149, 1995.

Osterkamp, H., Messung von atmosphärischen O_4-Profilen, Diploma thesis, University of Heidelberg, 1997.

Otten, C., Messungen stratosphärischer Spurenstoffe in den Wintern 1992/93 bis 1994/95 über Kiruna in Nordschweden, Dissertation, Institut für Umweltphysik, Universität Heidelberg, 1997.

Payan, S., C. Camy-Peyret, F. Lefevre, P. Jeseck, T. Hawat, and G. Durry, First direct simultaneous HCl and $ClONO_2$ profile measurements in the Arctic vortex, *Geophys. Res. Lett.*, **25**, 2663–2666, 1998.

Payan, S., et al., Diurnal and nocturnal distribution of stratospheric NO_2 from solar and stellar occultation measurements in the Arctic vortex: Comparison with models and ILAS satellite measurements, *J. Geophys. Res.*, **104**, 21,585–21,593, 1999.

Penndorf, R., Tables of the refractive index for standard air and the rayleigh scattering coefficient for the spectral region between 0.2 and 200 μ and their application to atmospheric optics, *J.Opt. Soc. Am.*, **47**, 176–182, 1957.

Perliski, L., and S. Solomon, On the evaluation of air mass factors for atmospheric near-ultraviolet and visible absorption spectroscopy, *J. Geophys. Res.*, **98**, 10,363–10,374, 1993.

Pfeilsticker, K., F. Erle, and U. Platt, Observation of the stratospheric NO_2 latitudinal distribution in the northern winter hemisphere, *J. Atmos. Chem.*, **32**, 101–120, 1999.

Pfeilsticker, K., H. Bösch, C. Camy-Peyret, R. Fitzenberger, H. Harder, and H. Osterkamp, First Atmospheric Profile Measurements of UV/Visible O_4 Absorption Band Intensities: Implications for the Spectroscopy and the Formation Enthalpy of the O_2-O-2 Dimer, *Geophys. Res. Lett.*, **28**, 4595–4598, 2001.

Pfeilsticker, K., et al., Lower stratospheric organic and inorganic bromine budget for the Arctic winter 1998/99, *Geophys. Res. Lett.*, **28**, 4595–4598, 2000.

Pfeilsticker, K., et al., Balloon-Borne DOAS Measurements of SCIAMACHY Level 1 and 2 Products, *Proceedings of the 16th ESA Symposium on European Rocket and Balloon Programmes and Related Research at St. Gallen, Switzerland*, 2003.

Platt, U., and D. Perner, Direct Measurements of Atmospheric CH_2O, HNO_2, O_3, NO_2 and SO_2 by Differential Optical Absorption in the Near UV, *J. Geophys. Res.*, **85**, 7453–7458, 1980.

Platt, U., and J. Stuz, *Differential Optical Absorption Spectroscopy (DOAS), Principle and Applications*, ISBN 3-340-21193-4, Springer Verlag, Heidelberg, 2005, in press.

Platt, U., D. Perner, and H. W. Pätz, Simultaneous Measurement of Atmospheric CH_2O, O_3 and NO_2 by Differential Optical Absorption, *J. Geophys. Res.*, **84**, 6329–6335, 1979.

Platt, U., D. Perner, G. W. Harris, A. M. Winer, and J. N. Pitts, Jr., Detection of NO_3 in the Polluted Troposphere by Differential Optical Absorption, *Geophys. Res. Lett.*, **7**, 89–92, 1980.

Portmann, R., S. Brown, T. Gierczak, R. Talukdar, J. Burkholder, and A. Ravishankara, Role of nitrogen oxides in the stratosphere: a reevaluation based on laboratory studies, *Geophys. Res. Lett.*, **26**, 2875–2878, 1999.

Prinn, R., et al., A history of chemically and radiatively important gases in air deduced from ALE/GAGE/AGAGE, *J. Geophys. Res.*, **105**, 17,751–17,792, 2000.

Pundt, I., J.-P. Pommereau, C. Phillips, and E. Latelin, Upper limit of iodine oxide in the lower stratosphere, *J. Atmos. Chem.*, **30**, 173–185, 1998.

Randall, C., et al., Validation of POAM III NO_2 measurements, *J. Geophys. Res.*, **107**, 4432–4435, 2002.

Renard, J., M. Pierre, C. Robert, and D. Huguenin, The possible detection of OBrO in the stratosphere, *J. Geophys. Res.*, **103**, 25,383–25,395, 1998.

Renard, J.-B., M. Pirre, C. Robert, G. Moreau, D. Huguenin, and J. R. III, Nocturnal vertical distribution of stratospheric O_3, NO_2, and NO_3 from balloon measurements, *J. Geophys. Res.*, **101**, 28,793–28,804, 1996.

Renard, J.-B., J. Ovarlez, G. Berthet, M. Pirre, J. Pommeraeu, and F. Goutail, SALOMON: A new, light balloon-borne UV-visible spectrometer for nighttime observations of stratospheric trace-gas species, *Appl. Optics*, **39**, 386–392, 2000.

Rinsland, C., et al., ATMOS measurements of H_2O+2CH_4 and total reactive nitrogen in the November 1994 Antarctic stratosphere: Dehydration and denitrification in the vortex, *Geophys. Res. Lett.*, **23**, 2397–2400, 1996.

Riviere, E., M.Pirre, G. Berthet, J.-B. Renard, F. Taupin, N. Huret, M. Chartier, B. Knudsen, and F. Lefèvre, On the interaction between nitrogen and halogen species in the Arctic polar vortex during THESEO and THESEO2000, *J. Geophys. Res.*, **108**, 8311, 2003.

Rodgers, C., *Inverse methods for atmospheric sounding*, World Scientific, Singapore, New Jersey, London, Hongkong, 2000.

Rodgers, C. D., Retrieval of Atmospheric Temperature and Composition From Remote Measurements of Thermal Radiation, *Rev. Geophys.*, **14**, 609–624, 1976.

Roedel, W., *Physik unserer Umwelt: die Atmosphäre*, Springer Verlag, Berlin, 2000, 3., überarb. und aktualisierte Aufl.

Roscoe, H. K., D. J. Fish, and J. R. L., Interpolation errors in UV-visible spectroscopy for stratospheric sensing: implications for sensitivity, spectral resolution, and spectral range, *Applied Optics*, **35**, 427–432, 1996.

Rothman, C., et al., The HITRAN molecular spectroscopic database: edition of 2000 including updates through 2001, *JQSRT*, **82**, 1–4, 2003.

Ruhnke, R., W. Kouker, and T. Reddmann, The influence of the OH+No+M reaction on the NO_y partitioning in the late winter 1992/1993 as studied with KASIMA, *J. Geophys. Res.*, **104**, 3755–3772, 1999.

Salawitch, R., D. Weisenstein, L. Kovalenko, C. Sioris, P. Wennberg, K. Chance, M. Ko, and C. Mclinden, Sensitivity of ozone to bromine in the lower stratosphere, *Geophys. Res. Lett.*, **32**, L05,811, 2005.

Sander, S., et al., Chemical Kinetics and Photochemical Data for Use in Atmospheric Studies, *JPL-Publication*, 2003.

Scaife, A., J. Austin, N. Butchart, S. Pawson, M. Keil, J. Nash, and I. James, Seasonal and interannual variability of the stratosphere diagnosed from UKMO TOVS analyzes, *Quart. J. Roy. Meteorol. Soc.*, **126**, 2585–2604, 2000.

Schulte, DAMF v1.22 - Direct Light Air Mass Factors, *internal paper*, 1996, IUP Heidelberg.

Seinfeld, J., and S. Pandis, *Atmospheric Chemistry and Physics: From Air Pollution to Climate Change*, 2000, john Wiley & Sons Inc., New York, Chichester, Weinheim, Brisbane, Singapore, Toronto.

Sherwood, S., and A. Dessler, A Model for Transport across the Tropical Tropopause, *J. Atm. Sci.*, **58**, 765–779, 2001.

Shine, K., The middle atmosphere in the absence of dynamical heat fluxes, *Q. J. R. Meteorol. Soc.*, **113**, 603–633, 1987.

Sioris, C., and W. Evans, Filling in of Fraunhofer and gas-absorption lines in sky spectra as caused by rotational Raman scattering, *Appl. Opt.*, **38**, 2706–2713, 1999.

Sioris, C., et al., Stratospheric profiles of nitrogen dioxide observed by OSIRIS on the Odin satellite, *J. Geophys. Res.*, **108**, 4215, 2003.

Solomon, S., Stratospheric ozone depletion: a review of concepts and history, *Rev. Geophys.*, **37**, 275–316, 1999.

Solomon, S., R. R. Garcia, F. S. Rowland, and D. J. Wuebbles, On the depletion of Antarctic ozone, *Nature*, **321**, 755–758, 1986.

Solomon, S., H. G. Mount, R. W. Sanders, and A. L. Schmeltekopf, Visible spectroscopy at McMurdo station, Antarctica 2. Observations of OClO, *J. Geophys. Res.*, **92**, 8329–8338, 1987.

Solomon, S., R. Garcia, and A. Ravishankara, On the role of iodine in ozone depletion, *J. Geophys. Res.*, **99**, 20,491–20,499, 1994.

Solomon, S., et al., Ozone depletion at mid-latitudes: coupling of volcanic aerosols and temperature variability to anthropogenic chlorine, *Geophys. Res. Lett.*, **25**, 1871–1874, 1998.

SPARC, SPARC Assessment of Upper Tropospheric and Stratospheric Water Vapor, SPARC Report No. 2, WCRP-113, WMO/TD-No 1043, SPARC Water Vapor Working Group, 2000.

Sturges, W., H. McIntyre, S. Penkett, J. Chappellaz, J.-M. Barnola, R. Mulvaney, E. Atlas, and V. Stroud, Methyl bromide, other brominated methanes, and methyl iodide in polar firn air, *J. Geophys. Res.*, **106**, 1595–1606, 2001.

Stutz, J., Messung der Konzentration troposhärischer Spurenstoffe mittels Differentieller-Optischer-AbsorptionsSpektroskopie: Eine neue Generation von Geräten und Algorithmen, Ph.D. thesis, Institut für Umweltphysik, Ruprecht-Karls-Universität Heidelberg, 1996, d455.

Stutz, J., and U. Platt, Numerical Analysis and Estimation of the Statistical Error of Differential Optical Absorption Spectroscopy Measurements with Least-Squares methods, *Appl. Opt.*, **35**, 6041–6053, 1996.

Stutz, J., and U. Platt, Improving long-path differential optical absorption spectroscopy with a quartz-fiber mode mixer, *Applied Optics*, **36**, 1105–1115, 1997.

Sugita, T., et al., Validation of O_3 measurements from the Improved Limb Atmospheric Spectrometer, *J. Geophys. Res.*, **107**, 8212–8215, 2002.

Thomason, L., and G. Taha, SAGE III aerosol extinction measurements: Initial Results, *Geophys. Res. Lett.*, **30**, 1631, 2003.

Thuillier, G., M. Herse, P. Simon, D. Labs, H. Mandel, and D. Gillotay, Observation of the UV solar irradiance between 200 and 350 nm during the ATLAS-1 mission by the SOLSPEC spectrometer, *Sol. Phys.*, **171**, 283–302, 1997.

Thuillier, G., M. Herse, P. Simon, D. Labs, H. Mandel, and D. Gillotay, Solar radiometry and solar spectral irradiance: Observation of the solar spectral irradiance from 200 nm to 870 nm during the ATLAS-1 and ATLAS-2 missions as measured by the SOLSPEC spectrometer, *Metrologia*, **35**, 689–697, 1998a.

Thuillier, G., M. Herse, P. Simon, D. Labs, H. Mandel, D. Gillotay, and T. Foujols, The visible solar spectral irradiance from 350 nm to 850 nm as measured by the SOLSPEC spectrometer during the ATLAS-1 mission, *Sol. Phys.*, **177**, 41–61, 1998b.

Toon, O., P. Hamill, R. Turco, and J. Pinto, Condensation of HNO_3 and HCl in the winter polar stratosphere, *Geophys. Res. Lett.*, **13**, 1284–1287, 1986.

van Leeuwen, S., Spectralon diffuser BRDF measurement, *ESA Technical Note TPD-SCIA-PhE-TN-009, issue 1*, 2003.

Vogt, R., R. Sander, R. von Glasow, and P. Crutzen, Iodine chemistry and its role in halogen activation and ozone loss in the marine boundary layer: a model study, *J. Atmos. Chem.*, **32**, 375–395, 1999.

Voigt, C., et al., Nitric Acid Trihydrate (NAT) in polar stratospheric clouds, *Science*, **290**, 1756–1758, 2000.

Voigt, S., J. Orphal, K. Bogumil, and J. P. Burrows, The temperature dependence (203-293 K) of the absorption cross-sections of O_3 in the 230 - 850 nm region measured by Fourier-transform spectroscopy, *J. of Photochemistry and Photobiology A: Chemistry*, **143**, 1–9, 2001.

von Friedeburg, C., Derivation of trace gas information combining Differential Optical Absorption Spectroscopy with Radiative Transfer modeling, Ph.d. thesis, IUP Heidelberg, Heidelberg, 2003.

von Friedeburg, C., TRACY manual, *internal paper*, IUP Heidelberg, 2004.

von Savigny, C., et al., Stratospheric Ozone Profiles retrieved from limb scattered sunlight radiance spectra measured by the OSIRIS instrument on the Odin satellite, *Geophys. Res. Lett.*, **30**, 1755–1758, 2003.

von Savigny, C., et al., The Ozone hole break-up in September 2002 as seen by SCIAMACHY on ENVISAT, *J. Atmosph. Sci. (in press)*, 2004.

Vradelis, P., Verbesserung der Ballon-DOAS-Messungen durch Streulichtunterdrückung und numerische Untersuchung des Auswerteprozesses, Diploma thesis, Institut für Umweltphysik, Universität Heidelberg, 1998.

Wagner, T., C. Leue, K. Pfeilsticker, and U. Platt, Monitoring of the stratospheric chlorine activation by Global Ozone Monitoring Experiment (GOME) OClO measurements in the austral and boreal winters 1995 to 1999, *J. Geophys. Res.*, **106**, 4971–4989, 2001.

Wagner, T., C. von Friedeburg, M. Wenig, C. Otten, and U. Platt, UV-visible observations of atmospheric O_4 absorptions using direct moonlight and zenith-scattered sunlight for clear-sky and cloudy sky conditions, *J. Geophys. Res.*, **107**, 4424, 2002.

Wagner, T., B. Dix, C. von Friedeburg, U. Frieß, S. Sanghavi, R. Sinreich, and U. Platt, MAX-DOAS O_4 measurements: A new technique to derive information on atmospheric aerosols - Principles and information content, *J. Geophys. Res.*, **109**, D22,205, 2004.

Wahner, A., A. R. Ravishankara, S. P. Sander, and R. R. Friedl, Absorption cross section of BrO between 312 and 385 nm at 298 and 223 K, *Chemical Physics Letters*, **152**, 507–512, 1988.

Walker, K., R. Saunders, J. Jackson, and D. McSparron, Spectral irradiance calibration, *NBS Special Publication*, p. 250, 1987.

Wang, H., D. Cunnold, L. Thomason, J. Zawodny, and G. Bodecker, Assessment of SAGE version 6.1 ozone data quality, *J. Geophys. Res.*, **?**, ?, 2002.

Wang, P., M. Bruns, M. Richter, J. Burrows, K.-P. Heue, I. Pundt, T. Wagner, and U. Platt, Validation of SCIAMACHY with AMAXDOAS measurements from the DLR Falcon, *Geophys. Res. Abstracts*, **5**, 9341, 2003.

Wennberg, P., J. Brault, T. Hanisco, R. Salawitch, and G. Mount, The atmospheric column abundance of IO: Implications for stratospheric ozone, *J. Geophys. Res.*, **102**, 8887–8898, 1997.

Wittrock, F., R. Müller, A. Richter, H. Bovensmann, and J. Burrows, Measurements of iodine monoxide (IO) above Spitsbergen, *Geophys. Res. Lett.*, **27**, 1471–1474, 2000.

WMO, Scientific Assessment of Ozone depletion: 1998, *World Meteorological Organization Global Ozone Research and Monitoring Project, Report 44*, 1999.

WMO, Scientific Assessment of Ozone depletion: 2002, *World Meteorological Organization Global Ozone Research and Monitoring Project, Report 47*, 2003.

Wofsy, S., M. McElroy, and L. Yung, The chemistry of atmospheric bromine, *Geophys. Res. Lett.*, **2**, 215–218, 1975.

Zöger, M., A. Engel, D. McKenna, C. Schiller, U. Schmidt, and T. Woyke, Balloon-borne in-situ measurements of stratospheric H_2O, CH_4, and H_2 at midlatitudes, *J. Geophys. Res.*, **104**, 1817–1826, 1999a.

Zöger, M., et al., Fast in-situ stratospheric stratospheric hygrometers: A new family of balloon-borne and airborne Lyman-α photofragment fluorescence hygrometers, *J. Geophys. Res.*, **104**, 1807–1816, 1999b.

Acknowledgements

Ein herzliches Dankeschön an alle, die mich während meiner Arbeit begleitet und unterstützt haben:

- Prof. Ulrich Platt für die Aufnahme am Institut und damit die Möglichkeit in einem so spannenden Umfeld arbeiten zu können.
- Prof. Konrad Mauersberger für die Übernahme der Begutachtung dieser Arbeit.
- Dr. Klaus Pfeilsticker für die Betreuung auf und zwischen den Meßkampagnen und die Impulse bei technischen und wissenschaftlichen Fragen.
- Den Mitgliedern der Ballongruppe (in order of appearance): Richard Fitzenberger, Hartmut Bösch, Martin Hirsekorn, Marcel Dorf, André Butz, Aaron Lindner und Ulrike Reichl für die tolle Atmosphäre ob am Institut, kalten Winternächten Kirunas, sonnigen Nachmittagen in "Apoolien" oder tropischen Nächten in Teresina. Besonderer Dank gebührt André Butz und Marcel Dorf für das aufmerksame Korrekturlesen.
- Den Erbauern des "großen" DOAS-Ballonspektrographen Frieder Ferlemann und Hartwig Harder, die auch nach ihrem Ausscheiden aus dem Institut immer mit Rat und Tat bei Problemen zur Verfügung standen.
- Den "Kalibrateuren" Wolfgang Gurlit und Konstantin Gerilowski für die nette Zusammenarbeit bei den zwar manchmal langwierigen aber schlußendlich doch immer erfolgreichen Nachtschichten.
- Merci beaucoup à Claude Camy-Peyret, Pascal Jeseck, Isabelle Pepin et le groupe de LPMA pour la bienne coorperation et l'aide pendent les campagnes. Merci aussi à Jean Evrard, André Laurens et l'équipe de CNES/Nacelles pointées pour l'aide avec la montage de l'instrument nouveau dans la nacelle et pour stabiliser l'azimuth.
- Hermann Oelhaf, Felix Friedl-Vallon, Anne Kleinert, Anton Lengel, Guido Maucher, Hans Nordmeyer und dem MIPAS-B2 Team für die Hilfe beim Einbau des Geräts auf deren Gondel und die Einführung in die kulinarischen Highlights Teresinas.
- Big thanks to Lorenzo Grassi for programming the Ocean Optics support for XDOAS and the "on-line help" during the Kiruna 2002 which made the miniDOAS virgin flight successful.
- Einen großen Dank auch an Stefan Kraus für die Implementierung meiner Sonderwünsche in das DOASIS-Program und seine stete Hilfe bei Computerproblemen.
- Und natürlich bei allen bisher nicht genannten Kollegen der Luftchemiegruppe und am IUP für die Gesprächskreise ob beim Mensaessen, Kaffeetrinken oder Stammtisch.
- Nicht zuletzt möchte ich mich bei meinen Eltern bedanken für die Unterstützung während des gesamten Studiums.